Production of *p*-wave Feshbach molecules from an ultra-cold Fermi gas

A thesis submitted in fulfilment of the requirements for the degree of Doctor of Philosophy at University College London

November 2011

UCL

Luke Austen

I, Luke Austen confirm that the work presented in this thesis is my own. Where information has been derived from other sources, I confirm that this has been indicated in the thesis.

Abstract

This thesis studies the dynamics of Feshbach molecule production from a gas of ultracold spin polarised Fermi atoms. A magnetic field is used to vary the strength of the interaction between the atoms exploring the limits of weakly paired atoms and tightly bound diatomic molecules. A mean field approximation is used to study the thermodynamics and dynamics of the system.

The two-body interaction is modelled using a separable potential that reproduces the near threshold behaviour of the system close to a Feshbach resonance. For atoms in the same internal state interactions occur in the *p*-wave, such that they have one quanta of relative orbital angular momentum ($\ell = 1$). The presence of a magnetic field fixes a quantisation axis for this angular momentum, leading to a splitting of the resonance feature into three components. It is shown that in certain cases these components may be treated separately on both a two-body and thermodynamic level. Consequently the many-body dynamics are also treated as if these components are distinct.

In order to study molecule production the gas is prepared in a state similar to the Bardeen-Cooper-Schrieffer (BCS) state in a superconductor. A linear sweep of the magnetic field through a Feshbach resonance is used to convert the weakly paired atoms into tightly bound molecules. The variation of the molecule production efficiency is studied as the initial temperature, density initial magnetic field and final magnetic field are varied. Also studied is the variation of molecule production as a function of the rate at which the magnetic field is varied. It is shown that high densities are needed to explore a range of initial magnetic fields and sweep rates.

Acknowledgements

Special thanks go to Dr Mark Lee and Dr Jordi Mur-Petit for their patience with my never-ending line of questions about physics, maths, Linux, Latex, Matlab and life. I also thank them for the help and mentoring they both provided me with over the past few years. I also thank Liam Cook for daily enlightening discussions on subjects most people would think impossible to discuss. I also thank Dr Marzena Szymańska for several illuminating discussions. I am also grateful to Prof. J. Tennyson for seeing me through the final stages of this work.

I thank Victoria for seeing me through this and never letting me down when I had given up on myself. Without saying my eternal gratefulness goes to my family and friends who have given me the much needed support throughout my studies.

I acknowledge the financial support from EPSRC. Further travel and summer school funds were provided by IOP, ESF and INTERCAN.

Contents

*This section follows Ref.[1]

List of Figures

List of Tables

Chapter 1

Introduction

In this chapter we lay the foundations for discussing the physics behind *p*-wave Feshbach molecule formation. We give a general introduction to the subject of cold gases and where the field stands in relation to other areas of physics. In particular we look at Fermi gases of ultracold atoms and compare them to condensed matter systems. We briefly look at the subject of the BCS-BEC crossover and why it has sparked interest in the physics community. We discuss some of the ways to cool and applications of cold molecules. Lastly we look at Feshbach resonances and introduce some experiments relative to the later content of the thesis. In particular we look at *p*-wave Feshbach resonances and *p*-wave molecule formation in ultracold gases.

1.1 Quantum matter

Quantum statistics are an essential tool in our modern understanding of the way the universe works. The restrictions imposed by them help us to understand the structure of matter at the microscopic level and the interactions that take place on that scale. The statistics that are derived in quantum mechanics are different from those which govern classical mechanics and for this reason they seem unfamiliar and at odds with our everyday experience. However, it is these strange laws that are directly responsible for the macroscopic world we see around us.

We would describe a classical gas using the Maxwell-Boltzmann distribu-

tion [5] which assumes that in principle every particle can be given a label that is distinguishable from every other particle; a view that makes sense to us in our everyday lives. With the birth of quantum mechanics it became obvious that the Maxwell-Boltzmann distribution could not account for certain phenomena; for example, the distribution of electrons in atomic orbitals. The explanation of the blackbody radiation spectrum provided by Planck [6] gave early indications of the non-classical behaviour of matter. Planck assumed the energy spectrum of a black body would be discrete and was thus able to derive his famous blackbody formula. It was the work of Bose [7] and Einstein [8] that extended this idea to an ideal gas of identical Bose atoms and by considering the number of particles in each mode they showed that at a sufficiently low temperature and high density the lowest mode would be populated by a significant fraction of the gas. This phenomenon has become known as Bose-Einstein condensation (see, for example [9, 10]). However, this is not true for all gases of particles. For a gas of identical fermions there can only ever be one particle per single particle state [11]. For this reason there will never be more than one particle in the lowest energy state. It would be a natural assumption that in some 'classical limit' the quantum statistics are well approximated by the Maxwell-Boltzmann statistics, which is the case, for example, at high temperature.

What is seen in fermions (particles with half-integer spin) is a manifestation of the Pauli exclusion principle which states that wave functions of identical fermions must be antisymmetric with respect to exchange of space or spin variables [11]. For identical bosons (particles with integer spin) the wave function must be symmetric. It is these statistics that lead to interesting non-classical physics.

In general, quantum matter refers to a substance in a state where quantum effects dominate over any others (e.g. thermal). One way of exploiting these quantum effects is to cool the system down in order to 'freeze' out the motion of the particles so that the only processes that can take place are those that are due to quantum mechanics. Examples of quantum matter include liquid helium, superconductors and ultracold atomic gases [12]. These examples have an important difference that we have neglected in the above discussion, which has only strictly referred to ideal gases where the particles are non-interacting. It turns out that

interactions between particles can significantly affect the behaviour of a system even when the interaction is very weak. Interactions are also important in an experimental sense since they are required to thermalize the system in order to cool it down to the point where the quantum nature of the substance can be explored. All of the examples just given require the presence of interactions to realise them experimentally. However, recent advances in experimental techniques enable experimentalists to probe degenerate Fermi gases with a degree of control hitherto unknown. For this reason they have attracted much attention over recent years, rewarding researchers with a wealth of new physics.

The physics of ultracold Fermi gases shares many properties with other Fermi systems. For this reason we start with a very broad introduction to systems of Fermi particles which should be familiar to an undergraduate student. This allows us to make some comparisons between ultracold Fermi gases and other systems of fermions.

1.1.1 Degenerate Fermi gases

An ideal gas of identical fermions will obey Fermi-Dirac statistics. This means that the number of particles per single particle state will be given by [5]

$$n(T,E) = \frac{1}{e^{\beta(E-\mu)}+1}. \tag{1.1}$$

Here, $\beta = 1/k_B T$, where k_B is Boltzmann's constant and T is the temperature of the gas. E is the energy of the single particle state and μ is the chemical potential of the gas. At zero temperature this becomes the step function

$$n(0,E) = \begin{cases} 1 & E < \mu \\ 0 & E > \mu \end{cases}. \tag{1.2}$$

In this case the chemical potential is referred to as the Fermi energy, E_F, which we have assumed to be positive, and all the single particle states are occupied by one, and only one, particle up to the Fermi energy. This is referred to as a degenerate Fermi gas. At finite temperatures the situation will not be so simple. The distribution function will deviate from the step function with increasing temperature.

This smooths the Fermi distribution about the chemical potential, which at finite temperature will no longer be equal to the Fermi energy. As the temperature is increased further the Fermi distribution will approach the limit

$$n(\infty, E) = \frac{1}{2}, \tag{1.3}$$

assuming that the chemical potential remains fixed and positive. This does not correspond to the classical limit described by Maxwell-Boltzmann statistics. For Maxwell-Boltzmann statistics to be valid we require that

$$e^{\beta(E-\mu)} \gg 1. \tag{1.4}$$

This same condition also has to be fulfilled for gases of bosons to behave as a classical gas. This limit is achieved for high values of T, provided the factor $(E - \mu)$ is positive.

1.1.2 The Fermi Liquid

The previous discussion refers only to a system of non-interacting fermions. When interactions are introduced further phenomena arise due to the quantum statistical properties of the particles. A weakly interacting system of Fermi particles is commonly referred to as a Fermi liquid, the theory of which was first developed by Landau [13, 14, 15, 16]. The foundation of this theory is to consider the excited states of the macroscopic system as a collection of elementary excitations, referred to as "quasi-particles", that are free to move in the volume occupied by the system. It is also assumed that the classification of the energy levels does not change when adiabatically going from a non-interacting system to a weakly interacting system. It can be shown that the quasi-particles that now form the system have a similar distribution function to that of the non-interacting system, specifically,

$$n(T, \epsilon[n]) = \frac{1}{e^{\beta(\epsilon[n]-\mu)} + 1}. \tag{1.5}$$

Here, $\epsilon[n]$ is the quasi-particle energy and is itself a functional, dependent on the specific density distribution. Again, a Fermi energy level, ϵ_F, will exist up to

which all the energy levels are filled and this energy level will, in general, not be the same as for the non-interacting system. This allows an effective mass to be defined for the quasi-particles,

$$m^\star = \frac{p_F}{v_F}. \tag{1.6}$$

Here $p_F = \sqrt{2m^\star \epsilon_F}$ is the Fermi momentum and $\mathbf{v}_F = \frac{\partial \epsilon}{\partial \mathbf{p}}_{p=p_F}$ is the velocity of the quasi-particles on the Fermi surface. The effective mass can then be used to determine the thermodynamic properties of the liquid by replacing the mass in the thermodynamic relations for the non-interacting gas by the effective mass.

Interactions between quasi-particles can be considered in how they affect the quasi-particle energy spectrum

$$\delta\epsilon(\mathbf{p}) = \int d^3p' f(\mathbf{p}, \mathbf{p}')\delta n(\mathbf{p}'), \tag{1.7}$$

where the function $f(\mathbf{p}, \mathbf{p}')$ is the second variational derivative with respect to δn of the total energy of the system per unit volume (see, for example [16]). Explicitly, this equation implies that a change in the density distribution of the particles will give rise to a change in the quasi-particle spectrum. It is also based on the assumption that the quasi-particles move in a self-consistent field due to the other quasi-particles. This is also true of non-equilibrium states of the system where the density distribution may also depend on spatial position and time. It can be shown that at a low enough temperature sound waves can propagate through the medium despite the fact that thermodynamic equilibrium is not established locally, a phenomenon known as zero sound. Quite how the density distribution is affected by the presence of interactions requires the use of the zero temperature Green's function method. It was shown by Migdal [17, 18] that the presence of interaction perturbs the Fermi distribution at zero temperature. For weak interactions the Fermi surface does not completely disappear and remains well defined. A detailed discussion of these ideas will not be reproduced here, but they are introduced in order to emphasise the importance of interactions in Fermi systems even at zero temperature. For a more detailed discussion the reader is directed towards the literature (for example [16]).

1.1.3 Fermi systems in nature

For an isotropic ideal gas of fermionic particles in an infinite three-dimensional square well it can be shown that there is a relationship between the volume of the box, V, the number of particles, N, and the value of the Fermi energy,

$$E_F = \frac{\hbar^2}{2m}\left(\frac{3\pi^2 N}{V}\right)^{2/3}. \tag{1.8}$$

This equation holds in the thermodynamic limit ($N \to \infty$, $V \to \infty$ with $\frac{N}{V}$ remaining constant). We can also define the Fermi temperature to be $T_F = E_F/k_B$.

From the above relations we can get some idea of to what extent systems of Fermi particles can be considered a degenerate Fermi gas. As a first example we can consider the free electrons in a metal and assume that the electrons are non-interacting. From Eq. (1.8) we can immediately guess that the Fermi energy, and hence Fermi temperature, is going to be high, unless the density is very small, due to the small mass of the electron. Now, the free electron density in copper is about 8.48×10^{28} m^{-3} which means that the Fermi temperature comes out on the order of 10^4 K. By putting this number into the Fermi distribution function shows that at room temperature (296 K) the function only deviates from the value 1 or 0 for energy levels with ±3 % of the Fermi energy. In other words the distribution of electrons in a metal at room temperature is near to that of a degenerate Fermi gas (See the solid blue line in Fig. 1.1).

Another naturally occurring Fermi system is a white dwarf star. White dwarf stars are very high density systems as they have a mass on the order of a solar mass but radii on the order of 10^{-2} solar radii. Under such conditions the electrons no longer bind to individual nuclei. The density of electrons in a white dwarf far exceeds that of metals at roughly 10^{36} m^{-3}. This gives a Fermi temperature on the order of 10^9 K. The internal temperature of a white dwarf is roughly 10^7 K meaning that the distribution of electrons will once again closely resemble that of a degenerate Fermi gas (see the dashed red line in Fig. 1.1).

These systems are interesting to study in themselves, however they can be difficult to access. In a solid the electrons have a complicated energy structure. The way the electrons interact with the lattice in a metal is not trivial and may involve

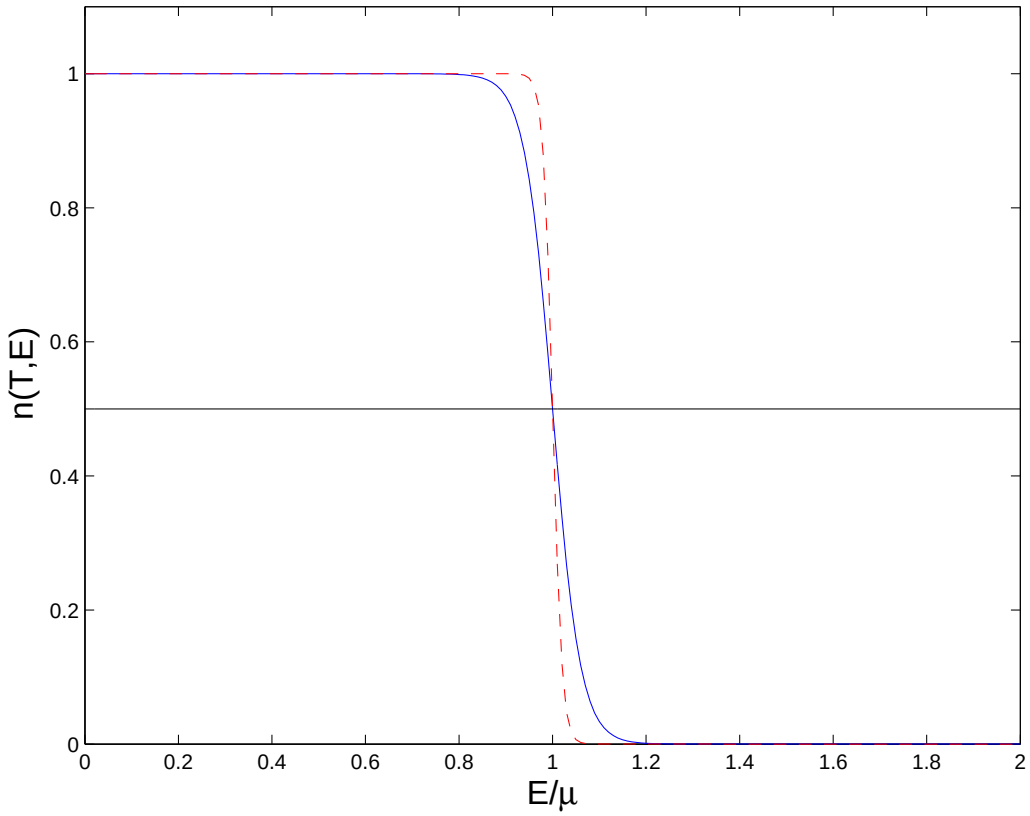

Figure 1.1: The Fermi distribution as a function of E/μ, where E is the single particle energy levels and μ is the chemical potential, which in this case has be taken to be constant and equal to the zero temperature Fermi energy. The red, dashed line corresponds to a ratio of $T_F/T \sim 10^2$ (for example, a white dwarf star). The solid, blue line corresponds to a ratio of $T_F/T \sim 10^1$ (for example, electrons in Copper at room temperature). The solid, black line corresponds to a ratio of $T_F/T \sim 10^{-6}$ (for example, an atomic gas of ^{40}K at room temperature). The atomic gas can be seen to be highly non-degenerate at room temperature.

complex scattering processes. This also makes it difficult to have control over the electron distribution in an experimental setting. White dwarfs are also experimentally unreachable for the time being. Ultracold Fermi gases provide systems that can be studied both theoretically and experimentally with a high degree of accuracy. The interactions between the atoms in the gas are generally quite well understood. The particles can also have few degrees of freedom making scattering processes relatively simple. Although the microscopics of the systems discussed here may differ considerably the macroscopics of the system can be quite similar. For this reason ultracold Fermi gases can be used to simulate phenomena in other Fermi systems and perhaps help us gain a better understanding of them.

1.2 Ultracold atomic gases

What about the Fermi energy/temperature of an atomic gas that has the density of air at room temperature? Assume that the density of air is on the order of 10^{25} m^{-3} and, for the sake of later discussion and the main focus of the thesis, consider ^{40}K, which is a fermionic isotope. In this case the Fermi temperature comes out as being on the order of 10^{-3} K, so that the ratio T_F/T is now on the order of 10^{-6}. The distribution function will now vary greatly from the step function associated with a degenerate Fermi gas, in particular for low energies the limiting value of the distribution is 0.5. In experiments performed on ultracold gases of atoms the densities are generally below 10^{15} m^{-3} giving a Fermi temperature on the order of 10^{-6} K and at room temperature the ratio T_F/T is now on the order of 10^{-9} (see the solid black line in Fig. 1.1). In order to recover the distribution that it is indicative of a degenerate Fermi gas in an atomic gas we have to increase the ratio T_F/T to a value greater than one. According to Eq. (1.8) this can be done by increasing the density of the gas, thus increasing the Fermi temperature. This is not always possible. The main reason for these gases being so dilute in the first place is to stop them forming solids. The main cause of solid formation is three body scattering processes. At the low densities reached in an ultracold gas the probability of three body scattering is negligible so that the gas state will remain. Another way to increase the ratio is to decrease the temperature of the gas. Recently, experimentalists have developed techniques that allow atomic Fermi

gases to be cooled to quantum degeneracy.

The subject of this thesis is molecule production in ultracold gases of spin-polarised Fermi atoms. Specifically we consider the case where a magnetic field that varies linearly with time is used to associate weakly paired Fermi atoms into tightly bound bosonic molecules [19]. From a descriptive point of view this sounds like a relatively simple problem. However, the physics underlying the problem can be complex and relies on phenomena associated with two-body physics and emergent phenomena associated with many-body physics.

Motivated by recent experiments that have produced ultracold molecules from single component Fermi gases [3, 20, 21, 22, 23] we study molecule production under similar conditions at the many-body mean field level. This approach has the advantage that it will include physics that is not included in a two-body approach. However, the mean field approximation will not account for all the physics in the experimental system. Further progress could be made by employing a Boltzmann equation [24], which would be a natural extension of this work. For the conditions we consider it should be possible to account for the majority of the physics by calculating the mean-field equations of the system.

We will see that there are differences between modelling a system of fermions where all the particles are in a single state and a system of fermions where the particles are in two different internal states. The source of this difference is the Pauli exclusion principle which states that wave functions of identical fermions must be anti-symmetric with respect to exchange of any variables. This affects the physics at a two-body level and consequently affects the physics at a many-body level.

1.2.1 Cooling and trapping atomic gases

The basic idea behind the cooling of atoms by laser light is relatively simple. An atom is subjected to two counterpropagating lasers such that the frequency of the lasers is detuned slightly below a resonance transition in the atom. When the atoms move in the direction of one of the lasers the Doppler shift will cause it to absorb photons from that direction. The photons will then be emitted randomly so that their velocity in the direction of the laser will decrease. Applied to a gas

of atoms this will cool the gas [9].

In practise the cooling of atoms is a very complicated and technically demanding procedure. Trapping the atoms so that they are able to stay in the path of the laser long enough to cool them is one of the hurdles that must be overcome. Usually a magneto-optical trap is used to do this. Given that the atoms are now in a magnetic field, a knowledge of their Zeeman structure becomes essential to understanding how they will behave. In fact it was shown that the Zeeman structure can be used to cool atoms to below the Doppler limit imposed by laser cooling alone, a technique now known as Sisyphus cooling [25]. The subject of laser cooling and the trapping of atomic gases is vast and is mentioned here to provide a background to the means by which atoms are cooled and the conditions under which experiments take place. The basics of laser cooling are covered in undergraduate textbooks [11] and several more advanced text books are available on the subject, for example [26].

The first laser cooling experiments were performed in 1978 on Mg ions [27] and Ba^+ ions [28]. These charged particles could be confined in an electric field configuration known as a Penning trap. The task still remained to cool neutral atoms that could not be contained in a Penning trap and did not have the long-range potential associated with an ion. This would mean cooling and then trapping the atoms in contrast to how ions had been trapped. Initial studies focused on solving two major problems: optical pumping and the changing Doppler shift. Optical pumping is due to the fact that the simplified model of laser cooling has assumed that an atom is a two level system. This is not the case and it can be possible for the atom to be put in a state that shuts off the further absorption of photons, thus precluding further cooling. This can be solved by using a repumping laser to put the atoms back into the correct states to allow further cooling. The changing Doppler shift is due to the slowing of the atoms as they cool. This means that a once resonant transition becomes inaccessible; the atom is seeing a different frequency of light. One solution to this was to change the frequency of the laser light to keep at the resonance frequency of the atoms [29, 30, 31, 32, 33]. The other solution is to change the energy of the atomic levels with a magnetic field to match them to the frequency of the laser [34, 35, 30, 36, 37, 38, 39].

Neutral atoms can still possess a magnetic moment which allows the atoms

to be trapped by a magnetic field. A variety of different magnetic field configurations have been used to trap neutral atoms [40, 41, 42, 43, 44]. One of the apparent limitations of laser cooling is the so-called Doppler limit which arises due to the equilibrium between the laser field and the spontaneous emission rate of the atoms. This means that the atoms can only be cooled so far. Evidence for cooling below the Doppler limit was observed [25] but not initially understood. Further experimental and theoretical investigation lead to an explanation of this occurrence [45]. The basic solution is that the atom is not a two level system, but has two possible ground states. As the polarisation of the laser light varies spatially it is possible to show that the potential an atom experiences is essentially an infinite hill against which it continually loses energy. This is known as Sisyphus cooling after the mythological Greek character condemned to repeatedly push a boulder up a hill only to have it roll down again. The success of these cooling methods, as well as the use of evaporative cooling, has lead to the achievement of Bose-Einstein condensation [46, 47] in neutral atoms and the onset of Fermi degeneracy a few years later [48]. Consequently Nobel prizes were awarded in 1997 for contributions to laser cooling and in 2001 for the achievement of Bose-Einstein condensation.

1.2.2 Ultracold Fermi gases as superfluids

The phenomenon of Bose-Einstein condensation (BEC) is characterised by a macroscopic occupation of the ground state of a many-particle system, such that the number of particles in the ground state is of the same order as the number of particles in the system [9, 10]. Bosons enter this region of quantum degeneracy when the interparticle spacing, $n^{-1/3}$, becomes comparable to the thermal de Broglie wavelength of the particles,

$$\lambda_T = \sqrt{\frac{2\pi\hbar^2}{mk_BT}}. \tag{1.9}$$

For a trapped gas the condensed fraction will now behave as a superfluid. An estimate can be made for the temperature at which BEC occurs, $T_{BEC} \sim \frac{2\pi\hbar^2}{mk_B}n^{2/3}$ and for ^{4}He this temperature turns out to be roughly 3 K, remarkably close to the experimentally measured temperature of 2.7 K. The masses of atoms are generally

within an order of magnitude of each other so it would be expected that the transition temperature for bosonic isotopes remains close to this estimate. However, the density of an atomic vapour can be of the order 10^{12}-10^{15} cm^{-3} as opposed to that of liquid ^{4}He which is typically 10^{22} cm^{-3}. This significantly lowers the transition temperature of the atomic vapour. We have already noted that the degeneracy temperature, E_F, of electrons in a metal can be several thousand Kelvin, but will not display any superfluid properties until roughly the same temperature at which ^{4}He displays superfluidity. To summarise this we can make a comparison between the degeneracy temperature, T_{Deg}, and the superfluid transition temperature T_{Tran} in bosons and in electrons in a metal (The term degeneracy temperature is here used to describe bosons and fermions for comparative purposes)

$$\text{Bosons} : T_{\text{Deg}} \sim T_{\text{Tran}},$$
$$\text{Electrons in metal} : T_{\text{Deg}} \gg T_{\text{Tran}}.$$

In 1986 Bednorz and Müller found that the compound $La_{2-x}Ba_xCuO_4$ was a superconductor at 35 K [49] and soon compounds were found with transition temperatures of above 100 K. So now the ratio $T_{\text{Tran}}/T_{\text{Deg}} \sim 10^{-2}$ for these so called high-T_C superconductors. It should be noted that the exact physics behind these high-T_C superconductors is not yet fully understood. What is important to note is that the process believed to be behind all superfluidity in weakly attractive Fermi systems is the formation of Cooper pairs. These are pairs of particles that have a binding energy due to many-body effects. Remarkably this means that no two-body bound state exists and the size of the pair can greatly exceed the average spacing of particles in the system. It is these pairs that then condense in a similar way to a system of bosons to form the superfluid state. This idea is the foundation of Bardeen-Cooper-Schrieffer (BCS) theory of superconductivity [50] which has had great success in describing the superfluid properties of Fermi systems and will be discussed in detail later. Up until now most of our discussion has focused on systems of non-interacting particles but we have mentioned that by adiabatically turning on a weak interaction we can end up with a Fermi liquid. In the case of superfluid Fermi systems this picture no longer applies as the single particle spectrum varies greatly from that of the non-interacting system. The many-body

binding energy we have discussed provides a gap in the energy spectrum, which is equal to the energy required to break a pair and, although no actual two-body bound state is present, it is necessary for the particles to have an attractive interaction. The superfluid state is one of the ways in which two-body interactions can lead to interesting many-body behaviour.

So what about the transition temperature in dilute gases of fermionic alkali atoms? We have already noted that the Fermi temperature (or degeneracy temperature), T_F, of Fermi gases of alkali atoms is on the order of 10^{-3} K at a density comparable to that of air and will be even smaller at the lower densities for which experiments are performed. It turns out that by using so-called Feshbach resonances the ratio $T_{\mathrm{Tran}}/T_{\mathrm{Deg}}$ can be as large as 0.2 for an ultracold gas of alkali atoms. There is then some hope that the study of ultracold Fermi gases can help with our understanding of high-T_C superconductors. It should also be noted that the existence of Feshbach resonances in gases of ultracold fermions is essential to studying this superfluid behaviour. Feshbach resonances allow the interaction strength between two atoms to be varied using a magnetic field to the extent that a pair with a large spatial extent can be converted to a molecule with a small spatial extent [19, 51]. One important difference between these two limits is that in the first the average spacing of the atoms in the gas is less than the average size of a pair. In the other limit the average extent of the molecule is much less than the average distance between atoms. There is a region in which the average distance between the atoms and the spatial extent of a pair will be on the same scale. This limit is referred to as the crossover (or BCS-BEC crossover, for reasons that will be explained later) region, which will be looked at in more detail later. It is also the case that electrons in high-T_C superconductors have a similar ratio of their pair size to their interparticle spacing as the atoms in this region. Another similarity between these situations is that above T_C both are expected to form non-condensed pairs. This is usually referred to as the pseudo-gap region. Recent studies have provided evidence for this ‘pre-pairing’ in Fermi gases [52, 53]. There is also evidence that above the transition temperature the gas may behave as a normal Fermi liquid [54, 55]. It should be remembered that in spite of these similarities in behaviour between high-T_c superconductors and ultracold Fermi gases the exact mechanisms behind the phenomena are very different in both cases.

1.2.3 Analogies with other systems

Systems of ultracold atoms can be used as model systems for studying other complex phenomena due to the level of control that can be implemented in a cold atom experiment. Interactions between atoms are generally well understood and have been the subject of significant investigation from a variety of disciplines. Furthermore, the diluteness of atomic gases means that, in many cases, it is only the long-range form of the interaction that is resolved and the short range behaviour can be approximated. These facts make them attractive to theorists and experimentalists alike and much progress has been made since atoms were first laser cooled [10, 56, 57].

We have already seen that systems of Fermi atoms have something in common with high-T_C superconductors when the system is strongly interacting. It is therefore hoped that by understanding the cold atom system further progress can be made into how high-T_C superconductors work. Similarly the neutrons in a neutron star will be strongly interacting. Other suitable strongly interacting systems can be found in quark matter [58]. There have also been attempts to test string theory by measuring the limit of the viscosity in a strongly interacting Fermi gas [59]. Cold atom systems therefore share some properties with systems from areas of physics that may not, initially, seem intuitive.

1.2.4 Feshbach resonances

In general a scattering resonance occurs due to the existence of a metastable state in the system [60]. This shows itself as an increase in the scattering cross-section peaked about some energy. These are widely studied in all areas of physics as they can provide so much useful information to test theory against experiment. Feshbach resonances occur when the scattering energy of a particle pair is coincident with a bound state of the two-body system [61, 62, 63]. In the context of cold gases it is possible to create zero-energy Feshbach resonances by manipulating the interparticle interaction using a magnetic field [19, 51]. What is remarkable is that this can have a profound effect on the many-body state of the system.

For the sake of simplicity we can start off by considering two asymptotically separated alkali atoms in a magnetic field. The hyperfine energy levels of the

atoms will be split by the magnetic field into Zeeman states that have a magnetic field dependent energy. As the atoms are brought together the valence electrons and the nuclei will start to respond to each other [11]. At some point the energy levels of the pair will deviate from that of a pair of asymptotically separated atoms. By changing the strength of the magnetic field it is then possible to alter the interaction between the particles to the extent that a two-body bound state forms between the particles. Furthermore it is possible to spatially localise these pairs so that they form a tightly bound diatomic molecule. If we imagine that the particles have zero relative motion then as the bound state appears in the system the zero-energy scattering cross-section will display a resonance [60]. This is referred to as a zero-energy Feshbach resonance. A more detailed discussion of the physics behind this two-body process is given in chapter 2.

Now what about the many-body system? If we start our system of Fermi atoms in the same situation as the two-body case in which all the particles are asymptotically separated from each other we will start with a non-interacting Fermi gas. We assume that the system is in the ground state and remains so as we increase the attraction between the atoms to form a superfluid with long-range Cooper pairs. We can further increase the interatomic attraction through a Feshbach resonance to the limit where the pairs are localised molecules forming a Bose-Einstein condensate. This is referred to as the BCS-BEC crossover as it takes the many-body state from a gas resembling a superconductor described by BCS theory to a a state describe by a Bose-Einstein condensate [56]. Questions still remain as to what happens in the intermediate region where the interparticle spacing is comparable to the size of the pairs in the gas. This is referred to as the strongly interacting region and it is where the zero energy two-body cross section is at its largest value.

We have here said nothing about the effects of the trapping potential. In a cold atom experiment the trapping potential often resembles that of a harmonic oscillator. The solution of the Schrödinger equation for a particle confined by a harmonic potential is a common undergraduate physics problem. It is well known that the single particle energy levels are evenly spaced and the ground state has a non-zero energy. For non-interacting fermions we could then fill up these single particle states with one particle in each state if the particles are in the same internal state. If the two particles interact we would have to solve the Schödinger equation

in the centre of mass frame. We can allow the strength of the two-body interaction to vary with a magnetic field across a Feshbach resonance so that a two-body bound state may exist between the pair. It turns out that as the system passes through the Feshbach resonance a molecular bound state only forms for the lowest energy state of the pair [64]. The other energy levels are shifted to a lower energy. This means that no matter how many Fermi particles are in the trap only two will ever form a molecule. This is not what happens in the experiments where a considerable fraction of the gas can be converted into molecules. The reason for this difference between the theory above and experiment is that we have ignored the many-body effects in the gas.

1.3 Cold molecules

The study of molecular gases and chemical reactions is complicated by the thermal motion of particles [65]. This not only affects the external degrees of freedom but the internal states of the participating particles. By cooling molecules it may be possible to study chemical reactions with fewer degrees of freedom revealing the mechanisms behind chemical reactions and perhaps discovering new chemistry.

At sub-mK temperatures scattering processes become relatively simple [66]. This regime of temperature is usually referred to as ultracold by cold molecule researchers [67]. At slightly higher temperatures, on the range of 1 mK to 2 K, more scattering channels become energetically available and the situation becomes more complicated. However, at these temperatures there can still be a finite number of scattering channels making the problem theoretically tractable. Even at these temperatures quantum effects are important as the de Broglie wavelength, Eq. (1.9), of even large molecules can start to exceed the interparticle spacing. This can mean that the effects of the trapping potential can be be resolved by the many-body system [68]. The ability to tune the trapping potential means that the chemical reaction rate may be altered by changing the external potential. It has been shown that chemical reaction processes are expected to be very efficient in these low temperature regions [69, 70, 71, 72].

Several methods for creating cold and ultracold molecules have been developed and can be broadly split into two categories. The first consists of cooling a

gas of atoms and then associating the atoms into molecules. The second method involves the direct cooling of preformed molecules. Molecules have a complex energy structure and this makes it difficult for them to be cooled using lasers, unlike atoms that can be cooled to ultracold temperatures. Recently there has been evidence of experimental success in laser cooling of a diatomic SrF molecule down to 300 μK [73]. This is possible due to the fortunate energy level structure of SrF. Creating molecules from ultracold gases of atoms has been a popular method of molecule production due to the success in laser cooling the atoms themselves. This usually done by either photoassociation [74], where a light pulse is used to excite the atoms into a molecular level, or by the use a Feshbach resonances [19] and in some cases both methods are used. These methods have the drawback that it is not yet possible to create large molecules of more than a few atoms and there are a limited number of systems that lend themselves to these techniques. Methods for directly cooling molecules include using high pressure vapours, Starck decelerators and buffer gas cooling. The drawback of these methods is that they do not allow the molecules to reach temperatures as low as those achieved with Feshbach association or photoassociation, but they can be applied to larger and a wider variety of molecules. Many of these techniques are still in their infancy but progress has been rapid since the first achievement of Bose-Einstein condensation in 1995 and the prospect of future development with an aim to observing cold chemistry looks extremely promising (see, for example, Krems [65] and the references therein).

Other applications of cold molecules range from practical to fundamental. Recently cold molecules experiments have been used to measure the magnetic moment of the electron [75]. It is also possible that cold molecules can open up new realisations of atomic and molecular lasers. There is also a lot of current research into the possibility of realising quantum computing. It is believed that cold molecules may be a candidate for realising such systems [76].

1.3.1 *s*-wave molecules

Even if we have restricted our discussion of molecule formation to fermions, quantum statistics still have a further role to play in the story of Feshbach molecule

production. We here briefly discuss some of the differences between molecules formed from pairs of Fermi atoms in different internal states and molecules formed from pairs of Fermi atoms in the same internal state. As already mentioned quantum wave functions of identical fermions must be antisymmetric with respect to exchange of any space or spin variables. So let us consider a gas of Fermi atoms in two equally populated internal states. We can assume that the total spin of the atom determines the internal state of the atom and label the two spin states 'up' and 'down', for the sake of argument. Furthermore, we choose the spin part of the wave function to be a spin singlet state. The total wave function of two particles with opposite spin will now be a product

$$\Psi(\mathbf{r}_1, \mathbf{r}_2) = \psi(\mathbf{r}_1, \mathbf{r}_2)\chi(\uparrow, \downarrow). \tag{1.10}$$

Under these circumstances the spin part of the wave function will be antisymmetric leaving the spatial part as symmetric. In the limit of low energy this turns out to be isotropic and assuming a spherical solution to the Schrödinger equation means we can write the spatial part of the wave function as

$$\psi(\mathbf{r}_1, \mathbf{r}_2) = \psi(|\mathbf{r}_1 - \mathbf{r}_2|)Y_{00}\left(\frac{\mathbf{r}_1 - \mathbf{r}_2}{|\mathbf{r}_1 - \mathbf{r}_2|}\right), \tag{1.11}$$

where $Y_{00}(\Omega) = \frac{1}{\sqrt{4\pi}}$ is the lowest order spherical harmonic. In the first experiments on creating Feshbach molecules from Fermi atoms a gas was prepared that has two spin states occupied like in the example above [77]. We refer to the molecules formed as *s*-wave molecules due to the symmetry of the pair wave function.

1.3.2 *p*-wave molecules

In the case of a Fermi gas where all the atoms occupy the same internal, or spin state, the wave function of an atom pair can be written as

$$\Psi(\mathbf{r}_1, \mathbf{r}_2) = \psi(\mathbf{r}_1, \mathbf{r}_2)\chi(\uparrow, \uparrow). \tag{1.12}$$

The space part of the wave function must now be antisymmetric and for low energies the lowest partial wave solution to the Schrödinger equation will be

$$\psi(\mathbf{r}_1, \mathbf{r}_2) = \psi(|\mathbf{r}_1 - \mathbf{r}_2|) Y_{1m_1}\left(\frac{\mathbf{r}_1 - \mathbf{r}_2}{|\mathbf{r}_1 - \mathbf{r}_2|}\right), \tag{1.13}$$

where $Y_{1m_1}(\Omega)$ is the ℓ=1 spherical harmonic. The subscript m_1 denotes the projection of the angular momentum onto the chosen z-axis. Because the ℓ=1 component is referred to spectroscopically as the p-wave we refer to the molecules that are formed as p-wave molecules. p-wave Fermi gases (gases in which the particles interact through a p-wave interaction) share some similar properties to ^{3}He [78, 79] and highly ferromagnetic superconductors such as Strontium Ruthenate [80, 81]. In the case of ultracold gases the experimental set up provides a natural z-axis for the system; namely the magnetic field axis. This implies that there are three possibilities for the projection of the angular momentum vector. This splitting between projections of the angular momentum vector has been seen in experiments [2].

1.3.3 Towards creating p-wave Feshbach molecules

The previous sections have given an introduction to where ultracold Fermi gases stand in the wider context of physics and more specifically a gentle introduction to the subject of cold molecule production. In this section we discuss the experimental progress that has been made with p-wave Feshach molecules.

Extensive experiments and theoretical investigations have been carried out to determine the parameters that classify the resonances in the fermionic species of ^{6}Li and ^{40}K. For theoretical purposes these parameters can be used to model the Feshbach resonances for further calculations, as they are in this thesis. Initial investigations on potassium isotopes determined the scattering lengths and low energy scattering cross sections [82, 83]. These investigations indicated that ^{40}K would be a likely candidate for cooling to the quantum degenerate regime. This limit was subsequently achieved [48]. Further investigation led to the determination of an s-wave magnetic-field Feshbach resonance located at a magnetic field strength of 202.1 G [84, 85]. It was this resonance that was first used to create ultracold molecules from a gas of Fermi atoms [86]. This experiment created

molecules in a gas at a temperature of less than 150 nK by using a sweep of the magnetic field with a linear time dependence. By changing the magnetic field from a value above the resonance to a value below it at a rate of down to 12.5 G/ms they created molecules with lifetimes on the order of 1 ms and measured the binding energy of these molecules. Subsequently a similar technique was used to show that it was possible to produce a BEC of the molecules by observing the emergence of a bimodal momentum distribution, a signature of BEC [87]. In these experiments the ratio T_F/T could be as high as 25 in the initial gas, meaning it would be highly degenerate if we assumed it to be an ideal gas. This system was also used to observe condensation of Cooper pairs on both sides of the resonance [88]. This differs from the previous case where molecules were condensed due to the fact that the particles forming the condensate retain fermionic degrees of freedom and the pairing occurs due to many-body effects. In this experiment linear sweeps of the magnetic field were used with a different purpose. The initial stage of the experiment involved holding the value of the magnetic field above the resonance to allow the BCS state to form. The sweeps in to the BEC side were performed at speeds that exceeded the average collision rate of the particles in the gas but slow enough to allow the creation of molecules. This would mean that any condensate fraction observed after the sweep would come from pairs condensed before the sweep and it was shown that this fraction could not come from a condensate formed during the sweep itself. It should be emphasised that in both the creation of the molecular condensate and the Cooper pair condensate a linear sweep of the magnetic field was an essential ingredient.

Investigations into ^{6}Li identified the existence of *s*-wave Feshbach resonances located at 800 G and 19800 G [89]. The low field resonance was later determined to be at 860 G, with a further narrow resonance existing at 530 G [90]. The 860 G resonance was used to observe the gas on the strongly interacting regime and subsequently, molecules have been created using both the 530 G [91] and the 860 G resonances [92]. Molecular condensation has also been achieved on the BEC side of the resonance [93, 94], as well as reclaiming the degenerate Fermi gas by sweeping the magnetic field back above the resonance [95].

The *s*-wave experiments have attracted a lot of attention as their experimental detection is somewhat easier. Interest in the *p*-wave resonances has arisen due

to the study of non-*s*-wave pairing in fermion systems, such as unconventional superconductors, as already mentioned. A variety of superfluid phenomena have been predicted for non-*s*-wave pairing [96, 97] and it is hoped that they can be realised in an ultracold gas of identical fermions with *p*-wave interactions [98, 99, 100].

Similar to the studies on *s*-wave molecules, initial experiments located the position of Feshbach resonances in ^{40}K [2, 101] and ^{6}Li [20, 102]. The first of these experiments, performed by Regal *et al*. [101], concentrated on ^{40}K and measured the first *p*-wave Feshbach resonance in a single component atomic gas. Remarkably this was located at 198.8 G which is very close to the location of the *s*-wave resonance in ^{40}K, but seemingly a complete coincidence. The JILA group continued to investigate this resonance [2] and identified a doublet feature of the resonance; as the gas was cooled below around 1 μK two distinct peaks were seen in the elastic cross section separated by about 0.5 G. This is explained by a non-vanishing dipole-dipole interaction in the *p*-wave, leading to the energy of the resonance state to depend upon the projection of the pair's relative orbital angular momentum onto the magnetic field axis.

Experiments on ^{6}Li identified three *p*-wave Feshbach resonances corresponding to three different hyperfine state combinations [20]. In one of these combinations it was possible to create molecules using a linear sweeps of the magnetic field. With a sweep rate of around 0.25 G/ms they were able to convert around 20 % of the atoms into molecules. A further experimental study by Schunck *et al*. [102] located the same three resonances. Two of these resonances arise from atoms prepared in the same internal state, while the other arises from atoms prepared in two different internal states but at a higher temperature, where the *p*-wave cross section is not yet suppressed. In contrast to the case of ^{40}K these resonances are at very different magnetic fields to the *s*-wave resonances. Another difference between the two atomic species is the absence of an observed dipole-dipole splitting in ^{6}Li.

More recently *p*-wave Feshbach molecules have been formed from a gas of ^{40}K [21]. In this experiment molecules were formed using a resonantly oscillating magnetic field and not by linear sweeps of the magnetic field. This allowed for a measurement of the binding energies of the molecules and also a measurement of

the magnetic moment. A similar method was used to create molecules in ^{6}Li [3]. A comparison of the results of these two experiments explains the reason why the dipole-dipole splitting was not observed (and has not been observed) in ^{6}Li, namely that the magnetic moment of the $^6Li_2$ molecule is much larger than that of the $^{40}K_2$ molecule.

Even more recently properties of the $^6Li_2$ *p*-wave Feshbach molecules were studied where the molecules were formed using linear sweep of the magnetic field [22, 23]. In these experiments ramp speeds of less than 0.4 G/ms were used to sweep the atoms into bound molecules, producing a comparatively small yield of molecules with 15 % by Inada *et al*. [22] and 3 % by Maier *et al*. [23]. Maier *et al*. [23] attribute the difference between the two values of the molecule production as coming from a temperature difference between the two experiments (9 μK [23] as opposed to 1 μK in [22]). As yet no condensation of Cooper pairs has been detected in these systems. These works also propose the use of an optical lattice to study *p*-wave superfluidity where even richer phases are predicted [103]. There have already been experimental studies into *p*-wave Fermi gases in optical lattices [104], where the interest is focused on Feshbach resonances and possible superfluidity in low dimensions.

Some of these experiments have measured the lifetimes of Feshbach molecules. Gaebler *et al*. [21] found the $m_1 = \pm 1$ ^{40}K molecules to have a lifetime of 1 ms and the $m_1 = 0$ ^{40}K molecules to have a lifetime of 2.3 ms, where the lifetime is defined as the time taken for the molecule density to reach $1/e$ of its initial value. These measurements were taken on the positive scattering length side of the resonance where a true molecular bound state exists and are somewhat shorter than predicted with a multichannel theory [21]. On the other side of the resonance the particles can be confined by the centrifugal barrier as 'quasi bound' molecules. The lifetime of these molecules decreases as the magnetic field moves away from the resonance and the tunnelling time through the centrifugal barrier decreases. The same group had previously measured the lifetimes of *s*-wave molecules for which the 'quasi bound' state does not exist [87, 105]. They showed that on the BEC side of the resonance the lifetime of the molecules can increase up to 100 ms. This is due to the long-range nature of *s*-wave Feshbach molecules, so such a situation is not expected to occur in *p*-wave Feshbach molecules as their spatial

extent is limited by the centrifugal barrier.

For ^{6}Li it was initially only possible to hold *p*-wave molecules in the magnetic trap for up to a few ms [3]. This is a short time compared to *s*-wave experiments in which $1/e$ lifetimes were measured up to 500 ms [92] and molecules were held in a trap for up to 1 s [91]. It was shown by Inada *et al*. [22] that a large contribution to molecule loss comes from atom-dimer collisions and it is possible to increase the molecule lifetime by removing unpaired atoms from the system. They also note that this still leaves a low elastic to inelastic collision ratio that would preclude cooling into a condensed state.

1.4 Outline of the thesis

We have introduced the topic of Feshbach molecule creation in ultracold gases and shown that it has links to many areas of physics from fundamental to practical. These seemingly simple systems can provide rich physics that has already been the subject of many studies and will continue to be so in years to come. We wish to study the mean field effects of *p*-wave Feshbach molecule production from a linear sweep of a magnetic field. If an ideal experiment were to be performed to test the results of this study it would follow this procedure:

1. The gas is cooled to a superfluid state at some fixed initial magnetic field, B_i, on the side of the resonance where no two-body bound state exists. This fixes the initial density and temperature of the gas.

2. The magnetic field is varied linearly with time to some final magnetic field position, B_f, on the other side of the resonance. The atomic density and temperature are held constant throughout the course of the experiment.

3. The number of molecules created from the gas is counted.

4. The experiment is repeated with the magnetic field varying at a different rate to before.

5. The whole process is repeated with varying values of B_i and B_f.

6. The initial temperature and density of the gas is varied and the process is repeated.

For the above procedure we can identify five independent variables can be varied: The initial atomic density, n, the initial temperature of the gas, T, the initial magnetic field, B_i, the final magnetic field B_f and the rate at which the magnetic field is varied, $\dot{B}$. It should be noted that experimentalists may not have the ability to control all of these variables in a real experiment. In order to achieve the aims of this study we have divided the thesis into three chapters, each providing a different ingredient. We have seen that Feshbach resonances are fundamental to our approach to creating cold molecules. In order to include this phenomenon we have to suitably model the two-body physics; the subject of Chapter 2. We have also related the importance of the BCS theory of superconductivity to understanding the behaviour of ultracold Fermi gases. This is the subject of chapter 3. Lastly, in Chapter 4 we consider the mean field dynamics of a single component Fermi gases and the role it plays in molecule production.

Chapter 2

Scattering theory and Bound states

The basics of single channel scattering are presented in a general manner. This is applied to the situation of low energy scattering between atoms in identical internal states. The two channel model is introduced so that scattering parameters can be related to the experimentally measurable quantities and the variation of these parameters in the vicinity of a Feshbach resonance is discussed. A separable model for the *p*-wave interaction is introduced and used to recover the binding energy of the *p*-wave molecule, as well as the low energy scattering properties of two atoms.

We have seen in the previous chapter that quantum statistics are important for the study of molecule formation in a single component atomic Fermi gas. In this chapter we will see how these laws affect the physics at the two particle level. We have also seen that the degeneracy temperature, the Fermi temperature, in these systems is very low compared to that of electrons in a metal. The source of this is the high mass of an atom (compared to an electron) and the low density of the atomic cloud. In an ultracold gas the kinetic energy of the particles is low and since we are considering ground state alkali atoms the collision energies will also be small and it is common to take the low energy limit when considering scattering processes. Furthermore, the density of an ultracold atomic gas is, in general, orders of magnitude lower than that of air, making collisions of more than two particles rare. We therefore neglect the probability of three or more

body collisions in the gas. This general statement about dilute ultracold gases has implications on how it is possible to model two-body interaction. In particular it is often the case that the all interactions are replaced by a single parameter, the scattering length. This approach has had much success in describing dilute atomic Bose-Einstein condensates [10, 9] and atomic Fermi gases [56]. The majority of these studies have focused on the modelling of *s*-wave interactions, due to their relative simplicity and the accessibility of experiments. More recently there have been studies into modelling interactions between fermions in the same internal state [97, 106, 99, 107], which have been motivated by experiments on *p*-wave interacting gases [101, 2, 102, 20, 21, 3]. These theoretical studies have extended methods used to model *s*-wave interaction in ultracold gases due to the success of these approaches in modelling *s*-wave gases close to resonance. In this thesis we take a similar approach to modelling the *p*-wave interaction by extending a method previously used to model the two-body interaction close to an *s*-wave Feshbach resonance.

In this chapter we review some of the basics of quantum scattering theory. We then apply this to a an atomic system close to a zero-energy *p*-wave Feshbach resonance. We derive a form of the two-body interaction that can be used in a many particle theory. To do this we require that our potential reproduces the low energy spectrum of the system as it is this region that is accessed in an ultracold gas of atoms and is especially relevant to the case of zero-energy Feshbach resonances [19].

2.1 Basics of scattering theory

In quantum mechanics a pair of scattered particles in free space with relative momentum **p** can be described in the centre-of-mass frame by a superposition of an incoming plane wave and an outgoing spherical wave [11]

$$\psi(\mathbf{r}) = \frac{1}{(2\pi\hbar)^{3/2}}\left(e^{ipz/\hbar} + f(p,\theta)\frac{e^{ipr/\hbar}}{r}\right). \tag{2.1}$$

Here, $p = |\mathbf{p}|$, the angle θ is measured with respect to the collision axis $\hat{\mathbf{z}}$, r is the interparticle distance and $f(p,\theta)$ is the scattering amplitude. In scattering

experiments the physically measurable quantity is the differential cross-section given by,

$$\frac{d\sigma}{d\Omega} = |f(p,\theta)|^2 , \tag{2.2}$$

where Ω is the solid angle in the direction of $\hat{\mathbf{p}}$. Quantum statistics modify the elastic scattering amplitude and therefore the differential cross-section for identical particles. The indistinguishability of the scattering product under particle exchange requires the scattering wave function to be symmetric (antisymmetric) for bosons (fermions)

$$\psi(\mathbf{r}) = \frac{1}{\sqrt{2}\,(2\pi\hbar)^{3/2}} \left(e^{ipz/\hbar} \pm e^{-ipz/\hbar} + [\, f(p,\theta) \pm f(p,\pi-\theta)] \, \frac{e^{ipr/\hbar}}{r} \right), \tag{2.3}$$

where the plus (minus) sign refers to bosons (fermions).

2.1.1 Single channel scattering in partial waves

In the case of a spherically symmetric potential it is often convenient to expand the wave function into its angular momentum components. The radial Schödinger equation in the centre-of-mass system for the ℓth partial wave is written [60]

$$\left[\frac{d^2}{dr^2} - \frac{\ell\,(\ell+1)}{r^2} - U(r) + k^2 \right] \psi_{\ell k}(r) = 0, \tag{2.4}$$

where

$$U(r) = \frac{2\mu V(r)}{\hbar^2}, \tag{2.5}$$

and μ is the reduced mass of the particles. The distance between the atoms is r and the angular wave number is k ($p = \hbar k$). $V(r)$ is the interparticle potential which at large interparticle separation is assumed to be of the form

$$V(r) = O\left(\frac{1}{r^\nu}\right), \tag{2.6}$$

where $\ell < (\nu - 3)/2$. This ensures that the following discussion of threshold behaviour is valid [60]. In the context of diatomic molecules $V(r)$ is usually determined by the Born-Oppenheimer approximation [11]. To describe scattering

Eq. (2.4) has the boundary conditions

$$\psi_{\ell k}(0) = 0, \tag{2.7}$$

and

$$\psi_{\ell k}(r) \underset{r\to\infty}{\sim} \hat{j}_\ell(kr) + k\, f_\ell(k)\hat{h}^+_\ell(kr), \tag{2.8}$$

where $\hat{j}_\ell(kr)$ and $\hat{h}^+_\ell(kr)$ are the Riccati-Bessel and Riccati-Hankel functions respectively. The Riccati-Bessel function is the solution to Eq. (2.4) in the absence of an interaction, so the presence of the potential is responsible for the second term in Eq. (2.8). The effects of the interaction are described by the partial wave scattering amplitude

$$f_\ell(k) = \frac{e^{i\delta_\ell(k)} \sin\delta_\ell(k)}{k}, \tag{2.9}$$

where $\delta_\ell(k)$ is the partial wave phase shift. By using the asymptotic form of the Riccati-Bessel functions as $r \to \infty$, the long range asymptotic form of the wave function can be written as

$$\psi_{\ell k}(r) \underset{r\to\infty}{\sim} e^{i\delta_\ell(k)} \sin\left(kr - \frac{\ell\pi}{2} + \delta_\ell(k)\right). \tag{2.10}$$

Hence, the phase shift describes the effect of the potential on the free radial wave function at large interparticle separation. In the vicinity of a resonance in a partial wave the corresponding cross-section is assumed to dominate. The partial wave phase shift changes rapidly as the energy of the system is varied near such a resonance. This causes a change in the partial wave scattering amplitude as given by Eq. (2.9).

In the low energy limit, the free solution (i.e. $V(r) = 0$) to the Schrödinger equation can be expressed using its asymptotic form

$$\hat{j}_\ell(kr) \underset{k\to 0}{\sim} \frac{(kr)^{\ell+1}}{(2\ell+1)!!}. \tag{2.11}$$

By solving Eq. (2.4) at zero momentum it is possible to obtain the zero-energy radial functions. These are functions of position only and can be normalised to recover Eq. (2.11) divided through by $k^{\ell+1}$. As an illustrative example the zero-

energy radial wave functions for the *s*-wave and *p*-wave are plotted in Fig. 2.1 for a square well potential.

The partial wave "scattering length" is defined as

$$a_\ell = \lim_{k\to 0}\left[-\frac{\tan\delta_\ell(k)}{k^{2\ell+1}}\right]. \tag{2.12}$$

For the $\ell = 1$ partial wave this quantity has the dimensions of volume. As the energy of the system goes to zero the relevant scattering parameter becomes the partial wave "scattering length" and it is related to the low energy scattering amplitude through

$$f_\ell(k) \approx -a_\ell k^{2\ell}. \tag{2.13}$$

The derivation of this quantity for ℓ=0 and ℓ=1 is presented in Appendix A for a spherical well and plotted in Fig. 2.1. The phase shift can be modified by varying the strength of the interatomic potential. In turn this causes a change in the partial wave scattering length according to Eq. (2.12). When the phase shift crosses $\pi/2$ the scattering length has a singularity, associated with the appearance or disappearance of a bound state in the potential [60]. The scattering length is positive when the potential supports a bound state close to the dissociation threshold energy. When the bound state becomes degenerate with the threshold the scattering length is singular and then becomes negative as the state becomes a resonance state moving into the continuum.

2.2 Physical origin of Feshbach resonances

In general, atoms have a complicated internal structure. The spin of the nucleus of the atom couples to the electronic spin which can also be coupled to the orbital angular momentum of the electrons [11]. Alkali atoms have only one valence electron and in the ground state this electron has no orbital angular momentum about the nucleus of the atom. This relative simplicity has made the study of alkali atoms accessible to theorists and experimentalists alike. The experimental success in the trapping and cooling of clouds of alkali metal atoms [108, 109, 25], culminating in the achievement of quantum degeneracy in both bosons [46] and

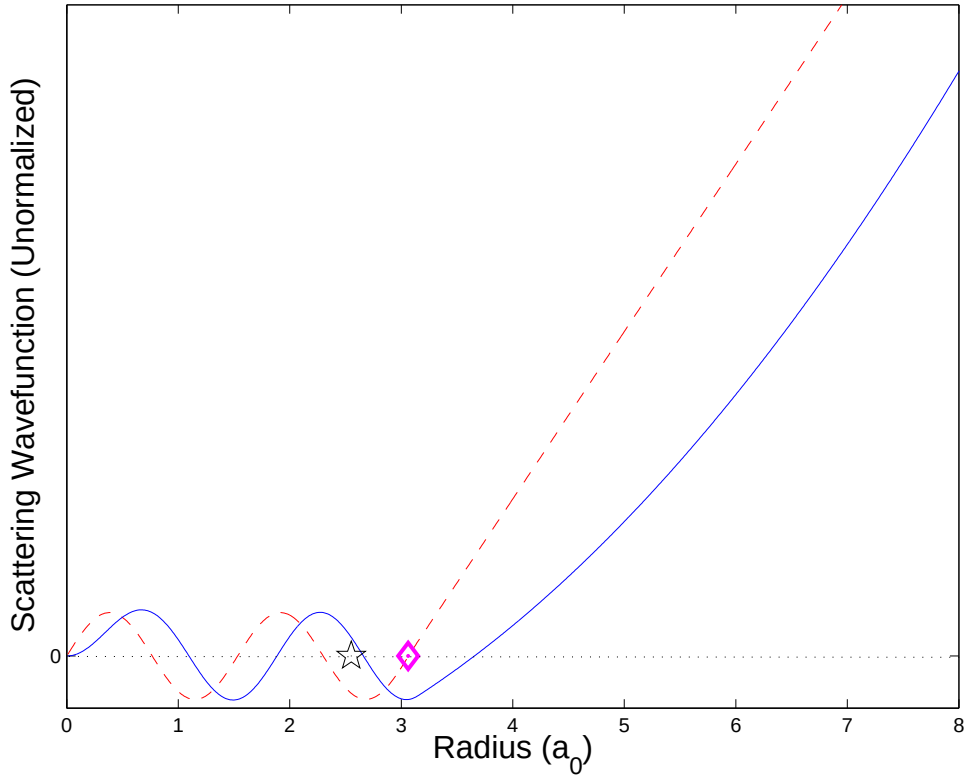

Figure 2.1: zero-energy radial wave functions for the model potential of a square well. The depth of the well is given by $2\mu V_0/\hbar^2 = 16.8$ a.u., while its radius is 3.15 a.u.. The dashed line is the *s*-wave solution and the solid line is the *p*-wave solution of Eq. (2.4). Their long range behaviours can be compared with Eq. (2.11) divided through by the appropriate factors of k. The diamond marks the position of the *s*-wave scattering length. This is also the point at which the asymptotic form of the scattering wave function crosses the radial axis. The star marks the position of the cube root of the *p*-wave scattering volume. This quantity is related to the point at which the asymptotic form of the scattering wave function crosses the radial axis through $r_1 = \sqrt[3]{3a_1}$.

fermions [48], has made them the most studied in the cold gas community. Different combinations of nuclear spin and electronic spin will give rise to different energy levels known as hyperfine energy levels and it is the value of the quantum number representing this total angular momentum that designates the atom as a composite boson (integer spin) or fermion (half-integer spin). This total angular momentum will couple to an external magnetic field splitting the hyperfine energy levels due to the Zeeman effect [110]. In the field of ultracold gases magnetic fields can be used to induce Feshbach resonances making it important to understand the interatomic interaction between atoms in the presence of this magnetic field.

A pair of asymptotically separated alkali metal atoms in a magnetic field can be described by their individual hyperfine and Zeeman states. For a full description of the two atom problem it would be necessary to include all the different hyperfine and Zeeman state configurations in a coupled-channels calculation [111]. Each configuration, known as a channel, of a pair of atoms can be given a unique label $\alpha = \left\{f_1 m_{f_1} f_2 m_{f_2} \ell m_\ell\right\}$, where f_i labels the hyperfine state of atom i at zero magnetic field, m_{f_i} labels the Zeeman state and ℓ and m_ℓ give the relative angular momentum of the two atoms and the projection of this vector onto the magnetic field axis, respectively. For collisions of identical particles in the same internal state there are restrictions on the values of ℓ for a given configuration: even values for bosons, odd values for fermions [60]. In other cases all values of ℓ are permitted.

The concept of open and closed channels is important in the discussion of magnetically induced Feshbach resonances in gases of ultracold atoms. Consider a pair of atoms asymptotically prepared in a particular spin configuration which we shall call the entrance channel. In the limit of zero-energy collisions the other Zeeman configurations can be labelled with respect to the energy of this channel. Configurations with energies lower than this channel are said to be open channels, while configurations with greater energy are said to be closed channels. For a single species of mass m the coupled channels Schrödinger equation is given by [111]

$$\frac{\partial^2 F_\alpha(r,E)}{\partial r^2} + \frac{m}{\hbar^2}\sum_\beta \left[E\delta_{\alpha\beta} - V^{\text{eff}}_{\alpha\beta}(r)\right] F_\beta(r,E) = 0. \tag{2.14}$$

Here, $F_\alpha(r,E) = r\psi_\alpha(r,E)$, where $\psi_\alpha(r,E)$ is the component of the full wave function in the asymptotically separated atom channel. The effective potential is given by

$$V^{\text{eff}}_{\alpha\beta}(r) = \left[E_{f_1 m_{f_1}} + E_{f_2 m_{f_2}} + \frac{\hbar^2 \ell(\ell+1)}{m r^2}\right]\delta_{\alpha\beta} + V^{\text{int}}_{\alpha\beta}(r), \tag{2.15}$$

which now includes the centrifugal part of the kinetic energy. The Zeeman energy of a non-interacting atom is given by $E_{f_i m_{f_i}}$. The part of the potential describing interactions can be separated into two terms

$$V^{\text{int}}_{\alpha\beta}(r) = V^{\text{el}}_{\alpha\beta}(r) + V^{ss}_{\alpha\beta}(r). \tag{2.16}$$

The first term arises from the strong electronic interaction and does not couple partial waves, but is non-diagonal in the single particle spin basis. This term usually contains the familiar Born-Oppenheimer potential curves. The second term has off diagonal elements in all indices and arises from the weak relativistic spin-spin interaction. When referring to ultracold gases a Feshbach resonance occurs when a molecular bound state corresponding to one of the open or closed channels is tuned to be degenerate with the zero energy threshold of the entrance channel. Fig. 2.2 illustrates a two channel model of a magnetically induced Feshbach resonance. The energy of the closed channel can be tuned with a magnetic field until it is degenerate with the threshold energy of the open channel. This is due to the individual Zeeman states of the atoms changing their energy as the magnetic field strength is varied and in turn the energy of the molecular states will change. If the open channel and close channel have different magnetic moments then their energy will change relative to each other. In this figure we choose the dissociation threshold of the open channel as the zero of energy, so that the energy of the closed channel is varied. When the resonance state supported by the closed channel becomes degenerate with the open channel dissociation threshold a bound state forms in the coupled system referred to as a Feshbach molecule.

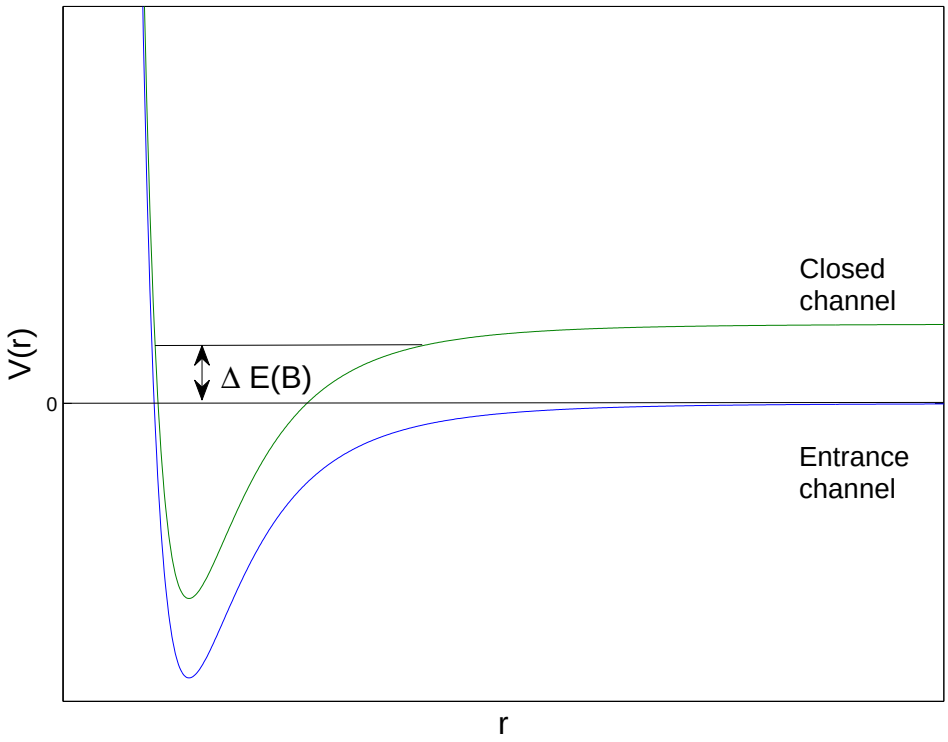

Figure 2.2: Cartoon of a Feshbach resonance. The two channels represent different Zeeman configurations of the asymptotically separated atoms. The atoms are initially prepared in the entrance channel and the closed channel supports the resonance state. The energy of the closed channel is tuned using a magnetic field. As the energy of the resonance state becomes degenerate with the zero of energy in the open channel a Feshbach resonance occurs and a bound state of the system appears.

2.3 Two-channel model of a Feshbach resonance

A full description of Feshbach resonance phenomena requires a solution to Eq. (2.14) with the inclusion of an external magnetic field that couples to the individual Zeeman states. Including this full coupled channels treatment in a many-body treatment is computationally taxing. Luckily, for many cases involving atom-atom collisions it is sufficient to consider only two Zeeman channels. The general Hamiltonian for the two-channel model is given by [112, 62, 61, 113]

$$H = \begin{pmatrix} H_{\rm bg} & W \\ W & H_{\rm cl} \end{pmatrix}. \tag{2.17}$$

Where $H_{\rm bg}$ supports the entrance channel scattering states in which the atoms are initially prepared and $H_{\rm cl}$ supports the resonance state, $|\phi_{\rm res}\rangle$, of energy $E_{\rm res}$, which satisfies the Schrödinger equation

$$H_{\rm cl}|\phi_{\rm res}\rangle = E_{\rm res}|\phi_{\rm res}\rangle. \tag{2.18}$$

Here W describes the interchannel coupling. The Hamiltonian of Eq. (2.17) will support two-component eigenstates corresponding to the entrance channel and a single closed channel. To model the physics of a magnetic field induced Feshbach resonance we allow $H_{\rm cl}$ to be magnetic field dependent ($H_{\rm cl} = H_{\rm cl}(B)$), this corresponds to the entrance and closed channel states possessing different magnetic moments. As the magnetic field is varied the energy difference between the two states varies. The Feshbach resonance occurs when the energy of the resonance state supported by $H_{\rm cl}(B)$ is degenerate with the entrance channel dissociation threshold. As in the coupled channels case described above, a bound state appears, referred to as a Feshbach molecule, on the positive scattering length side of the resonance. This Feshbach molecule has components in both channels.

It is useful to formulate this problem in terms of Green's operators with a complex argument, z, that has dimensions of energy. For the entrance channel component the Green's operator is

$$G_{\rm bg}(z) = \left(z - H_{\rm bg}\right)^{-1}. \tag{2.19}$$

For the closed channel component the Green's operator is

$$G_{\rm cl}(B,z) = (z - H_{\rm cl}(B))^{-1}\,, \tag{2.20}$$

where the magnetic field dependence of the closed channel Hamiltonian, and hence the closed channel Green's operator, has been made explicit. In the vicinity of a resonance it can be assumed that the detuning of the resonance energy from the entrance channel dissociation energy is small compared with the spacing between different vibrational energy levels in the closed channel. Therefore Eq. (2.20) will be dominated by the contribution from the resonance state leading to the single resonance approximation [66, 114],

$$G_{\rm cl}(B,E) \approx |\phi_{\rm res}\rangle \frac{1}{E - E_{\rm res}(B)} \langle \phi_{\rm res}|. \tag{2.21}$$

On the side of the resonance where the scattering "length" is negative the Hamiltonian of Eq. (2.17) describes scattering for positive energies. In the case where $H_{\rm bg}$ and $H_{\rm cl}$ support no deeply bound states, such that the resonance state is the only state supported by either Hamiltonian, the scattering solutions will be the only solutions to the Schödinger equation. In this situation the resonance state would be in the energetic continuum of the entrance channel and the components of the scattering wave function at momentum $\mathbf{p}$, take the form

$$|\phi_{\mathbf{p}}^{\rm bg}\rangle = |\phi_{\mathbf{p}}^{(+)}\rangle + G_{\rm bg}\left(\frac{p^2}{2\mu} + i0\right) W|\phi_{\mathbf{p}}^{\rm bg}\rangle, \tag{2.22}$$

$$|\phi_{\mathbf{p}}^{\rm cl}\rangle = G_{\rm cl}\left(B, \frac{p^2}{2\mu} + i0\right) W|\phi_{\mathbf{p}}^{\rm bg}\rangle \approx |\phi_{\rm res}\rangle \frac{\langle \phi_{\rm res}|W|\phi_{\mathbf{p}}^{\rm bg}\rangle}{\frac{p^2}{2\mu} - E_{\rm res}}, \tag{2.23}$$

where the single resonance approximation of Eq. (2.21) has been made in Eq. (2.23). The $i0$ term ensures the argument approaches the real axis from the upper half of the complex plane and corresponds to an outgoing spherical wave. This is also the meaning of the (+) superscript in the first term of Eq. (2.22). For the entrance

channel component the scattering component can be written as

$$|\phi_{\mathbf{p}}^{(+)}\rangle = |\mathbf{p}\rangle + G_0\left(\frac{p^2}{2\mu} + i0\right) T_{\rm bg}\left(\frac{p^2}{2\mu} + i0\right)|\mathbf{p}\rangle, \tag{2.24}$$

which is known as the Lippmann-Schwinger equation [115] and would fully describe the scattering problem in the absence of the closed channel. Here $T_{\rm bg}\left(\frac{p^2}{2\mu} + i0\right)$ is the T-matrix for background scattering [116], related to the background scattering amplitude through

$$f_{\rm bg}(\mathbf{p}, \mathbf{p}') = -(2\pi)^2\mu\hbar\langle\mathbf{p}|T_{\rm bg}\left(\frac{p^2}{2\mu} + i0\right)|\mathbf{p}'\rangle. \tag{2.25}$$

The plane wave state, $|\mathbf{p}\rangle$, can be expanded in the partial wave basis

$$\langle\mathbf{r}|\mathbf{p}\rangle = \frac{e^{i\frac{\mathbf{p}\cdot\mathbf{r}}{\hbar}}}{(2\pi\hbar)^{3/2}} = \sqrt{\frac{2}{\pi\hbar^3}}\sum_{\ell m} e^{i\frac{\pi}{2}\ell} j_\ell\left(\frac{pr}{\hbar}\right) Y_{\ell m}(\hat{\mathbf{r}}) Y^\star_{\ell m}(\hat{\mathbf{p}}), \tag{2.26}$$

where the functions $Y_{\ell m}(\Omega)$ are the spherical harmonics, a set of orthogonal angular solutions to Laplace's equation normalised on the unit sphere. In the position space basis Eq. (2.24) has the asymptotic long range expansion

$$\phi_{\mathbf{p}}^{(+)}(\mathbf{r}) = \frac{4\pi}{(2\pi\hbar)^{3/2}}\sum_{\ell m} Y_{\ell m}(\hat{\mathbf{r}})\left[i^\ell j_\ell\left(\frac{pr}{\hbar}\right) + f_\ell^{\rm bg}(p)\frac{e^{ipr/\hbar}}{r}\right] Y^\star_{\ell m}(\hat{\mathbf{p}}). \tag{2.27}$$

The partial wave background scattering length is defined as the low energy limit of the background partial wave scattering amplitude, such that in the limit $p \to 0$

$$f_{\ell m}^{\rm bg}(p) \approx -a_{\ell m}^{\rm bg}\frac{p^{2\ell}}{\hbar^{2\ell}}. \tag{2.28}$$

Here, $a_{\ell m}^{\rm bg}$ corresponds to the value of the scattering "length" at magnetic field values far from resonance and would be equivalent to Eq. (2.13) in the absence of the closed channel. By inserting Eq. (2.27) into Eq. (2.22) the full partial wave

scattering amplitude can be written as

$$f_{\ell m}(p) = f_{\ell m}^{\rm bg}(p) - \mu\pi\hbar \frac{\langle \phi_{p\ell m}^{(-)}|W|\phi_{\rm res}\rangle\langle\phi_{\rm res}|W|\phi_{p\ell m}^{(+)}\rangle}{\frac{p^2}{2\mu} - E_{\rm res} - \langle\phi_{\rm res}|WG_{\rm bg}\left(\frac{p^2}{2\mu}+i0\right)W|\phi_{\rm res}\rangle}. \tag{2.29}$$

In the low energy limit these parameters can be related to the physically relevant parameters associated with a zero-energy resonance. The denominator of the second term in Eq. (2.29) can be associated with the detuning of the resonance energy with respect to the zero-energy threshold

$$E_{\rm res} - \langle\phi_{\rm res}|WG_{\rm bg}\left(\frac{p^2}{2\mu}+i0\right)W|\phi_{\rm res}\rangle = \lim_{p\to 0} -\frac{\partial E_{\rm res}}{\partial B}(B - B_{\ell 0}). \tag{2.30}$$

Here, $B_{\ell 0}$ represents the value of the magnetic field at which the resonance occurs and $\frac{\partial E_{\rm res}}{\partial B}$ is the magnetic moment difference between the Feshbach resonance state and a pair of asymptotically separated atoms. The numerator can be identified with

$$\mu\pi\hbar\langle\phi_{p\ell m}^{(-)}|W|\phi_{\rm res}\rangle\langle\phi_{\rm res}|W|\phi_{p\ell m}^{(+)}\rangle = \lim_{p\to 0}\frac{p^{2\ell}}{\hbar^{2\ell}}a_{\ell m}^{\rm bg}\frac{\partial E_{\rm res}}{\partial B}\Delta B_\ell \tag{2.31}$$

with ΔB_ℓ representing the width of the resonance. This is measured as the range of magnetic fields from the resonance position to where the scattering length crosses zero. We can put these expression into Eq. (2.29) and taking the low energy limit we obtain an expression for the partial wave scattering "length" in terms of experimentally measurable quantities [113, 107],

$$a_\ell(B) = a_\ell^{\rm bg}\left(1 - \frac{\Delta B_\ell}{B - B_{\ell 0}}\right). \tag{2.32}$$

As the magnetic field in Eq. (2.32) is changed from a value greater than $B_{\ell 0}$ to a value less than $B_{\ell 0}$ the scattering length becomes singular and changes sign as required by the previous discussion of low energy Feshbach resonances. Therefore Eq. (2.32) provides a simple parametrisation of the scattering length in the vicinity of a resonance. A plot of the scattering length using this formula and the experimentally measured parameters listed in appendix B is shown in Fig. 2.32 about the 202.107 G s-wave resonance in ^{40}K. In the vicinity of a resonance this formula reproduces the experimentally measured scattering length very well. As the

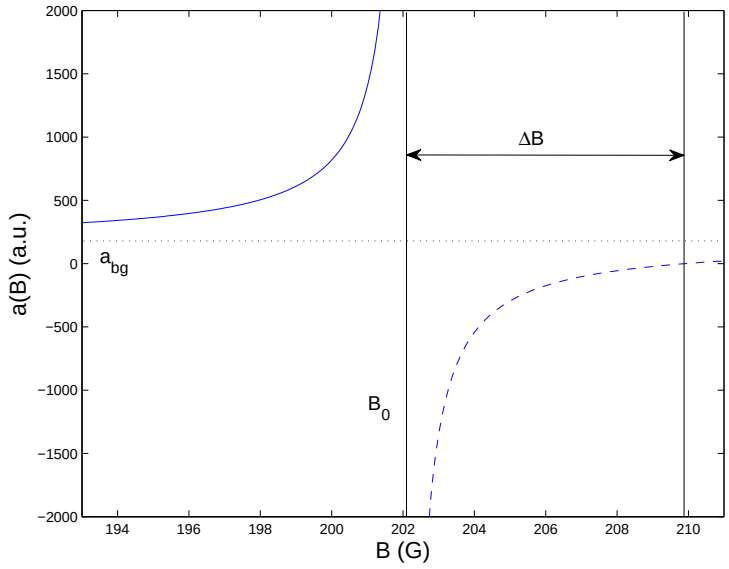

Figure 2.3: Variation of the *s*-wave scattering length about the 202.107 G resonance in ^{40}K. The position of the resonance, B_0, is indicated by a solid black line. The other parameters appearing in Eq. (2.32) are also indicated.

magnetic field value moves away from the resonance it is possible for effects not included in the two-channel model to have an influence on the scattering length. For example, other bound states in the entrance channel or closed channel or other Zeeman states. We will use Eq. (2.32) extensively throughout this thesis to model to partial wave scattering length. The parameters we use to model the resonances in ^{40}K and ^{6}Li are given in Tables 2.1, 2.2 and 2.3. An explanation of how these parameters are calculated is given in Appendix. B.

Table 2.1: Bound state energies E_{-1} associated with the highest excited vibrational states, C_6 coefficients, and *s*-wave scattering lengths for ^{40}K and ^{6}Li. The values of E_{-1} and a_0 quoted for $^{6}Li_2$ refer to the lithium triplet potential.

Species	C_6 (a.u.)	a_0^{bg} (a_{Bohr})	$\lvert E_{-1}\rvert / h$ (MHz)
^{40}K	3897 [117]	174 [118]	8.9 [119]
^{6}Li	1393.39 [120]	-2160 [121]	2.4×10^4 [121]

Table 2.2: Calculated *p*-wave resonance parameters for ^{40}K. All values are based on the experimental data found in Ticknor *et al*. [2]

Projection	B_{10} (G)	$a_1^{\rm bg}$ ($a^3_{\rm Bohr}$)	ΔB_1 (G)	$\frac{\partial E_b}{\partial B}$ (kHz/G)
$m_1 = 0$	198.85	-1049850	-21.95	188±2
$\|m_1\| = 1$	198.373	-905505	-24.99	193±2

Table 2.3: Calculated *p*-wave resonance parameters for ^{6}Li taken from Fuchs *et al*. [3]. It should be noted that the dipolar splitting (DPS) is on the order of mG for ^{6}Li. This is much lower than that observed in ^{40}K. In the experiments this splitting was not resolvable. The data is provided for atoms prepared in two hyperfine states $|F, m_F\rangle$. In this case $|1\rangle = |1/2, 1/2\rangle$ and $|2\rangle = |1/2, -1/2\rangle$

Channels	B_0 (G)	*DPS* (mG)	$\frac{\partial E_b}{\partial B}$ (μK/G)	$a_1^{\rm bg}$ ($a^3_{\rm Bohr}$)	ΔB_1 (G)
$\|1\rangle$-$\|1\rangle$	159	10	113	-42360	-40.51
$\|1\rangle$-$\|2\rangle$	185	4	111	-45290	-39.54
$\|2\rangle$-$\|2\rangle$	215	12	118	-42800	-25.54

2.4 Dipolar splitting of *p*-wave resonances

Collisions of ultracold fermions in different internal states can have zero relative angular momentum and therefore the wave function of the pair is isotropic. For ultracold fermions in the same internal state the lowest angular momentum state is the *p*-wave ($\ell = 1$). In this thesis we are concerned with atoms interacting with an external magnetic field. If we choose the axis of quantisation to be in the direction of the magnetic field then the form of the interaction between two atoms will now depend on the projection of the relative angular momentum vector onto the external magnetic field axis. In this case the dipole-dipole interaction will be modified depending on the relative position of the two atoms.

The operator for the spin-spin interaction between two alkali atoms is given by

$$H_{ss} = -\alpha^2 \frac{3(\hat{\mathbf{r}} \cdot \hat{\mathbf{s}}_1)(\hat{\mathbf{r}} \cdot \hat{\mathbf{s}}_2) - \hat{\mathbf{s}}_1 \cdot \hat{\mathbf{s}}_2}{r^3}. \tag{2.33}$$

Here $\alpha = 1/137.0426$ is the fine structure constant, $\hat{\mathbf{r}}$ defines the internuclear axis and $\hat{\mathbf{s}}_i$ is the spin of the valence electron on the ith atom. The value of this splitting

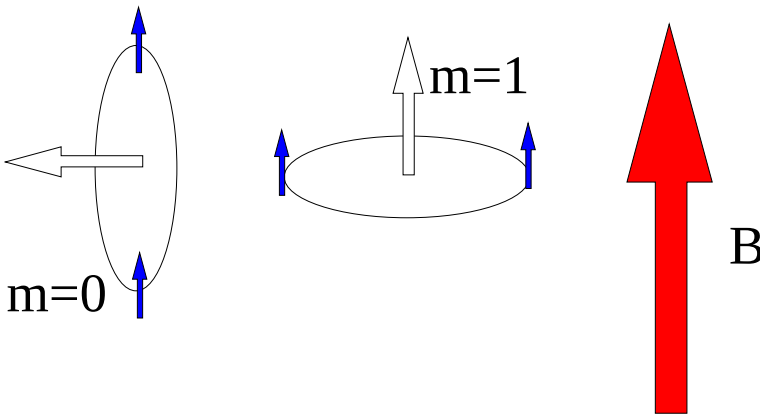

Figure 2.4: Semiclassical picture of the dipolar splitting. The thick white arrow is the relative angular momentum vector of the atom pair. The small blue arrows are the angular momentum vectors of the total atomic spins. The m=0 state has a lower energy due to the attractive interaction when the dipoles are on top of each other.

has been calculated for ^{40}K atoms in the same internal state [2] and shown to be responsible for the doublet feature of the resonance observed in the experiments on ^{40}K [21]. However, this splitting has not been resolved in the experiments on ^{6}Li [3, 122, 20]. This is accounted for by the difference in magnetic moment between the two species; the magnetic moment of the ^{6}Li molecule being approximately 12 times larger than that of the ^{40}K molecule [3].

A semiclassical picture of the dipolar splitting would have the two atoms with a relative angular momentum between them (see Fig. 2.4). In one case the projection of the relative angular momentum vector on the magnetic field would be unity, so the energy of the atoms remains constant as the two atoms rotate. In the other configuration the projection of the relative angular momentum vector on the magnetic field will be zero. In this situation when the dipoles are aligned vertically they will attract each other. This causes the average energy of the $m_1 = 0$ state to be lower than that of the $m_1 = 1$ state. It is possible to draw an analogy between the p-wave pairing in ultracold gases and pairing in liquid ^{3}He [78] as well as superconductors with p-wave pairing [80, 81]. Our model will have to include the effects this splitting has on the system.

2.5 Models for ultracold interatomic potentials

For the purpose of studying the many-body behaviour of a system it may not be practical to model the two-body physics with a coupled channels potential. In many cases it is possible to replace the full two-body interaction by an approximate form that recovers a number of physically relevant parameters of the actual potential. In Sec. 2.3 we simplified the Hamiltonian to include only two channels. This enabled us to reproduce the resonance formula of Eq. (2.32). In this section, and in the rest of the thesis, we further simplify our Hamiltonian to a single channel while using Eq. (2.32) to parametrise the scattering length close to the threshold. To this extent we replace the full potential of the system by a single channel pseudo potential that recovers the bound state and scattering spectrum close to threshold.

The large de Broglie wavelength of ultracold atoms means that the short-range features of the interaction remain unresolved. Thus it is sufficient to use a potential that approximates this short-range behaviour by recovering the phase shift at long-range. We are left with the problem of modelling the long-range part of the potential. We will see that this leaves us with a simple expression for the potential that will make our many particle calculations much less computationally demanding.

2.5.1 Van der Waals potential

If one neglects interchannel coupling, the low energy bound state and scattering spectrum of alkali metal atom pairs is dominated at long distance by the van der Waals interaction which arises from an induced dipole-induced dipole interaction derived from second order perturbation theory [11]. This potential decays as $1/r^6$ at large distances, with r being the interatomic distance. In order to model this long range behaviour we can introduce a potential of the form [60]

$$V(r) = \begin{cases} \infty & \text{for} \quad r < R_c \\ -\frac{C_6}{r^6} & \text{for} \quad r > R_c \end{cases}, \tag{2.34}$$

where C_6 is the van der Waals coefficient and R_c is the radius of a repulsive hard sphere. We can choose this hard sphere potential because we will approximate the short-range behaviour with a phase shift as explained above. A length scale can be associated with such a potential,

$$l_{\mathrm{vdW}} = \frac{1}{2}(2\mu C_6/\hbar^2)^{1/4}, \tag{2.35}$$

referred to as the van der Waals length [123, 51]. The van der Waals length is an important length scale in ultracold collisions [124]. For $r < l_{\mathrm{vdW}}$ the wave function oscillates rapidly since $V(r) = -\frac{C_6}{r^6}$ becomes large compared with typical collision energies. At separations greater than l_{vdW} the wave function takes on its asymptotic form and oscillates on the length scale of the de Broglie wavelength of the particles.

We have therefore chosen a pseudo potential that has the correct long range behaviour and we can alter the value of R_c to reproduce the phase shift caused by the short range features of the potential. This phase shift will be independent of how many bound states the potential holds, but sensitive to the energy of the bound state closest to threshold. The potential can be fixed to support fewer bound states than would be supported by a Born-Oppenheimer potential surface while recovering the off-resonant scattering length. For the potential of Eq. (2.34) the *s*-wave scattering length is given by [125]

$$a_0 = \bar{a}_0 \left[1 - \tan\left(\Phi - \frac{3\pi}{8}\right)\right], \tag{2.36}$$

where Φ is the semiclassical phase shift and

$$\bar{a}_0 \approx 0.95598\, l_{\mathrm{vdW}} \tag{2.37}$$

is referred to as the mean *s*-wave scattering length [125], which is completely determined by the asymptotic behaviour of the potential of Eq. (2.34). The semi-classical phase shift is given by

$$\Phi = \frac{1}{\hbar}\int_{R_c}^{\infty} dr\, \sqrt{-2\mu V(r)} = \frac{\sqrt{\mu C_6}}{\sqrt{2}\hbar R_c^2}. \tag{2.38}$$

This analytic formula allows the sphere radius R_c to be found for any given *s*-wave scattering length (provided we know the species of participating atoms and the C_6 coefficient). Several values of the core radius can correspond to a given scattering length, depending on how many bound states one wishes to include in the potential. Altering the value of the core radius also causes the energy of the bound states within the potential to be altered. A singularity appears in the scattering length at a sphere radius where a bound state becomes degenerate with the zero-energy threshold of the potential. By decreasing the sphere radius below this resonance value a new bound state can be added and by increasing it above this resonance value a bound state can be removed. In this way it is possible to model a zero-energy resonance by changing the one parameter of the sphere radius.

It has been shown in Gao [4] how it is possible to relate the parameters a_0 and a_1 to the highest excited molecular levels of the $-C_6/r^6$ potential near threshold. In order to compare these results, we have numerically solved the Schrödinger equation using the potential of Eq. (2.34) at zero-energy to determine the scattering length. This is done using a propagation method and analysing the long-distance behaviour of the scattering wave function. In a similar way the bound state energies can be found by ensuring that the wave function satisfies the appropriate boundary conditions below threshold. For the *s*-wave the bound state energy and the scattering length obtained from the numerical calculation have been plotted in Fig. 2.5. For comparison, the solid curve refers to the following analytic formula for the energy of the highest excited *s*-wave bound state derived in [4]:

$$E_s = -\frac{1}{(a_0 - \bar{a}_0)^2}\left[1 + \frac{c_1}{(a_0 - \bar{a}_0)} + \frac{c_2}{(a_0 - \bar{a}_0)^2}\right]. \tag{2.39}$$

Here the parameters a_0 and $\bar{a}_0$ have been scaled by $2l_{\mathrm{vdW}}$ and the energy has been scaled by $\hbar^2/\left[2\mu(2l_{\mathrm{vdW}})^2\right]$ with $c_1 = 0.4387552$ and $c_2 = -0.2163139$. Also shown in Fig. 2.5 is the universal energy for an *s*-wave bound state near threshold as given by [60]

$$E_s = -\frac{\hbar^2}{2\mu a_0^2}. \tag{2.40}$$

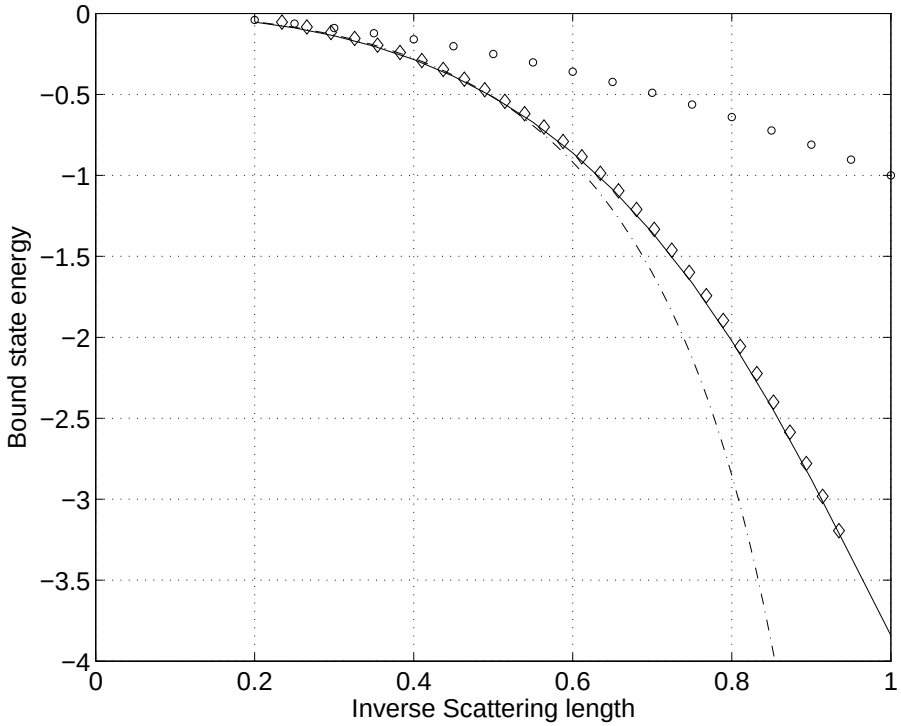

Figure 2.5: The near resonant s-wave bound state energy versus $1/a_0$ for different pseudo potential models for ^{40}K. The solid line is the analytic result of Eq. (2.39). The diamonds indicate the numerical bound state energy using the pseudo potential of Eq. (2.34). The dot-dashed line is the result using the separable potential. The circles refer to the universal formula of Eq. (2.40). All lengths have been scaled by $2l_{\mathrm{vdW}}$ and the unit of energy is $\hbar^2/\left[2\mu(2l_{\mathrm{vdW}})^2\right]$.

In a similar manner the values for the scattering volume, as well as the corresponding bound state energies, were numerically calculated for the p-wave. These results have been plotted in Fig. 2.6. According to [4] the highest excited bound state energy is then well approximated by

$$E_p = -\left(\frac{5\overline{a}_1}{a_1+\overline{a}_1}\right)\left[1+d_1\left(\frac{1}{a_1+\overline{a}_1}\right)^{1/2}+d_2\left(\frac{1}{a_1+\overline{a}_1}\right)\right]. \qquad (2.41)$$

Here the parameters a_1 and $\overline{a}_1$ have been scaled by $(2l_{\mathrm{vdW}})^3$, the energy has been scaled by $\hbar^2/\left[2\mu(2l_{\mathrm{vdW}})^2\right]$ and $d_1 = 0.4430163$ and $d_2 = 0.1639879$. The average

scattering volume is given by [4]

$$\overline{a}_1 = 0.1162277(2l_{\mathrm{vdW}})^3. \tag{2.42}$$

Equation (2.41) has also been plotted in Fig. 2.6 as a comparison against the numerical result.

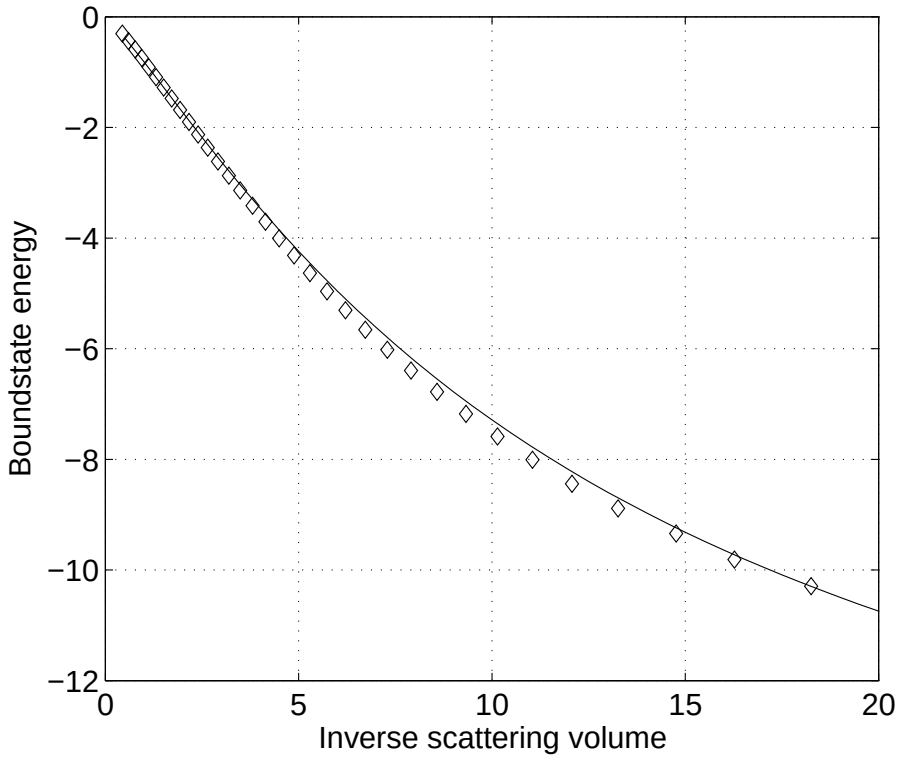

Figure 2.6: The near resonant p-wave bound state energy versus $1/a_1$ using a hard sphere + van der Waals pseudo potential for ^{40}K. The diamonds refer to the numerical result using the pseudo potential of Eq. (2.34), while the solid line is the analytical result of Eq. (2.41) for comparison. All lengths have been scaled by $2l_{\mathrm{vdW}}$ and the unit of energy is $\hbar^2/\left[2\mu(2l_{\mathrm{vdW}})^2\right]$.

2.5.2 Separable potential

In the context of many-body calculations it is desirable to seek an even simpler pseudo potential than the hard sphere plus Van der Waals potential to describe the

two-body interaction. This can be achieved by using a separable potential. This allows us to choose an analytic form for the potential that recovers the observables we wish to study and also allows us to find an analytic formula for the energy of the bound state, as we will see. A further advantage of this potential is that it is convenient for numerical integration, as it can be chosen to be continuous, with a continuous derivative; this will be important when solving the many-particle equations of later chapters. This form of potential has been previously employed in studies of few [126] and many-body systems [1, 127]. In our case we want to choose our separable potential to recover the low energy resonance behaviour close to a Feshbach resonance. Separable potentials have already been applied in the case of both *s*-wave Feshbach resonances [19] and *p*-wave Feshbach resonances [99, 97]. The model we use for the separable potential closely resembles one already successfully applied to *s*-wave Fermi gases [19, 128, 129]. We continue to use a single channel approach as this will be the simplest approximation to the problem.

The scattering wave function is formulated in terms of the Lippmann-Schwinger equation,

$$|\phi^+_{\mathbf{p}}\rangle = |\mathbf{p}\rangle + G_0(E_k + i0)V|\phi^+_{\mathbf{p}}\rangle. \tag{2.43}$$

Here $G_0(E_k + i0)$ is the free Green's operator

$$G_0(z) \equiv (z - H_0)^{-1}, \tag{2.44}$$

where H_0 is the interaction free Hamiltonian. The argument $z = E_p + i0$ indicates that the collision energy $E_p = p^2/(2\mu)$ is approached from the upper half of the complex plane, as in Eq. (2.22) and Eq. (2.23). A Lippmann-Schwinger equation can also be written for the T-matrix [116],

$$T(z) = V + VG_0(z)T(z). \tag{2.45}$$

Given the potential in the separable form

$$V = |\chi\rangle\xi\langle\chi|, \tag{2.46}$$

where the parameter ξ is referred to as the amplitude and $|\chi\rangle$ is the form factor, Eq. (2.45) can be iterated to infinite order to obtain the Born series. It is a feature of the separable potential that this series can be summed analytically and the T-matrix written as

$$T(z) = \frac{|\chi\rangle\xi\langle\chi|}{1 - \xi\langle\chi|G_0(z)|\chi\rangle}. \tag{2.47}$$

The T-matrix is related to the full scattering amplitude by

$$f(\mathbf{p}, \mathbf{p}') = -(2\pi)^2\mu\hbar\langle\mathbf{p}|T\left(\frac{p^2}{2\mu} + i0\right)|\mathbf{p}'\rangle. \tag{2.48}$$

It can also be shown that poles of the T-matrix correspond to bound state energies [60, 116]. In the s-wave case the scattering amplitude has the low energy asymptotic behaviour [60]

$$f_0(p) \underset{p\to 0}{\sim} -a_0, \tag{2.49}$$

where a_0 is the s-wave scattering length. The p-wave scattering amplitude has the low energy behaviour [60]

$$f_1(p) \underset{p\to 0}{\sim} -a_1\frac{p^2}{\hbar^2}, \tag{2.50}$$

where a_1 is here referred to as the p-wave scattering volume. The quantity $\langle\mathbf{p}|\chi\rangle$, which appears when Eq. (2.47) is inserted into Eq. (2.48), is the momentum representation of the form factor of the potential which we choose to determine the resonant bound state through the relation $G_0(E_{-1})|\chi\rangle \propto |\phi_{-1}\rangle$. As the form factor is unresolved for collisions in dilute, ultracold gases, a suitable and convenient expression can be chosen that reproduces the asymptotic conditions of Eq. (2.49) and Eq. (2.50).

s-wave

In the following, the s-wave form factor is chosen to be of Gaussian form [19],

$$\langle\mathbf{p}|\chi\rangle = \frac{1}{\sqrt{2}\pi\hbar^{3/2}}e^{-p^2\sigma^2/2\hbar^2}Y_{00}(\theta, \phi). \tag{2.51}$$

Here, $p = |\mathbf{p}|$ with θ as the zenith angle and ϕ as the azimuth angle of $\mathbf{p}$. The function $Y_{00}(\theta, \phi)$ is the spherical harmonic with ℓ=0 and m_ℓ=0. Using this expression

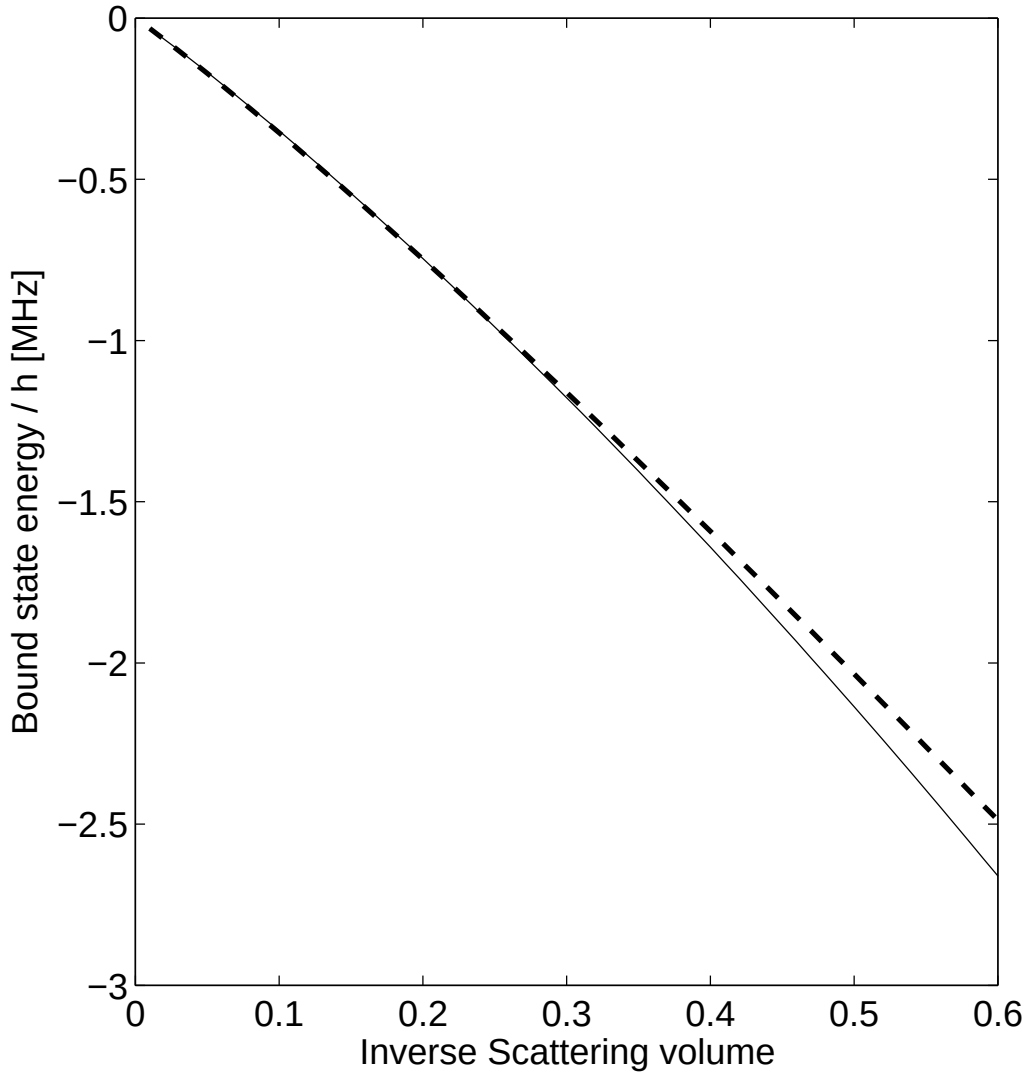

Figure 2.7: Variation of the *p*-wave bound state energy of $^{40}K_2$ with the inverse scattering volume. The dashed line is the analytic formula of Eq. (2.41), while the solid line is the numerical result using a separable potential. Here the energy scale is given in MHz as compared to Fig. 2.6. The scattering volume has been scaled by $(2l_{\rm vdW})^3$. This demonstrates that the separable potential is a good approximation over an energy range relevant to recent experiments. At higher binding energies the separable potential ceases to be accurate.

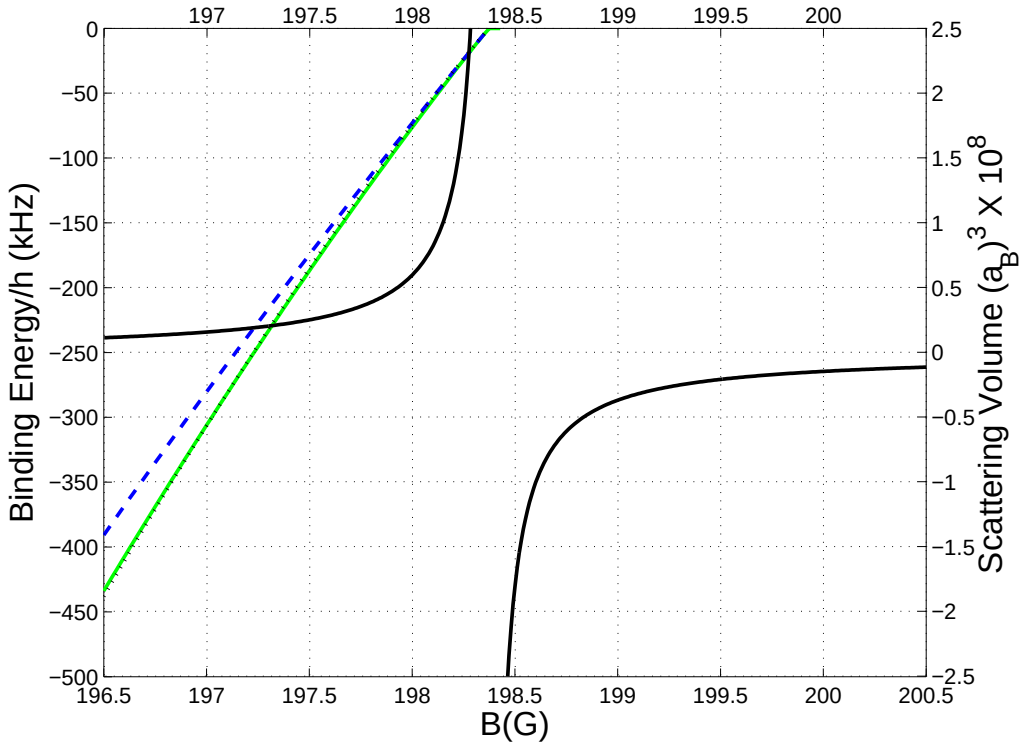

Figure 2.8: The emergence of the bound state for the m=1 resonance at 198.373G in ^{40} K. The green line is the bound state solution to Eq. (2.57). The black dotted line is the result of Eq. (2.41). The dashed blue line is the low energy expansion of Eq. (2.58).

the parameters σ and ξ can be chosen such that the condition

$$1 - \xi\langle\chi|G_0(z)|\chi\rangle = 0 \tag{2.52}$$

reproduces the pole in the T-matrix when the argument is equal to the energy of the least bound state of the potential, E_{-1}. In the case of the s-wave there is the additional condition, from the zero-energy limit of the T-matrix, that the scattering length is given by

$$a_0 = \sigma\frac{x}{1 + x/\sqrt{\pi}}, \tag{2.53}$$

where $x = \mu\xi/(2\pi\hbar^2\sigma)$ is dimensionless. The fulfilment of these conditions allows the parameter ξ to be varied in order to vary the position of the pole in the T-matrix when the system is close to threshold. This gives the condition that

$$1 + \frac{x}{\sqrt{\pi}}\left[1 - \sqrt{\pi}ye^{y^2}\,\mathrm{erfc}(y)\right] = 0, \tag{2.54}$$

where $y = \sigma\sqrt{-2\mu E_{-1}}/\hbar$ and $\mathrm{erfc}(y) = \frac{2}{\sqrt{\pi}}\int_y^\infty \exp(-u^2)\,du$ is the complementary error function. In the low energy limit the solution of Eq. (2.54) recovers the universal formula for the s-wave bound state energy given by Eq. (2.40). A numerical calculation of the bound state energy versus $1/a_0$ for ^{40}K using a separable potential in which the parameter σ is held constant is shown in Fig. 2.5. A formula for σ given in appendix B. The parameters we use are given in Tables 2.1, 2.2 and 2.3, and reproduced in the appendix B.

p-wave

Given the success of the s-wave separable potential in modelling interactions in an ultracold Fermi gas [19, 128, 129] we seek a similar form to describe p-wave interactions. The p-wave form factor can be chosen to be of the following Gaussian form:

$$\langle\mathbf{p}|\chi\rangle = \frac{\sigma}{\pi\hbar^{5/2}}pe^{-p^2\sigma^2/2\hbar^2}Y_{1m}(\theta,\phi). \tag{2.55}$$

Here the extra factor of p is due to the boundary condition on the p-wave bound state and scattering spectrum due to the presence of the centrifugal barrier. Taking the zero-energy limit of the T-matrix gives an expression for the scattering

volume,

$$a_1 = 2\sigma^3 \frac{x}{1 + x/\sqrt{\pi}}, \tag{2.56}$$

where the x is defined as before. The condition on the bound state energy is given by the expression

$$1 + \frac{x}{\sqrt{\pi}} \left(1 - 2y^2 \left[1 - \sqrt{\pi} y e^{y^2} \mathrm{erfc}(y)\right]\right) = 0. \tag{2.57}$$

A low energy expansion of Eq. (2.57) gives rise to an expression for the p-wave bound state energy close to threshold,

$$E_{-1} \approx -\frac{\sqrt{\pi}\sigma\hbar^2}{2\mu a_1}. \tag{2.58}$$

It should be noted that this is linear in the inverse scattering volume, in agreement with the first order approximation to Eq. (2.41). This result is also in agreement with previous theoretical results [107, 106]. Equation (2.58) and Eq. (2.32) can be used to find an expression for the magnetic moment close to the dissociation threshold in terms of the resonance parameters and the parameters of the separable potential. The value of the magnetic moment can be obtained from experiment [3, 21], allowing the value of the parameter σ to be fixed for a given resonance. For the case of ^{40}K and ^{6}Li this is done in Appendix B. We have also used this potential to calculate the low energy scattering amplitude and compare the cross-section obtained to that of coupled channels calculation. The derivation and results of this calculation are given in Appendix C.

The observed dipolar splitting of the resonance feature must also be accounted for, given that one bound state would now exist corresponding to the $m = 0$ molecules and one bound state corresponding to $|m| = 1$ molecules. This is done by introducing separable terms representing each component

$$V = |\chi_1\rangle\xi_1\langle\chi_1| + |\chi_0\rangle\xi_0\langle\chi_0| + |\chi_{-1}\rangle\xi_{-1}\langle\chi_{-1}|. \tag{2.59}$$

This allows for the $m = \pm 1$ components to be non-degenerate. The observed doublet feature of the experiments indicates, however, that they are degenerate. This is intuitive due to the symmetry of the system about the magnetic field axis

and we will investigate this further in Chapter 3.

2.5.3 Two channel model versus single channel model

It is common to see both single channel and two channel models used to model Feshbach resonances in ultracold gases. The validity of either model depends on the exact nature of the Feshbach resonance. It would seem intuitive that if it is possible to describe the system with a single channel then this should be preferred on the basis of simplicity. However, this is not always possible. We will begin by discussing *s*-wave resonances and then look at how *p*-wave resonances differ from them.

We have already mentioned that in the two-channel model a Feshbach molecule refers to an eigenstate of the Hamiltonian Eq. (2.17) which has components in the entrance channel and the resonance channel. We can therefore write a wave function for the Feshbach molecule in terms of these components

$$|\phi_{mol}\rangle = \sqrt{Z(B)}|\phi_{\rm cl}\rangle + \sqrt{1 - Z(B)}|\phi_{\rm bg}\rangle, \tag{2.60}$$

where $Z(B)$ is referred to as the wave function renormalisation constant [19] and represents the fraction of the wave function in the closed channel. Using a single resonance approximation, we can approximate the detuning of the resonance energy to be linear in the magnetic field. We can therefore assume that if the closed channel component of the Feshbach molecule is large then the energy dependence of the Feshbach molecule will also be linear, to a good approximation. However, we have seen that in the single channel model the *s*-wave bound state varies quadratically with the magnetic field when close to resonance. We can therefore assume that the energy of the molecule will vary quadratically when the closed channel component is small. This is indeed the case for *s*-wave resonances [130, 51] and we tend to classify Feshbach resonances as either closed channel dominated or entrance channel dominated depending on the behaviour of $Z(B)$. The situation is complicated by the fact that the closed channel component does not remain constant but varies as a function of the magnetic field. In the case of an entrance channel dominated resonance the closed channel component will

be small on the negative scattering length side of the resonance. As the closed channel bound state, referred to as the resonance state, approaches the threshold the closed channel component will increase. $Z(B)$ will continue to increase as the binding energy of the Feshbach molecule increases. It should be noted that a bound Feshbach molecule can exist when the resonance state is still above the entrance channel dissociation threshold. As the resonance energy crosses this threshold and the molecule becomes tightly bound the single channel model will become inadequate at some point and the binding energy of the Feshbach molecule will follow that of the linearly varying resonance state in the closed channel.

In the closed channel dominated resonances a rapid increase is seen in the closed channel component when the magnetic field is close to the resonance position. In this case the bound state of the system appears at a similar magnetic field to which the resonance energy level crosses the threshold. As the molecule becomes more tightly bound it may encounter a bound state supported by the entrance channel, in which case the closed channel component will decrease as the Feshbach molecule populates this bound state. The differences between the entrance channel dominated and closed channel dominated resonances are illustrated in a cartoon Fig. 2.9. The important factor here is that it is possible to use a single channel approach for entrance channel dominated resonances as the behaviour of the bound state of the coupled system is similar to that of the single channel model when close to resonance.

p-wave resonances are intrinsically closed channel dominated due to the existence of the centrifugal barrier [97]. It has been shown that this means that the amplitude of the closed channel remains large across the entire resonance [107] and the Feshbach molecule is always dominated by the closed channel component. When we compare this with the *s*-wave we could assume that this means we would have to use a two-channel model to describe the resonance. However, we have already seen that the energy of the *p*-wave bound state in the single channel model varies linearly with magnetic field detuning from the resonance, just like the resonance state supported by the closed channel. In the cases we have studied we have seen that this single channel model is sufficient at reproducing the near threshold properties of the Feshbach resonance. We therefore propose that this single channel model is sufficient, at least for use in a first study, in the region

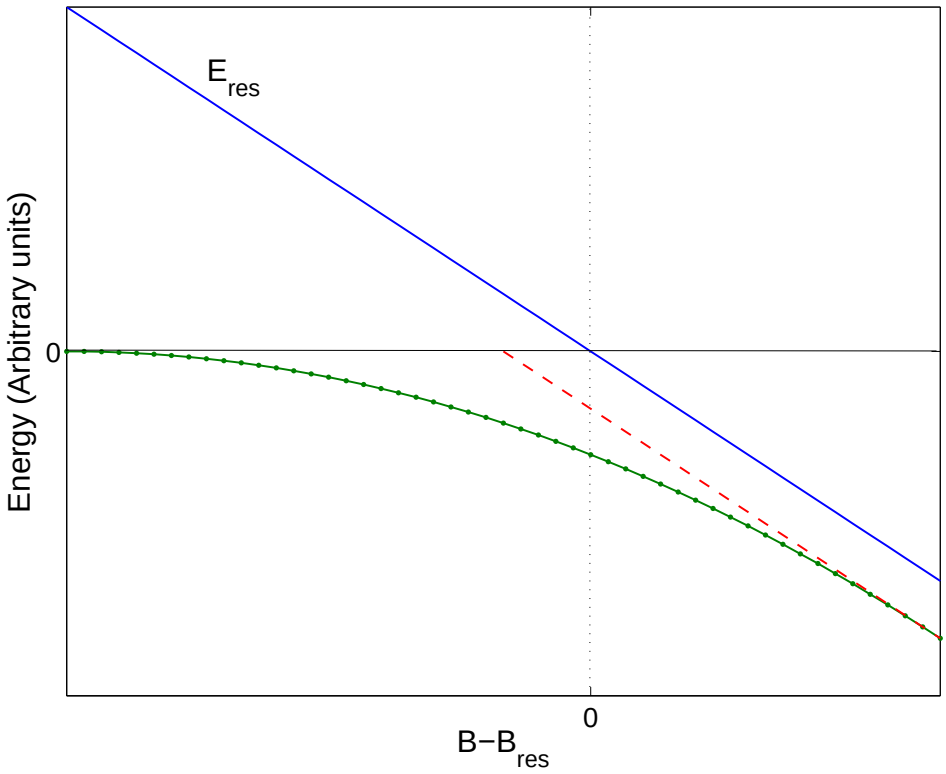

Figure 2.9: Cartoon to illustrate the different behaviours of the *s*-wave bound state in a closed channel dominated resonance and an open channel dominated resonance as a function of the detuning from the zero of the resonance energy. The solid blue line is the energy of the resonance state. The solid green dotted line is the bound state energy of the Feshbach molecule in an open channel dominated resonance. The dashed red line is the value of the Feshbach molecule energy in a closed channel dominated resonance. In fact the energy of the closed channel dominated resonance will still vary quadratically close to the threshold, but over a much smaller range of magnetic fields. This model diagram ignores effects far from resonance where other bound states can interfere with the energy levels.

close to the resonance.

2.6 Conclusion

In this chapter we have shown how one can model the two-body physics close to a *p*-wave Feshbach resonance. We have used a separable potential to determine the two-body bound state energy as a function of the magnetic field detuning from resonance, as well as the low energy scattering properties. Using an approach that has previously been successful in modelling the two-body physics close to an *s*-wave resonance we have shown good agreement with previous studies that use different models. We have seen that there are some differences between *s*-wave resonances and *p*-wave resonances. For instance, in the *s*-wave the resonance energy, as it approaches the threshold depends only on the *s*-wave scattering length, see Eq. (2.40). In the *p*-wave the resonance energy close to threshold depends on the *p*-wave scattering volume, but another length scale is needed in addition to this (see Eq. (2.58)).

We have derived a model that considerably simplifies the microscopic details involved in the collision of two ultracold alkali atoms. The motivation behind this has been to present a form of the interatomic potential that can be used in many-particle calculations. We now have a convenient, analytic form of the potential similar to one that has already been successfully employed in *s*-wave systems [19, 128, 129]. We now go on to use the potential of Eq. (2.59) with a form factor given by Eq. (2.55) to study the many-body physics at the mean field level. Our ultimate aim is to study the mean field dynamics of Feshbach molecule production. In order to do this we need to give our gas an initial condition from which to create molecules. The exact nature of this initial condition is the subject of the next chapter.

Chapter 3

Pairing in Fermi gases

The pairing approximation is introduced for a pair of particles interacting in the presence of filled Fermi sea. The BCS theory is discussed in the context of its historical development and its further application to Fermi systems including ultracold alkali gases. The model of the previous section is implemented to fix the initial conditions of the gas prior to investigating the many-body dynamics and molecule production. For the range of densities and temperatures investigated it is shown that the $m_1 = 0$ and $m_1 = \pm 1$ components can be considered separately in ^{40}K. The results of our model are compared with that of another model and are shown to agree reasonably well.

In this chapter we construct the initial state of the gas from which we will create molecules. In the introduction we mentioned that an ideal gas of Fermi atoms can exhibit non-classical behaviour and the inclusion of interactions can dramatically alter the state of the system. At zero temperature the particles of an ideal Fermi gas will fill up all the energy levels to some energy, E_F, called the Fermi energy. It could be assumed that the state of the gas will not change considerably as a weak interaction between the particles is introduced. However, we will see in this chapter that under certain conditions the state of the gas can change a great deal, even when the interaction is weak. The purpose of discussing this phenomenon in this thesis is that for our dynamic mean field equations (see Chapter 4) to produce molecules we need the gas to have an initial state in which the Fermi atoms form

long range pairs, known as Cooper pairs. We use the single channel separable potential proposed in the previous chapter to model this state of the gas close to a *p*-wave Feshbach resonance. It should be noted that in an experiment it may not be necessary to reach this paired state before creating molecules, but for studying the dynamics of molecule formation at the mean field level it is necessary. It turns out that the initial condition can be fixed by specifying two parameters, the chemical potential and a parameter that measures the amount of pairing in the gas. These parameters are in turn dependant on the temperature and density of the gas, as well as the strength of the two-body interaction between particles, and it is these physical parameters that we will choose to give us our initial state.

3.1 Introduction to the BCS theory

One of the greatest achievements in the study of systems at low temperature is the explanation of superconductivity provided by Bardeen, Cooper and Schrieffer [50] (alternative derivations of some of the same results were given by Bogoliubov [131] and Valatin [132]). Originally applied to superconducting metals and alloys this theory explained that below a certain temperature the ground state of the many body system would be one in which the electrons around the Fermi surface are paired by a weak attractive interaction. These pairs, referred to as Cooper pairs, can then condense into a state similar to that of a Bose-Einstein condensate. It seems odd that two electrons would have an attractive force between them since they are both negatively charged. However, the interaction is indirect and is mediated by phonons in the lattice which cause the net force to be attractive. Extensions of the BCS theory have been applied to other Fermi systems including liquid ^{3}He, ultracold gases and unconventional superconductors.

In metal alloys the transition to the superconducting state is not associated with any structural change in the crystal lattice so it is safe to assume that it is associated with a change in the electronic structure of the metal. The BCS theory was the first theory that explained the macroscopic properties of the superconductor from a microscopic basis. An essential ingredient of this transition is the formation of Cooper pairs.

In the BCS theory as originally proposed only a very weak attraction between

the particles is needed to form a Cooper pair. Further study showed that the applicability of the BCS equations extended beyond the limit of a weakly attractive interaction and in the case where the atoms form tightly bound molecules the BCS theory can also give a good description of the gas [133, 134]. However, in the intermediate region the BCS theory can only give a qualitative description of the gas. This is due to the divergence of the scattering length in this region so that perturbation theory no longer applies. There have been many attempts to extend the BCS theory into this 'strongly interacting' regime and it remains an active field of research. We only wish to fix the initial condition of our gas on the BCS side of the resonance in order to study the dynamics of molecule production at the mean field level and therefore stick closely to the mean field approximation of the BCS theory. We will then vary a magnetic field to produce tightly bound diatomic molecules. In order to achieve these two limits we are going to use Feshbach resonances as already discussed in the previous chapter. The side of the resonance where the scattering length is negative is associated with the BCS region of the gas. The side where the scattering length is positive and the potential supports a molecular bound state is associated with the BEC region.

3.1.1 The Cooper pair problem *

Cooper [135] showed that an attractive interaction between a pair of fermions above a filled Fermi sea will allow for a bound state no matter how weak the interaction is. This is in contrast to the normal three dimensional picture of a quantum mechanical bound state which appears only when the interaction is sufficiently strong. It should be emphasised that the existence of this bound state of two electrons, a Cooper pair, is a many body effect that only exists in the presence of a filled Fermi sea.

By considering a translationally invariant system with spin-independent forces the pair wave function can be written as

$$\psi(\mathbf{r}_1, \mathbf{r}_2) = \phi_{\mathbf{q}}(\mathbf{r}_1 - \mathbf{r}_2) e^{i\mathbf{q}\cdot\mathbf{R}/\hbar}, \tag{3.1}$$

*This section follows Ref.[1]

where **R** is the centre-of-mass coordinate of the pair and **q** is the centre of mass momentum of the pair. In the limit of zero total momentum, the part of the wave function that describes the relative motion of the pair can be expanded in a plane wave basis

$$\phi(\mathbf{r}_1 - \mathbf{r}_2) = \sum_{\mathbf{p}} c_{\mathbf{p}} e^{i(\mathbf{p}\cdot\mathbf{r}_1 - \mathbf{p}\cdot\mathbf{r}_2)/\hbar}. \tag{3.2}$$

Here the summation over the relative momentum, **p**, takes place over unoccupied states above the Fermi surface. This illustrates that the pair function is a superposition of states in which each pair has zero total momentum. The Schrödinger equation for the pair of particles can be written as

$$\left(E - 2E_p\right) c_{\mathbf{p}} = \sum_{\mathbf{p}'} \langle \mathbf{p}, -\mathbf{p}|V|\mathbf{p}', -\mathbf{p}'\rangle c_{\mathbf{p}'}. \tag{3.3}$$

Here $E_p = \frac{p^2}{2m} - \mu$ is the single particle energy measured relative to the chemical potential, μ. Again the sum only extends over unoccupied states. If the potential is factorisable as a separable potential and spherically symmetric so that

$$\langle \mathbf{p}, -\mathbf{p}|V|\mathbf{p}', -\mathbf{p}'\rangle = \sum_{\ell m} \lambda_\ell w_p^\ell w_{p'}^{\ell'} Y_{\ell m}(\hat{\mathbf{p}}') Y_{\ell m}^\star(\hat{\mathbf{p}}), \tag{3.4}$$

where λ_ℓ is an amplitude for the potential, w_p^ℓ is a form factor that depends on the magnitude of the momentum and $Y_{\ell m}(\hat{\mathbf{p}})$ is a spherical harmonic, then,

$$\frac{1}{\lambda_\ell} = \sum_p |w_p^\ell|^2 \frac{1}{E_{\ell m} - 2E_p}. \tag{3.5}$$

For an attractive potential, $\lambda_\ell < 0$, it can be shown that there is a solution for $E_{\ell m} < 0$ corresponding to a bound state. It is this pairing that gives rise to the superconducting state. This argument has only involved one pair of particles interacting above a Fermi sea. In practise the system will contain many such interacting pairs at a finite temperature, in which case the Fermi surface will not be sharp. For this reason it is necessary to develop some form of many particle theory that can include these effects. Fortunately methods of quantum field theory can be employed to describe the thermodynamic state of the system at a mean

field level. This is the BCS theory of superconductivity and has been successful in describing the many-body properties of Fermi systems with attractive interactions at low temperature [1, 127].

3.1.2 Liquid ^{3}He

For a long time liquid ^{3}He remained the only experimentally accessible electrically neutral Fermi system in which to study superfluidity and pairing. The two-body interaction is then due to the electrostatic force between the electrons and nuclei of the atoms. Even more relevant to the work of this thesis is the fact that due to the dominant triplet nature of the helium pairs the atom-atom interactions are in the p-wave. Early experiments on ^{3}He showed that at temperatures below 100 mK it behaved as a degenerate Fermi gas and this state remained stable down to 3 mK (the lowest temperatures then available). At the same time considerable progress was being made to explain the phenomenon of superconductivity in metals, culminating in the microscopic BCS theory in 1957 [50]. The BCS theory described electrons that could occupy two spin states. In this case a pair will form in which one of the electrons occupies a down spin state and the other electron occupies an up spin state. As discussed in the previous chapter the antisymmetry of the wave function requires this to be s-wave pairing at low enough energies. The p-wave nature of the interaction between ^{3}He atoms, as well as the additional degrees of freedom in the spin state means that the original BCS state is insufficient to describe the liquid ^{3}He state.

Anderson and Morel [136] considered states in which pairs were in the same state with respect to their centre-of-mass motion and also with respect to their internal degrees of freedom. In many ways this is similar to the original BCS treatment, however, the overall state is now anisotropic. They studied the case for which pairs with p-wave orbital symmetry could have spin projection $S_z = \pm 1$ onto the axis of angular momentum. This state has acquired the name of the Anderson-Brinkman-Morel (ABM) state. A second state was considered by Balian and Werthamer [137]. In this (BW) state the pairs occupy a superposition of all possible spin projections, and in turn it is possible to construct a state that is isotropic in all its properties. This state was also shown to be more stable than the

ABM state.

Subsequent experimental observations and further theoretical investigation of liquid ^{3}He has established that the ABM state accounts for the A phase of liquid ^{3}He and the BW state accounts for the B phase of liquid ^{3}He. For a summary of the vast amount of work devoted to superfluid ^{3}He the reader is directed to the review articles [78, 79]. It should be noted that the system studied in this thesis bears a resemblance to the A phase of liquid ^{3}He, or more specifically the A1 phase in which the symmetry is broken by the magnetic field.

3.1.3 Application to ultracold gases

In the introduction we explained that the physics of ultracold gases shares properties with many other systems including superconductors, but that the transition temperatures are orders of magnitude lower than in other systems due to the low density of the gas. For it to be possible to observe a superfluid state of an ultracold atomic Fermi gas the transition temperature must be raised to a value accessible by experiments. This is possible with the use of a Feshbach resonance. If we consider a system of Fermi atoms close to an *s*-wave Feshbach resonance then on the BCS side ($a_0 < 0$) of the resonance the transition temperature is given by [56]

$$T_c \approx 0.28 T_F e^{\frac{\pi}{2k_F a_0}}, \tag{3.6}$$

where T_F is the Fermi temperature defined by the Fermi energy $E_F = k_B T_F = \frac{\hbar^2 k_F^2}{2m}$ with k_F as the Fermi wave number (in this sense we expect a difference in the transition temperature between an ultracold gas and a superconductor due to the high atomic mass relative to the electron mass). Expressing the Fermi wave number in terms of the density of the gas,

$$k_F = (3\pi^2 n)^{1/3}, \tag{3.7}$$

and remembering that the scattering length is negative, it is possible to see that decreasing the density will lead to a decrease in the transition temperature to the superconducting state. Similarly it is obvious that increasing the magnitude of the scattering length will increase the transition temperature of the gas. It has

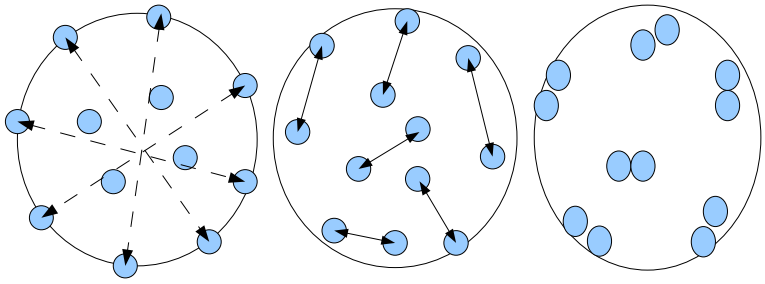

Figure 3.1: Cartoon of the BCS-BEC crossover. On the left the correlation length between two atoms greatly exceeds the interparticle spacing. In the crossover region (centre) the inter-particle spacing is of the same order as the typical interaction length. On the right hand side is the BEC region where the atoms have formed diatomic molecules whose equilibrium bond length is much less than the typical inter-particle spacing.

already been outlined in the previous chapter that a magnetic field can tune the interaction between atoms and thus make the scattering length large close to a Feshbach resonance. Furthermore the scattering length can be tuned to positive values by sweeping the magnetic field across the resonance. The atoms can then form tightly bound molecules and it is even possible to produce a condensate of these molecules [87]. This is referred to as the BCS-BEC crossover. A cartoon of this process is shown in Fig. 3.1. Much theoretical work has been devoted to the study of the BCS-BEC crossover. Eagles [133] observed that you could hold the interaction between the particles, or the scattering length, constant and increase the density of the gas. In the limit of very high density the size of the pairs can become less than the interparticle spacing and can be treated with Bose-Einstein statistics. A contrary approach was implemented by Leggett [134] with the density held constant and the scattering length varied to reach the same limit of bound molecules.

Given that the gas can be reversibly tuned from weak interactions to strong interactions the problem remains of determining the ground state and excitation spectrum of the system throughout the crossover region where the gas is both dilute, but at the same time strongly interacting. We have already noted in the introduction that this state of the gas is similar to that of a high temperature superconductor. It is not possible to find the ground state from the mean field approx-

imation provided by the BCS theory because perturbation theory can no longer be applied. In order to achieve this higher order approximations must be made to allow for the more complex processes in this region [138]. These ideas were later applied to Fermi gases close to unitarity [139, 140]. These many-body approaches introduced terms that couple free fermions to a bosonic molecule. This is often referred to as the Bose-Fermi model and we will discuss it towards the end of the chapter. It should be noted that the solution to the many-body problem throughout the cross-over region is still debated.

3.2 The p-wave BCS equations

3.2.1 Green's function equations in the pairing approximation

For the purposes of this study it is sufficient for our model to be valid on the BCS side of the resonance where the gas is initially prepared. Previous work on ultracold gases close to a p-wave Feshbach resonance have used the Bose-Fermi model to study the predicted superfluid phases of the gas [96, 97, 98]. This model includes coupling between the Fermi fields and Bose fields, but excludes Fermi-Fermi scattering in the entrance channel. Iskin and Williams employed a single channel model with a separable potential [99] and solved the BCS equations for a homogeneous system and in a harmonic trap. We choose to use the standard fermionic Hamiltonian which has been shown to give indistinguishable results to the Bose-Fermi model throughout the BCS-BEC crossover in the s-wave [128]. At the end of this chapter we will compare the results given by our model and the Bose-Fermi model. In our model the many-body Hamiltonian for the system can be written in second quantisation as [127]

$$H = \sum_{ij} \langle i|T|j\rangle a_i^\dagger a_j + \frac{1}{2}\sum_{klmn}\langle kl|V|mn\rangle \left(\langle a_k^\dagger a_l^\dagger\rangle a_m a_n + a_k^\dagger a_l^\dagger \langle a_m a_n\rangle\right), \tag{3.8}$$

where T is the single particle kinetic energy operator. Here the a_i and $a_i^\dagger$ are the usual Fermion destruction and creation operators obeying the fermionic anticommutation rules. The brackets $\langle ...\rangle$ represent an average over the thermodynamic state of the system in the grand canonical ensemble where particle number is not fixed. These are distinct from the single particle kets, $|i\rangle$ and two-particle kets, $|ij\rangle$.

The finite temperature Green's functions of the system can be defined as

$$g_{rs}(\tau,\tau') = -\langle T_\tau[a_r(\tau)a_s^\dagger(\tau')]\rangle, \tag{3.9}$$

$$F_{rs}^\dagger(\tau,\tau') = -\langle T_\tau[a_r^\dagger(\tau)a_r^\dagger(\tau')]\rangle. \tag{3.10}$$

The latter representing pairing in the gas. Here T_τ is the imaginary time ordering operator that puts the smallest value of τ to right. It is also useful to introduce a

new ket that represents a paired state in the gas

$$|\Phi\rangle = \sum_{ij} \langle a_i a_j \rangle |ij\rangle. \tag{3.11}$$

By working in the momentum representation and considering a translationally invariant system we can write down the Heisenberg equations of motion for these quantities (a detailed derivation of this section leading to Eq. (3.17) and Eq. (3.18) is given in appendix D)

$$\hbar \frac{\partial}{\partial \tau} g(\mathbf{p}, \tau, \tau') = -\hbar\delta(\tau - \tau') - E_p g(\mathbf{p}, \tau, \tau') + \Delta(\mathbf{p}) F^\dagger(\mathbf{p}, \tau, \tau'), \tag{3.12}$$

$$\hbar \frac{\partial}{\partial \tau} F^\dagger(\mathbf{p}, \tau, \tau') = E_p F^\dagger(\mathbf{p}, \tau, \tau'), + \Delta^\star(\mathbf{p}) g(\mathbf{p}, \tau, \tau'), \tag{3.13}$$

where we have introduced the gap function

$$\Delta(\mathbf{p}) = \langle \mathbf{p}|V|\Phi\rangle. \tag{3.14}$$

Here E_p is the single particle kinetic energy matrix element measured with respect to the chemical potential of the system. By making a Fourier transform with respect to the imaginary time variables these equations can be solved to give

$$g(\mathbf{p}, \omega_n) = \frac{-\hbar(i\hbar\omega_n + E_p)}{\hbar^2\omega_n^2 + E_p^2 + |\Delta(\mathbf{p})|^2}, \tag{3.15}$$

$$F^\dagger(\mathbf{p}, \omega_n) = \frac{\hbar\Delta^\star(\mathbf{p})}{\hbar^2\omega_n^2 + E_p^2 + |\Delta(\mathbf{p})|^2}. \tag{3.16}$$

Here the frequencies $\omega_n = (2n+1)\pi/\beta\hbar$ are called the Matsubara frequencies and ensure the correct Fermi statistics [141]. These equations have poles at $i\hbar\omega_n = \pm\sqrt{E_p^2 + |\Delta(\mathbf{p})|^2}$. These poles form the quasi particle excitation spectrum of the system which has a minimum value of $\Delta(\mathbf{p})$, interpreted as the minimum energy required to break a Cooper pair. Equations (3.15) and (3.16) can be inserted into Eq. (3.14) to give

$$\Delta^\star(\mathbf{p}) = -\int d^3q \langle \mathbf{q}|V|\mathbf{p}\rangle \frac{\Delta^\star(\mathbf{q})}{2\epsilon_\mathbf{q}} \tanh\left(\beta\frac{\epsilon_\mathbf{q}}{2}\right), \tag{3.17}$$

and

$$\frac{N}{V} = \frac{1}{2}\int d^3q \left[1 - \frac{E_q}{2\epsilon_{\mathbf{q}}}\tanh\left(\beta\frac{\epsilon_{\mathbf{q}}}{2}\right)\right]. \tag{3.18}$$

Here $\epsilon_{\mathbf{q}} = \left(\left(\frac{q^2}{2m} - \mu\right)^2 + |\Delta(\mathbf{q})|^2\right)^{1/2}$ and $\beta = 1/k_BT$, where k_B is Boltzmann's constant and T is the temperature of the gas. Equation (3.17) is commonly called the gap equation and Eq. (3.18) is commonly called the density equation. These are the BCS equations for the system and must be solved simultaneously. Experiments are usually performed at constant temperature, which fixes this parameter in our system. Trapped gases usually have anisotropic and inhomogeneous density distributions. However, we fix the density which may amount to an average of the density distribution over the trapped gas. This leaves the chemical potential, μ, and the gap, $\Delta(\mathbf{p})$, as parameters to be solved for.

3.2.2 Non-degenerate *p*-wave resonances

As stated in chapter 2 the *p*-wave potential consists of three components representing the projection of the angular momentum vector onto the magnetic field axis. Previous work on ultracold *p*-wave gases close to a Feshbach resonance has studied the ground state of the many-body system by minimising the free energy of the gas [96, 97], showing that the ground state of the gas is dependent on the splitting in energy between the $m_1 = \pm 1$ and the $m_1 = 0$ state. We therefore study what effect the coupling between the resonances has on the chemical potential and the gap parameter for the case of the measured resonances. Using Eq. (2.59) the energy gap can be written as

$$\Delta^\star(\mathbf{p}) = \langle\Phi|V|\mathbf{p}\rangle = \sum_{m_1}\langle\Phi|\chi_{m_1}\rangle\xi_{m_1}\langle\chi_{m_1}|\mathbf{p}\rangle = \sum_{m_1}\Delta^\star_{m_1}\chi_{m_1}(p)Y^\star_{1m_1}(\hat{\mathbf{p}}), \tag{3.19}$$

which can be inserted straight into the gap equation to give

$$\sum_{m_1} \Delta^\star_{m_1} Y^\star_{1m_1}(\hat{\mathbf{p}})\chi_{1m_1}(p) = \tag{3.20}$$
$$-\sum_{m_1 m_1'} \int d^3q \frac{\chi_{1m_1}(q)Y_{1m_1}(\hat{\mathbf{q}})\xi_{m_1} Y^\star_{1m_1}(\hat{\mathbf{p}})\chi_{1m_1}(p)\Delta^\star_{m_1'}\chi_{1m_1'}(q)Y^\star_{1m_1'}(\hat{\mathbf{q}})}{2\left(\left(\frac{q^2}{2m}-\mu\right)^2+|\Delta(\mathbf{q})|^2\right)^{1/2}}$$
$$\times \tanh\left[\frac{\beta}{2}\left(\left(\frac{q^2}{2m}-\mu\right)^2+|\Delta(\mathbf{q})|^2\right)^{1/2}\right].$$

This last line is written using the definition in Eq. (3.19). This can be done because we have excluded the possibility of the two-body interaction scattering a pair in an $m_1 = 0$ state into an $m_1 = \pm 1$ state, i.e.

$$V = \sum_{m_1 m_1'} |\chi_{m_1}\rangle \xi_{m_1 m_1'} \langle \chi_{m_1'}| \delta_{m_1 m_1'}, \tag{3.21}$$

where $\xi_{m_1 m_1'}$ is the amplitude for the coupling between states of different m_1. We can now remove the summation in Eq. (3.20) to give

$$\Delta^\star_{m_1} = -\sum_{m_1'} \int d^3q \frac{\chi_{1m_1}(q)Y_{1m_1}(\hat{\mathbf{q}})\xi_{m_1}\Delta^\star_{m_1'}\chi_{1m_1'}(q)Y^\star_{1m_1'}(\hat{\mathbf{q}})}{2\left(\left(\frac{q^2}{2m}-\mu\right)^2+|\Delta(\mathbf{q})|^2\right)^{1/2}} \tag{3.22}$$
$$\times \tanh\left[\frac{\beta}{2}\left(\left(\frac{q^2}{2m}-\mu\right)^2+|\Delta(\mathbf{q})|^2\right)^{1/2}\right].$$

We can write this in the abbreviated form

$$\Delta^\star_{m_1} = -\sum_{m_1'} \int d^3q g_{m_1 m_1'}(\mathbf{q}) Y_{1m_1}(\hat{\mathbf{q}})\xi_{m_1}\Delta^\star_{m_1'} Y^\star_{1m_1'}(\hat{\mathbf{q}}). \tag{3.23}$$

Here,

$$g_{m_1 m_1'}(\mathbf{q}) = \frac{\chi_{1m_1}(q)\chi_{1m_1'}(q)}{2\left(\left(\frac{q^2}{2m}-\mu\right)^2+|\Delta(\mathbf{q})|^2\right)^{1/2}} \tanh\left[\frac{\beta}{2}\left(\left(\frac{q^2}{2m}-\mu\right)^2+|\Delta(\mathbf{q})|^2\right)^{1/2}\right]. \tag{3.24}$$

Using the standard definition of the spherical harmonics

$$Y_{10}(\theta,\phi) = \sqrt{\frac{3}{4\pi}}\cos\theta, \tag{3.25}$$

$$Y_{1\pm1}(\theta,\phi) = \mp\sqrt{\frac{3}{8\pi}}\sin\theta e^{\pm i\phi}, \tag{3.26}$$

we can expand the summation

$$\begin{aligned}\Delta^{\star}_{m_1} = -\sqrt{\frac{3}{8\pi}}\int d^3q Y_{1m_1}(\hat{\mathbf{q}})\xi_{m_1}\Big[&g_{m_1-1}(\mathbf{q})\Delta^{\star}_{-1}\sin\theta e^{i\phi} \\ &+\sqrt{2}g_{m_10}(\mathbf{q})\Delta^{\star}_0\cos\theta - g_{m_11}(\mathbf{q})\Delta^{\star}_1\sin\theta e^{-i\phi}\Big].\end{aligned} \tag{3.27}$$

We can use some of the properties of $g_{m_1m'_1}(\mathbf{q})$ to write a matrix equation for this system. If we note that

$$g_{11}(\mathbf{q}) = g_{-1-1}(\mathbf{q}) = g_{1-1}(\mathbf{q}) = g_{-11}(\mathbf{q}), \tag{3.28}$$

and

$$g_{01}(\mathbf{q}) = g_{0-1}(\mathbf{q}) = g_{10}(\mathbf{q}) = g_{-10}(\mathbf{q}), \tag{3.29}$$

then we can write

$$\begin{pmatrix} \Delta_{-1} \\ \sqrt{\frac{\xi_1}{\xi_0}}\Delta_0 \\ \Delta_1 \end{pmatrix} = \begin{pmatrix} a & b & c \\ b^{\star} & d & -b \\ c^{\star} & -b^{\star} & a \end{pmatrix}\begin{pmatrix} \Delta_{-1} \\ \sqrt{\frac{\xi_1}{\xi_0}}\Delta_0 \\ \Delta_1 \end{pmatrix}. \tag{3.30}$$

The elements of the matrix are given by

$$a = -\frac{3\xi_1}{8\pi}\int d^3q g_{11}(\mathbf{q})\sin^2\theta, \tag{3.31}$$

$$b = -\frac{3}{4\pi}\sqrt{\frac{\xi_0\xi_1}{2}}\int d^3q g_{10}(\mathbf{q})\sin\theta\cos\theta e^{-i\phi}, \tag{3.32}$$

$$c = \frac{3\xi_1}{8\pi}\int d^3q g_{11}(\mathbf{q})\sin^2\theta e^{-2i\phi}, \tag{3.33}$$

$$d = -\frac{3}{4\pi}\xi_0 \int d^3q g_{00}(\mathbf{q}) \cos^2\theta. \tag{3.34}$$

The factors in the vectors on either side are chosen as to ensure that the matrix is Hermitian and so the eigenvalues will be real (as expected from physical considerations).

Any solution of the full non-linear problem will also be a solution of the linear equation. By finding all the non-trivial linear solutions we can then impose constraints to find which of these solutions correspond to the non-linear problem. The matrix here is Hermitian and so has real eigenvalues. Three equations can be written

$$(a-\lambda)X_1 + bX_2 + cX_3 = 0, \tag{3.35}$$

$$b^\star X_1 + (d-\lambda)X_2 - bX_3 = 0, \tag{3.36}$$

$$c^\star X_1 - b^\star X_2 + (a-\lambda)X_3 = 0, \tag{3.37}$$

where the X_i are components of the eigenvector. By multiplying Eq. (3.35) by $b^\star$ and Eq. (3.37) by b and adding them we can show

$$|\Delta_1| = |\Delta_{-1}|. \tag{3.38}$$

We can deduce some further properties of these equations by working in a cartesian basis. We can change basis with the following definitions

$$|\chi_{\pm 1}\rangle = \mp\frac{1}{\sqrt{2}}\left(|\chi_x\rangle \pm i|\chi_y\rangle\right), \tag{3.39}$$

$$|\chi_0\rangle = |\chi_z\rangle. \tag{3.40}$$

This allows the gap to be similarly transformed to give

$$\Delta_{\pm 1} = \mp\frac{1}{\sqrt{2}}\left(\Delta_x \pm i\Delta_y\right), \tag{3.41}$$

$$\Delta_0^\star = \Delta_z^\star. \tag{3.42}$$

In general the components will be complex quantities so that,

$$\Delta_x = \mathrm{Re}\Delta_x + i\mathrm{Im}\Delta_x, \tag{3.43}$$

$$\Delta_y = \mathrm{Re}\Delta_y + i\mathrm{Im}\Delta_y. \tag{3.44}$$

So in general the $m_1 = \pm 1$ components will be complex and given by

$$\Delta_{\pm 1} = \mp\frac{1}{\sqrt{2}}\left(\left(\mathrm{Re}\Delta_x \mp \mathrm{Im}\Delta_y\right) + i\left(\mathrm{Im}\Delta_x \pm \mathrm{Re}\Delta_y\right)\right), \tag{3.45}$$

which multiplied by its complex conjugate gives

$$|\Delta_{\pm 1}|^2 = \frac{1}{2}\left(\left(\mathrm{Re}\Delta_x \mp \mathrm{Im}\Delta_y\right)^2 + \left(\mathrm{Re}\Delta_y \pm \mathrm{Im}\Delta_x\right)^2\right). \tag{3.46}$$

Using Eq. (3.38) shows

$$\mathrm{Re}\Delta_x\mathrm{Im}\Delta_y = \mathrm{Re}\Delta_y\mathrm{Im}\Delta_x, \tag{3.47}$$

so that,

$$\frac{\mathrm{Im}\Delta_x}{\mathrm{Re}\Delta_x} = \frac{\mathrm{Im}\Delta_y}{\mathrm{Re}\Delta_y} = \pm\tan\alpha, \tag{3.48}$$

so Δ_x and Δ_y have the same phase α up to a multiple of π. We can pull this phase out of the definition of the $m_1 = \pm 1$ components to give

$$\Delta_{\pm 1} = \mp\frac{1}{\sqrt{2}}e^{i\alpha}\left(|\Delta_x| \pm ie^{in\pi}|\Delta_y|\right). \tag{3.49}$$

Here n is an integer. From Eq. (3.36)

$$X_2 = \frac{1}{d-\lambda}\left(bX_3 - b^\star X_1\right) \tag{3.50}$$

So that,

$$X_2 = \frac{-\sqrt{2}e^{i\alpha}}{(d-\lambda)}\left(\mathrm{Re}\left\{b|\Delta_x|\right\} - ie^{in\pi}\mathrm{Re}\left\{b|\Delta_y|\right\}\right) \tag{3.51}$$

which shares a phase with X_1 and X_3. This means that all three components, $\{x, y, z\}$, share a common phase that can be divided out on both sides of the gap

equation. The gap equation is given by Eq. (3.17) with,

$$\begin{aligned}\Delta(\mathbf{p}) &= \langle \mathbf{p}|V|\Phi\rangle \\ &= \langle \mathbf{p}|\chi_{-1}\rangle\xi_{-1}\langle\chi_{-1}|\Phi\rangle + \langle \mathbf{p}|\chi_0\rangle\xi_0\langle\chi_0|\Phi\rangle + \langle \mathbf{p}|\chi_1\rangle\xi_1\langle\chi_1|\Phi\rangle \\ &= \Delta_x\chi_x(\mathbf{p}) + \Delta_y\chi_y(\mathbf{p}) + \Delta_z\chi_z(\mathbf{p}) \\ &= \vec{\Delta}\cdot\vec{\chi}(\mathbf{p}). \end{aligned} \tag{3.52}$$

So we can write the gap equation with a vector notation,

$$\begin{aligned}\vec{\Delta}^\star\cdot\vec{\chi}(\mathbf{p}) = -\int d^3q\ \Big(&\langle \mathbf{p}|\chi_x\rangle\xi_1\langle\chi_x|\mathbf{q}\rangle + \langle \mathbf{p}|\chi_y\rangle\xi_1\langle\chi_y|\mathbf{q}\rangle \\ &+\langle \mathbf{p}|\chi_z\rangle\xi_0\langle\chi_z|\mathbf{q}\rangle\Big)\frac{\vec{\Delta}^\star\cdot\vec{\chi(\mathbf{q})}}{2\epsilon_\mathbf{q}}\tanh(\beta\frac{\epsilon_\mathbf{q}}{2}).\end{aligned} \tag{3.53}$$

We now divide out the common form factor on both sides to give an equation for the components of the gap parameter

$$\Delta_i^\star = -\int d^3q\ \xi_i\langle\chi_i|\mathbf{q}\rangle\frac{\vec{\Delta}^\star\cdot\vec{\chi}(\mathbf{q})}{2\epsilon_\mathbf{q}}\tanh(\beta\frac{\epsilon_\mathbf{q}}{2}), \tag{3.54}$$

with $i = x,y,z$ and $\xi_i = \xi_1$ for $i = x,y$ and ξ_0 for $i = z$. The components of the form factor vector are given by

$$\vec{\chi}(\mathbf{q}) = \left(\frac{3}{4\pi}\right)^{1/2}\begin{pmatrix}\chi_{11}(q)\sin\theta\cos\phi\\ \chi_{11}(q)\sin\theta\sin\phi\\ \chi_0(q)\cos\theta\end{pmatrix}. \tag{3.55}$$

The gap equation can now be written in the new basis as

$$\begin{aligned}\Delta_i^\star = -\int d^3q\ \xi_i\chi_i(\mathbf{q})&\frac{\vec{\Delta}^\star\cdot\vec{\chi}(\mathbf{q})}{2\left(\left(\frac{q^2}{2m}-\mu\right)^2+|\vec{\Delta}\cdot\vec{\chi}(\mathbf{q})|^2\right)^{1/2}} \\ &\times\tanh\left(\frac{\beta}{2}\left(\left(\frac{q^2}{2m}-\mu\right)^2+|\vec{\Delta}\cdot\vec{\chi}(\mathbf{q})|^2\right)^{1/2}\right).\end{aligned} \tag{3.56}$$

For every solution of this equation we will need to determine four parameters:

The three components of the gap function and the chemical potential (we fix the density and the temperature of the gas). We now show that this can be reduced to three parameters by eliminating one of the gap components. Assuming that there exists a solution in a set of coordinates rotated in the $x-y$ plane we can write

$$\left(\mathbb{D}\vec{\Delta}^{\star}\right)_i = -\int d^3q\, \xi_i \chi_i(\mathbf{q}) \frac{\left(\mathbb{D}\vec{\Delta}^{\star}\right)\cdot\vec{\chi}(\mathbf{q})}{2\left(\left(\frac{q^2}{2m}-\mu\right)^2 + |\left(\mathbb{D}\vec{\Delta}\right)\cdot\vec{\chi}(\mathbf{q})|^2\right)^{1/2}} \times \tanh\left(\frac{\beta}{2}\left(\left(\frac{q^2}{2m}-\mu\right)^2 + |\left(\mathbb{D}\vec{\Delta}\right)\cdot\vec{\chi}(\mathbf{q})|^2\right)^{1/2}\right) \tag{3.57}$$

where $\mathbb{D}$ is a rotation matrix in the $x-y$ plane. Now we can use the rotational invariance of the dot product, $\mathbb{D}\vec{\Delta}^{\star}\cdot\vec{\chi}(\mathbf{q}) = \vec{\Delta}^{\star}\cdot\mathbb{D}^{-1}\vec{\chi}(\mathbf{q})$, to write

$$\left(\mathbb{D}\vec{\Delta}^{\star}\right)_i = -\int d^3q\, \xi_i \left(\mathbb{D}\chi(\mathbb{D}^{-1}\mathbf{q})\right)_i \frac{\vec{\Delta}^{\star}\cdot\mathbb{D}^{-1}\vec{\chi}(\mathbf{q})}{2\left(\left(\frac{q^2}{2m}-\mu\right)^2 + |\vec{\Delta}\cdot\mathbb{D}^{-1}\vec{\chi}(\mathbf{q})|^2\right)^{1/2}} \times \tanh\left(\frac{\beta}{2}\left(\left(\frac{q^2}{2m}-\mu\right)^2 + |\vec{\Delta}\cdot\mathbb{D}^{-1}\vec{\chi}(\mathbf{q})|^2\right)^{1/2}\right). \tag{3.58}$$

We should first note that the volume element is rotationally invariant so this will be the same in both coordinate systems. We have used the unitary property of the rotation matrix to write $\chi_i(\mathbf{q}) = \left(\mathbb{D}\chi\left(\mathbb{D}^{-1}\mathbf{q}\right)\right)_i$. In order to perform the integration over ϕ it is instructive to make a change of variables. The original limits of the integration were from 0 to 2π, which means that the new range of integration will be from ζ to $2\pi+\zeta$, where ζ is the angle through which we have rotated the system in the $x-y$ plane. This will give the same answer as the original integration limits since it spans the entire space. We can therefore deduce that Eq. (3.58) is of the same form as Eq. (3.57) and rotating the system in the $x-y$ plane does not affect the physics.

In the cartesian basis a component of the gap equation can be written in the

form

$$\Delta_i^\star(\mathbf{p}) = -\int d^3q \frac{\langle \mathbf{q}|V_i|\mathbf{p}\rangle \vec{\Delta^\star}\cdot\vec{\chi(\mathbf{q})}}{2\left(\left(\frac{q^2}{2m}-\mu\right)^2+|\Delta(\mathbf{q})|^2\right)^{1/2}} \tanh\left[\frac{\beta}{2}\left(\left(\frac{q^2}{2m}-\mu\right)^2+|\Delta(\mathbf{q})|^2\right)^{1/2}\right]. \tag{3.59}$$

We can write the components of the gap parameter as

$$\Delta_i^\star = -\int d^3q\, f(\mathbf{q})\langle \mathbf{q}|\chi_i\rangle \xi_i \vec{\Delta^\star}\cdot\vec{\chi(\mathbf{q})}, \tag{3.60}$$

with $i = \{x, y, z\}$. In this equation a form factor has been divided out on both sides and

$$f(\mathbf{q}) = \frac{\tanh\left[\frac{\beta}{2}\left(\left(\frac{q^2}{2m}-\mu\right)^2+|\Delta(\mathbf{q})|^2\right)^{1/2}\right]}{2\left(\left(\frac{q^2}{2m}-\mu\right)^2+|\Delta(\mathbf{q})|^2\right)^{1/2}}. \tag{3.61}$$

Expanding the dot product gives.

$$\Delta_i^\star = -\left(\frac{3}{4\pi}\right)^{1/2}\int d^3q\, f(\mathbf{q})\langle \mathbf{q}|\chi_i\rangle\xi_i\left[\Delta_x^\star\,\chi_{11}(q)\sin\theta\cos\phi\right. \tag{3.62}$$
$$\left. +\Delta_y^\star\chi_{11}(q)\sin\theta\sin\phi + \Delta_z^\star\chi_0(q)\cos\theta\right].$$

We have shown that the system is rotationally invariant in the $x-y$ plane. The implies that we can set the y-component (or the x-component) to zero when solving our system of equations. This is not totally unexpected as we would suppose there to be rotational symmetry about the magnetic field axis (which we have chosen to be in the z-direction, see Fig. 2.4). This rotational invariance has been confirmed by the experiments of Ticknor *et al*. [2] who observed a degeneracy of the $m_1 = 1$ and $m_1 = -1$ states. We choose to set the y-component to zero to give

$$\Delta_i^\star = -\left(\frac{3}{4\pi}\right)^{1/2}\int d^3q\, f(\mathbf{q})\langle \mathbf{q}|\chi_i\rangle\xi_i\left[\Delta_x^\star\chi_{11}(q)\sin\theta\cos\phi + \Delta_z^\star\chi_0(q)\cos\theta\right]. \tag{3.63}$$

Since the equation for Δ_y now has a trivial solution only two equations remain

$$\Delta_x^\star = -\left(\frac{3}{4\pi}\right)\int d^3q\, f(\mathbf{q})\xi_x \left[\Delta_x^\star \chi_{11}^2(q)\sin^2\theta\cos^2\phi + \Delta_z^\star \chi_{11}(q)\chi_0(q)\cos\theta\sin\theta\cos\phi\right], \tag{3.64}$$

$$\Delta_z^\star = -\left(\frac{3}{4\pi}\right)\int d^3q\, f(\mathbf{q})\xi_z \left[\Delta_x^\star \chi_0(q)\chi_{11}(q)\cos\theta\sin\theta\cos\phi + \Delta_z^\star \chi_0^2(q)\cos^2\theta\right]. \tag{3.65}$$

As a matrix equation we can write

$$\begin{pmatrix} \Delta_x^\star \\ \sqrt{\frac{\xi_x}{\xi_z}}\Delta_z^\star \end{pmatrix} = \begin{pmatrix} \langle D_x(\mathbf{q}), D_x(\mathbf{q})\rangle & \langle D_x(\mathbf{q}), D_z(\mathbf{q})\rangle \\ \langle D_z(\mathbf{q}), D_x(\mathbf{q})\rangle & \langle D_z(\mathbf{q}), D_z(\mathbf{q}\rangle \end{pmatrix} \begin{pmatrix} \Delta_x^\star \\ \sqrt{\frac{\xi_x}{\xi_z}}\Delta_z^\star \end{pmatrix} = \underline{\mathbf{A}} \begin{pmatrix} \Delta_x^\star \\ \sqrt{\frac{\xi_x}{\xi_z}}\Delta_z^\star \end{pmatrix}. \tag{3.66}$$

Here,

$$D_x(\mathbf{q}) = i\sqrt{\frac{3f(\mathbf{q})\xi_x}{4\pi}}\chi_{11}(q)\sin\theta\cos\phi, \tag{3.67}$$

and

$$D_z(\mathbf{q}) = i\sqrt{\frac{3f(\mathbf{q})\xi_z}{4\pi}}\chi_0(q)\cos\theta. \tag{3.68}$$

The brackets $\langle ..., ... \rangle$ represent integrals of the product of these functions over all space. The Cauchy-Schwartz inequality gives

$$\langle D_x(\mathbf{q}), D_x(\mathbf{q})\rangle\langle D_z(\mathbf{q}), D_z(\mathbf{q})\rangle \geq |\langle D_x(\mathbf{q}), D_z(\mathbf{q})\rangle|^2. \tag{3.69}$$

This is consistent with physical intuition in that the cross terms should not contribute as much as the diagonal terms. The matrix is Hermitian, so the eigenvalues are real. From this it can be seen that the eigenvalues are bounded by

$$0 < \lambda < \langle D_x(\mathbf{q}), D_x(\mathbf{q})\rangle\langle D_z(\mathbf{q}), D_z(\mathbf{q})\rangle \tag{3.70}$$

The form factors in the equations for the components of the gap are given by

$$\chi_{10}(q) = \frac{\sigma_{10}}{\pi\hbar^{5/2}} q e^{-q^2\sigma_0^2/2\hbar^2} \tag{3.71}$$

$$\chi_{11}(q) = \frac{\sigma_1}{\pi\hbar^{5/2}} q e^{-q^2\sigma_1^2/2\hbar^2} \tag{3.72}$$

as shown in Chapter 2. The equations become

$$\Delta_x^\star = -\left(\frac{3\sigma_1}{4\pi^3\hbar^5}\right)\int d^3q\, f(\mathbf{q}) q^2 \xi_x \left[\Delta_x^\star \sigma_1\ e^{-q^2\sigma_1^2/\hbar^2} \sin^2\theta\cos^2\phi \right. \tag{3.73}$$
$$\left. + \Delta_z^\star \sigma_0 e^{-q^2(\sigma_1^2+\sigma_0^2)/2\hbar^2} \cos\theta\sin\theta\cos\phi\right],$$

$$\Delta_z^\star = -\left(\frac{3\sigma_0}{4\pi^3\hbar^5}\right)\int d^3q\, f(\mathbf{q}) q^2 \xi_z \left[\Delta_x^\star \sigma_1 e^{-q^2(\sigma_1^2+\sigma_0^2)/2\hbar^2}\ \cos\theta\sin\theta\cos\phi \right. \tag{3.74}$$
$$\left. + \Delta_z^\star \sigma_0 e^{-q^2\sigma_0^2/\hbar^2} \cos^2\theta\right].$$

In the cartesian basis the modulus squared of the gap appearing in the function $f(\mathbf{q})$ can be written as

$$|\Delta(q)|^2 = \left(\frac{3}{4\pi}\right)\left[\chi_{11}(q)^2|\Delta_x|^2 \sin^2\theta\cos^2\phi + \chi_0(q)^2|\Delta_z|^2\cos^2\theta\right]. \tag{3.75}$$

Now the matrix elements of Eq. (3.66) can be written as

$$A_{11} = -\left(\frac{3\sigma_1}{4\pi^3\hbar^5}\right)\int d^3q\, f(\mathbf{q}) q^2 \xi_x \sigma_1 e^{-q^2\sigma_1^2/\hbar^2} \sin^2\theta\cos^2\phi \tag{3.76}$$

$$A_{12} = A_{21} = -\left(\frac{3\sigma_1}{4\pi^3\hbar^5}\right)\int d^3q\, f(\mathbf{q}) q^2 \sqrt{\xi_x\xi_z}\sigma_0 e^{-q^2(\sigma_1^2+\sigma_0^2)/2\hbar^2} \cos\theta\sin\theta\cos\phi \tag{3.77}$$

$$A_{22} = -\left(\frac{3\sigma_0}{4\pi^3\hbar^5}\right)\int d^3q\, f(\mathbf{q}) q^2 \xi_z \sigma_0 e^{-q^2\sigma_0^2/\hbar^2} \cos^2\theta \tag{3.78}$$

The corresponding density equation for this system is given by Eq. (3.18) with the gap function given by Eq. (3.19). In order to solve the system of equations the temperature and density are fixed as already mentioned. The density equation (3.18) is solved for a range of μ, Δ_x and Δ_z. By interpolation it is then possible to find the corresponding value of μ for every $\{\Delta_x, \Delta_z\}$ such that

$$\mu = \mu(\Delta_x, \Delta_z). \tag{3.79}$$

The matrix elements of equations (3.76), (3.77) and (3.78) can then be given as a function of $\{\Delta_x, \Delta_z\}$. This is done at a fixed magnetic field where the ξ_i is given by Eq. (2.56), with the scattering volume given by the usual resonance formula, Eq. (2.32). This will lead to two sets of eigenvalues; again these will be functions of $\{\Delta_x, \Delta_z\}$ and will form a surface in this space. The solution to the problem can be found through the constraint

$$\|\underline{\mathbf{A}X} - \lambda_A \underline{X}\| = 0, \tag{3.80}$$

where $\underline{X}$ are the eigenvectors, corresponding to the correct values of $\{\Delta_x, \Delta_z\}$ as a solution to the system.

3.2.3 Evaluation of the cross terms

The magnitude of A_{12} in Eq. (3.77) will determine to what extent it is possible to exclude these cross terms when solving the BCS equations. It is only possible to judge the magnitude of these terms in relation to the diagonal terms, which according to Eq. (3.66) we would expect to be of order unity. We can write

$$a_{12} = \int_0^\infty q^2 dq \int_0^\pi \sin\theta d\theta \int_0^{2\pi} d\phi \Xi(\mathbf{q}) \cos\phi, \tag{3.81}$$

where the function $\Xi(\mathbf{q})$ contains everything in the integrand of Eq. (3.77) except the $\cos\phi$ factor. It is easily seen that this integral will be zero if $\Xi(\mathbf{q})$ is independent of ϕ. The terms containing ϕ are contained in the function $f(\mathbf{q})$ and appear in such a way that they always give a positive contribution to the integral. This means that the magnitude of the cross term A_{12} will depend on how much weight these terms give to the integral over ϕ. Eq. (3.18) suggests that an increased integrand will lead to an increased density. This can be achieved by increasing the denominator of the second term. For a fixed chemical potential this can be achieved by increasing the gap parameter. The corollary of this is that increasing the density of the system for a fixed chemical potential will increase the value of the gap parameter. This suggests that we would expect to see an increase in the coupling between the two resonances as the density increases.

The terms A_{11}/ξ_x and A_{22}/ξ_z have been plotted in Fig. 3.2 as a function of the gap terms Δ_x/E_F and Δ_z/E_F for a density of 10^{13} cm^{-3} about the 198.85G resonance in ^{40}K. For a comparison the $A_{12}/\sqrt{\xi_x\xi_z}$ term is plotted in Fig. 3.3 for the same density. It can be seen that this cross term is orders of magnitude smaller than the diagonal terms. Fig. 3.4 shows that the cross terms remain orders of magnitude smaller than the diagonal terms up to a density of 10^{16}cm^{-3}. This is likely to be a higher density than experiments would normally be performed at. In this case then it may be possible to treat the $m_1 = 0$ and $m_1 = \pm 1$ separately. We now move on to implement this separation of the resonances and see what differences this introduces.

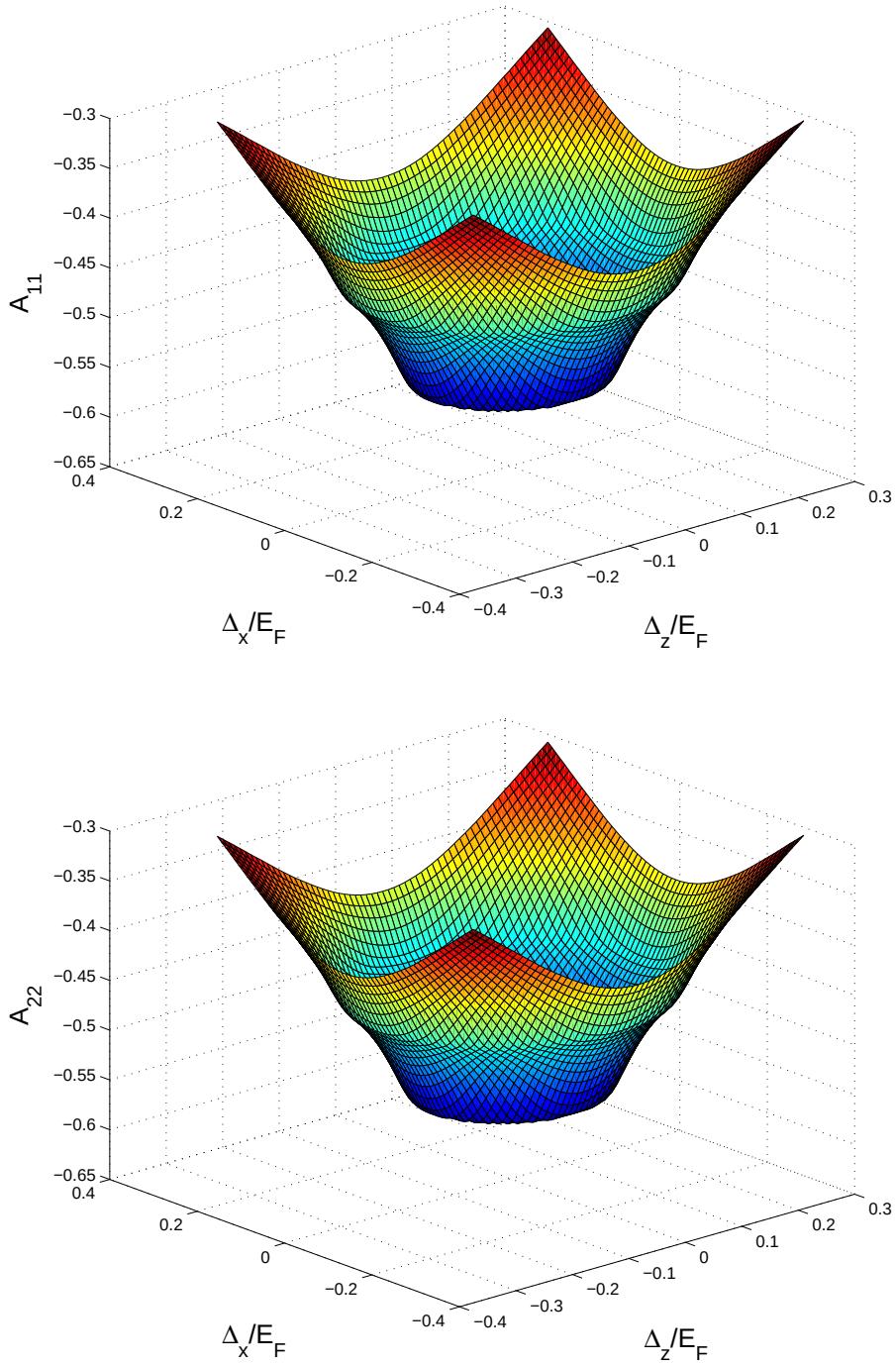

Figure 3.2: Plot of the diagonal terms in the gap equation as a function of Δ_x/E_F and Δ_z/E_F at a density of 10^{13}cm^{-3}.

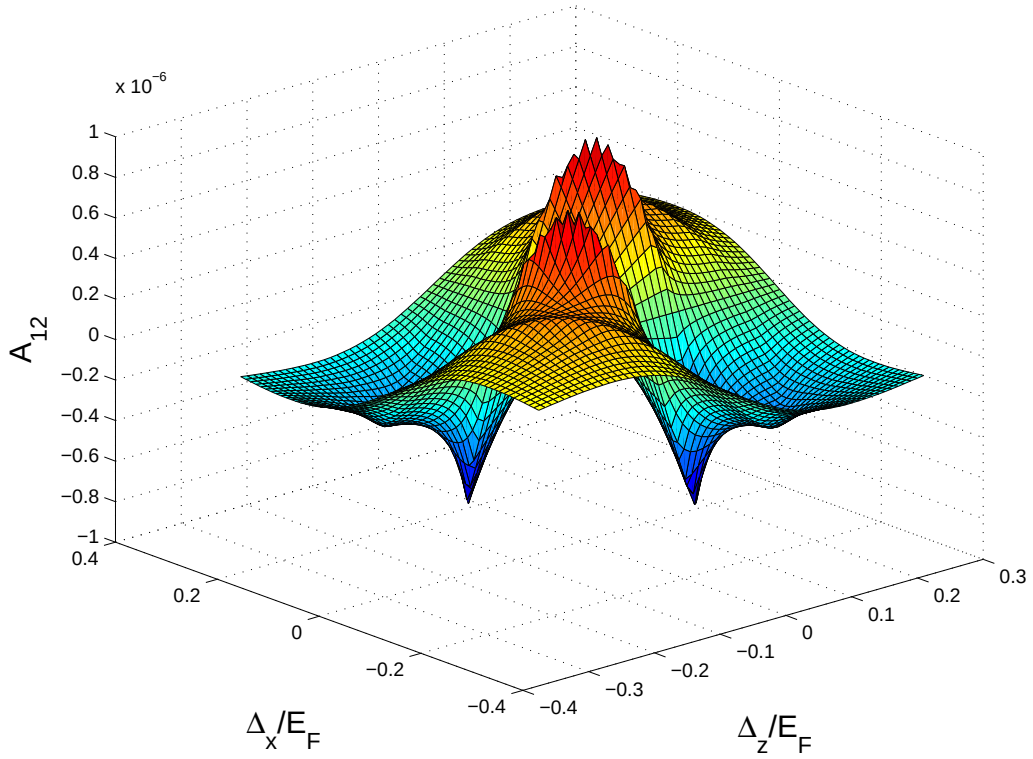

Figure 3.3: Cross term as a function of Δ_x/E_F and Δ_z/E_F at a density of 10^{13} cm^{-3}. The diagonal terms would be expected to be on the order of unity. It can be seen here that the cross term is orders of magnitude smaller than the diagonal terms.

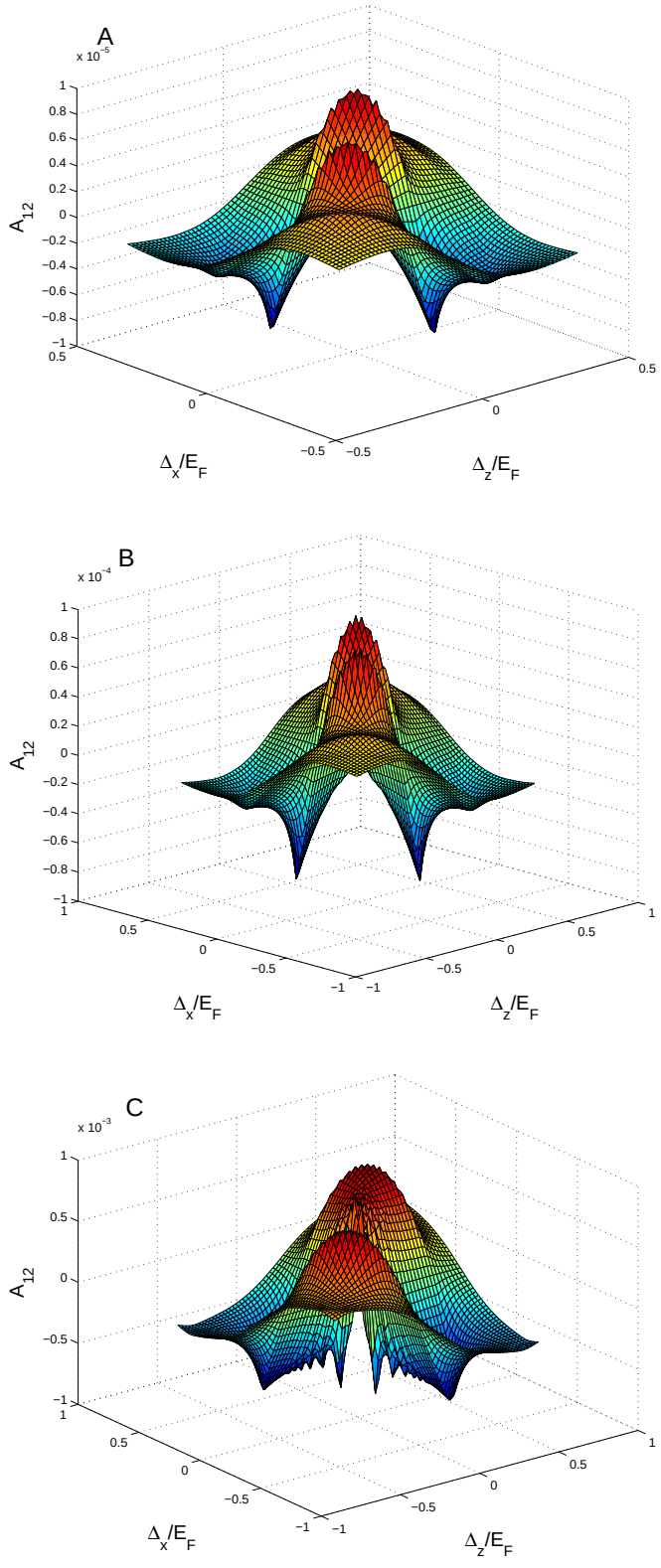

Figure 3.4: Cross terms as a function of Δ_x/E_F and Δ_z/E_F at a density of A) 10^{14}cm^{-3}, B)10^{15}cm^{-3} and C) 10^{16}cm^{-3}. It can be seen that the magnitude of the cross term increases with increasing density. However, up to a density of 10^{16}cm^{-3} this term remains orders of magnitude smaller than the diagonal terms.

3.2.4 Separated resonances

In the cases where the coupling is small, such as the situation in the ^{40}K resonance, it should be possible to treat the $m_1 = \pm 1$ and $m_1 = 0$ resonances as if they are independent of each other. The $m_1 = 0$ resonance is easily treated by neglecting the $m_1 = \pm 1$ components leaving only one separable term in the potential. The definition of the $m_1 = \pm 1$ resonance is slightly more subtle since we have to consider two degenerate terms.

By inserting the expression for the spherical harmonics into the gap equation we can write a matrix equation for the $m_1 = \pm 1$ components

$$\begin{pmatrix} \Delta_1^\star \\ \Delta_{-1}^\star \end{pmatrix} = \begin{pmatrix} -\int d^3q h(\mathbf{q}) & \int d^3q h(\mathbf{q}) e^{2i\phi} \\ \int d^3q h(\mathbf{q}) e^{-2i\phi} & -\int d^3q h(\mathbf{q}) \end{pmatrix} \begin{pmatrix} \Delta_1^\star \\ \Delta_{-1}^\star \end{pmatrix}. \tag{3.82}$$

The function $h(\mathbf{q})$ is given by

$$h(\mathbf{q}) = \frac{3}{16\pi} \frac{|\chi(q)|^2 \sin^2\theta\xi}{\left(\left(\frac{q^2}{2m} - \mu\right)^2 + |\Delta(\mathbf{q})|^2\right)^{1/2}} \tanh\left[\frac{\beta}{2}\left(\left(\frac{q^2}{2m} - \mu\right)^2 + |\Delta(\mathbf{q})|^2\right)^{1/2}\right], \tag{3.83}$$

where the gap function includes only the $m_1 = \pm 1$ components,

$$\Delta(\mathbf{q}) = \langle \mathbf{q}|\chi_1\rangle \xi_1 \Delta_1 + \langle \mathbf{q}|\chi_{-1}\rangle \xi_{-1} \Delta_{-1}. \tag{3.84}$$

By solving the eigenvalue problem and finding the eigenvectors it can easily be shown that the values of $\Delta_1^\star$ and $\Delta_{-1}^\star$ differ only by a complex phase, which we will label α. This leads to two equations from multiplying out the matrix

$$1 = \int d^3q h(\mathbf{q}) \left(e^{i(2\phi+\alpha)} - 1\right), \tag{3.85}$$

$$1 = \int d^3q h(\mathbf{q}) \left(e^{-i(2\phi+\alpha)} - 1\right). \tag{3.86}$$

By adding these two equations together we can show that

$$1 = -2 \int d^3q g(\mathbf{q}) \sin^2\left(\phi + \frac{\alpha}{2}\right). \tag{3.87}$$

The term containing the gap in the denominator can be written as

$$|\Delta(\mathbf{q})|^2 = |\Delta_1|^2\chi(q)^2|Y_{11}(\hat{\mathbf{q}})|^2 + |\Delta_{-1}|^2\chi(q)^2|Y_{1-1}(\hat{\mathbf{q}})|^2 + 2Re\left[\Delta_1^\star\Delta_{-1}\chi(q)^2Y_{11}^\star(\hat{\mathbf{q}})Y_{1-1}(\hat{\mathbf{q}})\right]. \tag{3.88}$$

Using the fact that the gaps only differ by a phase allow this to be written as

$$|\Delta(\mathbf{q})|^2 = \frac{3}{2\pi}|\Delta_1|^2\chi(q)^2\sin^2\theta\sin^2\left(\phi+\frac{\alpha}{2}\right). \tag{3.89}$$

We can therefore define a new function

$$\mathfrak{H}\left(q,\sin^2\theta\,\sin^2\left(\phi+\frac{\alpha}{2}\right)\right) = h(\mathbf{q})\sin^2\left(\phi+\frac{\alpha}{2}\right) \tag{3.90}$$

$$= \frac{3}{16\pi}\frac{|\chi(q)|^2\sin^2\theta\sin^2\left(\phi+\frac{\alpha}{2}\right)\xi}{\left(\left(\frac{q^2}{2m}-\mu\right)^2+\frac{3}{2\pi}|\Delta_1|^2|\chi(q)|^2\sin^2\theta\sin^2\left(\phi+\frac{\alpha}{2}\right)\right)^{1/2}} \tag{3.91}$$

$$\times\tanh\left[\frac{\beta}{2}\left(\left(\frac{q^2}{2m}-\mu\right)^2+\frac{3}{2\pi}|\Delta_1|^2|\chi(q)|^2\sin^2\theta\sin^2\left(\phi+\frac{\alpha}{2}\right)\right)^{1/2}\right].$$

The phase can be absorbed into the ϕ integration and we can write

$$1 = -\frac{3}{8\pi}\int d^3q\frac{|\chi(q)|^2\sin^2\theta\sin^2\phi\xi}{\left(\left(\frac{q^2}{2m}-\mu\right)^2+\frac{3}{2\pi}|\Delta_1|^2|\chi(q)|^2\sin^2\theta\sin^2\phi\right)^{1/2}} \tag{3.92}$$

$$\times\tanh\left[\frac{\beta}{2}\left(\left(\frac{q^2}{2m}-\mu\right)^2+\frac{3}{2\pi}|\Delta_1|^2|\chi(q)|^2\sin^2\theta\sin^2\phi\right)^{1/2}\right].$$

The two angular integrals in this equation can be reduced to one integral. We show how this is achieved in Appendix E. This allows the entire gap equation to be rewritten in terms of one linear integral and one parametrised angular integral

$$1 = -\frac{3}{2}\frac{\int q^2dq\int_0^1 dx|\chi(q)|^2x^2\xi}{\left(\left(\frac{q^2}{2m}-\mu\right)^2+\frac{3}{2\pi}|\Delta_1|^2|\chi(q)|^2x^2\right)^{1/2}}\tanh\left[\frac{\beta}{2}\left(\left(\frac{q^2}{2m}-\mu\right)^2+\frac{3}{2\pi}|\Delta_1|^2|\chi(q)|^2x^2\right)^{1/2}\right]. \tag{3.93}$$

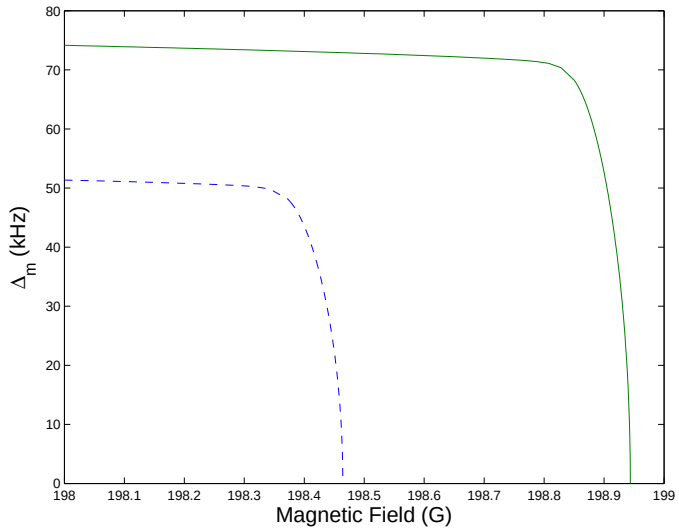

Figure 3.5: Variation of the parameter Δ_m with magnetic field for the p-wave resonance in ^{40}K for a density of 10^{13} cm^{-3} and a temperature of $70nK$. The solid green line is the value of the $m = 0$ resonance and the dashed blue line is for the $|m| = 1$ resonance. There is no significant difference between the value obtained when coupling between the components is included and when the coupling is excluded.

3.2.5 Results

Equation (3.93) is solved at fixed density and temperature together with the density equation to provide values for the separated gap parameters, Δ_0 and Δ_1, and the chemical potential corresponding to each component. A plot of the gap parameters as a function of magnetic field is given in Fig. 3.5 for the p-wave resonance in ^{40}K close to 199 G for a temperature of 70 nK and a density of 10^{13} cm^{13}. In the BEC limit the $m_1 = 1$ component appears to be smaller by a factor of $\sqrt{2}$. The origin of this factor is the degeneracy of the $m_1 = \pm 1$ states and they both equally contribute to the value of the gap parameter. For this resonance the results given by the coupled resonance model presented in the previous section and the separated resonance model just described are indistinguishable. This was indicated by the relatively small values calculated for the cross term Eq. (3.81). In Fig. 3.6 we plot the value of the gap parameters, Δ_0, throughout the resonance region for various densities with the temperature held constant. As the value of the magnetic field is decreased further and further below the resonance the value

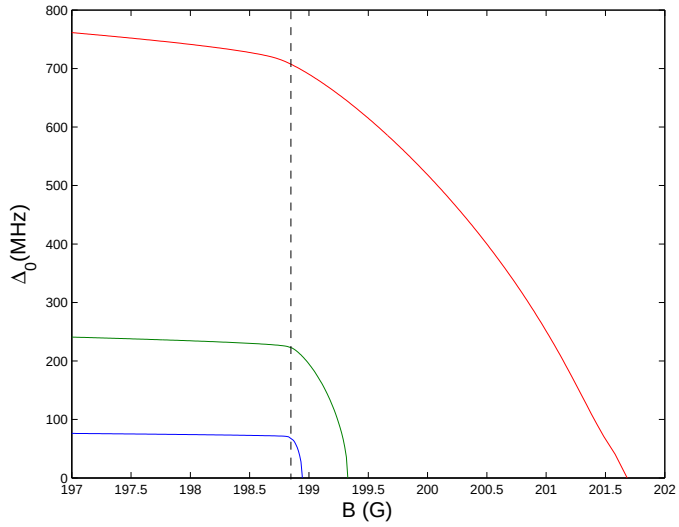

Figure 3.6: The value of the gap parameter, Δ_0, around the resonance position as a function of magnetic field. The different lines correspond to densities of 10^{15} cm^{-3} (top, red),10^{14} cm^{-3} (middle, green) and 10^{13} cm^{-3} (bottom, blue). The temperature is held constant at 70 nK. The dashed line is the position of the *p*-wave resonance at 198.85 G.

of the gap parameter changes less and less, but for a fixed magnetic field it can be seen that the value of the gap parameter increases with increasing density. Similarly, in Fig. 3.7 we present the results of keeping the density constant and varying the temperature. We see that on the BCS side of the resonance the value of the gap parameter increases with decreasing temperature. In the BEC limit the value of the gap parameter is independent of the temperature and fixed by the density of the gas. We have repeated these calculations for the observed resonances in ^{6}Li and found similar conclusions. In particular we have found that the results of the coupled system of Eq. (3.66) and the separated resonance approximation of Eq. (3.93) are indistinguishable. For the remainder of this thesis we therefore use the separated resonance approximation when referring to our BCS state.

It can be seen from Figs. 3.5, 3.6 and 3.7 that at a particular magnetic field the value of the parameter Δ_{m_1} goes to zero. This is when there ceases to be any pairing and the gas becomes a weakly interacting Fermi liquid. For the case of using mean field dynamic equations to create molecules it is necessary for the gap

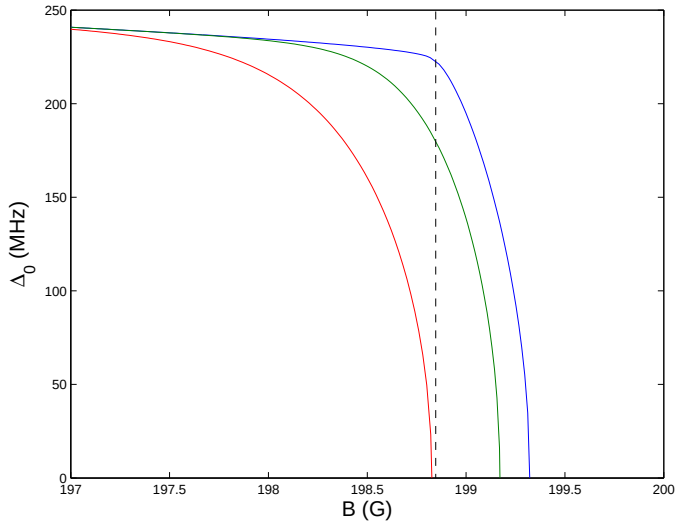

Figure 3.7: The value of the gap parameter, Δ_0, around the resonance position as a function of magnetic field. The different lines correspond to temperatures of 100 nK (top, blue),1000 nK (middle, green) and 2000 nK (bottom, red). The density is held constant at 10^{14} cm^{-3}. The dashed line is the position of the *p*-wave resonance at 198.85 G.

to have a non-zero value in the initial state. This limits the range of magnetic fields that can be used as an initial condition and we cannot start infinitely far away from the resonance. In Fig. 3.8 we plot the magnetic field position at which the gap parameter goes to zero as a function of density for the $m_1 = 0$ resonance in ^{40}K. As the density is increased the value of the magnetic field at which the gap parameter disappears increases away from the resonance. This allows a larger range of magnetic fields to be accessed by the initial conditions. Similarly as the temperature is decreased the value of the magnetic field at which the gap parameter goes to zero moves away from the resonance position; this can also be seen in Fig 3.7. It would then seem that a high density and low temperature is favourable to observe a paired BCS state of the gas and would therefore provide a wider range of magnetic fields from which to begin the mean field calculations.

The question may be asked as to which species would be better suited to producing *p*-wave Feshbach molecules from the mean field dynamics: ^{6}Li or ^{40}K? A comparison of the initial conditions may give some indication of the feasibility

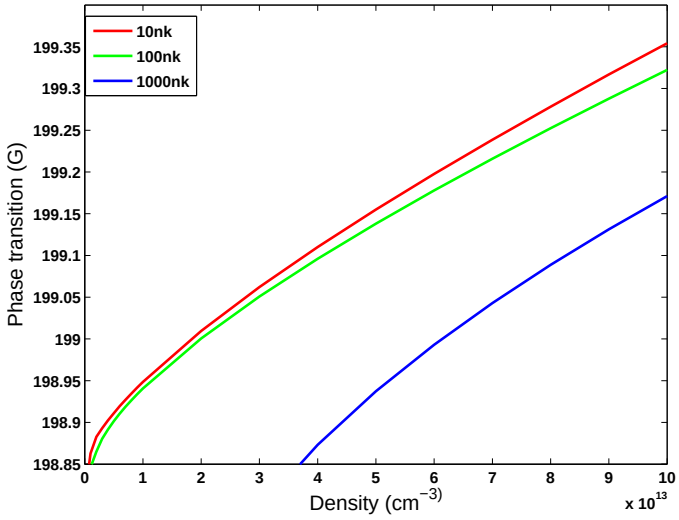

Figure 3.8: Value of the magnetic field at which the gap disappears for the $m = 0$ resonance in ^{40}K. The different lines represent different temperatures. It can be seen that at reasonable experimental temperatures one has to go to a high density in order to explore a significant range of magnetic fields on the BCS side of the resonance.

of producing molecules in either system (We will see in chapter 4 that the value of the initial gap parameter is related to the number of molecules produced in the gas). Fig. 3.9 shows the value of the magnetic field detuning from the resonance at which the gap parameter goes to zero as a function of density for both ^{6}Li and ^{40}K. It can be seen that for ^{40}K it is possible to explore a wider range of magnetic fields for the initial conditions than for ^{6}Li. This is due to the fact that the magnetic moment of the ^{6}Li molecules are approximately 12 times larger than that of the ^{40}K molecules [3].

Fig. 3.10 shows a plot of the chemical potential for $m_1 = 0$ and $m_1 = \pm 1$ pairs about the p-wave resonance in ^{40}K. As the value of the gap parameter goes to zero the value of the chemical potential approaches that of an ideal Fermi gas. On the BEC side of the resonance the chemical potential approaches half the value of the binding energy of the molecules. The slope of the chemical potential is therefore given approximately by the value of the magnetic moment of the molecule. This explains why the the gap parameter exists for a larger range of magnetic fields in ^{40}K than in ^{6}Li; the lower magnetic moment. This suggests that ^{40}K would

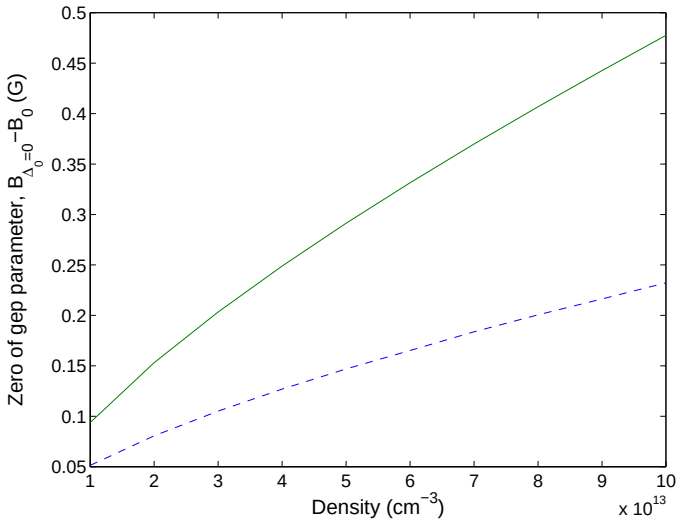

Figure 3.9: Variation of the magnetic field position at which the gap parameter goes to zero for the $m_1 = 0$ resonance in ^{40}K at 198 G (solid line) and ^{6}Li(dashed line) at 215 G. It can be seen that ^{40}K resonance offers a larger range of magnetic fields in which to realise a BCS state on the negative scattering length side. This is due to the magnetic moment of the ^{6}Li molecule being about 12 times larger the magnetic moment of the ^{40}K molecule.

provide a more promising system from which to study the mean field dynamics due to the larger range of available magnetic fields. For this reason we will use this ^{40}K resonance to perform our mean field calculations in the next chapter. This, of course, does not take account of effects beyond the mean field and any experimental issues that may have to be overcome.

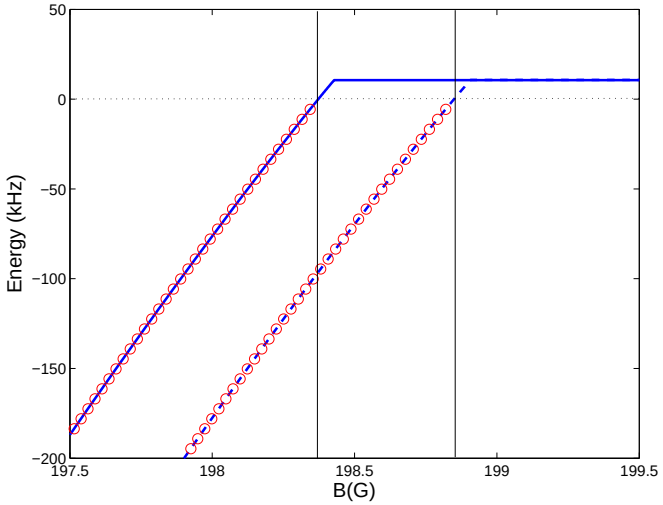

Figure 3.10: Values of twice the p-wave chemical potential for the resonance in ^{40}K at around $198G$. The solid line is the $|m_1| = 1$ chemical potential. The dashed line is the $m_1 = 0$ resonance. The values for coupled resonances at separate resonances are indistinguishable. The red circle are the values of the respective binding energies. The values of the binding energy and the chemical potential approach each other much more rapidly than in the case of the s-wave. The position of the resonances is marked by the vertical line. The zero of chemical potential is given by the horizontal dotted line.

3.3 Bose-Fermi model

Our approach so far has been to calculate correlation functions in terms of ensemble averages of products of Fermi operators. One alternative approach, referred to here as the Bose-Fermi model, is to treat the bound molecules as composite bosons and introduce a coupling between free fermions and bosonic pairs. This model has been extensively studied in both the *s*-wave and *p*-wave [142, 97]. In the case of the *s*-wave it was shown that there is no significant difference in the results given by the single channel model and the Bose-Fermi model when applied about a Feshbach resonance [128]. In this section we compare the results of the model we have presented to one that uses a different form of the potential and a different parameterisation of the scattering volume.

A Hamiltonian for the Bose-Fermi model can be generally written as

$$H_{2-ch} = \sum_{\mathbf{p}} \left(E_{\text{bare}} + \frac{p^2}{4m} \right) b^\dagger_{\mathbf{p}} b_{\mathbf{p}} + \sum_{\mathbf{q}} \frac{q^2}{2m} a^\dagger_{\mathbf{q}} a_{\mathbf{q}} + \sum_{\mathbf{q}.\mathbf{p}} W(q) (b_{\mathbf{p}} a^\dagger_{\mathbf{q}+\frac{\mathbf{p}}{2}} a^\dagger_{-\mathbf{q}+\frac{\mathbf{p}}{2}} + b^\dagger_{\mathbf{p}} a_{-\mathbf{q}+\frac{\mathbf{p}}{2}} a_{\mathbf{q}+\frac{\mathbf{p}}{2}}), \tag{3.94}$$

which is written in the momentum representation to avoid confusion between single particle boson states and single particle fermion states. The operators $a_q^{(\dagger)}$ are the Fermi annihilation (creation) operators, while the the operators $b_q^{(\dagger)}$ are the boson annihilation (creation) operators. $W(q)$ is the coupling between the Fermi channel and the Bose channel, its form depending on the nature of the interaction. In this Hamiltonian it is obvious that scattering between fermions has been neglected. The bosons in this case are the bound molecules with an energy E_{bare} when the molecule is not dressed by the surrounding atoms. The review of Gurarie *et al*. [97] studies this Hamiltonian in both the *s*-wave and the *p*-wave. In the *p*-wave the coupling is linear in its argument, reflecting the low energy properties of the scattering amplitude. This is a similar constraint to that which we imposed in chapter 2 in order to derive our separable potential. A momentum cut off, Λ, is introduced in order to calculate integrals. In contrast our model uses a separable potential that has a Gaussian factor so that our integrals converge automatically, although we still need an extra range parameter, σ. In the Bose-Fermi model the low energy parameters of the system are fitted by including the effective range in the low energy expansion of the scattering amplitude.

Neglecting scattering in the Fermi channel causes the parametrisation of the scattering length to change, so that

$$a(B) = -\frac{a_{\rm bg}\Delta B}{B - B_0} \tag{3.95}$$

For the p-wave model the coupling term is given by

$$W(q) = \frac{g_p q}{\sqrt{V}}, \tag{3.96}$$

where V is a normalisation volume and g_p is a coupling constant. In this model the density equation is given by

$$n = \int \frac{d^3q}{2(2\pi\hbar)^3}\left(1 - \frac{\frac{q^2}{2m} - \mu}{\left(\left(\frac{q^2}{2m} - \mu\right)^2 + 4g_p^2|\mathbf{\Delta}_{\rm B-F}\cdot\mathbf{q}|^2\right)^{1/2}} \times \tanh\left[\frac{\beta}{2}\left(\left(\frac{q^2}{2m} - \mu\right)^2 + 4g_p^2|\mathbf{\Delta}_{\rm B-F}\cdot\mathbf{q}|^2\right)^{1/2}\right]\right) \tag{3.97}$$

The gap equation is given by

$$(\epsilon_\alpha - 2\mu)\,\Delta_{{\rm B-F},\alpha} = \sum_\gamma I^{(T)}_{\alpha\gamma}[\mathbf{B}]\Delta_{{\rm B-F},\gamma} \tag{3.98}$$

with

$$I^{(T)}_{\alpha\gamma}[\mathbf{B}] = g_p^2\int \frac{d^3q}{(2\pi\hbar)^3}\frac{q_\alpha q_\gamma}{\left(\left(\frac{q^2}{2m} - \mu\right)^2 + 4g_p^2|\mathbf{\Delta}_{\rm B-F}\cdot\mathbf{q}|^2\right)^{1/2}} \times \tanh\left[\frac{\beta}{2}\left(\left(\frac{q^2}{2m} - \mu\right)^2 + 4g_p^2|\mathbf{\Delta}_{\rm B-F}\cdot\mathbf{q}|^2\right)^{1/2}\right]. \tag{3.99}$$

The indices α and γ refer to the x,y and z components in the equations, and the g_p represents the Bose-Fermi coupling. The quantity ϵ_α is the energetic detuning of the molecular state to the zero energy Fermi collision state. As usual $\beta = 1/k_BT$ where k_B is Boltzmann's constant and T is the temperature of the gas.

Equations (3.97), (3.98) and (3.99) bear a relation to the BCS equations (3.17) and (3.18) derived in our single channel approach and we can identify

$$\Delta(\mathbf{q}) = 2g_p \mathbf{\Lambda}_{\mathrm{B-F}} \cdot \mathbf{q}. \tag{3.100}$$

The coupling constant can be related to the two-body parameters we introduced in chapter 2

$$g_p^2 = \frac{3\pi a_{\ell m}^{\mathrm{bg}} \frac{\partial E_{res}}{\partial B} \Delta B}{\mu \hbar^2}. \tag{3.101}$$

The momentum cut off is related to our resonance parameters through

$$\Lambda = \frac{\pi \hbar}{2\sigma}. \tag{3.102}$$

Here, σ is the range parameter we introduced in the form factor of the separable potential, Eq. (2.55). We use these definitions to solve the equations for the Bose-Fermi model numerically. The solutions for the parameter Δ_0 have been plotted in Fig. 3.11 for the case where we have treated the resonances in ^{40}K separately, such that we have excluded coupling between the $m_1 = 0$ and $m_1 = \pm 1$ states. This shows that at low densities the solutions are very similar. At higher densities the solutions deviate from each other, with the zero of the gap parameter appearing at a higher magnetic field in our single channel model than in the Bose-Fermi model. This deviation is due to the inclusion of off resonant background scattering in the parametrisation of the scattering length in our model. A comparison of the chemical potentials has been plotted in Fig. 3.12. Here, the solutions agree well close to the resonance and deviate from each other far from the resonance. This is also to be expected due to the different parametrisation used in each model. Overall, the solutions are qualitatively very similar and do not vary greatly quantitatively.

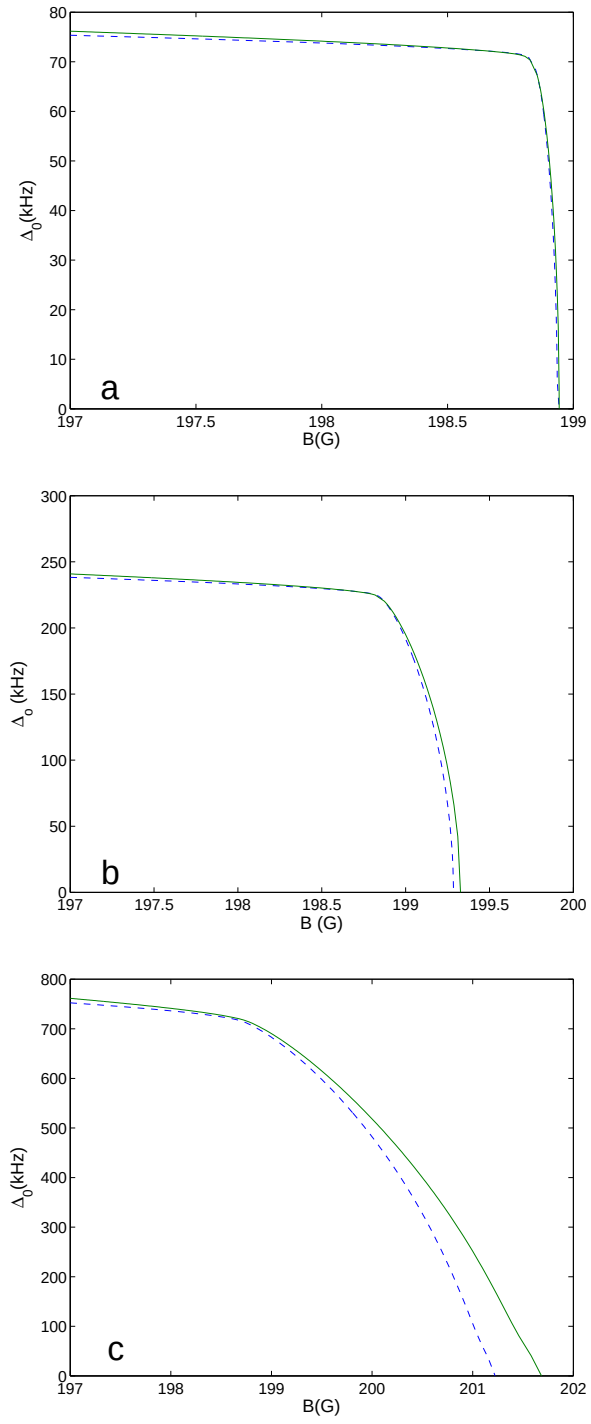

Figure 3.11: Comparison of the parameter Δ_0 using the two channel model (dashed blue line) and the single channel model (Solid green line) for densities of a) 10^{13} cm^{-3}, b) 10^{14} cm^{-3}, c) 10^{15} cm^{-3}. All calculations were performed at 70nK for the $m = 0$ resonance at around 198.85G in ^{40}K. At low densities the solutions are very similar. At higher densities there is a deviation with the position of the zero of the parameter being higher for the single channel model than for the two channel model. This is due to the inclusion of the off resonant scattering in the single channel model.

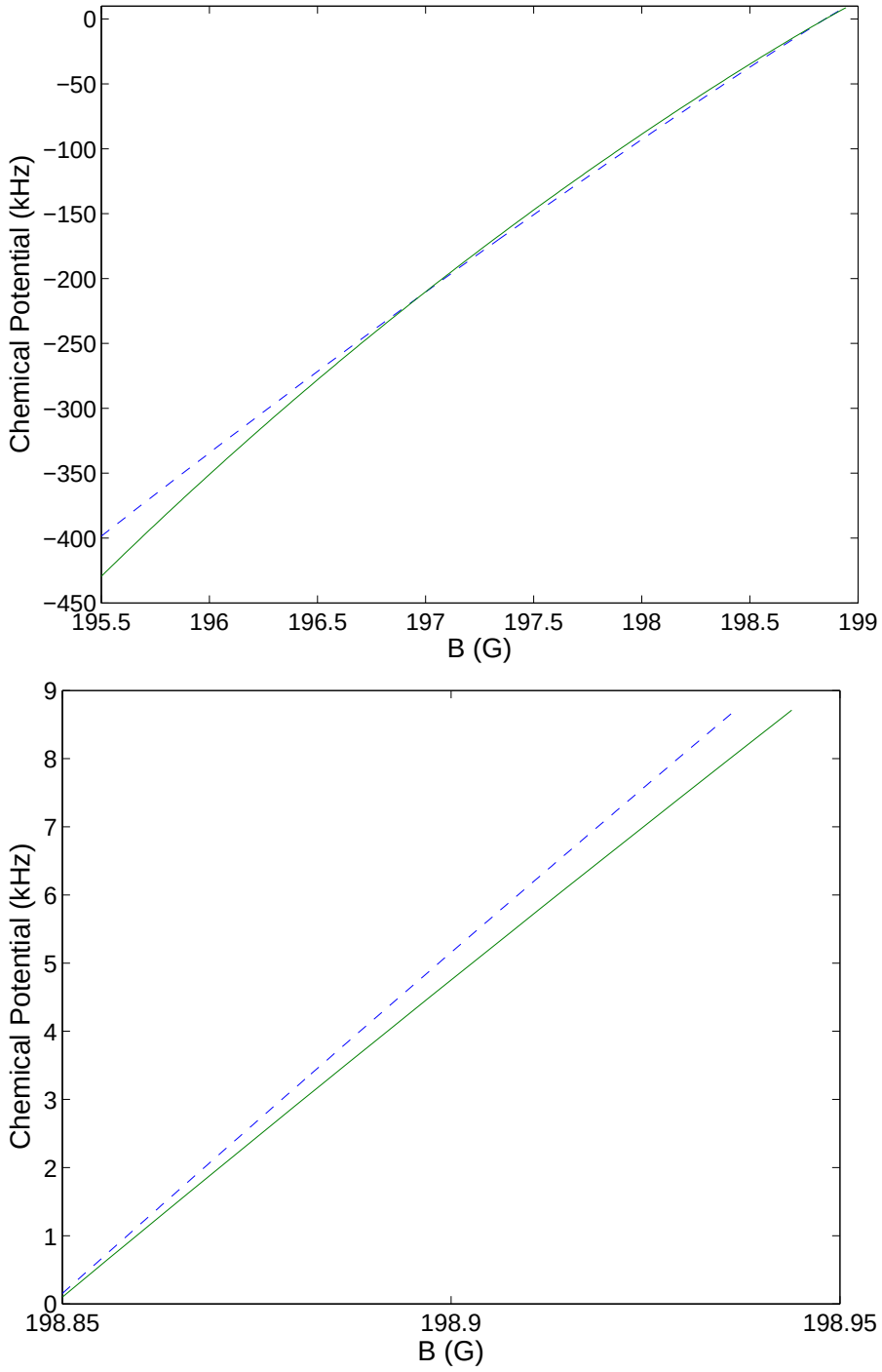

Figure 3.12: Comparison of the chemical potential using the two channel model (dashed blue line) and the single channel model (Solid green line). In both figures the density is 10^{13} cm^{-3} and the temperature is 70 nK. The top panel shows the chemical potential for values of the magnetic field throughout the crossover. The lower panel shows the chemical potential on the BCS side of the resonance up to the points where the parameter Δ_0 falls to zero. The two models give very similar predictions that differ as the magnetic field is tuned far from resonance.

3.4 Conclusions

In this section we have presented the thermodynamic theory that fixes the initial state of the gas from which we will study molecule production using a magnetic field that varies linearly with time. We have implemented the separable potential derived in the previous chapter for *p*-wave interactions and shown that for the parameters studied it may be possible to treat the $m_1 = 0$ and $m_1 = \pm 1$ resonances as separate resonances. In chapter 4 we will continue to treat the resonances separately and focus on the case of ^{40}K. We have studied how the relevant parameters affect the feasibility of producing a BCS state under *p*-wave pairing. In particular we have seen that low temperatures and high densities will allow for a larger range of magnetic fields to be accessed as initial conditions for the dynamic mean field equations. This was expected from previous studies, but we have shown this still applies about the *p*-wave Feshbach resonance by solving the BCS equations numerically. There is also a suggestion that ^{40}K may be a more suitable candidate than ^{6}Li for observing a BCS state due to the fact that we can have a non-zero value of the gap parameter on the BCS side of the resonance for a larger range of magnetic fields. This feature is explained by the magnetic moment of the *p*-wave molecules, which is approximately 12 times larger for ^{6}Li than for ^{40}K. We have also compared the results of our single channel approach against a Bose-Fermi model showing that there is no significant difference between the two models in the region close to the resonance, at least in the case of the *p*-wave resonance in ^{40}K. In the next chapter we derive the time dependent equivalent of the BCS equations. We use the results of this section to fix the initial condition of our gas on the BCS side of the resonance and then apply the dynamic equations while varying the magnetic field linearly with time.

Chapter 4

Many Body dynamics

The dynamic mean-field equations are derived for fermions with p-wave interactions. These are applied to a gas of Fermi atoms prepared in a BCS state close to a Feshbach resonance. Linear sweeps of the magnetic field are applied to convert the system from a weakly paired BCS gas into a BEC of bound molecules. The molecule production efficiency is calculated and studied as a function of the initial conditions of the gas, as well as the rate at which the magnetic field is varied.

Our aim is to produce Feshbach molecules from a single component Fermi gas through a linear sweep of the magnetic field. In this chapter we study the dynamics of this process using a mean-field approach similar to that of ref. [129]. We use the results of the previous chapter to determine the initial state of the gas on the BCS side of the resonance and the separable potential of chapter 2 to model the two-body interaction that appears in the dynamic equations. We calculate the molecule production efficiency on the BEC side of the resonance and study the effects that the initial and final conditions, as well as the rate at which we change the magnetic field, have on the system.

The use of a time-varying magnetic field to tune the interaction strength between a pair of atoms in an ultracold gas makes use of the Zeeman splitting between different hyperfine states as explained in chapter 2. The interaction can be

tuned such that free atoms can be associated into diatomic molecules by varying the magnetic field about a Feshbach resonance [19]. Diatomic Feshbach molecules have been produced from atomic BECs of ^{85}Rb [143, 144, 145], ^{133}Cs [146, 147], ^{23}Na and ^{87}Rb [148]. Two-component Fermi gases have also been used to create Feshbach molecules in gases of ^{40}K [77] and ^{6}Li [91, 92, 149]. More recently experiments have been successful in producing heteronuclear Feshbach molecules of ^{40}K^{87}Rb [150, 151] and ^{85}Rb^{87}Rb [152]. Subsequent experiments on Fermi gases used Feshbach resonances to produce molecular BECs [87, 93], as well as regaining the initial Fermi gas by sweeping the magnetic field back into the BCS region [95]. The formation of *p*-wave Feshbach molecules has been achieved in single component ultra cold gases of ^{40}K [21] and ^{6}Li [20, 3, 22, 23]. More details on the experiments performed in Fermi gases have been given in section 1.3.3.

4.1 Linear Sweeps

In the first experiments on molecule production via a magnetically tunable Feshbach resonance in ^{87}Rb, a rapid pulse was applied close to the resonance position [143]. This involved holding the magnetic field close to the resonance for a period of time and detecting atom loss from the gas resulting in a coherent superposition of atoms and molecules. Despite its success this method suffered from a low yield of molecules and atom loss due to heating of the gas.

In Fermi gases it is possible to produce *s*-wave molecules by holding the magnetic field on the positive scattering length side and observing atom loss due to the enhanced three body collision rate [149, 92]. Using this method it was possible to achieve a conversion efficiency of up to 85% [92].

A further magnetic field variation was implemented by Thompson *et al*.[144] to produce molecules in ^{85}Rb. They set the value of the magnetic field close to the resonance position and applied a sinusoidal oscillation to associate the molecules. The production efficiency was shown to be strongly dependent on the frequency, amplitude and duration of the field variation.

The method of sweeping a magnetic field across a Feshbach resonance has been successful in producing *s*-wave molecules from gases of fermions [77, 91]

and bosons [146, 153, 148, 147, 145]. The production of molecules from bosonic gases is suppressed due to an enhanced inelastic loss rate close to the resonance [148, 154], as well as problems caused by density dependent heating [145]. A much higher production efficiency using magnetic field sweeps has been observed in *s*-wave Fermi gases. Using this technique it was possible to convert a gas of fermionic atoms into a BEC of diatomic molecules [87, 93] and sweep back in to the BCS side of the resonance to regain the initial state [95].

We study the situation in which the magnetic field is varied linearly with time

$$B(t) = -\dot{B}t + B_i, \tag{4.1}$$

where B_i is the value of the initial magnetic field above the resonance position B_0. Several experiments have used linear sweeps of the magnetic field to associate *p*-wave molecules of ^{6}Li [20, 22, 23]. In these experiments relatively low yields were achieved, at most around 20 % by Zhang *et al*. [20]. This can be compared to the 85 % achieved in the *s*-wave experiments of a similar nature [92]. For our mean field study it is necessary to have a state that includes pairing in the initial condition. It has not been shown that this state has been achieved experimentally and it is possible that our initial condition differs from that of the experiment. Other experiments have used sinusoidally modulated magnetic fields to associate *p*-wave molecules [3, 21].

4.2 Two-body dynamics

Before we study the dynamics of the gas at the many-body mean-field level we will look at the two-body dynamics of the system. This may highlight some differences between the two-body and the many-body results and will help establish to what extent many-body effects are important in the systems we are looking at. The results of this section are based on previous work [155] and only apply to the case of two particles under tight harmonic confinement. This situation is experimentally relevant, as atom pairs can be isolated on the site of an optical lattice. We later solve the mean-field equations in free space, so we would expect some differences between the results given by the two approaches due to this change

of circumstance. In appendix G we then solve the problem for two particles in spherical box. In the limit of a large box we would then expect the results of this calculation to be analogous to those of a homogeneous gas and we could therefore compare this to our mean-field dynamics, which we solve for a homogeneous gas.

We consider the solution of the problem of a pair of particles interacting under a time-dependent interatomic potential. We use the separable potential of chapter 2 to include the effects of a magnetic field that can alter the strength of the interaction between the particles through the Zeeman effect. Deep in the potential well of an optical lattice the confinement is assumed to be harmonic and therefore the centre of mass and relative motion of the atoms can be separated, just as for particles in free space. It is then necessary to solve the time-dependent Schrödinger equation to determine the pair dynamics,

$$i\hbar\frac{\partial}{\partial t}|\Psi(t)\rangle = H_{2B}(t)|\Psi(t)\rangle. \tag{4.2}$$

Here, $|\Psi(t)\rangle$ is the wave function of the pair and $H_{2B}(t)$ is the Hamiltonian governing their evolution. The two-body time evolution operator, $U_{2B}(t,t')$, obeys a similar Schrödinger equation

$$i\hbar\frac{\partial}{\partial t}U_{2B}(t,t_i) = H_{2B}(t)U_{2B}(t,t_i), \tag{4.3}$$

where t_i is the initial time. This can then be used to calculate the probability for pair association through

$$P_{fi} = |\langle\phi_b(B_f)|U_{2B}(t_f,t_i)|\Psi(t_i)\rangle|^2, \tag{4.4}$$

where t_i is the final time and $\phi_b(B_f)$ is the bound state wave function at the final magnetic field position. The exact structure of the wave function will depend on how the system is modelled. In the approximation where only two Zeeman configurations are considered, the wave function will have two components corresponding to the entrance channel and the closed channel. For a linear sweep of the magnetic field, and when the closed channel supports a single resonance state, it is possible to calculate the exact time evolution of the pair. This is the two-channel model of chapter 2 where we discussed the time-independent problem to

determine the near threshold behaviour. We also pointed out that the Feshbach molecule in this two-channel model is a linear superposition of the open channel and closed channel components.

A generic approach that can be applied to the two-body dynamics was developed independently by Landau and Zener in 1932 [156, 157]. This is similar to the approach above, but the entrance channel now contains just a single state, effectively reducing the problem to a two-level system. In the limit of zero ramp speed a pair of atoms prepared in the entrance channel will form a bound molecule in the closed channel. This approach assumes that the sweep has the limits $t_i \to -\infty$ and $t_f \to \infty$. Finite ramp speeds will lead to states where the atom pair is in a superposition of a bound molecule and a free pair. The probability for molecule association can be calculated analytically if the same time limits are assumed [158, 114].

This approach only accounts for the statistics of the participating particles in the form of interaction introduced as in chapter 2. Experiments performed about the 1007 G resonance in bosonic ^{87}Rb [159] have shown good agreement with the Landau-Zener theory. For a system where the equilibrium state is described by the BCS theory of the previous chapter, it would not be intuitive to include only the two-body dynamics of an atom pair to calculate molecule production; we have already seen that many-body effects are important in these systems. Given the success of the BCS theory, we will later look at the time evolution of the distribution functions at the mean-field level and use these to calculate the molecule production.

The Landau-Zener formula for molecule association is given by [19]

$$P = 1 - e^{-2\pi\delta_{\mathrm{LZ}}}, \tag{4.5}$$

where P is the probability of the atom pair forming a closed channel molecule at the end of the magnetic field sweep. In the p-wave the Landau-Zener coefficient, δ_{LZ}, is given by [155]

$$\delta_{\mathrm{LZ}}^{p-wave} = \frac{5\sqrt{10}\hbar}{4\pi\mu a_{\mathrm{ho}}^5}\left|\frac{a_{1m}^{\mathrm{bg}}\Delta B}{\dot{B}}\right|. \tag{4.6}$$

Here, a_{ho} is the harmonic oscillator length, a_{1m}^{bg} is the background scattering vol-

ume, ΔB is the width of the resonance, $\dot{B}$ is the speed of the linear magnetic field sweep and μ is the reduced mass of the atom pair. For a Fermi gas in a harmonic trap a typical length scale is the Thomas-Fermi radius (see Giorgini *et al*. [56] Section II. B.)

$$R_{\mathrm{TF}} = a_{\mathrm{ho}} \, (48N)^{1/6} \, , \tag{4.7}$$

where N is the number of atoms in the trap and it has been assumed that the trap is isotropic. It should be noted that this discussion is a very rough approximation that enables us to relate the density, in a many-body sense, to the parameters that can describe a tight harmonic trap, used to confine two particles. The density distribution of the cloud is given by

$$n(r) = \frac{8}{\pi^2} \frac{N}{R_{\mathrm{TF}}^3} \left(1 - \left(\frac{r}{R_{\mathrm{TF}}} \right)^2 \right)^{3/2} \, , \tag{4.8}$$

where r is the radial coordinate from the centre of the trap. In the centre of the trap the density will then be

$$n(0) = \frac{8}{\pi^2} \frac{N}{R_{\mathrm{TF}}^3}. \tag{4.9}$$

We can then find the harmonic oscillator length as a function of the density in the centre of the trap

$$a_{\mathrm{ho}}^3 = \sqrt{\frac{4N}{3}} \frac{1}{\pi^2 n(0)}. \tag{4.10}$$

To analyse the behaviour of the Landau-Zener parameter we scale the equations with a background scattering volume, $a_{\ell m}^{\mathrm{bg}}$. More precisely we can define a length scale as the cube-root of the modulus of the scattering volume,

$$a_{\mathrm{sc}} = |a_{\ell m}^{\mathrm{bg}}|^{1/3}. \tag{4.11}$$

The Landau-Zener parameter now comes out as

$$\delta_{\mathrm{LZ}}^{p-wave} = \frac{5\sqrt{10}}{4\pi \tilde{a}_{\mathrm{ho}}^5} \left| \frac{\Delta B}{\dot{\tilde{B}}} \right| , \tag{4.12}$$

with $a_{\rm ho} = a_{\rm sc}\tilde{a}_{\rm ho}$. In this equation

$$\dot{B} = \frac{\hbar}{\mu a_{\rm sc}^2}\tilde{\dot{B}}. \tag{4.13}$$

The harmonic oscillator angular frequency is defined by

$$\omega_{\rm ho} = \frac{\hbar}{2\mu a_{\rm ho}^2}. \tag{4.14}$$

This can be used along with Eq. (4.10) to estimate the density in the centre of the trap in terms of the trap parameters

$$n(0) = \left(\frac{\hbar}{2\omega_{\rm ho}\mu}\right)^{3/2}\sqrt{\frac{4N}{3}}\frac{1}{\pi^2}. \tag{4.15}$$

We have plotted the Landau-Zener probability as a function of the sweep rate in

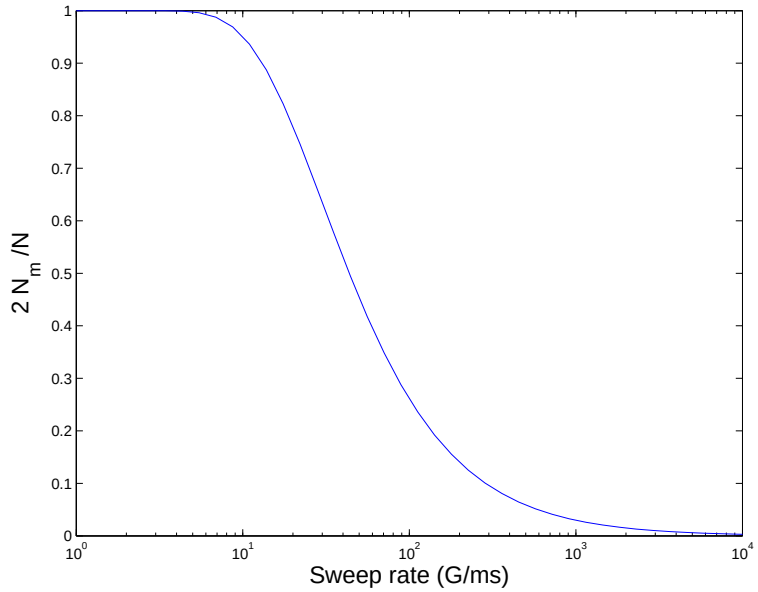

Figure 4.1: The variation of the Landau-Zener probability for two atoms in a tight harmonic trap as function of the sweep rate. The resonance parameters refer to the m_1=0, 198.85 G p-wave resonance in ^{40}K. N_m is the number of molecules and N is the number of atoms. This gives a clear indication that we expect the molecule production efficiency to increase as we decrease the ramp speed and below about 10 G/ms we have complete conversion of atoms to molecules.

Fig. 4.1. The molecule production increases as the ramp speed is lowered and below about 10 G/ms there is a 100 % conversion of atoms to molecules. We have used a harmonic oscillator frequency of $\omega_{\rm ho} = 2\pi\times 70$ kHz similar to that used in experiments on Fermi gases [2].

4.2.1 Behaviour analysis

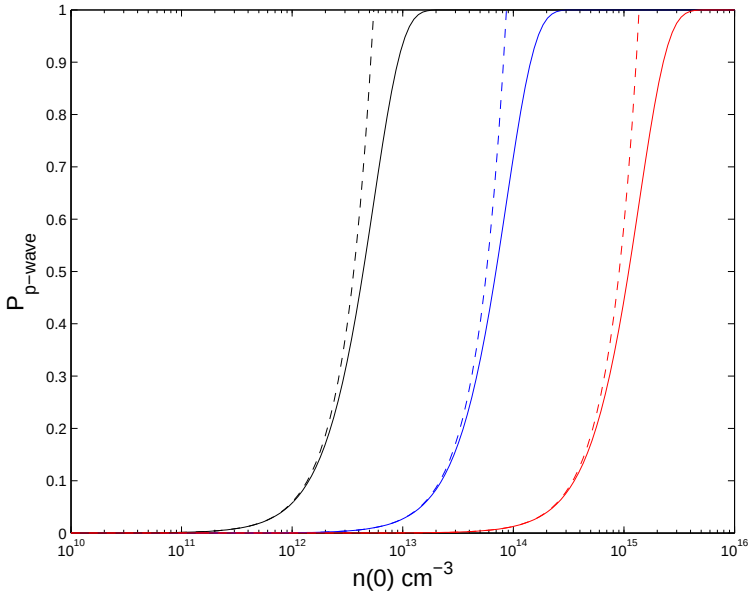

Figure 4.2: A plot of the association probability for 2 (N=2) particles using the Landau-Zener method as a function of $n(0)$. The black, blue and red lines represent ramp speeds of 0.1, 10 and 10^3 G/ms, respectively. The solid lines are the association probability given by Eq. (4.5) while the dashed lines are the fast sweep (low density) approximation given by Eq. (4.21)

We can use Eq. (4.10) to write the Landau-Zener parameter as a function of the density

$$\delta_{\rm LZ}^{p-wave} = \frac{5\sqrt{10}}{4\pi}\left(\frac{3}{6N}\right)^{5/6}\pi^{10/3}\tilde{n}(0)^{5/3}\left|\frac{\Delta B}{\tilde{B}}\right| \sim \tilde{n}(0)^{5/3}, \tag{4.16}$$

where $\tilde{n}(0)^{5/3} = a_{\rm sc}^5 n(0)^{5/3}$ and the number of atoms remains fixed. A derivation for the Landau-Zener parameter in a spherical well is given in appendix G, where

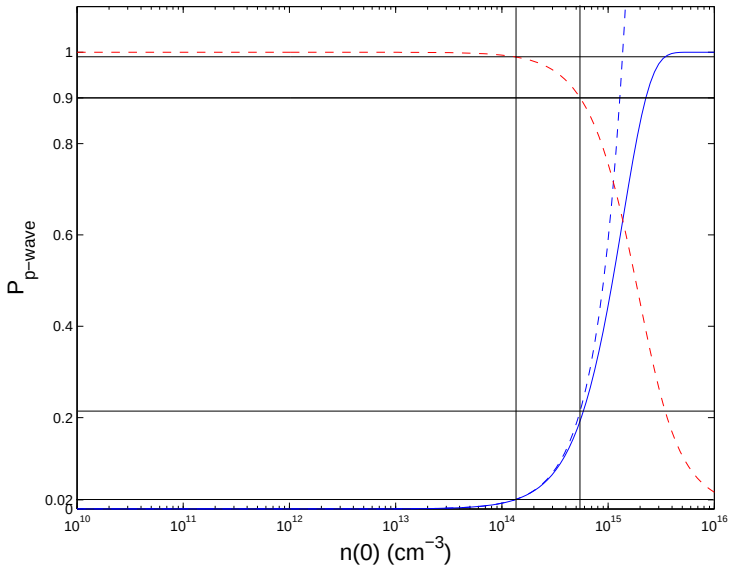

Figure 4.3: A graphical comparison of the full Landau-Zener formula against the approximation of Eq. (4.21) for a sweep speed of 10^3 G/ms as a function of the atomic density. The solid, blue line is the full Landau-Zener formula, while the blue, dashed line is the approximation of Eq. (4.21). The red, dashed line is the ratio of the full formula to the high speed approximation. It can be seen that at a density of 1×10^{14} cm^{-3} there is less than a 0.01% factor between the 2 values. This has increased to over 10% by 5×10^{15} cm^{-3}. These two points correspond to exponents of approximately 0.02 and 0.21, respectively.

we find the same $n^{5/3}$ scaling. In terms of a sphere with volume $V = \frac{4}{3}\pi R^3$, we have

$$\delta_{\mathrm{LZ}}^{\mathrm{SW}} = 570.236 \frac{\hbar\pi}{V\mu R^2} \left| \frac{a_{1m_\ell}^{\mathrm{bg}} \Delta B_1}{\dot{B}} \right|, \tag{4.17}$$

where the superscript SW denotes a spherical well. Assuming a uniform density, such that $n = \frac{N}{V}$, gives

$$\delta_{\mathrm{LZ}}^{\mathrm{SW}} = 570.236 \frac{\hbar\pi}{\mu} \left(\frac{4}{3}\right)^{2/3} \left| \frac{a_{1m_\ell}^{\mathrm{bg}} \Delta B_1}{\dot{B}} \right| \left(\frac{n}{N}\right)^{5/3}. \tag{4.18}$$

This differs from Eq. (4.16) by only a numerical factor if we take the density at the centre of the trap to be the uniform density in Eq. (4.18). It should be

noted that in both cases the parameter remains dependent on the system size and a thermodynamic limit can not be taken, even in the limit of fast sweeps, in contrast to the *s*-wave [114]. We can compare this with the Landau-Zener expression for the *s*-wave [19],

$$\delta_{\mathrm{LZ}}^{s-wave} = \frac{\sqrt{6\hbar}}{2\mu\pi a_{\mathrm{ho}}^3}\left|\frac{a_{\mathrm{bg}}\Delta B}{\dot{B}}\right|. \tag{4.19}$$

This equation can be scaled using the *s*-wave scattering length, a_{bg} to give

$$\delta_{\mathrm{LZ}}^{s-wave} = \frac{\sqrt{6}\pi}{2}\left(\frac{3}{4N}\right)^{1/2}\tilde{n}(0)\left|\frac{\Delta B}{\tilde{\dot{B}}}\right| \sim \tilde{n}(0). \tag{4.20}$$

From these expressions for the Landau-Zener parameters it can be seen that in the limit of fast sweep (and low enough density) we can approximate Eq. (4.5) to be

$$P \approx 2\pi\delta_{\mathrm{LZ}}. \tag{4.21}$$

This predicts that for fast ramp speeds the *p*-wave association probability will behave like

$$P_{p-\mathrm{wave}} \sim \tilde{n}(0)^{5/3}. \tag{4.22}$$

A comparison of the association probability of the Landau-Zener formula Eq. (4.5) and its approximation Eq. (4.21) is plotted as a function of density in Fig. 4.2 for the $m_1 = 0$ *p*-wave resonance around 198.85 G in ^{40}K for various ramp speeds.

The extent to which the approximation of Eq. (4.21) can be used can also be analysed. In Fig. 4.3 we have plotted the ratio of the full formula to the high speed approximation for a sweep speed of 10^3 G/ms (red, dashed line). We can see that the production efficiencies stay within a factor of 0.01% of each other up to around 10^{14} cm^{-3}. This corresponds to an exponent in Eq. (4.5) (or production efficiency in Eq. (4.21)) of around 0.02. This line is essentially a plot of the function

$$f(g(n(0))) = \frac{1 - e^{-g(n(0))}}{g(n(0))}, \tag{4.23}$$

so we would expect a similar region of validity in terms of the value of the exponent no matter what partial wave we are looking at (assuming that the Landau-Zener formula is valid). We can therefore compare the value of the exponent in

the *p*-wave and the *s*-wave to give

$$\frac{\delta_{\mathrm{LZ}}^{p-wave}}{\delta_{\mathrm{LZ}}^{s-wave}} = \frac{5\sqrt{5}}{4\sqrt{2}}\pi^{4/3} n(0)^{2/3} \frac{|a_{1m}^{\mathrm{bg}} \Delta B^{p}|}{|a_{0}^{\mathrm{bg}} \Delta B^{s}|}, \tag{4.24}$$

where the superscripts denote the *s*-wave and the *p*-wave. In the limit of fast magnetic field sweeps this will also give an approximation of the relative molecule production between the *p*-wave and the *s*-wave. It should be noted that this expression is independent of the ramp speed. Equation (4.24) has been plotted in Fig. 4.4 as a function of $n(0)$. The *s*-wave parameters used correspond to the 202.1 G resonance in ^{40}K. It can be seen that the density has to be very high for the molecule production to be comparable in the *s*-wave and *p*-wave, otherwise the molecule production in the *p*-wave is significantly lower. For Eq. (4.24) to estimate the relative molecule production the ramp speed would then have to be very fast (greater than 10^8 G/ms).

Fig. 4.5 compares the probability for *s*-wave and *p*-wave molecule production. At lower ramp speeds the value given by Eq. (4.24) gives a much smaller value than the ratio of actual probabilities, so that the yield of *p*-wave molecules is under-represented by this approximation. However, Fig. 4.6 shows that there is a range of densities at which the *s*-wave production can be 100 % while the *p*-wave production can be less than 1 % and even at a low ramp speed of 10 G/ms the density must still be in excess of 10^{14} cm^{-3} to get a ratio of greater than 0.9.

We see that from a two-body point of view we expect different behaviour of the *s*-wave and *p*-wave production efficiencies as a function of atomic density. This analysis has been restricted to the case of a tightly confining harmonic trap, but the main difference is the threshold behaviour reflected in the evaluation of matrix elements when calculating the Landau-Zener parameter [155]. In appendix G we find similar behaviour of the Landau-Zener parameter in a spherical box, to its behaviour in a tight harmonic trap, corroborating the above statement. Numerically, the resonance parameters, $a_{\ell m_\ell}^{\mathrm{bg}}$ and ΔB, will play a role in determining the overall ratio of production efficiencies. In the system we have applied this to, we expect that a higher atomic density will be required in the *p*-wave case than in the *s*-wave. The limitations of the Landau-Zener approach lie in the neglecting of many-body

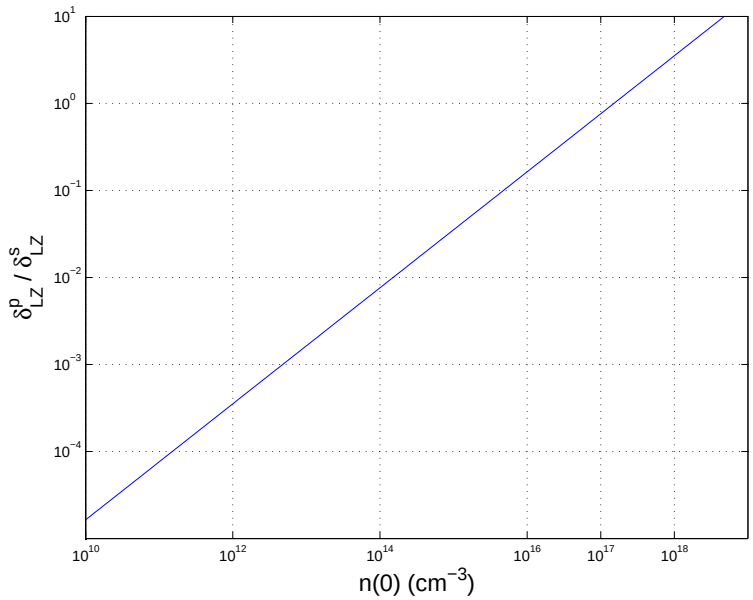

Figure 4.4: The ratio $\delta_{\mathrm{LZ}}^{p-wave}/\delta_{\mathrm{LZ}}^{s-wave}$ as a function of density. The *s*-wave resonance values are given by $a_0^{\mathrm{bg}} = 174$ a.u. [118] and $\Delta B = 7.8$ G [87] for the 202.1 G *s*-wave resonance in ^{40}K. This will also be an estimate for the relative molecule production between the *s*-wave and the *p*-wave in the limit of a fast sweep. The density has to be very high for the molecule production to be comparable.

effects and in the requirement of an infinitely long sweep of the magnetic field. We have seen in chapter 3 that many-body effects can have implications on the thermodynamics and we will now look at the more comprehensive approach of the mean-field dynamics. This will also enable us to study a range of different initial and final conditions.

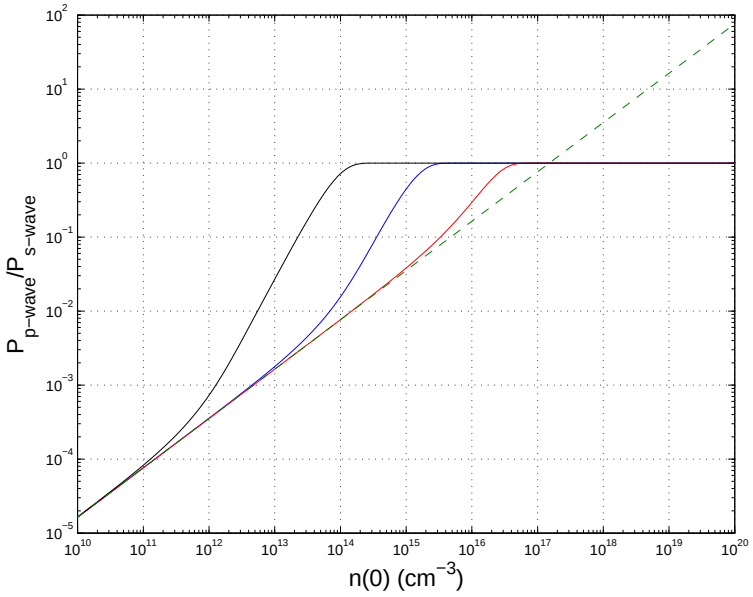

Figure 4.5: The ratio P_{p-wave}/P_{s-wave} as a function of density. The *s*-wave resonance values are given by $a_0^{bg} = 174$ a.u. [118] and $\Delta B = 7.8$ G [87] for the 202.1 G *s*-wave resonance in ^{40}K. This will also be an estimate for the relative molecule production between the *s*-wave and the *p*-wave in the limit of a fast sweep. The density has to be very high for the molecule production to be comparable. The black, blue and red lines represent ramp speeds of 10, 10^3 and 10^5 G/ms, respectively. The dashed, green line is the high ramp speed approximation of Eq. (4.24).

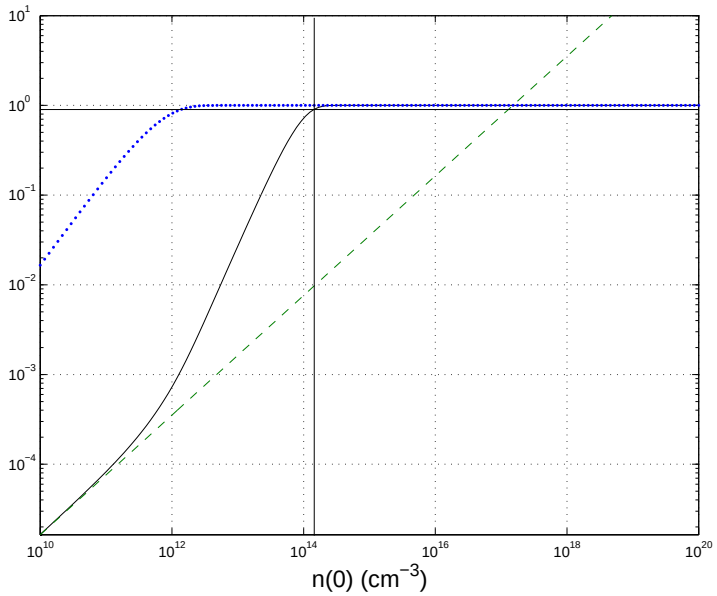

Figure 4.6: The ratio P_{p-wave}/P_{s-wave} as a function of density. The *s*-wave resonance values are given by $a_0^{bg} = 174$ a.u. [118] and $\Delta B = 7.8$ G [87] for the 202.1 G *s*-wave resonance in ^{40}K. This will also be an estimate for the relative molecule production between the *s*-wave and the *p*-wave in the limit of a fast sweep. The ramp speed is 10 G/ms. The blue-dotted line is the *s*-wave production efficiency as calculated from the Landau-Zener formula. The dashed, green line is the high ramp speed approximation of Eq. (4.24). This shows that the production efficiency of the *s*-wave molecules can be 100 % at densities where the efficiency is less than 1 % for the *p*-wave molecules. At this low ramp speed a density in excess of 10^{14} cm^{-3} is required to produce a 90 % production efficiency in the *p*-wave

4.3 Many-body Dynamics

Many-body approaches have previously been employed to calculate *s*-wave molecule production in ultracold gases [24, 114, 160, 161]. In the case of Bose gases the Bose-Einstein condensate can be taken into account when calculating the many-body dynamics of the system. Beyond this we would have to consider the density of the non-condensed particles and pairs correlated in the gas. The situation can be similar in the case of Fermi gases where no true condensate exists, but particles can still be correlated to form Cooper pairs in the BCS state.

The phenomenon of the BCS-BEC crossover opens up the possibility for physicists to probe the fundamental question of what constitutes a fermion and what constitutes a boson. We have already seen how many-body effects are important in ultra cold Fermi gases in the previous chapter. Given that we can already see many-body effects at the mean-field level in the thermodynamics of the system we will study the mean-field dynamics in the *p*-wave using methods previously applied to *s*-wave paired fermions [129]. In this study the time-evolution of the order parameter describing the BCS state was studied following an abrupt switch of the magnetic field values from the initial value. The time dependence of the molecule density was also studied after the magnetic field variation. We will first use a finite linear sweep of the magnetic field to study molecule production. Later, we will repeat the study of Szymańska *et al*. [129] for the *p*-wave resonance in ^{40}K.

4.3.1 Mean-field dynamics

In Fermi gases the mean-field dynamics evolves a many-body state consisting of pre-paired atoms. To describe the onset of pairing in the gas we would have to use a higher-order approximation, such as a quantum Boltzmann equation that has already been applied to bosons [24], which is beyond the scope of this thesis.

The stationary solution of the previous chapter provides the initial state for the study of molecule formation in the gas, determined by our chosen initial conditions, such as temperature, density and initial magnetic field. We then dynamically

evolve the pair function, defined by

$$\Phi_{i_1 i_2}(t) = \langle a_{i_2} a_{i_1} \rangle_t, \tag{4.25}$$

and the one body density matrix defined by

$$\Gamma_{ij}(t) = \langle a_j^\dagger a_i \rangle_t. \tag{4.26}$$

Here the indices represent single-particle states and the brackets $\langle ... \rangle_t$ are ensemble averages at time t. The pair function is related to the gap parameter of the previous chapter through the relation

$$\Delta_{ij} = \sum_{kl} \langle ij|V|kl\rangle \langle a_k^\dagger a_l^\dagger \rangle = \sum_{kl} \langle ij|V|kl\rangle \Phi_{lk}(t). \tag{4.27}$$

The equations of motion are derived in full in appendix F, but we here give some of the main results. The full Heisenberg equation of motion for the density matrix is given by

$$\begin{aligned} i\hbar \frac{\partial}{\partial t}\Gamma_{ij}(t) = & \sum_k \langle i|H_{1B}|k\rangle \Gamma_{kj}(t) - \sum_l \langle l|H_{1B}|j\rangle \Gamma_{il}(t) \\ & + \sum_{klh} \langle il|V|kh\rangle \left[\Gamma^{(2,2)}_{khjl}(t) + \Phi^\star_{jl}(t)\Phi_{kh}(t) + \Gamma_{kj}(t)\Gamma_{hl}(t) - \Gamma_{hj}(t)\Gamma_{kl}(t)\right] \\ & - \sum_{klh} \langle lh|V|jk\rangle \left[\Gamma^{(2,2)}_{iklh}(t) + \Phi^\star_{lh}(t)\Phi_{ik}(t) + \Gamma_{il}(t)\Gamma_{kh}(t) - \Gamma_{kl}(t)\Gamma_{ih}(t)\right], \end{aligned} \tag{4.28}$$

where H_{1B} is the single-particle Hamiltonian containing the single-particle kinetic energy operator and any external potential. The corresponding equation for the pair function is given by

$$\begin{aligned} i\hbar \frac{\partial}{\partial t}\Phi_{i_1 i_2}(t) = & \sum_{k_1 k_2} \langle i_1 i_2|H_{2B}|k_1 k_2\rangle \Phi_{k_1 k_2}(t) + \sum_{k_1 k_2 lh} \langle i_1 i_2 l| \sum_{j=1}^{2} V_{j3}|k_1 k_2 h\rangle \\ & \times \left[\Gamma^{(3,1)}_{k_1 k_2 hl}(t) + \Gamma_{hl}(t)\Phi_{k_1 k_2}(t) + \Gamma_{k_1 l}(t)\Phi_{k_2 h}(t) - \Gamma_{k_2 l}(t)\Phi_{k_1 h}(t)\right]. \end{aligned} \tag{4.29}$$

The higher-order terms in these equations are given by

$$\Gamma^{(m,n)}_{i_1\ldots i_m,j_1\ldots j_n}(t) = \langle a^\dagger_{j_1}\ldots a^\dagger_{j_n} a_{i_m}\ldots a_{i_1}\rangle^c_t. \tag{4.30}$$

These represent correlations in the gas far from equilibrium. The superscript, c, denotes these quantities as cumulants [162]. It can be seen that a full solution of these equations would produce an infinite hierarchy of equations including higher and higher-orders of these correlations. This is intractable, so at some point a truncation of the series must take place if we wish to solve this system of equations. Motivated by the success of the stationary theory in the mean-field approximation, we can neglect the higher-order terms in which n or m are greater than 1. The cumulant approach allows this truncation to take place at arbitrary order provided the system remains relatively close to equilibrium. It should be noted that for fermions the cumulant of two creation/annihilation operators is equivalent to the expectation value of the operators. Furthermore, given the diluteness of the gas it should also be possible to neglect any terms that are products of single-particle density matrices. In fact, this amounts to neglecting the Hartree-Fock contributions to the dynamical equations. A similar procedure is used to derive the BCS equations and the Gross-Pitaevskii equation for Bosons.

By neglecting the higher-order terms one arrives at the mean-field equations for fermions

$$\begin{aligned} i\hbar\frac{\partial}{\partial t}\Gamma_{ij}(t) = &\sum_k \langle i|H_{1B}|k\rangle\Gamma_{kj}(t) - \sum_l \langle l|H_{1B}|j\rangle\Gamma_{il}(t) \\ &+ \sum_l \left[\Phi^\star_{jl}\langle il|V|\Phi(t)\rangle - \langle\Phi(t)|V|jl\rangle\Phi_{il}(t)\right], \end{aligned} \tag{4.31}$$

$$i\hbar\frac{\partial}{\partial t}\Phi_{i_1i_2}(t) = \langle i_1 i_2|H_{2B}|\Phi(t)\rangle + \sum_l \left[\Gamma_{i_1l}(t)\langle i_2 l|V|\Phi(t)\rangle - \Gamma_{i_2l}(t)\langle i_1 l|V|\Phi(t)\rangle\right]. \tag{4.32}$$

Here, H_{2B} is the two-body Hamiltonian containing the kinetic energy and interaction of two particles. For a homogeneous system in the momentum representation these equations become

$$i\hbar\frac{\partial}{\partial t}\Gamma(\mathbf{p},t) = 2(2\pi\hbar)^{3/2} i\mathrm{Im}\left(\Phi^\star(\mathbf{p},\mathrm{t})\langle\mathbf{p}|\mathrm{V}|\Phi(\mathrm{t})\rangle\right), \tag{4.33}$$

$$i\hbar\frac{\partial}{\partial t}\Phi(\mathbf{p},t) = \langle\mathbf{p}|H_{2b}|\Phi(t)\rangle - \langle\mathbf{p}|V|\Phi(t)\rangle\Gamma(-\mathbf{p},t)(2\pi\hbar)^{3/2} - \langle\mathbf{p}|V|\Phi(t)\rangle\Gamma(\mathbf{p},t)(2\pi\hbar)^{3/2}. \tag{4.34}$$

In the previous chapters we have expanded our single-particle state into the angular momentum basis. Similarly we can express the many particle distribution functions in terms of their partial wave components given by

$$\Phi_{\ell m}(p,t) = i^{\ell}\int d\Omega Y^{\star}_{\ell m}(\Omega)\Phi(\mathbf{p},t), \tag{4.35}$$

$$\Gamma_{\ell m}(p,t) = i^{\ell}\int d\Omega Y^{\star}_{\ell m}(\Omega)\Gamma(\mathbf{p},t), \tag{4.36}$$

where Ω is the solid angle in $\mathbf{p}$. This allows mean-field equations for the partial wave components of the pair function and one body density matrix to be written as

$$i\hbar\frac{\partial}{\partial t}\Gamma_{\ell m}(p,t) = 2(2\pi\hbar)^{3/2}i^{\ell+1}\int d\Omega Y^{\star}_{\ell m}(\Omega) \times \mathrm{Im}\left(\sum_{\ell' \mathrm{m}'\ell''\mathrm{m}''} \mathrm{i}^{\ell'-\ell''}\mathrm{Y}^{\star}_{\ell'\mathrm{m}'}(\Omega)\mathrm{Y}_{\ell''\mathrm{m}''}(\Omega)\Phi^{\star}_{\ell'\mathrm{m}'}(\mathrm{p},\mathrm{t})\langle \mathrm{p}\ell''\mathrm{m}''|\mathrm{V}|\Phi(\mathrm{t})\rangle\right), \tag{4.37}$$

$$\begin{aligned} i\hbar\frac{\partial}{\partial t}\Phi_{\ell m}(p,t) &= \frac{p^2}{m}\Phi_{\ell m}(p,t) + \langle p\ell m|V|\Phi(t)\rangle \\ &- (2\pi\hbar)^{3/2}\sum_{\ell' m'\ell'' m''} i^{\ell-\ell'+\ell''}\int d\Omega Y^{\star}_{\ell m}(\Omega)Y_{\ell' m'}(\Omega)Y_{\ell'' m''}(\Omega)\langle p\ell' m'|V|\Phi(t)\rangle\Gamma_{\ell'' m''}(p,t) \\ &- (2\pi\hbar)^{3/2}\sum_{\ell' m'\ell'' m''} i^{\ell-\ell'-\ell''}\int d\Omega Y^{\star}_{\ell m}(\Omega)Y_{\ell' m'}(\Omega)Y_{\ell'' m''}(\Omega)\langle p\ell' m'|V|\Phi(t)\rangle\Gamma_{\ell'' m''}(p,t). \end{aligned} \tag{4.38}$$

It should be noted that this leads to an infinite set of equations corresponding to the different values of ℓ and m_ℓ. However, the angular integrals over the spherical harmonics can be done analytically which may simplify the solution of these equations, computationally, if the series converges sufficiently quickly.

4.3.2 Lowest order approximation

As a first approximation we can retain the lowest order, in ℓ, partial wave which includes the p-wave interaction and from which we can calculate molecule production. We note that in Eq. (4.38) we keep only the ℓ=1 components, but in Eq. (4.37) we go down to the ℓ=0 component. We now have

$$i\hbar\frac{\partial}{\partial t}\Gamma_{00}(p,t) = \frac{2(2\pi\hbar)^{3/2}i}{\sqrt{4\pi}} Im\left(\sum_{m'}\chi_{1m'}(p)\xi_{m'}\int q^2 dq \chi_{1m'}(q)\Phi_{1m'}(q,t)\Phi^{\star}_{1m'}(p,t)\right), \tag{4.39}$$

$$\begin{aligned} i\hbar\frac{\partial}{\partial t}\Phi_{1m}(p,t) = {} & \frac{p^2}{m}\Phi_{1m}(p,t) + \chi_{1m}(p)\xi_m\int q^2 dq \chi_{1m}(q)\Phi_{1m}(q,t) \\ & - \frac{(2\pi\hbar)^{3/2}}{\sqrt{\pi}}\chi_{1m}(p)\xi_{1m}\Gamma_{00}(p,t)\int q^2 dq \chi_{1m}(q)\Phi_{1m}(q,t), \end{aligned} \tag{4.40}$$

where the matrix elements have been rewritten using the separable potential of chapter 2. There are actually three equations here with two for the pair function components, corresponding to $m = \pm 1$ and $m = 0$ and one for the $\ell = 0$ density matrix. In the previous chapter we showed that, in certain cases, it is possible to treat the $m = 0$ and $m = 1$ components separately. If we choose the initial state to be a gas in which only one angular projection state is present then we will prohibit the possibility of populating the other projection. This is one of the limitations within the mean-field regime. We also showed in the previous chapter that when we solved the BCS equations with coupling between the two projections, the off diagonal terms were several orders of magnitude less than the dominant component. This suggests that even if we included the possibility of populating states in which the final m_ℓ differed from the initial value we would be justified in neglecting such terms.

4.4 Calculating molecule production

Once we have solved the dynamic equations we will be left with a final state from which to calculate molecule production. The quantum mechanical observable for

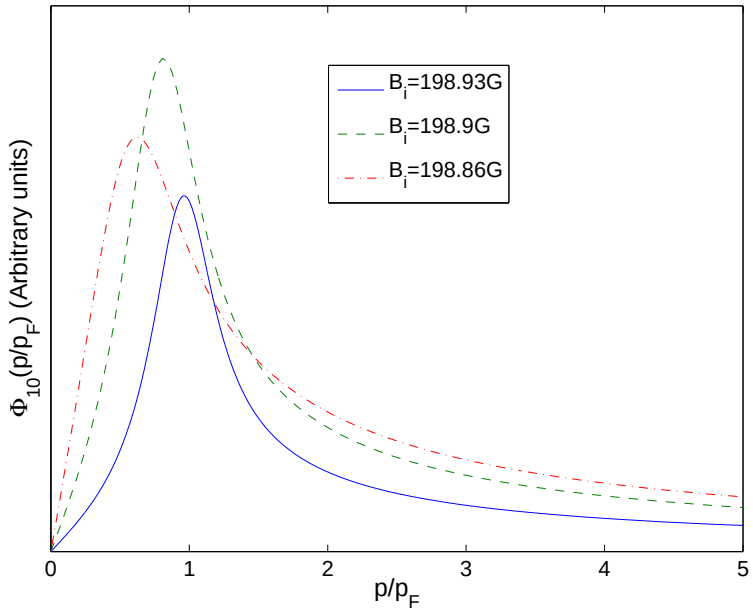

Figure 4.7: Initial pair functions, $\Phi_{10}(p,0)$, for a density of 10^{13} cm^{-3}. Here p_F is the Fermi momentum of the non-interacting gas at zero temperature. As shown in Chapter 2 the chemical potential goes to the Fermi energy of the non-interacting gas as the potential gets weaker. The pair function reflects this fact through the position of the peak which is close to $p/p_F = 1$ at high magnetic field and decreases as the value of the magnetic field moves towards the resonance and hence the chemical potential is lowered.

a bound state of two atoms with a relative position **r** can be written as

$$O = \int d\mathbf{R}|\phi_b, \mathbf{R}\rangle\langle\phi_b, \mathbf{R}|, \tag{4.41}$$

where **R** is the centre of mass coordinate of the atom pair. By considering a box of volume $\mathcal{V}$, the single-particle states can be treated as plane waves of the form $\langle\mathbf{x}|\mathbf{p}\rangle = \frac{1}{\mathcal{V}}e^{i\frac{\mathbf{p}\cdot\mathbf{x}}{\hbar}}$, so that the matrix element of the bound state operator is

$$\langle\mathbf{p}_1,\mathbf{p}_2|O|\mathbf{p}_3,\mathbf{p}_4\rangle = \frac{1}{\mathcal{V}}\int d\mathbf{r}_1\int d\mathbf{r}_2\delta\left(\mathbf{p}_1+\mathbf{p}_2-\mathbf{p}_3-\mathbf{p}_4\right) \tag{4.42}$$
$$\times\,\phi_b(\mathbf{r}_1)\phi_b^\star(\mathbf{r}_2)e^{-i\mathbf{r}_1\cdot(\mathbf{p}_1-\mathbf{p}_2)/2\hbar}e^{i\mathbf{r}_2\cdot(\mathbf{p}_3-\mathbf{p}_3)/2\hbar}.$$

Defining the Fourier transform of the bound state, $\phi_b(\mathbf{p}) = \frac{1}{\sqrt{\mathcal{V}}}\int d\mathbf{r} e^{-i\mathbf{p}\cdot r/\hbar}\phi_b(\mathbf{r})$, it is possible to write

$$\langle \mathbf{p}_1, \mathbf{p}_2 | O | \mathbf{p}_3, \mathbf{p}_4 \rangle = \delta\left(\mathbf{p}_1 + \mathbf{p}_2 - \mathbf{p}_3 - \mathbf{p}_4\right) \phi_b\left(\frac{\mathbf{p}_1 - \mathbf{p}_2}{2}\right) \phi_b^\star\left(\frac{\mathbf{p}_3 - \mathbf{p}_4}{2}\right). \tag{4.43}$$

The second quantised operator that counts the number of molecules in the gas will then be given by

$$N_{\mathrm{mol}} = \frac{1}{2}\sum_{\mathbf{p}_1\mathbf{p}_2\mathbf{p}_3\mathbf{p}_4} \delta\left(\mathbf{p}_1 + \mathbf{p}_2 - \mathbf{p}_3 - \mathbf{p}_4\right) \phi_b\left(\frac{\mathbf{p}_1 - \mathbf{p}_2}{2}\right) \phi_b^\star\left(\frac{\mathbf{p}_3 - \mathbf{p}_4}{2}\right) a^\dagger_{\mathbf{p}_1} a^\dagger_{\mathbf{p}_2} a_{\mathbf{p}_3} a_{\mathbf{p}_4}. \tag{4.44}$$

The expectation value of this operator can be expanded using Wick's theorem to obtain an expression for the number of molecules in the gas. A similar argument can be used to neglect the products of density as when deriving the mean-field equations. This means the density of molecules can be written as

$$n_{\mathrm{mol}} = \frac{1}{2}\left|\int d^3 p \phi_b^\star(\mathbf{p})\Phi(\mathbf{p})\right|^2. \tag{4.45}$$

This allows us to calculate the molecule production from an overlap of the bound state wave function with the pair function. We expand the pair function into the partial wave basis, so in fact we are calculating various partial wave contributions to the molecule density, but note that we have done the same to the bound state wave function and that different partial wave components will obey the orthogonality condition of the spherical harmonics. The probability of molecule association will then be given as

$$P = \frac{2n_{\mathrm{mol}}}{n}, \tag{4.46}$$

where n is the atomic density of the gas that remains fixed throughout the time dependent calculation.

4.4.1 Bound state wave function

The wave function for the bound state can be calculated from the Lippmann-Schwinger equation with appropriate boundary conditions

$$|\phi_b\rangle = G_0(E_b)V|\phi_b\rangle, \tag{4.47}$$

where $|\phi_b\rangle$ is the wave function for the bound state and $G_0(E_b)$ is the free Green's function evaluated at the value of the binding energy, E_b. This equation is, of course, equivalent to the Schrödinger equation with the condition that the wave function is zero at infinity and at the origin. Using the separable potential and the fact that the $m = \pm 1$ components are degenerate (as already shown), we can write

$$|\phi_b\rangle = G_0(E_b)|\chi_1\rangle\xi_1\langle\chi_1|\phi_b\rangle + G_0(E_b)|\chi_0\rangle\xi_0\langle\chi_0|\phi_b\rangle. \tag{4.48}$$

The $m_1 = 0$ and $m_1 = \pm 1$ components of the wave function would be expected to be orthogonal to each other and, as already shown, it is possible in certain cases, including those of this thesis, to treat the two resonances separately so that each component can be given an independent energy argument

$$\langle \mathbf{p}|\phi_b\rangle_{m_1} = \frac{\langle \mathbf{p}|\chi_{m_1}\rangle\xi_{m_1}\langle\chi_{m_1}|\phi_b\rangle_{m_1}}{E_b - \frac{p^2}{2\mu}}. \tag{4.49}$$

The factor $\xi_{m_1}\langle\chi_{m_1}|\phi_b\rangle_{m_1}$ can be treated as a normalisation constant that can be found numerically. This provides an analytic form for the bound state. The only parameter to be determined is the bound state energy which we found in chapter 2.

4.5 Results

Now we have all the parameters and functions necessary to perform the many-body dynamic calculations. In the introduction we outlined the procedure of the ideal experiment we would conduct to investigate all the variable parameters. In this section we present the various investigations performed and give more details on what parameters were kept constant or varied in each calculation. We then present the results of these calculations for the lowest order approximation

introduced above.

Initially we vary the parameters that define the initial state of the system, namely the the atomic density, the temperature and the initial magnetic field position at which to begin the linear sweep of the magnetic field. The mean-field equations were propagated using an adaptive step size Runge-Kutta method. The results presented below are for the $m_1 = 0$ resonance in ^{40}K. Later we will look at how these compare to the results of the $m_1 = 1$ calculations.

4.5.1 Initial magnetic field

In this investigation we vary the value of the magnetic field at which we start the magnetic field sweep and all other parameters are held constant. The result of this is plotted in Fig.4.8. We have kept the temperature at 70 nK and plotted separate lines to represent different atomic densities. All of the solutions are propagated to the same magnetic field value below the resonance which is located at 198.85 G. For a given density it is possible to see that the number of molecules produced increases as the initial magnetic field value gets closer to the resonance. This can be explained by the fact that as we move closer to the resonance there is more pairing present in the initial state and therefore more molecules are produced at the end of the sweep. The parameter that determines the initial amount of pairing in the gas is the gap parameter, Δ_0, and we have seen in the previous chapter that this increases as the magnetic field moves towards the resonance from the BCS side. The sweep rate of the magnetic field is held constant for all combinations of density and initial field. Although we will see that the sweep rate does have an effect on the molecule production we do not expect it to change the behaviour of the molecule production as a function of initial magnetic field since the initial value of Δ_0 will be independent of the sweep rate. It is important to note that at some value of the initial magnetic field the molecule production goes to zero. This is due to there being no initial pairing in the gas and means that in the mean-field dynamics it is not possible to start infinitely far away from the resonance in contrast to the Landau-Zener problem studied above.

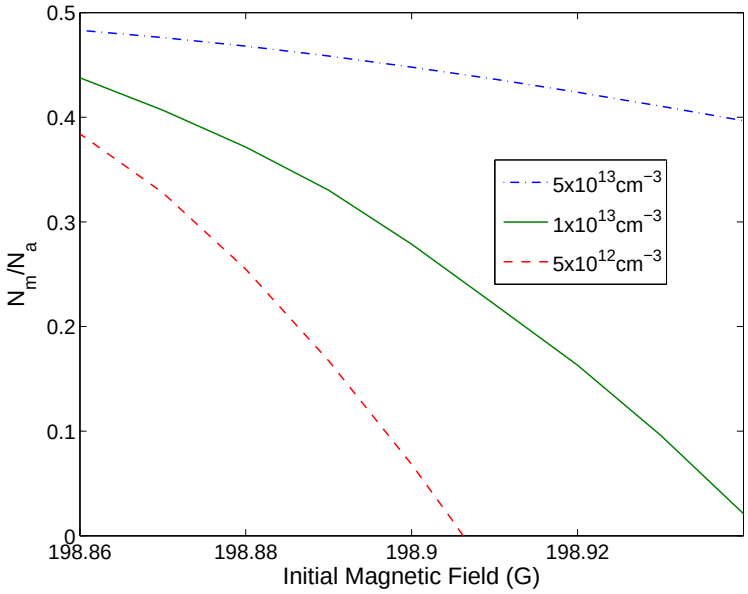

Figure 4.8: Fraction of atoms converted into molecules as a function of initial magnetic field position at the start of the sweep for the $m_1 = 0$ resonance at 198.85 G in ^{40}K. The different curves represent different densities. In these calculations the temperature was held constant at 70 nK and the sweep speed remained constant at 60 G/ms. It can be seen that starting closer to the resonance increases the molecule production efficiency and increasing the density also has the same effect.

4.5.2 Initial density and temperature

In a similar way to how we have studied the effect of the initial magnetic field value on the molecule production, we can also study the effect of the initial atomic density and the temperature. It should be remembered that both these quantities remain constant throughout the calculation (and for the time being we hold the sweep rate constant too). We can immediately deduce from Fig. 4.8 that by holding the temperature and the initial magnetic field position constant that we can increase the molecule production by increasing the atomic density, a prediction also made by the Landau-Zener approach. The explanation for this comes from an increased pairing in the initial state, which can be seen from the results of the previous chapter where as we increased the density we also increased the value of Δ_0 (see Fig. 3.8 and Fig. 3.9). However, we also note that the density plays a role in the dynamics, due to the presence of the density matrix in the dynamic equation governing the evolution of the pair function.

We can see the effect that temperature has on molecule production from Fig. 4.9. In this graph each line represents a different temperature and the atomic density is varied with the initial magnetic field held constant. It can clearly be seen that the molecule production increases with decreasing temperature. Again we have discussed in the previous chapter that a decrease in temperature will lead to an increase in the parameter Δ_0, and this will cause there to be more pairing in the gas and thus more molecules (see Fig. 3.8) at the end of the sweep.

4.5.3 Sweep rate

We now vary the rate at which the magnetic field is varied. The result of this is shown in Fig. 4.10 for a density of 10^{13} cm^{-3}, a temperature of 70 nK and an initial magnetic field position of 198.9 G, fairly close to the resonance position. There is only a small change in the production efficiency as the sweep rate is varied over a large range of magnetic sweep speeds. It can be seen from Fig. 3.8 and Fig. 3.9 that, at a density of 10^{13} cm^{-3} and a temperature of 70 nK, there is only 0.1 G of available magnetic fields on the BCS side to act as the initial condition for the dynamics.

By increasing the density above values at which experiments would normally

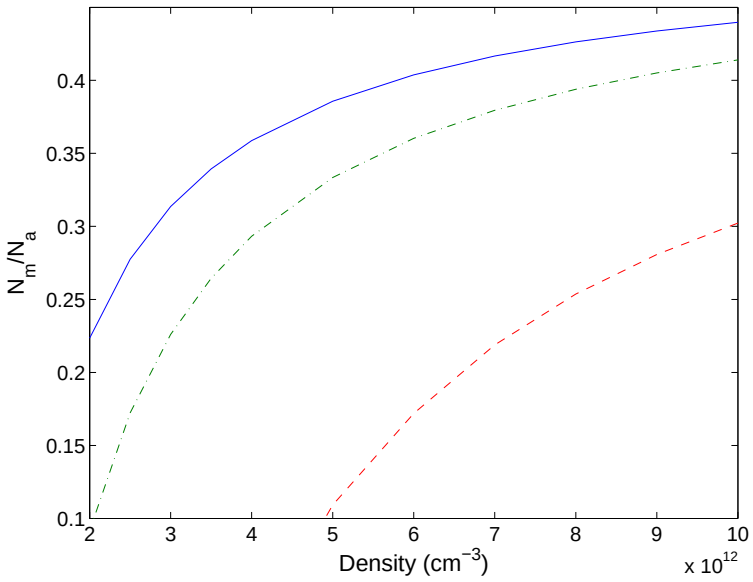

Figure 4.9: Fraction of atoms converted into molecules as a function of atomic density at the start of the sweep for the $m_1 = 0$ resonance at 198.85 G in ^{40}K. The different curves represent temperatures of 70 nK (solid blue), 100 nK (dot-dashed green) and 200 nK (dashed red). In these calculations the sweep speed remained constant at 60 G/ms. It can be seen that increasing the density and decreasing the temperature both increase the molecule production efficiency.

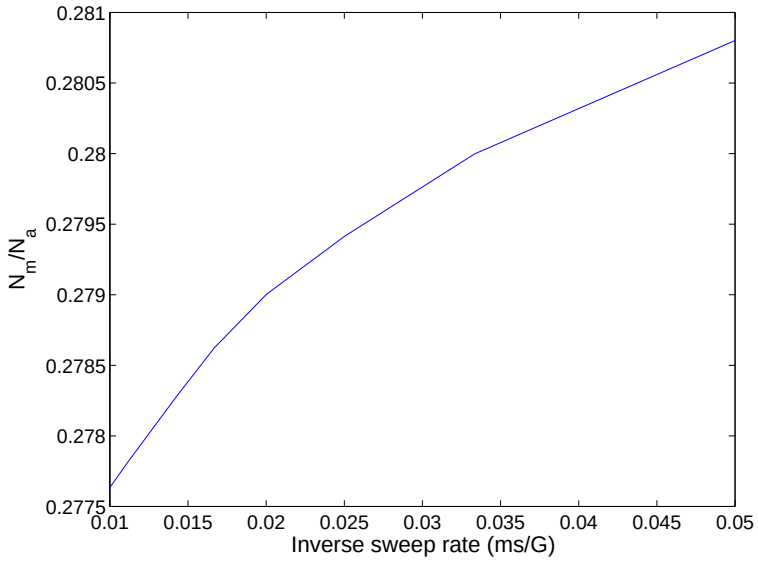

Figure 4.10: Variation in final molecule production efficiency as a function of inverse sweep rate of the magnetic field. The density is kept constant at 10^{13} cm^{-3} and the temperature at 70 nK. The initial magnetic field is close to the resonance at B_i=199.9 G. It can be seen that over a large range of sweep speeds the production efficiency does not greatly vary from its value at high ramp speeds. This suggests that the dynamics are not significantly affected by the change in ramp speed.

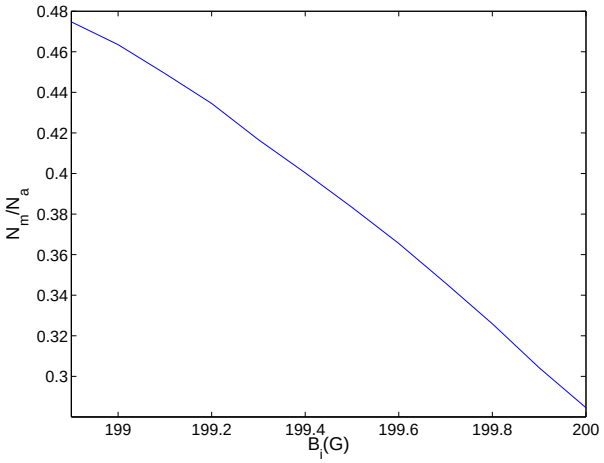

Figure 4.11: Molecule production efficiency as a function of initial magnetic field position for the initial state pair function overlapped with the bound state wave function at the final magnetic field position for a density of 10^{15} cm^{-3}. This can be compared with the values of the production efficiency for high ramp speeds in Fig. 4.13.

be performed, it is possible to use a greater range of magnetic fields for the initial conditions. This may be feasible for a trapped *p*-wave gas. Iskin and Williams [99] have shown that in a trapped *p*-wave superfluid it is possible to achieve densities that are orders of magnitude greater than in an *s*-wave superfluid. The result of increasing the density to a magnitude of 10^{15} cm^{-3} is shown in Fig. 4.13. In this figure the molecule production efficiency is plotted as a function of the sweep speed of the magnetic field for four different initial values of the magnetic field. As the initial value of the magnetic field moves away from the resonance, it is possible to produce more molecules by sweeping the magnetic field, such that although we may have less molecules with a fast sweep we can have a comparable molecule production with slower sweeps. At high sweep rates the production efficiency is well approximated by a jump in the magnetic field value from the initial value above the resonance to the final value below the resonance. Fig. 4.11 shows the molecule production for this case and can be directly compared with the values of the limit of fast sweeps in Fig. 4.13. In the limit of slow sweep speeds, the molecule production becomes independent of the value of the initial magnetic field at the start of the sweep. Allowing the initial value of the magnetic field to move away from the resonance position allows more molecules to be produced due to the dynamics alone and not just from the initial pairing in the gas. Fig. 4.12 shows the variation of the molecule production as the final magnetic field position is changed for an infinitely fast sweep. The choice of the final magnetic field position will provide a lower bound on how many molecules are produced from the atomic gas.

It may still be possible to find a lower density at which a significant number of molecules can be produced from the dynamics. A natural test is to see how many molecules are produced from a slow sweep in comparison to a fast sweep. It is easy to deduce from Fig. 4.13 that this number will increase as the initial magnetic field position is moved away from the resonance. However, this number should also be sensitive to the density of the atomic gas since, according to Fig. 4.8, at high density the number of molecules produced from the dynamics will be small because there will already be so much pairing in the gas for initial magnetic fields close to the resonance. For fields close to the point where pairing in the gas is lost, it will be necessary to go very slow in sweep rate in order to produce a significant

number of molecules. This suggests that there will be a value of the magnetic field at which there is an optimal production efficiency for a given density. Fig. 4.14 shows the molecule production efficiency from a sweep of the magnetic field at 10 G/ms minus the molecule production efficiency at a sweep speed of 500 G/ms. This calculation is done for various initial magnetic fields demonstrating that for the range of densities and magnetic fields covered the fraction of molecules created from the dynamics increases as the magnetic field increases provided the density is high enough. At lower densities it may be that more molecules can be produced from the dynamics by starting closer to the resonance. This is due to the fact that at some value of the magnetic field there will be so little pairing in the gas that the sweep would have to be even slower to allow molecules to form. It would be expected that for an infinitely slow magnetic field sweep for the lower sweep rate more atoms would be converted to molecules from the dynamics the further away from the resonance the initial magnetic field is, independent of the density.

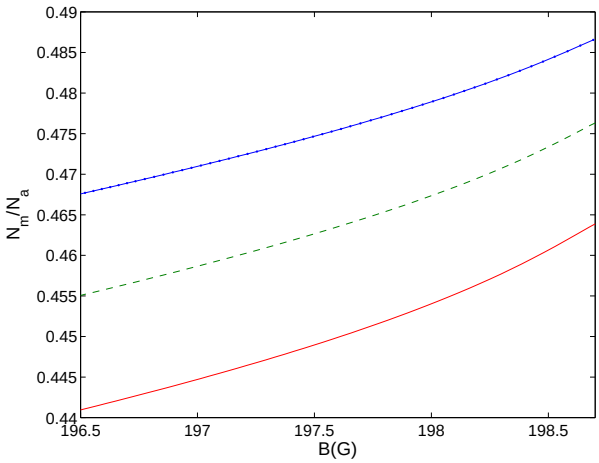

Figure 4.12: Molecule production as a function of final magnetic field position for an immediate projection of the initial state pair function onto the molecular bound state at the given magnetic field. The lines represent initial magnetic fields of 199.9 G (Blue dotted line), 200 G (Green dashed line) and 200.1 G (red solid line). It would be expected that all lines converge to $N_m/N_a = 0$ in the limit that the magnetic field is infinitely deep in the BEC side.

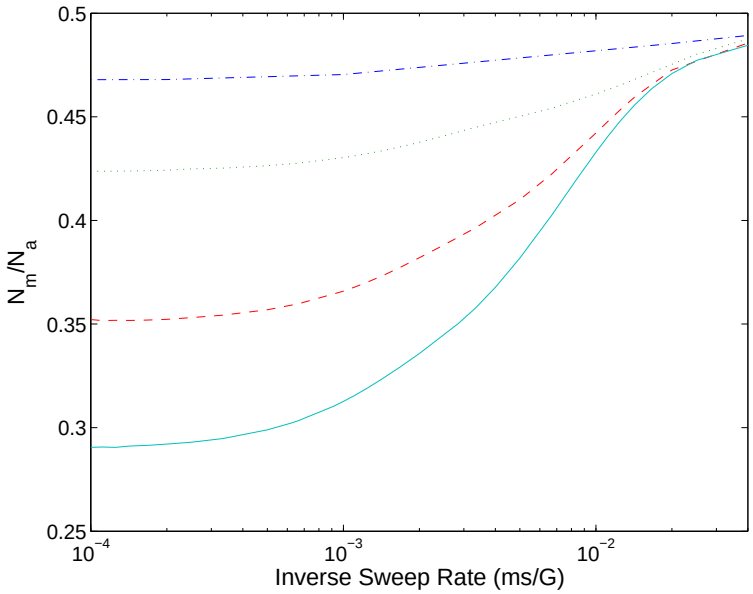

Figure 4.13: Variation in final molecule production efficiency as a function of inverse sweep rate of the magnetic field. The density is kept constant at 10^{15} cm^{-3} and the temperature at 70 nK. the different lines represent initial magnetic fields of 200 G (solid light blue line), 199.7 G (dashed red line), 199.3 G (dotted green line) and 199 G (dot-dashed blue line). It can be seen that it is possible to produce more molecules from changing the ramp speed by changing the initial value of the magnetic field to be further away from the resonance.

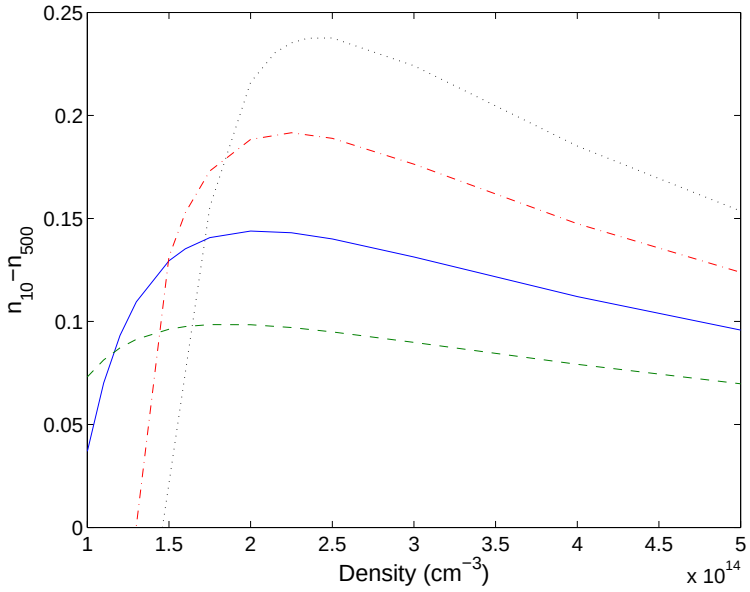

Figure 4.14: The difference in the molecule production efficiency from a sweep of 10 G/ms and a sweep of 500 G/ms as a function of density. Here, $n_{\dot{B}}$ is the number of molecules over the number of atoms after a sweep at a speed equal to $\dot{B}$ in G/ms for a temperature of 70 nK. This shows how many molecules are actually produced during the dynamics. The different curves represent initial magnetic field positions of 199.2 G (green dashed), 199.3 G (solid blue), 199.4 G (dot-dashed red) and 199.5 G (dotted black). It can be seen that there is an optimum density at which to produce molecules from the dynamics.

4.5.4 Atom-molecule coherence

Donley *et al*. [143] applied rapid variations of the magnetic field on a ^{85}Rb Bose-Einstein condensate. In this experiment the value of the magnetic field was kept on the positive scattering length side but rapidly varied to a value further from the resonance position t_{evolve}. They observed persistent oscillations in the number of atoms detected as a function of t_{evolve}, with a frequency fixed by the value of the molecule binding energy at the final magnetic field and an amplitude comparable to the total atomic number. They concluded that the undetected atoms had been transferred into molecules. This phenomenon is interpreted as a signature of atom-molecule coherence.

In experiments on *s*-wave molecules rapid sweeps of the magnetic field were used to probe the state of the Fermi gas in the region about the resonance. It was hypothesised that if the magnetic field was swept into the BEC side fast enough, such that the typical sweep time was less than the typical collision time, then it would be possible to extract information about the gas in the strongly interacting region [88]. The question then arises of how the state evolves after such a sweep. If the final state, held at a fixed field value, undergoes processes that significantly change it, then this method may not be a reliable way of probing the gas. For the *s*-wave it has been shown that the under such a magnetic field variation the final molecule production efficiency will oscillate but with a small, decreasing amplitude [129]. We use an essentially identical method to show that this is also true in the *p*-wave and it would not be possible to observe atom-molecule coherence with this approach.

Fig. 4.15 shows the variation in the production efficiency as a function of time after such a magnetic field variation. In this figure, the different lines correspond to different final magnetic fields. The variation in the molecule production over this time period is given as a percentage and seen to be on the order of 0.001 %, which is very small. The oscillations in the production are heavily damped with the frequency and damping of the oscillations increasing as the final magnetic field moves away from the resonance. For the case where the final field is located at 196.5 G the oscillations are not visible on this scale after 20 μs.

In Fig. 4.16 the initial magnetic field is varied and the final magnetic field

held constant. Again the oscillations for all detunings are on the order of 10^{-3}%. Both the frequency and amplitude of the oscillations increase as the initial field moves further from the resonance, but not significantly. It should be noted that this appears to be in contrast to the *s*-wave where the amplitude increases as the initial field moves towards the resonance [129]. However, in both cases the amplitude of the oscillations is very small (the results compared to in the *s*-wave correspond to a density of 1.5×10^{13} cm^{-3}). The *s*-wave resonance studied by Szymańska *et al*. [129] is the open-channel dominated resonance in ^{40}K that we looked at in chapter 2. We have already mentioned that *p*-wave resonances are closed channel dominated and therefore note that in this respect the nature of the resonance does not qualitatively affect the time dependence of the molecule density, but damping appears to be higher in the *p*-wave. It is difficult to identify a single reason for the increased damping in the *p*-wave because the problem is highly non-linear.

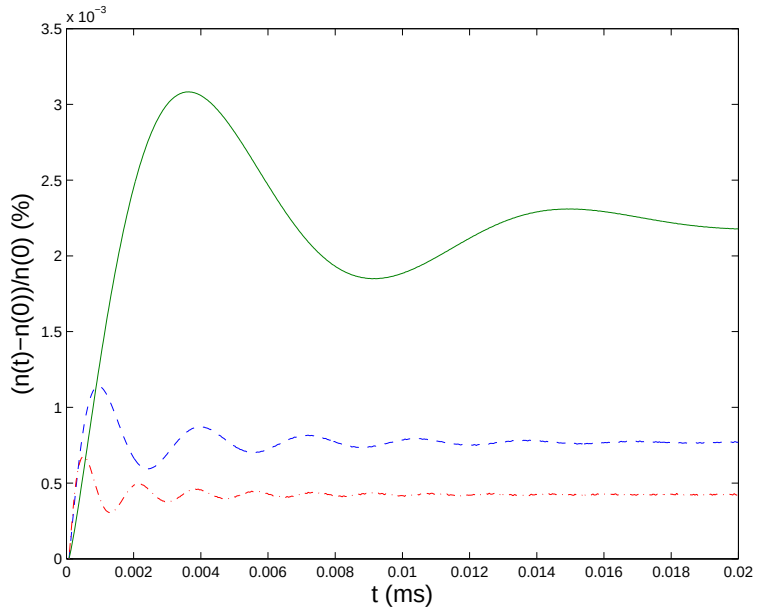

Figure 4.15: Evolution of the molecule production efficiency after an infinitely fast sweep of the magnetic field across the 198.85 G resonance in ^{40}K. The initial magnetic field is 199 G, just above the resonance. The different lines correspond to differing final magnetic fields of 198.5 G (solid, green line), 197.5 G (dashed, blue line) and 196.5 G (dot-dashed, red line). n(t) is the density of molecules as a function of time where n(o) is the density of molecules directly after the magnetic field variation.

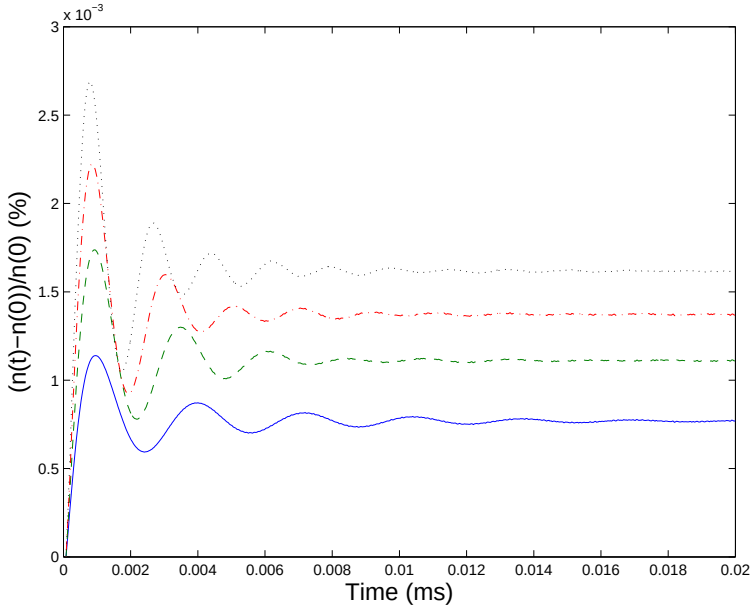

Figure 4.16: Evolution of the molecule production efficiency after an infinitely fast sweep of the magnetic field across the 198.85 G resonance in ^{40}K. The final field is held constant at 197.5 G. The different lines represent different initial magnetic fields of 199 G (solid, blue line), 199.5 G (dashed, green line), 200 G (dot-dashed, red line) and 200.5 G (dotted, black line). n(t) is the density of molecules as a function of time where n(o) is the density of molecules directly after the magnetic field variation.

We have also studied how the order parameter varies after such a magnetic field variation. In this case the gap parameter is a function of time defined by

$$\Delta(t) = \xi \int d^3q \langle \chi | \mathbf{q} \rangle \langle \mathbf{q} | \Phi(t) \rangle, \tag{4.50}$$

where we have used the separable potential to divide out a form factor from each side of the equation. We note that the value of the binding energy does not enter this equation directly. We compare this value against the value of the gap parameter when the system is in equilibrium at the final magnetic field position. We note that, in general, the quantity in Eq. (4.50) is complex. As for the case of the density variation, we vary the initial and final magnetic fields.

We plot the time evolution of the gap parameter in Fig. 4.17. The top and bottom panel refer to final magnetic fields of 197 G and 198 G, respectively. In each

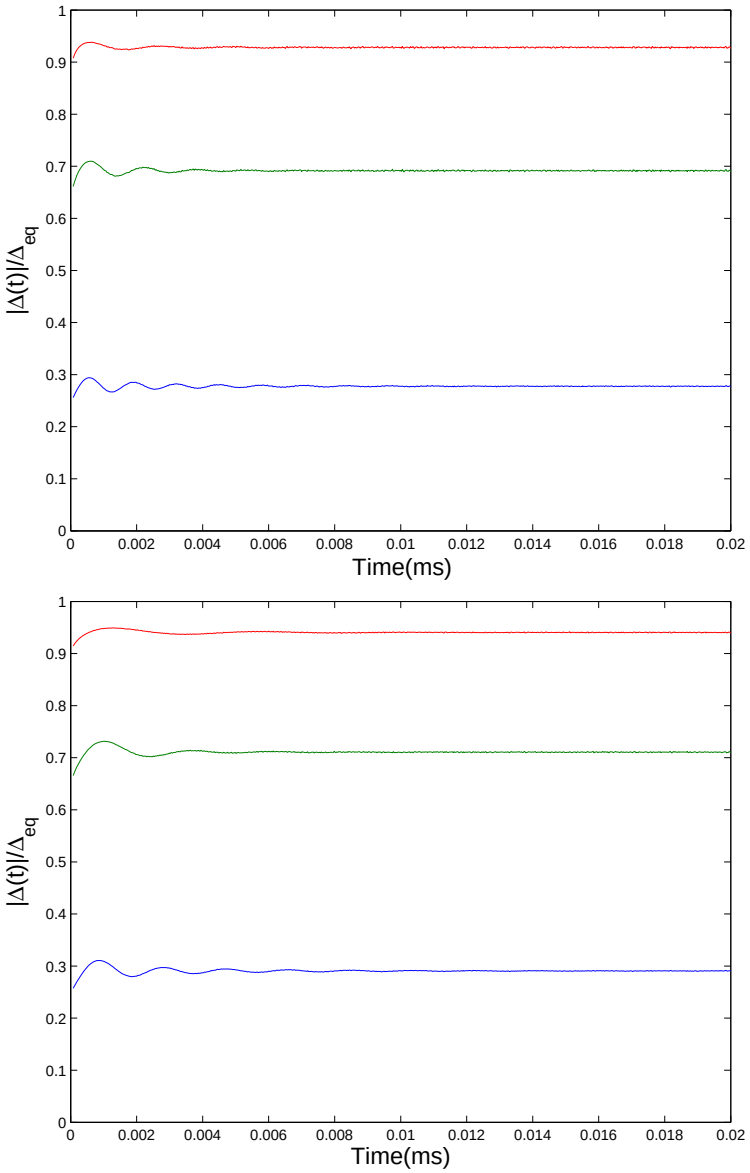

Figure 4.17: Variation of the quantity $|\Delta(t)|/\Delta_{eq}$ with time for final magnetic fields of 197 G (top panel) and 198 G (bottom panel). The different lines correspond to different initial magnetic field positions of 198.2 G (top, red), 200.2 G (middle, green) and 201.2 G (bottom, blue).

panel the different lines correspond to different initial magnetic field positions of 198.2 G (top, red), 200.2 G (middle, green) and 201.2 G (bottom, blue). It can be seen that the closer the initial and final field are to each other the closer the value

of the gap parameter is to the stationary state value at the final magnetic field position, denoted here by Δ_{eq}. In all case the oscillations have a small amplitude and quickly decay.

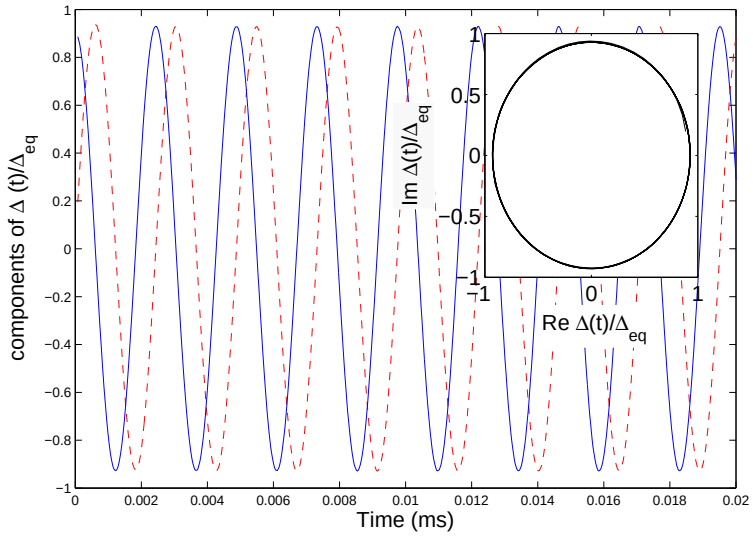

Figure 4.18: Real (solid, blue line) and imaginary (dashed, red line) parts of the parameter $\Delta(t)/\Delta_{eq}$ for B_I =199.2 G and B_F =197 G. The inset shows a phase space plot of the same data for which the absolute value remains largely unchanged. The real and imaginary parts appear to differ by little more than a phase shift.

Fig. 4.18 plots the real and imaginary parts of the gap parameter as a function of time. In this plot it appears that both components quickly settle into sinusoidal oscillations with a fixed frequency and phase between the components. The inset shows a phase space plot of the real and imaginary parts of the gap parameter showing that the oscillations have essentially a fixed amplitude. To determine the frequency of the oscillations we have performed Fourier transforms of the parameters studied in Fig. 4.17. The results of these Fourier transforms have been plotted in Fig. 4.19 for a final field of 197 G and Fig. 4.20 for a final field of 198 G. For each plot the real (blue lines) and a imaginary (red lines) parts oscillate at a frequency that corresponds to the energy of the bound state at the final magnetic field position. This is expected and serves as a test on the numerics. To evaluate the Fourier transform of the absolute value we renormalise it by subtracting off the value at large times, removing an initial large spike in the data. For this reason the

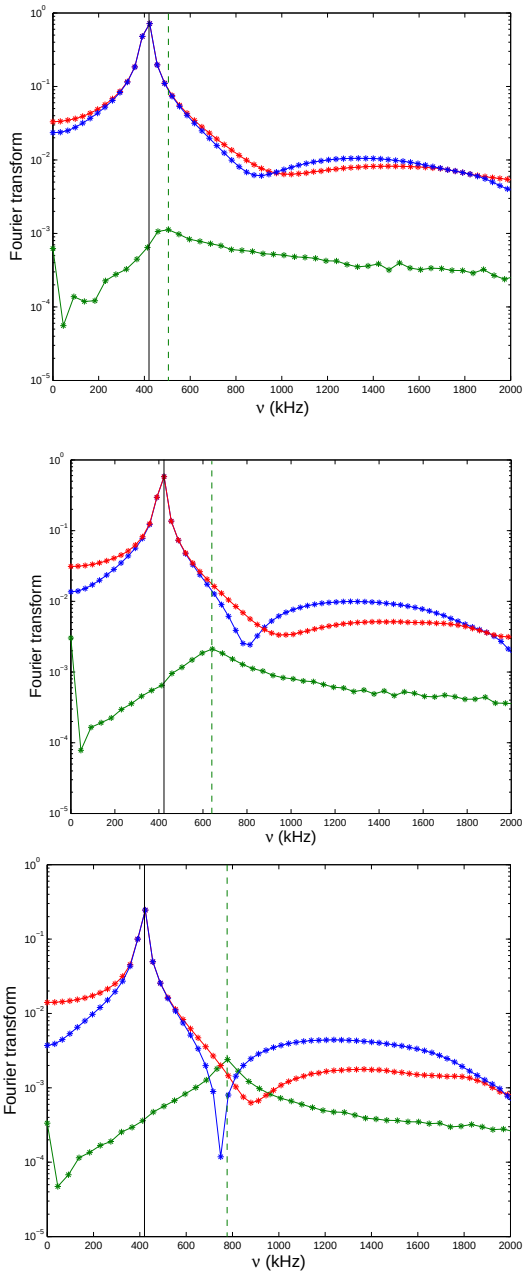

Figure 4.19: Fourier transforms of the gap parameter as a function of the frequency ν. The blue, red and green lines correspond to the real, imaginary and absolute value respectively. The absolute value has been renormalised prior to taking the Fourier transform in order to remove the initial spike in the data. The final field is held constant at 197 G in all 3 figures with the initial field set to 199.2 G (top), 200.1 G (middle) and 201.2 G (bottom). The solid vertical line is the value of the bound state energy at the final field. The dashed vertical line represents the peak value of the absolute value frequency which is approximately equal to $(|E_b(B_F)| + 2\mu(B_I))/h$.

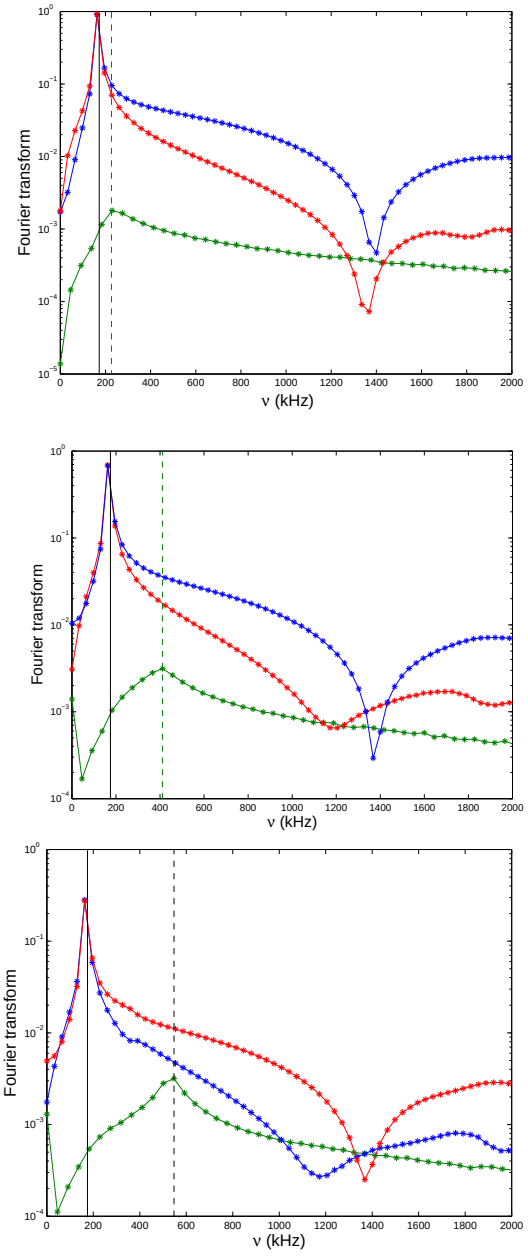

Figure 4.20: Fourier transforms of the gap parameter as a function of the frequency ν. The blue, red and green lines correspond to the real, imaginary and absolute value respectively. The absolute value has been renormalised prior to taking the Fourier transform in order to remove the initial spike in the data. The final field is held constant at 198 G in all 3 figures with the initial field set to 199.2 G (top), 200.1 G (middle) and 201.2 G (bottom). The solid vertical line is the value of the bound state energy at the final field. The dashed vertical line represents the peak value of the absolute value frequency and is approximately equal to $(|E_b(B_F)| + 2\mu(B_I))/h$.

B_I (G)	$2\mu/h$ (kHz)
199.2	84.3
200.2	243.6
201.2	363.6

B_F (G)	E_b/h (kHz)
197	-420.6
198	-177.7

Table 4.1: Values of the chemical potential at the initial magnetic field (left table) and the bound state energy at the final field (right table).

amplitude of the Fourier transform of the absolute value is much smaller than the real and imaginary parts. We have plotted the data with a log y axis since we only wish to extract the peak frequency of the oscillations. The value of this frequency increases as the initial magnetic field moves away from the resonance position and approximately corresponds to the sum of the final bound state energy and twice the initial chemical potential energy. The determination of the value of the peak frequency is complicated by the fact that the oscillations are heavily damped and soon reach an amplitude that is difficult to determine above numerical noise.

We have also studied the decay rate of the absolute value of the gap parameter. In order to estimate this decay rate we have chosen the maxima of the functions plotted in Fig. 4.17 and taken off the value of the function at large times. This is plotted in Fig. 4.21, where the blue line represents the trend of these values, but is, of course, not a continuous function. Also plotted are error estimates that correspond to an estimate of the numerical noise about the specific data point. In order to estimate the decay rate we have fitted the data to exponential curves corresponding to either $\exp(bt + c)$ or $\exp(b\sqrt{t} + c)$.* Curves corresponding to these estimates are plotted in Fig. 4.21 with the different colours denoting which functions have been plotted. In all cases the fits are not very good over the whole range of data points, indicating that the decay does not follow a simple exponential trend.

The conclusion of this section is that it would not be feasible to observe atom-molecule oscillations in this *p*-wave resonance due to the small, vanishing amplitude of the density oscillations. This is the essentially the same conclusion reached in Szymańska *et al*. [129] but extends this result to the closed channel

*It should be noted that for the case where the initial field was at 198.2 G, it was not possible to extract enough data points to fit to a curve of this form accurately.

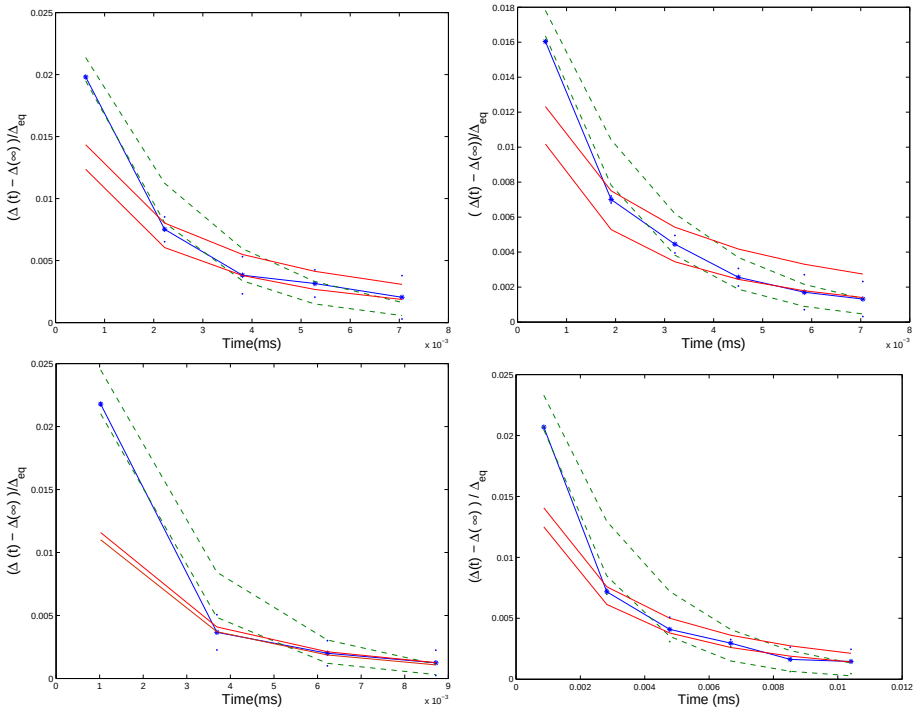

Figure 4.21: Plot of the decay of the maximum of the oscillations seen in Fig. 4.17. The blue stars are the data point and the line that connects them is simply illustrative. The blue dots are an estimate of the error on each value due to numerical noise. The green, dashed lines are fits to $\exp(bt + c)$ while the solid red lines are fits to $\exp(b\sqrt{t} + c)$. There is some suggestion that the exponent varies like t for short times and like $\sqrt{t}$ for long times. However, it is most likely that the decay is not exponential at all.

dominated *p*-wave resonance in ^{40}K. This also suggests that the method of fast sweeps to probe a fermionic pair condensate would be a suitable method to probe the condensate were such conditions favourable. It remains a question as to why the magnitude of the oscillations in the molecule density relative to the initial molecule density shows different behaviour with respect to the initial magnetic field between the *s*-wave and the *p*-wave.

4.6 Higher-order components

The results of the previous section depend on neglecting the higher ℓ partial wave components of the pair function and the density matrix. The other components of the pair function will be orthogonal to the p-wave bound state due to orthogonality of the spherical harmonics and will therefore only contribute to the molecule production through the dynamic equations.

4.6.1 Including Γ_{20}(p,t)

Equation (4.36) shows that any component of the density matrix that is non-zero in the separated resonances approximation will have $m_\ell = 0$. Now consider the integral appearing in Eq. (4.38) and take the pair function to be $\Phi_{10}(p,t)$ and interactions to only be in the p-wave. This leaves an integral

$$\int d\Omega Y_{10}^\star(\Omega) Y_{10}(\Omega) Y_{l''0}(\Omega) = \begin{cases} \frac{1}{\sqrt{4\pi}} & \ell'' = 0 \\ \frac{1}{\sqrt{5\pi}} & \ell'' = 2 \\ 0 & \ell'' \neq 2 \text{ or } 0 \end{cases} \tag{4.51}$$

showing that the next order correction in this equation comes from the $\Gamma_{20}(p,t)$ component of the density matrix. A new equation for this component is

$$i\hbar \frac{\partial}{\partial t}\Gamma_{20}(p,t) = -\frac{2(2\pi\hbar)^{3/2} i}{\sqrt{5\pi}} \mathrm{Im}\left(\chi_{10}(\mathrm{p})\xi_0 \int \mathrm{q}^2 \mathrm{dq} \chi_{10}(\mathrm{q})\Phi_{10}(\mathrm{q,t})\Phi_{10}^\star(\mathrm{p,t})\right). \tag{4.52}$$

The equation for the $\Gamma_{00}(p,t)$ component remains unchanged. An extra term is added to the equation for $\Phi_{10}(p,t)$

$$\begin{aligned} i\hbar \frac{\partial}{\partial t}\Phi_{\ell m}(p,t) = \frac{p^2}{m}\Phi_{\ell m}(p,t) + \chi_{\ell m}(p)\xi_{\ell m} \int q^2 dq \chi_{\ell m}(q)\Phi_{\ell m}(q,t) \\ - \frac{(2\pi\hbar)^{3/2}}{\sqrt{\pi}}\chi_{10}(p)\xi_0\Gamma_{00}(p,t)\int q^2 dq \chi_{10}(q)\Phi_{10}(q,t) \\ - \frac{2(2\pi\hbar)^{3/2}}{\sqrt{5\pi}}\chi_{10}(p)\xi_0\Gamma_{20}(p,t)\int q^2 dq \chi_{10}(q)\Phi_{10}(q,t). \end{aligned} \tag{4.53}$$

This gives three coupled differential equations to be solved.

4.6.2 Including Φ_{30}(p,t)

The previous equations suppress a term present in the dynamic equation for the $\Gamma_{20}(p,t)$ component of the density matrix. The relevant angular integral is

$$\int d\Omega Y_{20}^{\star}(\Omega)Y_{\ell' 0}(\Omega)Y_{10}(\Omega) = \begin{cases} \frac{1}{\sqrt{5\pi}} & \ell' = 1 \\ \frac{3}{2}\sqrt{\frac{3}{35\pi}} & \ell' = 3 \\ 0 & \ell' \neq 3 \text{ or } 1 \end{cases} \tag{4.54}$$

Obviously the integral in Eq. (4.54) will vanish for any $m' \neq 0$. This suggests that we must calculate the time evolution of the pair function component $\Phi_{30}(p,t)$.

$$i\hbar\frac{\partial}{\partial t}\Phi_{30}(p,t) = \frac{p^2}{m}\Phi_{30}(p,t) - 3(2\pi\hbar)^{3/2}\sqrt{\frac{3}{35\pi}}\chi_{10}(p)\xi_0\Gamma_{20}(p,t)\int q^2 dq\chi_{10}(q)\Phi_{10}(q,t). \tag{4.55}$$

The equation for the $\Gamma_{20}(p,t)$ component becomes

$$\begin{aligned} i\hbar\frac{\partial}{\partial t}\Gamma_{20}(p,t) = &-\frac{2(2\pi\hbar)^{3/2}i}{\sqrt{5\pi}}\mathrm{Im}\left(\chi_{10}(\mathrm{p})\xi_0\int \mathrm{q}^2\mathrm{dq}\chi_{10}(\mathrm{q})\Phi_{10}(\mathrm{q,t})\Phi_{10}^{\star}(\mathrm{p,t})\right) \\ &- 3(2\pi\hbar)^{3/2}\sqrt{\frac{3}{35\pi}}\mathrm{Im}\left(\chi_{10}(\mathrm{p})\xi_0\int \mathrm{q}^2\mathrm{dq}\chi_{10}(\mathrm{q})\Phi_{10}(\mathrm{q,t})\Phi_{30}^{\star}(\mathrm{p,t})\right). \end{aligned} \tag{4.56}$$

The equations for the other components remain unchanged. This now requires the propagation of four equations.

4.6.3 Conclusion of adding higher-order terms

We have performed similar calculations to those performed using only the lowest order partial wave components, but also including the next order terms given above. The result of adding these terms does not change the molecule production efficiency significantly (less than 1 %) over the range of parameters investigated, such that the variation in the molecule production is not visible to the naked eye. This means that the majority of the dynamic production is attributed to the lowest order terms in the $m_1 = 0$ case.

4.7 Comparison with Landau-Zener approach

We can compare the results of the mean-field dynamics with that of the Landau-Zener approach. To do this the sweep rate is held constant and the density is varied. According to the Landau-Zener approach a power law in the density is observed in the molecule production for two particles in a tight harmonic trap when the sweep rate is sufficiently rapid, Eq. (4.16). This shows itself as a straight line on a log-log plot. Fig. 4.22 shows a comparison of the mean-field dynamics with the Landau-Zener formula. The initial conditions for the mean-field dynamics are taken at two different magnetic fields. Over the range of densities available the molecule production shows no indication of a power law in the density.

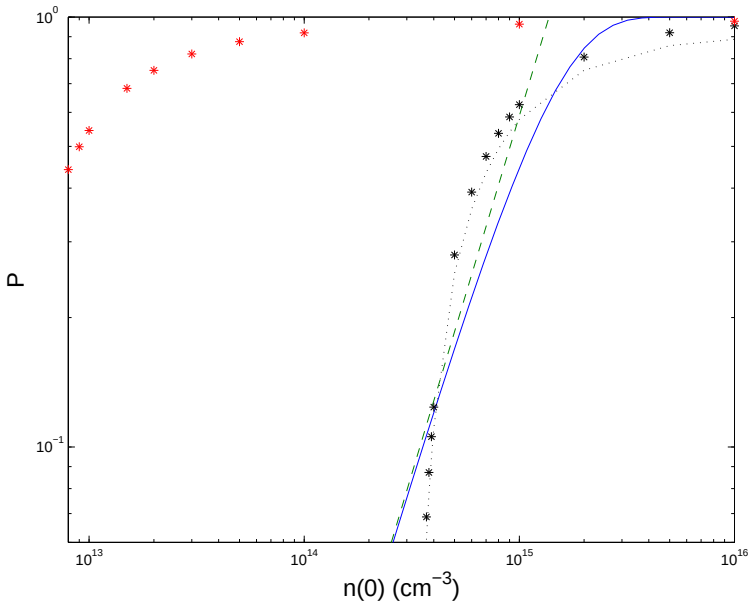

Figure 4.22: A comparison of the Landau-Zener approach with mean-field dynamics. The solid, blue line is the Landau-Zener formula of Eq. (4.5) with dashed, green line being the high speed (low density) approximation. The red stars are the results of the mean-field dynamics at an initial magnetic field position of 198.9 G. The black stars are the results of the mean-field dynamics at an initial magnetic field position of 200 G. The sweep speed is kept constant at 1000 G/ms. For comparison the result of the mean-field theory with an infinite ramp speed has been plotted (dotted, black line). Under these conditions the mean-field molecule production closely follows that of the infinite sweep and displays no power law in the density.

4.8 $|m_1 = 1|$ dynamics

Using the same assumption of separated resonances there will also be a set of equations for the $|m_1| = 1$ projections of the orbital angular momentum. The lowest order approximation for $|m_1| = 1$ will be given by

$$i\hbar\frac{\partial}{\partial t}\Phi_{11}(p,t) = \frac{p^2}{m}\Phi_{11}(p,t) + \chi_{11}(p)\xi_{11}\int q^2 dq\chi_{11}(q)\Phi_{11}(q,t) \qquad (4.57)$$
$$- \frac{(2\pi\hbar)^{3/2}}{\sqrt{\pi}}\chi_{11}(p)\xi_{11}\Gamma_{00}(p,t)\int q^2 dq\chi_{11}(q)\Phi_{11}(q,t),$$

with an analogous equation for the $m_1 = -1$ component

$$i\hbar\frac{\partial}{\partial t}\Gamma_{00}(p,t) = \frac{2(2\pi\hbar)^{3/2}i}{\sqrt{4\pi}}\mathrm{Im}\left(\chi_{11}(\mathrm{p})\xi_1\int \mathrm{q}^2\mathrm{dq}\chi_{11}(\mathrm{q})\Phi_{11}(\mathrm{q,t})\Phi^{\star}_{11}(\mathrm{p,t}) \qquad (4.58)\right.$$
$$\left. +\chi_{1-1}(p)\xi_{-1}\int q^2 dq\chi_{1-1}(q)\Phi_{1-1}(q,t)\Phi^{\star}_{1-1}(p,t)\right).$$

Using the previous definitions and assumptions about the $|m_1| = 1$ states we can assume $\Phi_{11}(p,t) = \Phi_{1-1}(p,t)$. This means that only one equation for the pair function has to be propagated and the equation for the $\Gamma_{00}(p,t)$ component of the pair function is modified in a trivial way. These lowest order equations are then nearly identical to those for the $m_1 = 0$ component of the pair function.

4.8.1 Comparison of the $m_1 = 0$ and $|m_1| = 1$ dynamics

We note that the equations governing the dynamics of the $|m_1| = 1$ and the $m_1 = 0$ states are identical. The differences will arise from the resonance parameters entering the equations and we note that in the case of ^{40}K the resonance parameters are very similar for both relative angular momentum projections, the main difference being the shift in the resonance position. We can therefore predict that the numbers of molecules produced in each projection will be very similar if we use the same input conditions. From a physical point of view we may not expect this similarity to be the case in every atomic species, especially in cases where the dipole-dipole interaction dominates at low energy, but in this case we would not be able to use our model potential because it relies on the assumptions about

the long-range form of the potential at low energy. In the ^{6}Li experiments, there was no observed dipole-dipole splitting so the resonances corresponding to the different projections will have identical parametrisation in our model.

Fig. 4.23 shows the ratio of the $m_1 = 0$ molecules to the $m_1 = \pm 1$ molecules as function of inverse ramp speed, where the molecule production is calculated from the Landau-Zener formula. At low enough ramp speeds both components produce 100 % molecules so the ratio is unity. At high ramp speeds the molecule production can be approximated by $2\pi\delta_{\mathrm{LZ}}^{m_1}$ and the ratio of this factor of the components corresponds to the quantity $\frac{a_{\mathrm{bg}}^0 \Delta B^0}{a_{\mathrm{bg}}^1 \Delta B^1}$, where the superscripts denote the value of m_1. This quantity is marked on the figure by the dotted, black line. It should be noted that this quantity is independent of the trap parameters and although we expect both efficiencies to vanish as the ramp speed goes to infinity, the ratio of the efficiencies goes to a constant that is not equal to unity.

We have already seen that in the many-body dynamics the molecule production from an infinitely fast sweep of the magnetic field will not be expected to be zero. In fact it is possible to produce a large number of molecules provided we start close enough to the resonance. This is because of the many body pairing in the initial state of the gas and the fact that we can only start at a finite magnetic field detuning from the resonance. In the other extreme of slow magnetic field sweeps it is not so easy to predict the behaviour. The problem is highly nonlinear and it may be that many parameters play a role in determining the ratio of molecule production between the two components.

In order to study how molecule production varies between the various projections of the relative angular momentum vector, we fix the density and the detuning of the magnetic field for the initial and final states. We study the variation as a function of the sweep rate to produce a figure analogous to Fig. 4.23, but using the mean-field equations.

To look at how the initial condition may affect the ratio of the molecule productions in the different components we vary the initial magnetic field and calculate the molecule production from an infinitely fast sweep. This is plotted in Fig. 4.24 and it can be seen that in contrast to the Landau-Zener case plotted in Fig. 4.23 the ratio is not constant but increases as the initial field detuning is increased. However at some value of the detuning we expect the production from

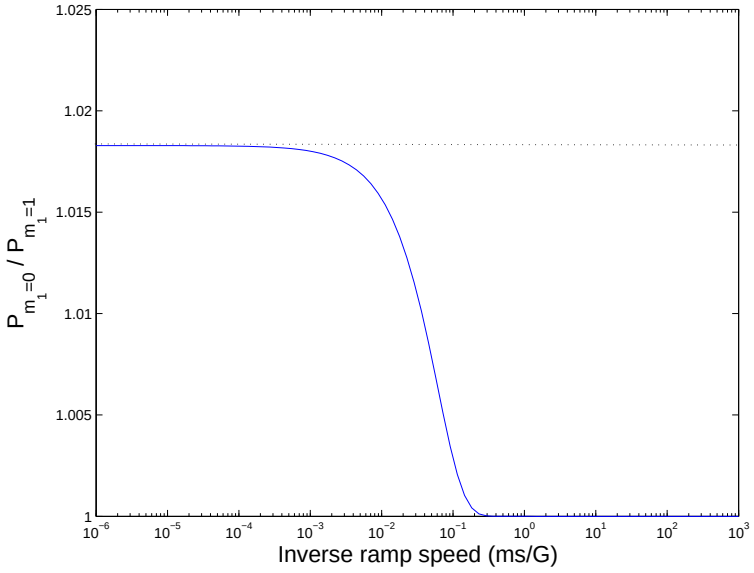

Figure 4.23: Comparison of the Landau-Zener association probability between $m_1 = 0$ and $m_1 = 1$ molecules represented as a quotient. At high low ramp speeds the two probabilities converge upon each other as they both approach 100 %. At higher ramp speeds the quotient approaches the value 1.018, shown by the dotted line. This corresponds to the ratio $\frac{a_{\rm bg}^0 \Delta B^0}{a_{\rm bg}^1 \Delta B^1}$, where the superscripts denote the projection of the angular momentum vector. The reason for this limit can be seen from Eq. (4.6) and is dependent only upon the resonance parameters.

both components to be zero, with the $|m_1| = 1$ going to zero before the other component, so that if we extended this curve to higher detunings it would be discontinuous. In Fig. 4.25 we vary the final magnetic field at which the molecule production is calculated. We see that the ratio does depend on the value of the final magnetic field position, but the difference remains fairly small. In contrast to the Landau-Zener approach, we see that the ratio is sensitive to the initial and final conditions.

In Fig. 4.26 we have plotted the molecule production efficiency for both the $m_1 = 0$ (solid lines) and $|m_1| = 1$ (dashed lines) molecules. The different colours show different initial magnetic field positions. The final magnetic field is held constant at a value below the resonance. It can be seen that the results of the $|m_1| = 1$ dynamics are at least qualitatively similar to those of the $m_1 = 0$ molecules and

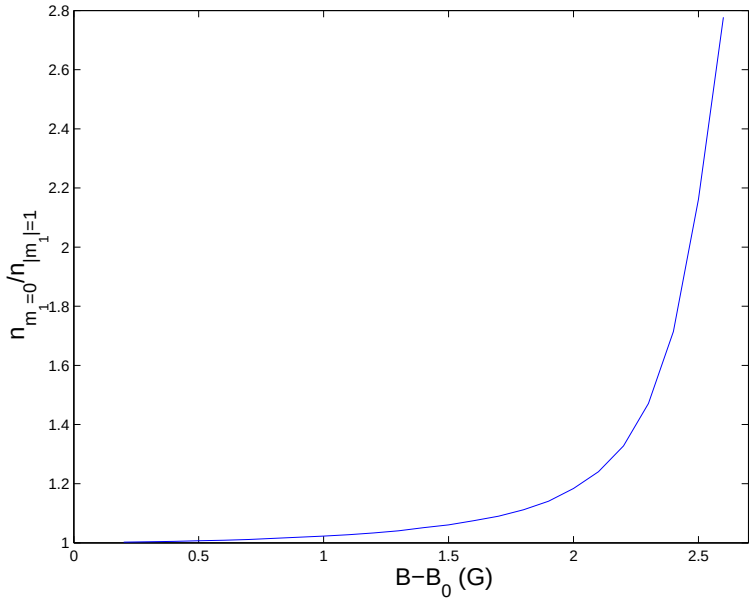

Figure 4.24: Ratio of the molecule production in the $m_1 = 0$ component to the $|m_1| = 1$ component as a function of the initial magnetic field detuning from the resonance. The sweep rate is infinite and the final magnetic field is held at a constant detuning below the resonance. In contrast to Fig. 4.23 the ratio of the molecule productions varies with the initial magnetic field detuning and increases as the field moves away from the resonance. At some point the molecule production in both components will be zero, so we would expect this curve to be discontinuous if extended to higher detunings.

do not significantly differ in value. We make a comparison of the two projections by plotting the ratio of the number of molecules produced as a function of ramp speed in Fig. 4.27 with each line corresponding to the same initial magnetic field detuning in as Fig. 4.26. As the ramp speed is reduced the lines converge such that the number of molecules produced is independent of the initial magnetic field and the projection of the angular momentum vector. We conclude that there is no significant difference between the molecule production in different relative angular momentum projections.

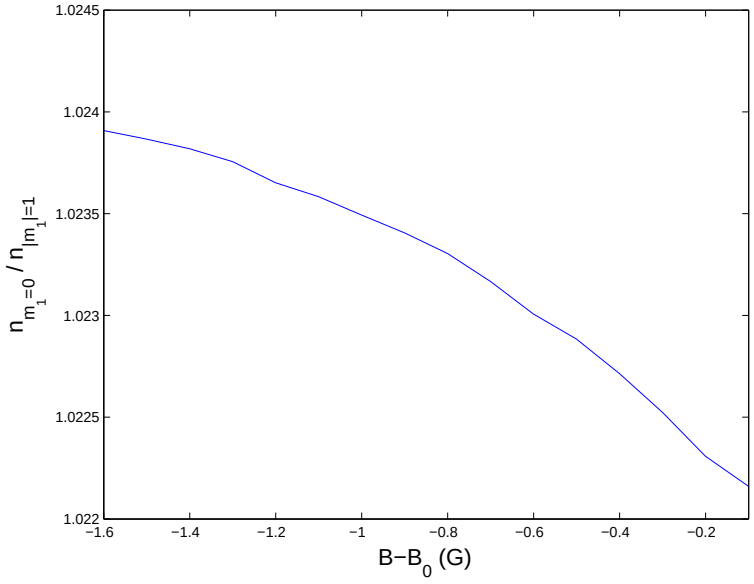

Figure 4.25: Ratio of the molecule production in the $m_1 = 0$ component to the $|m_1| = 1$ component as a function of the final magnetic field detuning from the resonance. The sweep rate is infinite and the initial magnetic field is held at a constant detuning above the resonance. The number of $m_1 = 0$ molecules increases relative to the other component as the final field moves away from the resonance, but the variation is small.

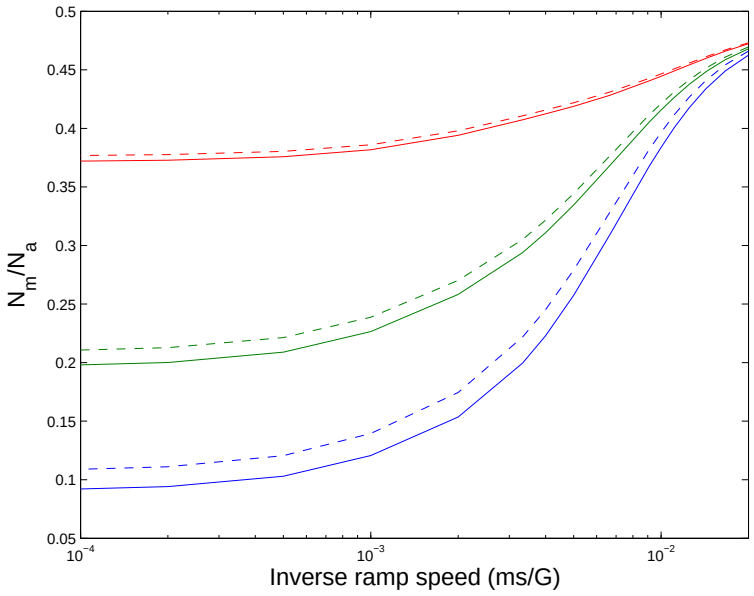

Figure 4.26: Molecule production efficiency as a function of the inverse ramp speed. The solid lines represent $m_1 = 0$ molecules the dashed lines represent $|m_1| = 1$ molecules. The different colours represent different magnetic field detunings from the resonance of 0.727 G (red), 1.527 G (green) and 2 G (blue).

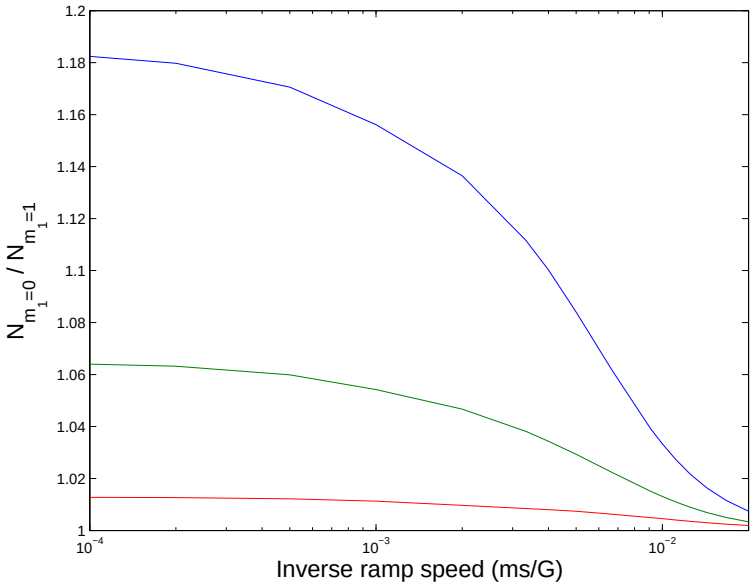

Figure 4.27: The ratio of the molecules produced for the different projections of the angular momentum vector as a function of the inverse ramp speed. The different colour lines represent different magnetic field detunings from the resonance of 0.727 G (red), 1.527 G (green) and 2 G (blue). As the initial magnetic field approach the resonance the number of molecules produced in either component becomes comparable. At low enough ramp speeds the ratios converge to unity.

4.9 Conclusion

We have derived the dynamic mean-field equations for fermions in an ultra cold gas and solved these equations to calculate the molecule production from a linear sweep of the magnetic field across a Feshbach resonance, showing that the number of molecules produced depends on the initial conditions. In particular, we have shown that in order to produce a high yield of molecules from the dynamics a high density is required, so that a larger range of magnetic fields can be accessed. We have shown that it is possible to study the dynamics of the system by retaining only lowest order partial wave components in the mean-field equations and have taken this approach to both the $m_1 = 0$ and the $|m_1| = 1$ dynamics.

We have shown that after a fast sweep of the magnetic field, the state of the system does not change significantly as the magnetic field is held constant at the final magnetic field position. The oscillations in the molecule production are highly damped and only slightly increase as the initial and final fields move away from the resonance position. We have shown that there is no significant difference between the values of the molecule production between the different components corresponding to the different projections of the relative angular momentum vector.

We have compared the results of a Landau-Zener calculation for two atoms in a tight harmonic trap against our mean-field results. We have seen that there are some qualitative similarities between the two cases in regards to the molecule production as a function of inverse ramp speed. However, there are important differences between the two approaches. Some of the differences stem from the fact that in the many-body calculation we can have a variety of initial conditions. In the Landau-Zener calculation we only consider the two-body states infinitely far from the resonance. Another feature of the Landau-Zener approach is the presence of a trapping potential that we have not included in the many-body calculation. However, by looking at the solution to the Landau-Zener problem in a spherical box (appendix G), it seems unlikely that the harmonic trap is the source of the discrepancy and there is some many-body effect behind the differing behaviour.

In principle we could produce 100 % conversion of atoms to molecules with a slow enough ramp speed. In experiments on *p*-wave Feshbach molecules using

linear sweeps of the magnetic field it has not been possible to achieve more than 25 % atom to molecule conversion. This suggests that there are processes that have been neglected in our model. Most likely is that the initial state is not a BCS paired state in the experiments. We have also neglected loss mechanisms, such as three-body recombination and the finite lifetime of the molecules.

Chapter 5

Conclusion

We have studied molecule production in a single component ultracold Fermi gas from linear sweeps of a magnetic field. We have shown that at the two-body level the interactions will be dominated by *p*-wave scattering and have used the near threshold behaviour of the system to derive a model separable potential. We have then applied this to the BCS theory to fix the initial state of the gas from which we will produce molecules. We have derived the dynamical mean field equations and applied them to linear sweeps of the magnetic field across a *p*-wave Feshbach resonance to study molecule production.

We have shown that in the two-body case it was possible to provide a reasonable description of the system close to threshold using a single channel model. We argued that although in the two channel model *p*-wave Feshbach resonances are dominated by the closed channel component, the behaviour of the bound state and the resonance state mirror each other and therefore the use of a single channel model is sufficient, at least for an initial study. The result is a *p*-wave binding energy that, close to threshold, varies linearly with magnetic field detuning from the resonance. This can be compared to the *s*-wave binding energy that varies quadratically with magnetic field detuning from the resonance. Our results are in agreement with previous theoretical and experimental studies [20, 3, 21, 2, 97, 99, 101, 102, 106, 107].

We have shown that in the case of ^{40}K it is possible to have two separate thermodynamic states corresponding to the different projections of the angular

momentum vector onto the magnetic field axis. We have compared our model of the BCS state to a Bose-Fermi model that neglects the background scattering in the entrance channel and introduces a cut-off momentum, and shown that there is little difference between the results of the two models.

To study the dynamics we have varied the temperature and density of the gas, as well is the initial magnetic field, the final magnetic field and the rate at which the magnetic field is varied across a Feshbach resonance. We have seen that the initial state of the gas has a large impact on the molecule production. Specifically high densities and low temperatures are needed to allow for a broad range of initial magnetic fields from which to produce molecules. Motivated by the results of the BCS chapter we have treated the $m_1 = 0$ and the $|m_1| = 1$ dynamics separately and shown that there is little difference between molecule production in the two components. We have used the equations for the lowest order partial wave components, but shown that adding higher order components does not significantly change the molecule production. Using the mean-field dynamical equations it is possible to convert near to 100 % of atoms into molecules using linear sweeps of the magnetic field. It is also possible to produce a significant number of molecules by projecting the initial state of the gas onto the final bound state.

We have studied the dynamics of the molecule production after an infinitely fast sweep of the magnetic field and shown that there is little variation in the molecule density following the magnetic field variation. Specifically we have observed minute oscillations of the molecule density with very high damping, more so than in the *s*-wave case [129]. In contrast to the *s*-wave case we have found that the amplitude of the oscillations increases as the initial magnetic field moves away from the resonance and the final magnetic field position. The reason for this is not clear as the problem is highly non-linear and may be the subject of a future study. What can be inferred from this is that it may not be possible to observe atom-molecule coherence in these gases.

In certain cases we have compared our results with those of the Landau-Zener approach for two atoms in a tight harmonic trap for which analytic results can be derived. We have seen that there is some behavioural similarity between the results of the Landau-Zener calculation and the the many-body calculation in relation to varying ramp speed. This highlights an important restriction of both

approaches; namely that the Landau-Zener sweep begins and ends infinitely far from the resonance, whereas the many-body calculation must start within a range of magnetic field for which pairing already exists. A more numerically demanding approach to the two-body problem could begin the sweep within a finite magnetic field range. We have seen that the molecule production efficiencies in the many-body and Landau-Zener approach have different dependencies on the density. By solving the Landau-Zener problem in a spherical well we have found that the Landau-Zener parameter has the same dependence on the density as it does in a harmonic trap. This demonstrates some difference in the results of the two-body and many-body approaches.

The dynamical mean-field equations used in this thesis provide a lowest order approximation to the many-body dynamics of a Fermi gas at low temperature. These can act as a test on higher-order approximations and determine to what extent these higher-orders have an effect on the dynamics. In particular, a non-Markovian Boltzmann equation, that includes contributions from higher-order correlation functions, could be used to study molecule formation from unpaired atoms; such an approach has already been implemented in Bose gases [24]. A natural extension of this thesis would be to apply the quantum Boltzmann equation to fermions with a view to study *p*-wave molecule formation. This would allow for a broader range of magnetic field variations and initial conditions from which to produce molecules. In particular, it would be possible to study the formation of *p*-wave Feshbach molecules using a resonantly oscillating magnetic field, similar to the experiments of Gaebler *et al*. [21] and Fuchs *et al*. [3]. A Boltzmann equation requires the evolution of higher order correlation functions and is significantly more computationally demanding than the mean-field approach of this thesis.

A direct comparison of our results to experimental data is not currently possible, since when deriving our model we excluded certain processes. In particular, we have neglected three-body processes and the molecule lifetime in our model, which may be important in determining *p*-wave molecule production efficiencies. Experiments on *p*-wave molecules have failed to produce more than a 25 % yield of molecules, despite the ramp speeds being less than 1 G/ms [20, 22, 23]. It should be noted that these experiments were performed at temperatures on the

order of μK and it was not possible to extract density profiles of the gas. It has been suggested that for the *p*-wave resonances studied that the formation of a superfluid state may not be possible in 3D [163], due to high decay rates. Moreover, experiments have shown that *p*-wave molecules have a short lifetime [21] making it difficult to study the properties of the molecules after their formation. Inada *et al*. [22] have shown that the ratio of inelastic to elastic collisions in the systems studied may preclude cooling to quantum degeneracy via conventional techniques. This case shares similarities with the difficulties encountered in Bose condensing caesium. Initially it was not possible to cool caesium to quantum degeneracy due to a large Feshbach resonance close to 0 G [164]. This caused the three-body loss rate coefficient to be large in this region resulting in heating of the gas and atom loss. Three body loss mechanisms can be very complex and can depend on the Zeeman structure of a system, exhibiting maxima and minima that vary by several orders of magnitude. A knowledge of the three body loss mechanisms in caesium eventually led to the realisation of Bose-Einstein condensation of ^{133}Cs [164]. By analogy, it could be hoped that further investigation may lead to the development of new cooling techniques allowing quantum degeneracy to be realised in these systems. Furthermore, there may be other spin configurations or atomic species in which these challenges are easier to overcome.

The separable potential that we have derived could be adapted for use with other atomic species, should *p*-wave Feshbach resonances be identified and measured in them. In fact, this potential was derived only to model the behaviour of the system close to threshold and could therefore be used to study other scattering processes in this regime, for example modelling three-body scattering. The model of the BCS state could be used to study other atomic species in the same regime and perhaps assess the feasibility of producing a resonant condensate in that system.

The methods given here may also be used to study molecule production in higher order partial waves, should such systems become available for study. In this case the interaction potential would have to be re-derived to account for the threshold behaviour. Higher order partial wave symmetry has already been observed in ultra cold gases [165] and is believed to play a role in unconventional superconductivity. The field of cold and ultracold atomic gases is expanding to an

extent that it would be difficult to predict every topic to which this thesis would be relevant but as stated in the introduction the inter disciplinary nature of research in this field is indicative of wide applications in the future.

Appendix A

Spherical well scattering solution

In this appendix we consider the scattering of two particles from a spherical well potential. This is an illustrative example that we can solve analytically to find the low energy scattering probability in both the *s*-wave and the *p*-wave. Consider a potential of the form

$$V(r) = \begin{cases} -V_0 & \text{for} \quad r < r_s \\ 0 & \text{for} \quad r > r_s, \end{cases} \tag{A.1}$$

where r is the radial coordinate in the centre of mass frame. Starting with the radial Schrödinger equation

$$\left[\frac{d^2}{dr^2} - \frac{\ell(\ell+1)}{r^2} - U(r) + k^2\right]\psi_{\ell k}(r) = 0, \tag{A.2}$$

where ℓ is the quantum number representing the magnitude of the relative angular momentum, k is the angular wave number and

$$U(r) \equiv \frac{2\mu V(r)}{\hbar^2} \tag{A.3}$$

is the reduced potential. The problem be separated into two regions; one for $r < r_s$ and one for $r > r_s$.

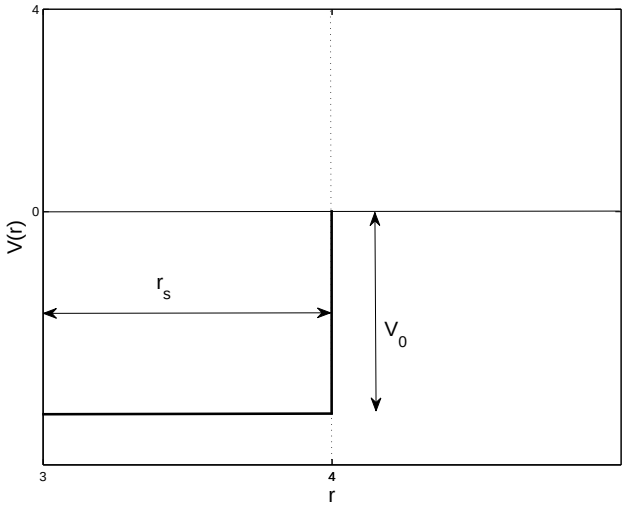

Figure A.1: Spherical well potential. a is the radius of the well and V_0 is the depth of the well

A.1 $r < r_s$

Inside the well the Schrödinger equation becomes

$$\left[\frac{d^2}{dr^2} - \frac{\ell(\ell+1)}{r^2} + 2\mu V_0 + k^2\right]\psi_{\ell k}(r) = 0. \tag{A.4}$$

By defining

$$K^2 = k^2 + 2\mu V_0, \tag{A.5}$$

the solution inside the well is the Ricatti-Bessel function [60, 116]

$$\psi^i_{\ell k}(r) = \hat{j}_\ell(Kr), \tag{A.6}$$

where the normalisation constant has been set to one. Detailed properties of Bessel functions can be found in Abramowitz and Stegun [166].

A.2 $r > r_s$

Outside of the well the potential is equal to zero so that the solution for positive energies will just be the free solution of the radial Schödinger equation

$$\left[\frac{d^2}{dr^2} - \frac{\ell(\ell+1)}{r^2} + k^2\right]\psi_{\ell k}(r) = 0, \tag{A.7}$$

which is the linear combination

$$\psi^o_{\ell k}(r) = B_\ell \hat{j}_\ell(kr) + C_\ell \hat{n}_\ell(kr), \tag{A.8}$$

where B_ℓ and C_ℓ are normalisation constants. For negative energies the wave function will be zero for $r > r_s$ leading to bound state solutions. For a finite well there will be a finite number of solutions that correspond to bound states.

A.3 Matching solutions

In order that the wave function is continuous the solutions and their derivatives must now be matched at $r = r_s$. Matching the wave functions gives

$$\hat{j}_\ell(Kr_s) = B_\ell \hat{j}_\ell(kr_s) + C_\ell \hat{n}_\ell(kr_s). \tag{A.9}$$

Matching the derivatives yields

$$K\hat{j}'_\ell(Kr_s) = kB_\ell \hat{j}'_\ell(kr_s) + kC_\ell \hat{n}'_\ell(kr_s), \tag{A.10}$$

where $\hat{j}'_\ell(z) = d\hat{j}_\ell(z)/dz$ and $\hat{n}'_\ell(z) = d\hat{n}_\ell(z)/dz$. The logarithmic derivative can then be matched to give the condition

$$\frac{K\hat{j}'_\ell(Kr_s)}{\hat{j}_\ell(Kr_s)} = \frac{k\hat{j}'_\ell(kr_s) + k\frac{C_\ell}{B_\ell}\hat{n}'_\ell(kr_s)}{\hat{j}_\ell(kr_s) + \frac{C_\ell}{B_\ell}\hat{n}_\ell(kr_s)}. \tag{A.11}$$

Given the asymptotic form of the full scattering radial wave function

$$\psi_{\ell k}(r) \to \lim_{r\to\infty} e^{i\delta_\ell(k)} \sin\left(kr - \frac{l\pi}{2} + \delta_\ell(k)\right), \tag{A.12}$$

where $\delta_\ell(k)$ is the partial wave phase shift, and the asymptotic form of the Riccati functions

$$\hat{j}_\ell(z) \to \lim_{z\to\infty} \sin\left(z - \frac{\ell\pi}{2}\right), \tag{A.13}$$

$$\hat{n}_\ell(z) \to \lim_{z\to\infty} -\cos\left(z - \frac{\ell\pi}{2}\right), \tag{A.14}$$

it is possible to write

$$\tan\delta_\ell(k) = -\frac{C_\ell}{B_\ell}. \tag{A.15}$$

This allows Eq. (A.11) to be solved for $\tan\delta_\ell$ giving

$$\tan\delta_\ell(k) = \frac{k\hat{j}'_\ell(kr_s)\hat{j}_\ell(Kr_s) - K\hat{j}_\ell(kr_s)\hat{j}'_\ell(Kr_s)}{k\hat{n}'_\ell(kr_s)\hat{j}_\ell(Kr_s) - K\hat{n}_\ell(kr_s)\hat{j}'_\ell(Kr_s)}. \tag{A.16}$$

The partial wave scattering lengths are found from the definition

$$a_\ell = \lim_{k\to 0} -\frac{\tan\delta_\ell(k)}{k^{2\ell+1}}. \tag{A.17}$$

.

A.4 *s*-wave scattering length

Using the definitions of the Riccati functions for $\ell = 0$ [116]

$$\hat{j}_0(z) = \sin(z), \tag{A.18}$$

$$\hat{j}'_0(z) = \cos(z), \tag{A.19}$$

$$\hat{n}_0(z) = -\cos(z), \tag{A.20}$$

$$\hat{n}'_0(z) = \sin(z). \tag{A.21}$$

We can then insert these into Eq. (A.16) to give

$$\tan\delta_0(k) = \frac{k\cos(kr_s)\sin(Kr_s) - K\sin(kr_s)cos(Kr_s)}{k\sin(kr_s)\sin(Kr_s) + K\cos(kr_s)\cos(Kr_s)}, \tag{A.22}$$

and dividing out the cosine factors

$$\tan\delta_0(k) = \frac{k\tan(Kr_s) - K\tan(kr_s)}{k\tan(kr_s)\tan(Kr_s) + K}. \tag{A.23}$$

Using the fact that at low values of k then $\tan(kr_s) \approx kr_s$ we can write

$$a_0 = r_s\left(1 - \frac{\tan(K_0r_s)}{K_0r_s}\right), \tag{A.24}$$

where $K_0 = \sqrt{2\mu V_0}$. It is interesting to note that at values of $K_0r_s = \pi$ the scattering volume is equal to the radius of the well. Fig. A.2 is a plot of the scattering length as a function of K_0r_s. The scattering length has singularities at values of $K_0r_s = \pi/2$ which are associated with the appearance of a bound state in the system, as discussed in chapter 2

A.5 *p*-wave scattering volume

We start with the asymptotic expression for the Riccati functions in the limit of small argument

$$\hat{j}_1(z) \to \frac{z^2}{3}, \tag{A.25}$$

$$\hat{j}_1'(z) \to \frac{2z}{3}, \tag{A.26}$$

$$\hat{n}_1(z) \to -\frac{1}{z}, \tag{A.27}$$

$$\hat{n}_1'(z) \to \frac{1}{z^2}. \tag{A.28}$$

Substituting these into Eq. (A.16) and replacing K with K_o gives

$$\frac{\tan\delta_1(k)}{k^3} = \frac{\frac{2}{3}r_s^3\hat{j}_1(K_0r_s) - K_0\hat{j}_1'(K_0r_s)\frac{r_s^4}{3}}{\hat{j}_1(K_0r_s) + r_sK\hat{j}_1'(K_0r_s)}. \tag{A.29}$$

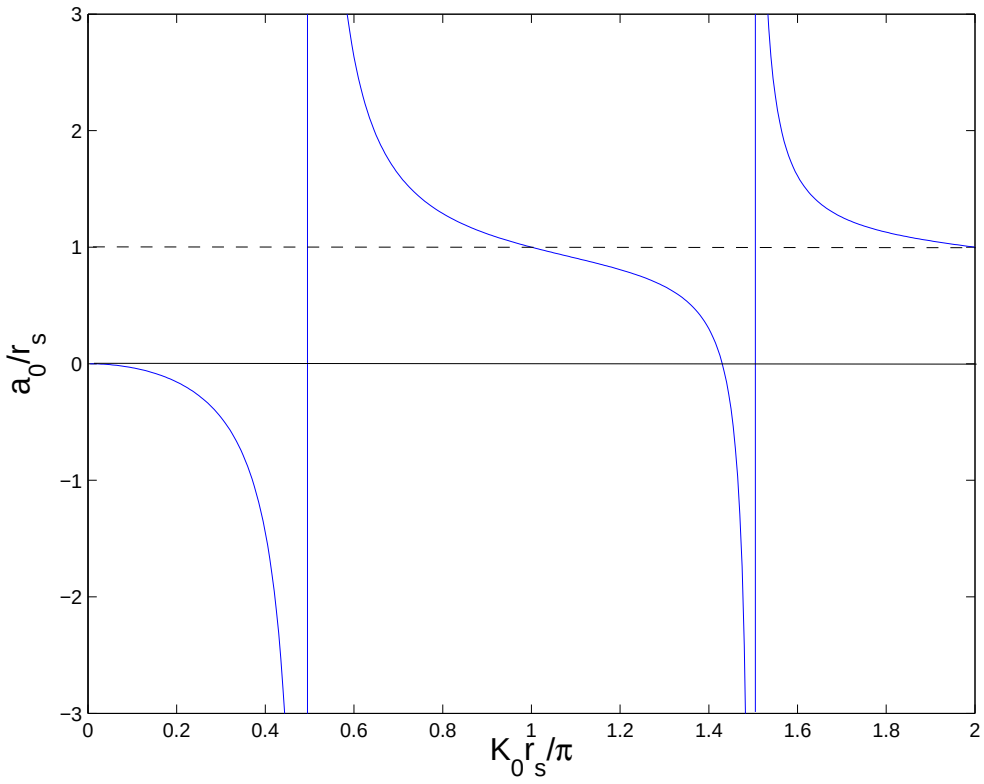

Figure A.2: Plot of a_1/r_s as a function of $K_0 r_s/\pi$. For fixed r_s we can interpret the increasing argument with an increasing well depth. For $K_0 r_s = \pi$ the scattering length is equal to the radius of the well. For values of $K_0 r_s = \pi/2$ there is a singularity in the scattering length which is associated with a bound state entering the system.

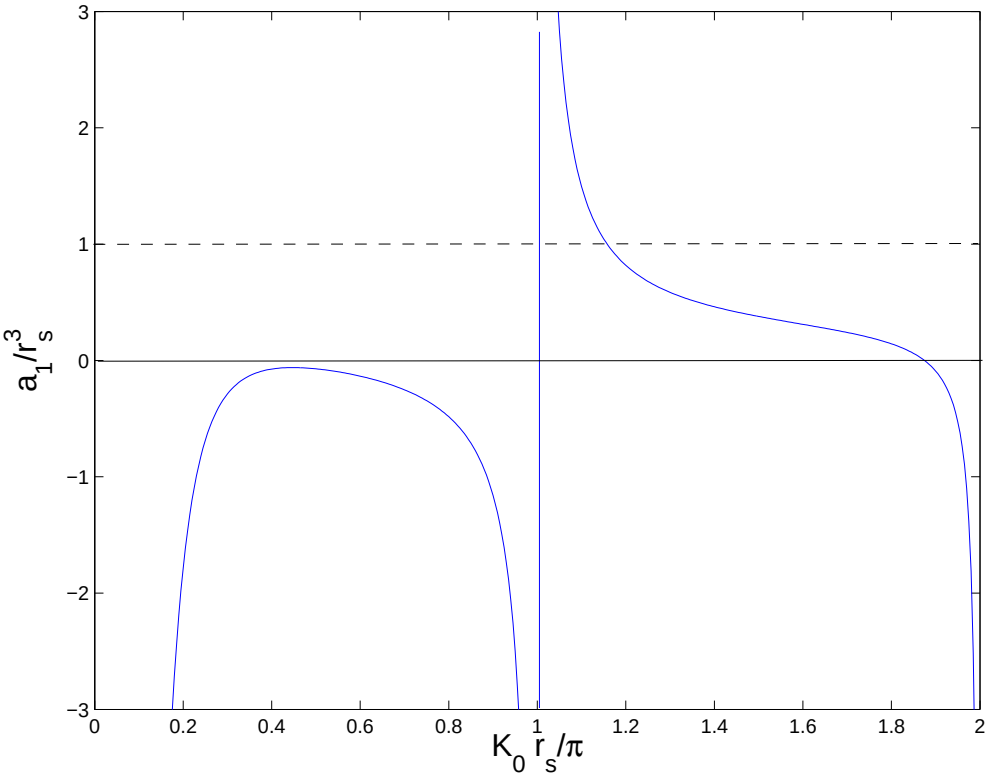

Figure A.3: Plot of a_1/r_s^3 as a function of $K_0 r_s/\pi$. The scattering volume has a singularity at $K_0 r_s = \pi$ and at integer multiples of π.

Given that for $\ell = 1$ the Ricatti-Bessell function is given by [60]

$$\hat{j}_1(z) = \frac{1}{z}\sin(z) - \cos(z), \tag{A.30}$$

and

$$\hat{j}_1'(z) = \frac{1}{z}\cos(z) + \sin(z) - \frac{1}{z^2}\sin(z), \tag{A.31}$$

the p-wave scattering volume can be written as

$$a_1 = \frac{r_s^3\cos(K_0 r_s) + \frac{K_0 r_s^4}{3}\sin(K r_s) - \frac{r_s^2}{K_0}}{r_s K_0 \sin(K_0 r_s)}. \tag{A.32}$$

Fig. A.3 is a plot of the p-wave scattering volume as a function of $K_0 r_s$. The scattering volume has a singularity for values of $K_0 r_s = \pi$, associated with the

appearance of a bound state in the system as discussed in Chapter 2. Interestingly this a $\pi/2$ phase shift from the values at which the s-wave bound state appears. The values for which $a_1 = r_s^3$ can only be found numerically.

A.6 Plotting the s-wave radial function at zero energy

At zero energy the wave functions become functions of position only. For the $\ell = 0$ wave function we can match the solution at the edge of the well

$$\sin(K_o r_s) = B_0 r_s - C_0. \tag{A.33}$$

We also match the derivative

$$K_0 \cos(K_0 r_s) = B_0. \tag{A.34}$$

By combining these two equations we get

$$\sin(K_o r_s) = K_0 r_s \cos(K_0 r_s) - C_0. \tag{A.35}$$

This allows the zero energy wave function in the outer region to be written as

$$\psi_{00}^o(r) = K_0 \cos(K_0 r_s) r + \sin(K_0 r_s) - K_0 r_s \cos(K_0 r_s). \tag{A.36}$$

By solving this equation for the point where $\psi_{00}^o(r) = 0$ it can be seen that the value of the radius at this point coincides with the value of the scattering length given in Eq. (A.24).

A.7 Plotting the *p*-wave radial function at zero energy

Matching the solutions with the low momentum asymptotic conditions gives the relations

$$\frac{1}{K_0 r_s}\sin(K_0 r_s) - \cos(K_0 r_s) = B_1\frac{r_s^2}{3} - C_1\frac{1}{r_s}, \tag{A.37}$$

and

$$\frac{\cos(K_0 r_s)}{r_s} + K_0\sin(K_0 r_s) - \frac{\sin(K_0 r_s)}{K_0 r_s^2} = B_1\frac{2r_s}{3} + C_1\frac{1}{r_s^2}. \tag{A.38}$$

These can be solved to give the constants

$$B_1 = \frac{K_0}{r_s}\sin(K_0 r_s), \tag{A.39}$$

and

$$C_1 = r_s\cos(K_0 r_s) + \frac{r_s^2 K_0}{3}\sin(K_0 r_s) - \frac{1}{K_0}\sin(K_0 r_s). \tag{A.40}$$

The *p*-wave radial function in the outer region can be written as

$$\psi_{10}^o(r) = \frac{K_0}{3r_s}\sin(K_0 r_s)r^2 - \left(r_s\cos(K_0 r_s) + \frac{r_s^2 K_0}{3}\sin(K_0 r_s) - \frac{1}{K_0}\sin(K_0 r_s)\right)\frac{1}{r}. \tag{A.41}$$

Solving this equation for r^3 at the point where the function crosses the radial axis, r_1, we can see that,

$$r_1^3 = 3a_1 \tag{A.42}$$

on comparison with Eq. (A.32). Fig. 2.1 shows a plot of the *s*-wave and *p*-wave radial function and the positions of the *s*-wave scattering length as well as the position of the cube root of the *p*-wave scattering volume.

Appendix B

Resonance and threshold parameters

In this section we summarise the resonance parameters used to model both the *s*-wave and *p*-wave Feshbach resonances. For the *s*-wave resonances we quote values previously obtained in other studies. The parameters for modelling the two-body interaction close to a *p*-wave resonance are calculated from the experimental data given in Gaebler *et al*. [21] and Ticknor *et al*. [2] for ^{40}K and Fuchs *et al*. [3] for ^{6}Li. In the vicinity of a resonance the scattering length is given by Eq. (2.32)

$$a_\ell(B) = a_\ell^{\mathrm{bg}}\left(1 - \frac{\Delta B_\ell}{B - B_{\ell 0}}\right). \tag{B.1}$$

The inverse of this can be expanded in a Taylor series about $B - B_{\ell 0} = 0$,

$$\frac{1}{a(B)} = -\frac{B - B_0}{a_{\mathrm{bg}}\Delta B} - \frac{(B - B_0)^2}{a_{\mathrm{bg}}(\Delta B)^2} + O(B - B_0)^3, \tag{B.2}$$

where the ℓ dependence has been dropped for brevity. Provided the parameter $|\Delta B a_{\mathrm{bg}}| >> 1$ this can be written as a power series in B to second order,

$$\frac{1}{a(B)} = -\frac{\Delta B + B_0^2}{a_{\mathrm{bg}}(\Delta B)^2} + \frac{2B_0 - \Delta B}{a_{\mathrm{bg}}(\Delta B)^2}B - \frac{1}{a_{\mathrm{bg}}(\Delta B)^2}B^2. \tag{B.3}$$

This equation can be directly compared with Eq. (8) in Ticknor *et al*. [2] to give the parameters for the *p*-wave resonance in ^{40}K. The results of this matching are given in Table B.2. These can be checked by numerically solving the Schrödinger equation and matching to the long-range form of the wave function. To do this a C_6/r^6 potential was used where the C_6 parameter is given in Table B.1. The *s*-wave binding energy was fixed by the value given in the same table. The scattering length for the *s*-wave is given by

$$a_0 = 174.82 \text{ a.u.}$$

and for the scattering volume in the *p*-wave

$$a_1 = -1126660 \text{ a.u.}$$

Another check on these values is the use of Eq. (25) of Gao [4] that relates the *s*-wave length and *p*-wave scattering volume. The result of each angular momentum projection is given in Table. B.3. Having established the resonance parameters it is now necessary to relate these to the parameters of the separable potential. The low energy expansion of the *p*-wave binding energy is given by

$$E_{-1} \approx -\frac{\sqrt{\pi}\sigma\hbar^2}{2\mu a_1}, \tag{B.4}$$

where the m_1 dependence has been dropped. The values of the magnetic moments of the ^{40}K molecules was measured in Gaebler *et al*. [21] and are reproduced in Table. B.2. Using the parametrisation of the scattering length Eq. (2.32) an expression for the magnetic moment close to threshold can be obtained

$$\frac{\partial E}{\partial B} \approx \frac{\sigma\sqrt{\pi}\hbar^2}{2\mu\Delta B a_{\text{bg}}}, \tag{B.5}$$

and rearranging this gives

$$\sigma \approx \frac{2\mu\Delta B}{\sqrt{\pi}\hbar^2}\frac{\partial E}{\partial B}a_{\text{bg}}. \tag{B.6}$$

This same procedure can be used to fix the parameter σ in ^{6}Li. In this case the magnetic moment was measured in Fuchs *et al*. [3] and is reproduced in Ta-

ble. B.4. As far as we are aware a similar formula for ^{6}Li to Eq. (8) in Ticknor *et al*.. [2] does not exist. The width, ΔB, was therefore calculated [167] and is reproduced in Table. B.4.

Table B.1: Bound state energies E_{-1} associated with the highest excited vibrational states, C_6 coefficients, and *s*-wave scattering lengths for ^{40}K and ^{6}Li. The values of E_{-1} and a_0 quoted for $^6Li_2$ refer to the lithium triplet potential.

Species	C_6 (a.u.)	a_0^{bg} (a_{Bohr})	$\lvert E_{-1}\rvert/h$ (MHz)
^{40}K	3897 [117]	174 [118]	8.9 [119]
^{6}Li	1393.39 [120]	-2160 [121]	2.4×10^4 [121]

Table B.2: Calculated *p*-wave resonance parameters for ^{40}K. All values are based on the experimental data found in Ticknor *et al*. [2]

Projection	B_{10} (G)	a_1^{bg} (a_{Bohr}^3)	ΔB_1 (G)	$\frac{\partial E_b}{\partial B}$ (kHz/G)
$m_1 = 0$	198.85	-1049850	-21.95	188±2
$\lvert m_1\rvert = 1$	198.373	-905505	-24.99	193±2

Table B.3: Values of the *s*-wave scattering length calculated using Eq. (25) of Gao [4]. The inputs are the scattering volumes given in Table. B.2. The values given are close to the literature value of 174 a.u. given in Table. B.1

$\lvert m_\ell\rvert$	a_0 ($a.u.$)
0	182.349
1	203.526

Table B.4: Calculated *p*-wave resonance parameters for ^{6}Li taken from Fuchs *et al*. [3]. It should be noted that the dipolar splitting (DPS) is on the order of mG for ^{6}Li. This is much lower than that observed in ^{40}K. In the experiments this splitting was not resolvable. The data is provided for atoms prepared in two hyperfine states $|F, m_F\rangle$. In this case $|1\rangle = |1/2, 1/2\rangle$ and $|2\rangle = |1/2, -1/2\rangle$

Channels	B_0 (G)	DPS (mG)	$\frac{\partial E_b}{\partial B}$ (μK/G)	a_1^{bg} (a_{Bohr}^3)	ΔB_1 (G)
$\|1\rangle$-$\|1\rangle$	159	10	113	-42360	-40.51
$\|1\rangle$-$\|2\rangle$	185	4	111	-45290	-39.54
$\|2\rangle$-$\|2\rangle$	215	12	118	-42800	-25.54

Appendix C

The scattering cross-section

As well as finding the binding energy of the p-wave molecule we can use the separable potential of Chapter 2 to study the low energy scattering cross-section and compare this to the result of a coupled channels calculation. The T-matrix for a partial wave component is given by

$$T_{1m_1}(z) = \frac{|\chi_{1m_1}\rangle\xi_{1m_1}\langle\chi_{1m_1}|}{1-\xi_{1m_1}\langle\chi_{1m_1}|G_0(z)|\chi_{1m_1}\rangle}. \tag{C.1}$$

This is related to the partial wave scattering amplitude through

$$f_{\ell m_\ell}(p) = -\frac{\pi m\hbar}{2}\langle p\ell m_\ell|T_{\ell m_\ell}\left(\frac{p^2}{2\mu}+i0\right)|p\ell m_\ell\rangle, \tag{C.2}$$

where it should be remembered that m is the single particle mass and m_ℓ denotes the projection of the relative angular momentum vector onto the z-axis. We therefore need to calculate the quantity

$$\langle p\ell m_\ell|T_{\ell m_\ell}\left(\frac{p^2}{2\mu}+i0\right)|p\ell m_\ell\rangle = \frac{\langle p\ell m_\ell|\chi_{1m_1}\rangle\xi_{1m_1}\langle\chi_{1m_1}|p\ell m_\ell\rangle}{1-\xi_{1m_1}\langle\chi_{1m_1}|G_0(z)|\chi_{1m_1}\rangle}. \tag{C.3}$$

Remembering that $x = m\xi_{m_1}/(4\pi\hbar^2\sigma_{m_1})$ and

$$\langle p\ell m_\ell|\chi_{1m_1}\rangle = \frac{p\sigma_{m_1}}{\pi\hbar^{5/2}}e^{-p^2\sigma_{m_1}^2/2\hbar^2} \tag{C.4}$$

so,

$$\begin{aligned}1-\xi_{1m_1}\langle\chi_{1m_1}|G_0(z)|\chi_{1m_1}\rangle =& 1-\xi_m\frac{\sigma_m^2}{\pi^2\hbar^{5/2}}\int q^4dq\frac{e^{-q^2\sigma_m^2/\hbar^2}}{E-\frac{q^2}{m}+i0} \\ =& 1-\xi_m\frac{\sigma_m^2}{\pi^2\hbar^5}\int q^4dqe^{-q^2\sigma_m^2/\hbar^2}\left[-i\pi\delta\left(E-\frac{q^2}{m}\right)+\mathcal{P}\frac{1}{E-\frac{q^2}{m}}\right] \\ =& 1+i\xi_m\frac{\sigma_m^2}{2\pi\hbar^5}m^{5/2}E^{3/2}e^{-mE\sigma_m^2/\hbar^2}-\frac{\xi_m\sigma_m^2}{\pi^2\hbar^5}\mathcal{P}\int q^4dq\frac{e^{-q^2\sigma_m^2/\hbar^2}}{E-\frac{q^2}{m}} \\ =& 1+i\xi_m\frac{\sigma_m^2}{2\pi\hbar^5}m^{5/2}E^{3/2}e^{-mE\sigma_m^2/\hbar^2}+\frac{\xi_m m}{4\pi^{3/2}\sigma_m\hbar^2}+\frac{\xi_m\sigma_m m^2}{2\pi^{3/2}\hbar^4}E\end{aligned} \tag{C.5}$$

where a low energy expansion has been used in the last line and $\mathcal{P}$ represents the principal part. Writing $E=\frac{p^2}{m}$

$$f_{1m}(p)=\frac{-mp^2\sigma_m^2\xi_m}{2\pi\hbar^4}\frac{e^{-p^2\sigma_m^2/\hbar^2}}{1+i\xi_m\frac{\sigma_m^2}{2\pi\hbar^5}mp^3e^{-p^2\sigma_m^2/\hbar^2}+\frac{\xi_m m}{4\pi^{3/2}\sigma_m\hbar^2}+\frac{\xi_m\sigma_m m}{2\pi^{3/2}\hbar^4}p^2} \tag{C.6}$$

Using the low energy effective range expansion

$$\frac{p^{2\ell}}{f_{\ell m}(p)\hbar^{2\ell}}=-\frac{1}{a_\ell}+\frac{r_\ell p^2}{2\hbar^2}-\frac{ip^{2\ell+1}}{\hbar^{2\ell+1}}, \tag{C.7}$$

in the limit $p\to 0$ we find that

$$a_1=2\sigma_m^3\left(\frac{1}{\frac{1}{x_m}+\frac{1}{\pi^{1/2}}}\right) \tag{C.8}$$

$$r_1=-\frac{2}{\pi^{1/2}\sigma_m} \tag{C.9}$$

By looking for the pole in the scattering amplitude (and hence the T-matrix) we can show that in the limit $p\to 0$

$$p^2=-\frac{\sqrt{\pi}\sigma_m\hbar^2}{a_1} \tag{C.10}$$

which is the same expression that is obtained for the low energy expansion of the bound state energy. This shows that the resonance energy is continuous going

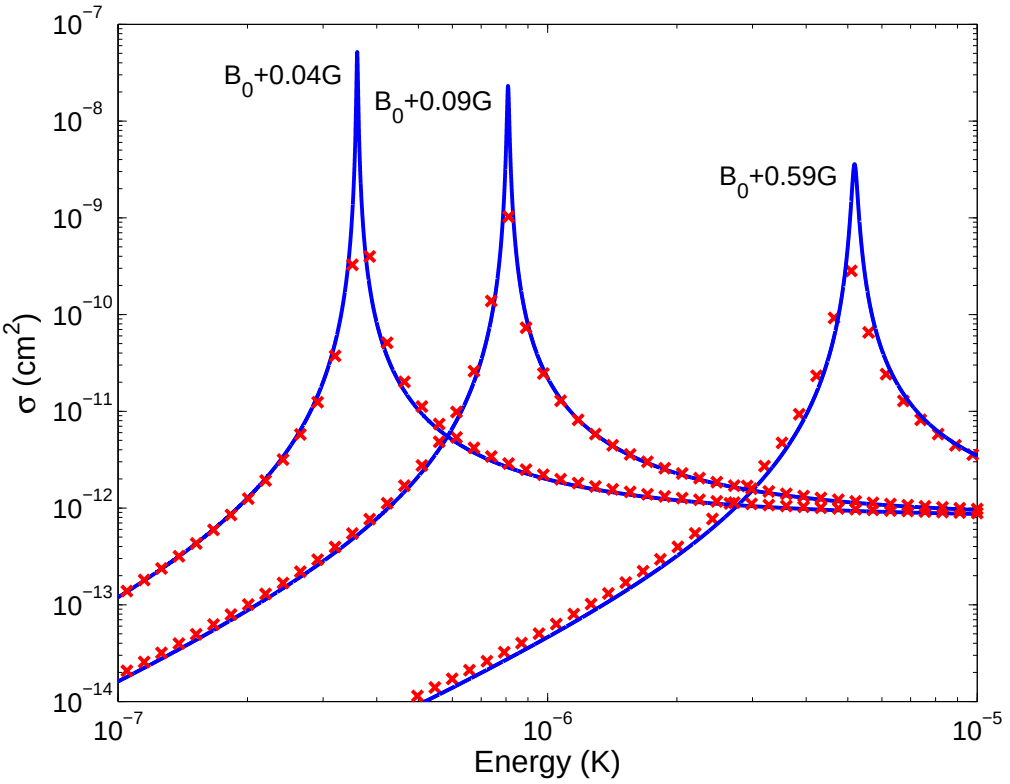

Figure C.1: *p*-wave elastic scattering cross section for ^{40}K colliding in the $|9/2, -7/2\rangle$ channel as a function of collision energy. The solid blue line corresponds to the pseudo potential model. The red crosses are from a coupled-channel calculation [168].

from positive to negative detuning. The partial wave cross-section is given by

$$\sigma_\ell = 4\pi\,(2\ell+1)\,|f_\ell(p)|^2 \tag{C.11}$$

A comparison of the result obtained using the separable potential model presented in this thesis and a coupled channels calculation using Born-Oppenheimer potentials is given in Fig. C.1 [168] for a range of magnetic fields above the resonance.

Appendix D

BCS Solution

D.1 The Green's function and the pairing function

In the pairing approximation the many-body Hamiltonian can be written in second quantisation as

$$H = \sum_{ij}\langle i|T|j\rangle a_i^\dagger a_j + \frac{1}{2}\sum_{ijkl}\langle ij|V|kl\rangle a_i^\dagger a_j^\dagger\langle a_l a_k\rangle + \frac{1}{2}\sum_{ijkl}\langle ij|V|kl\rangle\langle a_i^\dagger a_j^\dagger\rangle a_l a_k. \quad \text{(D.1)}$$

Here, T and V are the single particle kinetic energy operator and the two particle interaction operator, respectively. The brackets $\langle ...\rangle$ represent averages over the thermodynamic state where the particle number is not conserved. In the finite-temperature formalism the equations of motion for the single-particle creation and annihilation operators in the pairing approximation are given by

$$\hbar\frac{\partial}{\partial\tau}a_r^\dagger(\tau) = \sum_i\langle i|T|r\rangle a_i^\dagger(\tau) - \sum_i\langle\Phi|V|ri\rangle a_i(\tau), \quad \text{(D.2)}$$

$$\hbar\frac{\partial}{\partial\tau}a_r(\tau) = -\sum_i\langle r|T|i\rangle a_i(\tau) + \sum_i\langle ri|V|\Phi\rangle a_i^\dagger(\tau), \quad \text{(D.3)}$$

with the useful definition

$$|\Phi\rangle = \sum_{ij}\langle a_i a_j\rangle|ij\rangle. \quad \text{(D.4)}$$

Here τ is imaginary time as explained in the literature [127]. Two other facts have also been used that correspond to systems of fermions:

$$|ij\rangle = -|ji\rangle, \tag{D.5}$$

$$\langle a_i a_j\rangle = -\langle a_j a_i\rangle. \tag{D.6}$$

The single-particle Green's function is defined as

$$g_{rs}(\tau,\tau') = -\langle T_\tau[a_r(\tau)a_s^\dagger(\tau')]\rangle. \tag{D.7}$$

Here T_τ is the imaginary time ordering operator that places the lowest value of τ to the right. We can find the equation of motion for this function to be

$$\hbar\frac{\partial}{\partial\tau}g_{rs}(\tau,\tau') = -\hbar\frac{\partial}{\partial\tau}\langle T_\tau[a_r(\tau)a_s^\dagger(\tau')]\rangle, \tag{D.8}$$

$$\hbar\frac{\partial}{\partial\tau}g_{rs}(\tau,\tau') = -\hbar\delta(\tau-\tau')\delta_{rs} - \hbar\langle T_\tau[\frac{\partial}{\partial\tau}a_r(\tau)a_s^\dagger(\tau')]\rangle, \tag{D.9}$$

$$\hbar\frac{\partial}{\partial\tau}g_{rs}(\tau,\tau') = -\hbar\delta(\tau-\tau')\delta_{rs}+\langle T_\tau[\sum_i\langle r|T|i\rangle a_i(\tau)a_s^\dagger(\tau')-\sum_i\langle ri|V|\Phi\rangle a_i^\dagger(\tau)a_s^\dagger(\tau')]\rangle. \tag{D.10}$$

We define a new function that represents pairing in the gas

$$F_{rs}^\dagger(\tau,\tau') = -\langle T_\tau[a_r^\dagger(\tau)a_s^\dagger(\tau')]\rangle. \tag{D.11}$$

This allows us to write the equation of motion as

$$\hbar\frac{\partial}{\partial\tau}g_{rs}(\tau,\tau') = -\hbar\delta(\tau-\tau')\delta_{rs} - \sum_i\langle r|T|i\rangle g_{is}(\tau,\tau') + \sum_i\langle ri|V|\Phi\rangle F_{is}^\dagger(\tau,\tau'). \tag{D.12}$$

The equation for the pair function can be written as

$$\hbar\frac{\partial}{\partial\tau}F_{rs}^\dagger(\tau,\tau') = -\langle T_\tau[\sum_i\langle i|T|r\rangle a_i^\dagger(\tau)a_s^\dagger(\tau') - \sum_i\langle\Phi|V|ri\rangle a_i(\tau)a_s^\dagger(\tau')]\rangle. \tag{D.13}$$

Using the definition of the Green's function

$$\hbar\frac{\partial}{\partial\tau}F^{\dagger}_{rs}(\tau,\tau') = \sum_i \langle i|T|r\rangle F^{\dagger}_{is}(\tau,\tau') - \sum_i \langle\Phi|V|ri\rangle g_{is}(\tau,\tau'). \tag{D.14}$$

Now putting the equation in the momentum representation and setting the spin indices on the LHS of the equation we define

$$|r\rangle = |\mathbf{p}_1\alpha\rangle, \tag{D.15}$$

$$|s\rangle = |\mathbf{p}_2\beta\rangle, \tag{D.16}$$

$$|i\rangle = |\mathbf{q}\gamma\rangle. \tag{D.17}$$

Equation (D.14) can now be written as

$$\begin{aligned}\hbar\frac{\partial}{\partial\tau}F^{\dagger}_{\alpha\beta}(\mathbf{p}_1,\mathbf{p}_2,\tau,\tau') = &\sum_{\mathbf{q}\gamma}\langle\mathbf{q}\gamma|T|\mathbf{p}_1\alpha\rangle F^{\dagger}_{\gamma\beta}(\mathbf{q},\mathbf{p}_2,\tau,\tau') \\ &- \sum_{\mathbf{q}\gamma}\langle\Phi|V|\mathbf{p}_1\mathbf{q}\alpha\gamma\rangle g_{\gamma\beta}(\mathbf{q},\mathbf{p}_2,\tau,\tau').\end{aligned} \tag{D.18}$$

Using the properties of a translationally invariant system we write

$$\begin{aligned}\hbar\delta(\mathbf{p}_1+\mathbf{p}_2)\frac{\partial}{\partial\tau}(2\pi\hbar)^{3/2}F^{\dagger}_{\alpha\beta}(\mathbf{p}_1,\tau,\tau') = &\\ \sum_{\mathbf{q}\gamma} E_{p_1}\delta(\mathbf{q}-\mathbf{p}_1)\delta(\mathbf{q}+\mathbf{p}_2)\delta_{\gamma\alpha}(2\pi\hbar)^{3/2}F^{\dagger}_{\gamma\beta}(\mathbf{q},\tau,\tau') &\\ - \sum_{\mathbf{q}\gamma}\langle\Phi|V|\frac{\mathbf{p_1}-\mathbf{q}}{2}\alpha\gamma\rangle\delta(\mathbf{q}+\mathbf{p}_1)\delta(\mathbf{q}-\mathbf{p}_2)\delta_{\beta\gamma}(2\pi\hbar)^{3/2}g_{\gamma\beta}(\mathbf{q},\tau,\tau').&\end{aligned} \tag{D.19}$$

The delta functions come from functions expressing pairs that have zero momentum and also from the single particle Green's function expressing translational invariance. The factors of $(2\pi\hbar)^{3/2}$ come from the normalisation of the pair and Green's function. Evaluating the summations using the delta functions and divid-

ing out the common delta function gives

$$\hbar\frac{\partial}{\partial\tau}F^{\dagger}_{\alpha\beta}(\mathbf{p},\tau,\tau') = E_p F^{\dagger}_{\alpha\beta}(\mathbf{p},\tau,\tau') - \sum_{\gamma}\langle\Phi|V|\mathbf{p}\alpha\gamma\rangle g_{\gamma\beta}(\mathbf{p},\tau,\tau'). \tag{D.20}$$

We have used the fact that $g_{\gamma\beta}(\mathbf{p},\tau,\tau') = g_{\gamma\beta}(-\mathbf{p},\tau,\tau')$. The equation for the Green's function can be written using a similar representation

$$\begin{aligned}\hbar\frac{\partial}{\partial\tau}g_{\alpha\beta}(\mathbf{p}_1,\mathbf{p}_2,\tau,\tau') = &-\hbar\delta(\tau-\tau')\delta(\mathbf{p}_1-\mathbf{p}_2)\delta_{\alpha\beta}\\ &-\sum_{\mathbf{q}\gamma}\langle\mathbf{p}_1\alpha|T|\mathbf{q}\gamma\rangle g_{\gamma\beta}(\mathbf{q},\mathbf{p}_2,\tau,\tau')\\ &+\sum_{\mathbf{q}\gamma}\langle\mathbf{p}_1\mathbf{q}\alpha\gamma|V|\Phi\rangle F^{\dagger}_{\gamma\beta}(\mathbf{q},\mathbf{p}_2,\tau,\tau').\end{aligned} \tag{D.21}$$

We again use the properties of the homogeneous system to factor out the delta functions

$$\begin{aligned}\hbar\delta(\mathbf{p}_1-\mathbf{p}_2)\frac{\partial}{\partial\tau}g_{\alpha\beta}(\mathbf{p}_1,\tau,\tau') = &-\hbar(2\pi\hbar)^{-3/2}\delta(\tau-\tau')\delta(\mathbf{p}_1-\mathbf{p}_2)\delta_{\alpha\beta}\\ &-\sum_{\mathbf{q}\gamma}E_p\delta(\mathbf{p}_1-\mathbf{q})\delta_{\alpha\gamma}\delta(\mathbf{q}-\mathbf{p}_2)g_{\gamma\beta}(\mathbf{q},\tau,\tau')\\ &+\sum_{\mathbf{q}\gamma}\langle\frac{\mathbf{p}_1-\mathbf{q}}{2}\alpha\gamma|V|\Phi\rangle\delta(\mathbf{q}+\mathbf{p}_2)\delta(\mathbf{p}_1+\mathbf{q})F^{\dagger}_{\gamma\beta}(\mathbf{q},\tau,\tau').\end{aligned} \tag{D.22}$$

We evaluate the summations and divide out the common delta function to give

$$\begin{aligned}\hbar\frac{\partial}{\partial\tau}g_{\alpha\beta}(\mathbf{p},\tau,\tau') = &-\hbar(2\pi\hbar)^{-3/2}\delta(\tau-\tau') - E_p g_{\alpha\beta}(\mathbf{p},\tau,\tau')\\ &+\sum_{\gamma}\langle\mathbf{p}\alpha\gamma|V|\Phi\rangle F^{\dagger}_{\gamma\beta}(-\mathbf{p},\tau,\tau').\end{aligned} \tag{D.23}$$

We introduce the notation

$$\Delta_{\alpha\beta}(\mathbf{p}) = \langle\mathbf{p}\alpha\beta|V|\Phi\rangle. \tag{D.24}$$

This quantity is commonly referred to as the gap function. We now write Eq. (D.23) as

$$\hbar\frac{\partial}{\partial\tau}g_{\alpha\beta}(\mathbf{p},\tau,\tau') = -\hbar(2\pi\hbar)^{-3/2}\delta(\tau-\tau') - E_p g_{\alpha\beta}(\mathbf{p},\tau,\tau') - \sum_\gamma \Delta_{\alpha\gamma}(\mathbf{p})F^\dagger_{\gamma\beta}(\mathbf{p},\tau,\tau'), \tag{D.25}$$

and Eq. (D.20) as

$$\hbar\frac{\partial}{\partial\tau}F^\dagger_{\alpha\beta}(\mathbf{p},\tau,\tau') = E_p F^\dagger_{\alpha\beta}(\mathbf{p},\tau,\tau') - \sum_\gamma \Delta^\star_{\alpha\gamma}(\mathbf{p})g_{\gamma\beta}(\mathbf{p},\tau,\tau'). \tag{D.26}$$

We define the Fourier representation to be

$$\begin{aligned} g_{\alpha\beta}(\mathbf{p},\tau,\tau') &= \frac{1}{\beta\hbar}\sum_n e^{-i\omega_n(\tau-\tau')}g_{\alpha\beta}(\mathbf{p},\omega_n) \\ F^\dagger_{\alpha\beta}(\mathbf{p},\tau,\tau') &= \frac{1}{\beta\hbar}\sum_n e^{-i\omega_n(\tau-\tau')}F^\dagger_{\alpha\beta}(\mathbf{p},\omega_n) \end{aligned} \tag{D.27}$$

where $\omega_n = (2n+1)\pi/\hbar\beta$ provides the correct statistics for fermions [127]. The equations can be written as algebraic expressions

$$-i\hbar\omega_n g_{\alpha\beta}(\mathbf{p},\omega_n) = -\hbar(2\pi\hbar)^{-3/2} - E_p g_{\alpha\beta}(\mathbf{p},\omega_n) - \sum_\gamma \Delta_{\alpha\gamma}(\mathbf{p})F^\dagger_{\gamma\beta}(\mathbf{p},\omega_n), \tag{D.28}$$

$$-i\hbar\omega_n F^\dagger_{\alpha\beta}(\mathbf{p},\omega_n) = E_p F^\dagger_{\alpha\beta}(\mathbf{p},\omega_n) - \sum_\gamma \Delta^\star_{\gamma\alpha}(\mathbf{p})g_{\gamma\beta}(-\mathbf{p},\omega_n). \tag{D.29}$$

These are the BCS equations and can be solved for the Green's function and the function we introduced to represent pairing

$$g(\mathbf{p},\omega_n) = \frac{-\hbar(i\hbar\omega_n + E_p)}{(2\pi\hbar)^{3/2}\left(\hbar^2\omega_n^2 + E_p^2 + |\Delta(\mathbf{p})|^2\right)}, \tag{D.30}$$

$$F^\dagger(\mathbf{p},\omega_n) = \frac{\hbar\Delta^\star(\mathbf{p})}{(2\pi\hbar)^{3/2}\left(\hbar^2\omega_n^2 + E_p^2 + |\Delta(\mathbf{p})|^2\right)}. \tag{D.31}$$

In the last lines we have dropped the spin indices since we wish to describe a single component spin polarised gas.

D.2 Evaluation of the gap function

We wish the evaluate Eq. (D.24) at a fixed temperature and density. We therefore write

$$\Delta^\star(\mathbf{p}) = -\frac{(2\pi\hbar)^{3/2}}{\beta\hbar}\int d^3q \sum_n e^{-i\omega_n\eta}\langle \mathbf{p}|V|\mathbf{q}\rangle F^\dagger(\mathbf{q},\omega_n), \tag{D.32}$$

$$\Delta^\star(\mathbf{p}) = -\frac{1}{\beta}\int d^3q \sum_n e^{-i\omega_n\eta}\langle \mathbf{p}|V|\mathbf{q}\rangle \frac{\hbar\Delta^\star(\mathbf{q})}{\hbar^2\omega_n^2 + E_q^2 + |\Delta(\mathbf{q})|^2}, \tag{D.33}$$

$$\Delta^\star(\mathbf{p}) = -\frac{1}{\beta\hbar}\int d^3q \sum_n e^{-i\omega_n\eta}\langle \mathbf{p}|V|\mathbf{q}\rangle \frac{\hbar\Delta^\star(\mathbf{q})}{\hbar^2\omega_n^2 + \epsilon_q^2}, \tag{D.34}$$

where we have defined $\epsilon_q^2 = E_q^2 + |\Delta(\mathbf{q})|^2$. Now,

$$\Delta^\star(\mathbf{p}) = \frac{1}{\beta\hbar}\int d^3q \sum_n e^{-i\omega_n\eta}\langle \mathbf{p}|V|\mathbf{q}\rangle \frac{\hbar\Delta^\star(\mathbf{q})}{2\epsilon_q}\left(\frac{1}{i\hbar\omega_n - \epsilon_q} - \frac{1}{i\hbar\omega_n + \epsilon_q}\right). \tag{D.35}$$

We can now use Cauchy's integral formula to calculate the summation over the frequencies, ω_n, through

$$\frac{1}{2\pi i}\int_c f(z)dz = \sum_n f(z_n). \tag{D.36}$$

We now define the function

$$f(z) = \frac{1}{z - \frac{\beta}{2}\epsilon_q} - \frac{1}{z + \frac{\beta}{2}\epsilon_q}, \tag{D.37}$$

so that the sum over the residues is given by

$$S = \frac{\beta}{2}\sum_n f(z_n) \tag{D.38}$$

where

$$z_n = \frac{\beta\hbar\omega_n}{2}i = \frac{2n+1}{2}\pi i \tag{D.39}$$

that ensures the correct Fermi statistics, as already mentioned. it can be seen that $\tanh(z)$ has poles at the positions $z = z_n$. Now we can consider the sum

$$S = \frac{\beta}{2}\frac{1}{2\pi i}\int_C dz\, f(z)\tanh(z) \tag{D.40}$$

The contour encloses the imaginary axis but will not enclose the poles on the real axis at $z = \pm\frac{\beta}{\hbar}\epsilon_k$. The contour can thus be deformed to travel around these points. The contour around the outside of these points will not contribute as $|z| \to \infty$. This leaves the summation of the function evaluated at the poles. Thus

$$S = -\beta\tanh\left(\beta\frac{\epsilon_q}{2}\right). \tag{D.41}$$

The minus sign comes from the fact that the contour encloses the poles in the mathematically negative sense. This gives the gap equation finally as

$$\Delta^\star(\mathbf{p}) = -\int d^3q\langle\mathbf{p}|V|\mathbf{q}\rangle\frac{\Delta^\star(q)}{2\epsilon_q}\tanh\left(\beta\frac{\epsilon_q}{2}\right). \tag{D.42}$$

Now the separable potential can be used to write the gap equation as

$$\Delta^\star(\mathbf{p}) = -\int d^3q\langle\mathbf{p}|\chi\rangle\xi\langle\chi|\mathbf{q}\rangle\frac{\Delta^\star(\mathbf{q})}{2\epsilon_q}\tanh\left(\beta\frac{\epsilon_q}{2}\right). \tag{D.43}$$

Furthermore the gap terms contain a separable term so that

$$\langle\mathbf{p}|\chi\rangle\xi\langle\chi|\Phi\rangle = -\int d^3q\langle\mathbf{p}|\chi\rangle\xi\langle\chi|\mathbf{q}\rangle\frac{\langle\mathbf{q}|\chi\rangle\xi\langle\chi|\Phi\rangle}{2\epsilon_q}\tanh\left(\beta\frac{\epsilon_q}{2}\right) \tag{D.44}$$

Dividing out the common factors gives

$$1 = -\int\frac{d^3q\xi\langle\chi|\mathbf{q}\rangle\langle\mathbf{q}|\chi\rangle}{2(E_q^2 + |\Delta(q)|^2)^{1/2}}\tanh\left(\beta\frac{(E_q^2 + |\Delta(\mathbf{q})|^2)^{1/2}}{2}\right). \tag{D.45}$$

D.3 Evaluation of the particle density

The density of a system can bw related to the single particle Green's function through

$$n(\mathbf{x}) = g(\mathbf{x}, \mathbf{x}, \tau, \tau^+), \tag{D.46}$$

where τ^+ denote that $\tau' \to \tau$ from positive values. We therefore consider

$$g(\mathbf{x}, \mathbf{x}, \tau, \tau') = \frac{1}{\beta\hbar} \int d^3q \sum_n e^{i\omega_n \eta} g(\mathbf{q}, \omega_n), \tag{D.47}$$

$$g(\mathbf{x}, \mathbf{x}, \tau, \tau') = -\frac{1}{\beta\hbar(2\pi\hbar)^{3/2}} \int d^3q \sum_n e^{i\omega_n \eta} \frac{\hbar(i\hbar\omega_n + E_p)}{\hbar^2\omega_n^2 + \epsilon_q^2}. \tag{D.48}$$

We can expand the integrand to give

$$g(\mathbf{x}, \mathbf{x}, \tau, \tau') = -\frac{1}{\beta(2\pi\hbar)^{3/2}} \int d^3q \sum_n e^{i\omega_n \eta} \left[\frac{i\hbar\omega_n}{\hbar^2\omega_n^2 + \epsilon_q^2} + \frac{E_q}{\hbar^2\omega_n^2 + \epsilon_q^2} \right]. \tag{D.49}$$

Now we consider only the first term of the integrand

$$\frac{1}{2\beta} \int d^3q \sum_n e^{i\omega_n \eta} \left[\frac{1}{\epsilon_q + i\hbar\omega_n} - \frac{1}{\epsilon_q - \hbar\omega_n} \right]. \tag{D.50}$$

The terms in the brackets can be written as integrals with a dummy time variable

$$\frac{1}{2\beta\hbar} \int d^3q \sum_n e^{i\omega_n \eta} \left[\int_0^\infty dt e^{-(\epsilon_q + i\hbar\omega_n)\frac{t}{\hbar}} - \int_0^\infty dt e^{-(\epsilon_q - i\hbar\omega_n)\frac{t}{\hbar}} \right]. \tag{D.51}$$

This can be rearranged to give

$$\frac{1}{2\beta\hbar} \int d^3q \sum_n \left[\int_0^\infty dt e^{-\frac{\epsilon_q t}{\hbar}} e^{-i\omega_n(t-\eta)} - \int_0^\infty dt e^{-\frac{\epsilon_q t}{\hbar}} e^{i\omega_n(t+\eta)} \right]. \tag{D.52}$$

This expression can be rewritten using the fact that the frequencies are restricted to $\omega_n = (2n+1)\pi/\hbar\beta$ and the Dirac comb relation

$$\frac{1}{T} \sum_n e^{i2\pi nt/T} = \sum_m \delta(t - mT). \tag{D.53}$$

We can write the expression with $T = \beta\hbar$ as

$$\frac{1}{2}\int d^3q \sum_m \left[\int_0^\infty dt e^{-\frac{\epsilon_q t}{\hbar}}\delta(-t+\eta-m\beta\hbar)e^{-\frac{i\pi}{\beta\hbar}(t-\eta)} - \int_0^\infty dt e^{-\frac{\epsilon_q t}{\hbar}}\delta(t+\eta-m\beta\hbar)e^{\frac{i\pi}{\beta\hbar}(t+\eta)}\right] \tag{D.54}$$

By splitting the summations and ignoring the $m = 0$ term in the second term because t and τ are positive quantities we arrive at the expression

$$\begin{aligned}
&\frac{1}{2}\int d^3q \left[\int_0^\infty dt \sum_{m=-\infty}^{-1} e^{-\frac{\epsilon_q t}{\hbar}}\delta(-t+\eta-m\beta\hbar)e^{-\frac{i\pi}{\beta\hbar}(t-\eta)}\right.\\
&+\int_0^\infty dt \sum_{m=1}^{\infty} e^{-\frac{\epsilon_q t}{\hbar}}\delta(-t+\eta-m\beta\hbar)e^{-\frac{i\pi}{\beta\hbar}(t-\eta)}\\
&-\int_0^\infty dt \sum_{m=-\infty}^{-1} e^{-\frac{\epsilon_q t}{\hbar}}\delta(t+\eta-m\beta\hbar)e^{\frac{i\pi}{\beta\hbar}(t+\eta)}\\
&-\int_0^\infty dt \sum_{m=1}^{\infty} e^{-\frac{\epsilon_q t}{\hbar}}\delta(t+\eta-m\beta\hbar)e^{\frac{i\pi}{\beta\hbar}(t+\eta)}\\
&\left.+\int_0^\infty dt e^{-\frac{\epsilon_q t}{\hbar}}\delta(t-\eta)e^{\frac{i\pi}{\beta\hbar}(t-\eta)}\right].
\end{aligned} \tag{D.55}$$

By evaluating the delta functions and at last allowing η to go to zero we get

$$\frac{1}{2}\int d^3q[1] \tag{D.56}$$

This has to be added to the contribution from the second term, which can be deduced by comparison with the gap equation. This finally gives the equation for the density to be

$$g(\mathbf{x},\mathbf{x},\tau,\tau^+) = \frac{1}{2(2\pi\hbar)^{3/2}}\int d^3q\left[1-\frac{E_q}{\epsilon_q}\tanh\left(\beta\frac{\epsilon_q}{2}\right)\right] \tag{D.57}$$

Appendix E

Angular integral in the gap equation

We want to do the integral

$$\int_0^{\pi} \sin\theta d\theta \int_0^{2\pi} d\phi \mathfrak{H}(\sin^2\theta \sin^2\phi). \tag{E.1}$$

By making the substitution that $x = \sin\theta \sin\phi$ we can write

$$8 \int_0^{\frac{\pi}{2}} d\theta \int_0^{\sin\theta} dx \frac{\mathfrak{H}(x^2)}{\sqrt{1 - \frac{x^2}{\sin^2\theta}}}. \tag{E.2}$$

Now we make the substitution $y = \sin\theta$ to give

$$8 \int_0^1 dy \int_0^y dx \frac{y\mathfrak{H}(x^2)}{\sqrt{(1-y^2)(y^2-x^2)}}. \tag{E.3}$$

This equation can be rewritten so as to give new limits on the integrations

$$8 \int_x^1 dy \int_0^1 dx \frac{y\mathfrak{H}(x^2)}{\sqrt{(1-y^2)(y^2-x^2)}}. \tag{E.4}$$

This integral is of the form

$$I = \int_x^1 \int_0^1 dx \frac{y f(x^2)}{\sqrt{1-y^2}\sqrt{y^2-x^2}} \tag{E.5}$$

This can be integrated by parts to give

$$\int_0^1 dx f(x^2)\left(\left[iyF\left(\sin^{-1}\left(\frac{y}{x}\right),x^2\right)\right]_x^1 - i\int_x^1 dyF\left(\sin^{-1}\left(\frac{y}{x}\right),x^2\right)\right). \tag{E.6}$$

Here, $F(\phi,m)$ is an elliptical integral of the first kind defined by [169]

$$F(\phi,m) = \int_0^{\sin\phi} \frac{dk}{\sqrt{1-k^2}\sqrt{1-m^2k^2}}. \tag{E.7}$$

It should be noted that the term

$$\left[iyF\left(\sin^{-1}\left(\frac{y}{x}\right),x^2\right)\right]_x^1, \tag{E.8}$$

is ill-defined on the upper limit since $\sin^{-1}\left(\frac{1}{x}\right)$ has no inverse for $x<0$. However, we will see that this term cancels out. The indefinite integral for the second term can be defined on the intervals $0<x<1$ and $x<y<1$ so that,

$$i\int dyF\left(\sin^{-1}\left(\frac{y}{x}\right),x^2\right) = iyF\left(\sin^{-1}\left(\frac{y}{x}\right),x^2\right) - iln\left(2x\left(i\sqrt{1-y^2}+\sqrt{y^2-x^2}\right)\right). \tag{E.9}$$

The first term is seen to cancel Eq. (E.8). This allows Eq. (E.5) to be written as

$$\begin{aligned} I &= i\int_0^1 dx f(x^2)\left[ln(2x\left(\sqrt{1-x^2}+\sqrt{y^2-x^2}\right)\right]_x^1 \\ &= i\int_0^1 dx f(x^2) ln\left(\frac{2x\sqrt{1-x^2}}{2xi\sqrt{1-x^2}}\right) \\ &= \frac{\pi}{2}\int_0^1 dx f(x^2). \end{aligned} \tag{E.10}$$

We can therefore write

$$\int_0^\pi \sin\theta d\theta \int_0^{2\pi} d\phi \mathfrak{H}(\sin^2\theta\sin^2\phi) = 4\pi\int_0^1 dx \mathfrak{H}(x^2). \tag{E.11}$$

Appendix F

Derivation of the dynamical mean-field equations

The two body Hamiltonian operator is given by

$$H_{2B} = T_1 + T_2 + V_{12}, \tag{F.1}$$

where T_i are the kinetic energy operators of single particles and V_{12} is the operator for the interparticle interaction. We write the second quantised operator as

$$\hat{H}_{2B} = \frac{1}{2}\sum_{ijkl}\langle ij|H_{2B}|kl\rangle a_i^\dagger a_j^\dagger a_k a_l, \tag{F.2}$$

where the indices represent single particle states. For the dynamics operators obey the Heisenberg equation of motion

$$i\hbar\frac{\partial}{\partial t}\hat{O} = \left[\hat{O}, \hat{H}\right]. \tag{F.3}$$

The pair function is a thermal average of the operator $a_m a_n$ so we can find an equation of motion from the commutator

$$\begin{aligned}\left[a_m a_n, a_i^\dagger a_j^\dagger a_k a_l\right] = {} & a_k a_l \delta_{mj}\delta_{ni} - a_j^\dagger a_m a_k a_l \delta_{ni} - a_k a_l \delta_{nj}\delta_{mi} + a_j^\dagger a_n a_k a_l \delta_{mi} \\ & + a_i^\dagger a_m a_k a_l \delta_{nj} - a_i^\dagger a_n a_k a_l \delta_{mj} + a_i^\dagger a_j^\dagger a_m a_n a_k a_l.\end{aligned} \tag{F.4}$$

This gives us

$$i\hbar\frac{\partial}{\partial t}(a_m a_n) = \sum_{kl}\langle nm|H_{2B}|kl\rangle a_k a_l + \sum_{jkl}\left[\langle mj|H_{2B}|kl\rangle a_j^\dagger a_n a_k a_l + \langle jn|H_{2B}|kl\rangle a_j^\dagger a_m a_k a_l\right]. \tag{F.5}$$

The single particle Hamiltonian parts of the second sum on the right hand side cancel to give

$$i\hbar\frac{\partial}{\partial t}(a_m a_n) = \sum_{kl}\langle nm|H_{2B}|kl\rangle a_k a_l + \sum_{jkl}\left[\langle mj|V_{12}|kl\rangle a_j^\dagger a_n a_k a_l + \langle jn|V_{12}|kl\rangle a_j^\dagger a_m a_k a_l\right]. \tag{F.6}$$

By introducing a Kronecker delta with a summation we write

$$i\hbar\frac{\partial}{\partial t}(a_m a_n) = \sum_{kl}\langle nm|H_{2B}|kl\rangle a_k a_l + \sum_{jklh}\left[\langle mj|V_{12}|kl\rangle\delta_{nh}a_j^\dagger a_h a_k a_l + \langle jn|V_{12}|kl\rangle\delta_{mh}a_j^\dagger a_h a_k a_l\right]. \tag{F.7}$$

Now using the normalisation of the single particle states

$$i\hbar\frac{\partial}{\partial t}(a_m a_n) = \sum_{kl}\langle nm|H_{2B}|kl\rangle a_k a_l + \sum_{jklh}\left[\langle nmj|V_{23}|klh\rangle a_j^\dagger a_h a_k a_l + \langle nmj|V_{13}|klh\rangle a_j^\dagger a_h a_k a_l\right], \tag{F.8}$$

which can be abbreviated to

$$i\hbar\frac{\partial}{\partial t}(a_m a_n) = \sum_{kl}\langle nm|H_{2B}|kl\rangle a_k a_l + \sum_{jklh}\langle nmj|\sum_{b=1}^{2}V_{b3}|klh\rangle a_j^\dagger a_h a_k a_l \tag{F.9}$$

For the density matrix the Hamiltonian is given by

$$H = \sum_{ij}\langle i|T|j\rangle a_i^\dagger a_j + \frac{1}{2}\sum_{ijkl}\langle ij|V|kl\rangle a_i^\dagger a_j^\dagger a_k a_l. \tag{F.10}$$

A direct calculation of the quantity $\left[a_m^\dagger a_n, H\right]$ leads to the equation

$$i\hbar\frac{\partial}{\partial t}\left(a_m^\dagger a_n\right) = \sum_j \langle n|H_{1B}|j\rangle a_m^\dagger a_j - \sum_i \langle i|H_{1B}|m\rangle a_i^\dagger a_n + \sum_{jkl}\langle nj|V|kl\rangle a_m^\dagger a_j^\dagger a_k a_l - \sum_{jkl}\langle lj|V|km\rangle a_i^\dagger a_j^\dagger a_k a_n \tag{F.11}$$

Thermal averages can be taken of both sides of the equations. This leads to thermal averages of products of four operators in each equation. These products can be expanded using Wick's theorem for cumulants [162]

$$\langle a_j^\dagger a_h a_k a_l\rangle = \langle a_j^\dagger a_h a_k a_l\rangle^c + \langle a_j^\dagger a_h\rangle^c\langle a_k a_l\rangle^c - \langle a_j^\dagger a_k\rangle^c\langle a_h a_l\rangle^c + \langle a_j^\dagger a_l\rangle^c\langle a_k a_h\rangle^c, \tag{F.12}$$

$$\langle a_i^\dagger a_j^\dagger a_k a_n\rangle = \langle a_i^\dagger a_j^\dagger a_k a_n\rangle^c + \langle a_i^\dagger a_j^\dagger\rangle^c\langle a_k a_n\rangle^c - \langle a_i^\dagger a_k\rangle^c\langle a_j^\dagger a_n\rangle^c + \langle a_i^\dagger a_n\rangle^c\langle a_j^\dagger a_k\rangle^c. \tag{F.13}$$

The cumulant expansion allows the subsequent hierarchy of equations to be truncated at any desired order, provided we assume the system remains relatively close to equilibrium. By inserting these definitions into Eq. (F.11) and Eq. (F.9), we obtain Eq. (4.28) and Eq. (4.28).

Appendix G

Landau-Zener parameter for a spherical well

In this section we give an expression for the Landau-Zener parameter in a spherical well of volume $V = \frac{4}{3}R^3$, where R is the radius of the well. In free space the solutions to the p-wave Schrödinger equation are given by

$$j_1(kr) = \frac{1}{kr}\sin(kr) - \cos(kr), \tag{G.1}$$

$$n_1(kr) = \frac{1}{kr}\cos(kr) + \sin(kr). \tag{G.2}$$

Only Eq. (G.1) is finite at the origin, so we choose these solutions. By requiring $j_1(kR) = 0$ we get the condition on the wave number to satisfy

$$\tan(kR) = kR. \tag{G.3}$$

The Landau-Zener parameter is given by [114]

$$\delta_{L-Z} = \frac{|\langle\phi_{\text{res}}|W|\phi_{0\ell m}\rangle|}{\hbar|\dot{E}|}. \tag{G.4}$$

We can write the closure relation for box states and it's relation to scattering states as

$$\sum_n |\phi_{n\ell m}\rangle\langle\phi_{n\ell m}| \approx \int p^2 dp |\phi^{(+)}_{p\ell m}\rangle\langle\phi^{(+)}_{p\ell m}|. \tag{G.5}$$

Now we want to relate the spacing of the energy levels in the box to the spacing of the momentum states in free space. The energy levels in the box then depend on R and n, a quantum number that denotes the box state level. We define a quasi-momentum as

$$p_R = \sqrt{2\mu E}. \tag{G.6}$$

We can use the chain rule to write

$$\Delta p_R = \frac{dp_R}{dE}\frac{dE}{dn}\Delta n. \tag{G.7}$$

Now, we know that

$$\frac{dp_R}{dE} = \sqrt{\frac{\mu}{2E}}, \tag{G.8}$$

and we use this to write

$$\sum_n |\phi_{n\ell m}\rangle\langle\phi_{n\ell m}| \approx \sum_n |\phi_{n\ell m}\rangle\langle\phi_{n\ell m}| \sqrt{\frac{2E}{\mu}}\left(\frac{dE}{dn}\right)^{-1} \Delta p_R, \tag{G.9}$$

where we have used the fact that $\Delta n = 1$. In the limit that we take the spacing to be continuous $\Delta p_R \to dp_R$, we can approximate this expression as

$$\int dp_R |\phi_{n\ell m}\rangle\langle\phi_{n\ell m}| \sqrt{\frac{2E}{\mu}}\left(\frac{dE}{dn}\right)^{-1} \approx \int p^2 dp |\phi^{(+)}_{p\ell m}\rangle\langle\phi^{(+)}_{p\ell m}|, \tag{G.10}$$

We can identify

$$|\phi_{n\ell m}\rangle = \sqrt{\frac{\mu}{p_R}\left(\frac{dE}{dn}\right)} p_R |\phi^{(+)}_{p\ell m}\rangle. \tag{G.11}$$

We are now left with finding an appropriate expression for $\frac{dE}{dn}$, which comes from solving Eq. (G.3) for $k = p_R/\hbar$. By using a series solution to Eq. (G.3) kR is given by [170] (see also [171])

$$kR \approx q - \frac{1}{q} - \frac{2}{3q^3}, \tag{G.12}$$

where

$$q = \frac{\pi}{2}(2n + 1), \tag{G.13}$$

and n is a positive integer. The series in Eq. (G.12) has been truncated as it usually possible to retain only these terms. Including higher order terms in this series would only change our final answer by a numerical factor and we assume that this change is small. This gives us our box state quasi-momenta,

$$p_R \approx \frac{\hbar}{R}\left(q - \frac{1}{q} - \frac{2}{3q^3}\right). \tag{G.14}$$

Now we use the chain rule to write

$$\frac{dE}{dn} = \frac{dE}{dp_R}\frac{dp_R}{dq}\frac{dq}{dn}. \tag{G.15}$$

This can easily be evaluated to give

$$\frac{dE}{dn} = \frac{p_R\hbar}{\mu R}\left(1 + \frac{1}{q^2} + \frac{2}{q^4}\right) = \frac{p_R\hbar}{\mu R}C_n, \tag{G.16}$$

where C_n is a numerical factor with an obvious definition. We can then write Eq. (G.11) as

$$|\phi_{n\ell m}\rangle = \sqrt{\frac{\hbar C_n}{R}}\, p_R |\phi^{(+)}_{p\ell m}\rangle. \tag{G.17}$$

Putting this into the Landau-Zener formula gives

$$\delta_{L-Z} = \frac{C_n}{R|\dot{E}|} p_R^4 \lim_{p\to 0} \frac{|\langle\phi_{\rm res}|W|\phi^{(+)}_{p\ell m}\rangle|^2}{p^2}. \tag{G.18}$$

Using the relation between the coupling matrix elements and the resonance parameters [155] we can rewrite this as

$$\delta_{L-Z} = \frac{C_n}{R\mu\pi\hbar^3} p_R^4 \left|\frac{a^{\rm bg}_{1m_\ell}\Delta B_1}{\dot{B}}\right|. \tag{G.19}$$

Using the numerical values

$$C_1 = 1.04909, \tag{G.20}$$

$$p_R = 4.493409\frac{\hbar}{R}, \tag{G.21}$$

we write the Landau-Zener paramter as

$$\delta_{L-Z} = 427.677 \frac{\hbar}{R^5 \mu \pi} \left| \frac{a^{\mathrm{bg}}_{1m_\ell} \Delta B_1}{\dot{B}} \right|. \tag{G.22}$$

In terms of the volume, V, of the box this is

$$\delta_{L-Z} = 570.236 \frac{\hbar \pi}{V \mu R^2} \left| \frac{a^{\mathrm{bg}}_{1m_\ell} \Delta B_1}{\dot{B}} \right|. \tag{G.23}$$

Assuming a uniform density, such that $n = \frac{N}{V}$, gives

$$\delta_{L-Z} = 570.236 \frac{\hbar \pi}{\mu} \left(\frac{4}{3}\right)^{2/3} \left| \frac{a^{\mathrm{bg}}_{1m_\ell} \Delta B_1}{\dot{B}} \right| \left(\frac{n}{N}\right)^{5/3}. \tag{G.24}$$

This expression is dependent on the size of the system and even in the case of fast sweeps it is not possible to take the thermodynamic limit. This is different from the *s*-wave case where an expression for the association probability in the limit of fast ramps is independent of the system size [114].

Bibliography

[1] J. R. Schrieffer, *Theory of superconductivity*. Benjamin, 1964.

[2] C. Ticknor, C. A. Regal, D. S. Jin, and J. L. Bohn, "Multiplet structure of Feshbach resonances in nonzero partial waves," *Phys. Rev. A*, vol. 69, no. 4, p. 042712, 2004.

[3] J. Fuchs, C. Ticknor, P. Dyke, G. Veeravalli, E. Kuhnle, W. Rowlands, P. Hannaford, and C. J. Vale, "Binding energies of ^{6}Li *p*-wave Feshbach molecules," *Phys. Rev. A*, vol. 77, no. 5, p. 053616, 2008.

[4] B. Gao, "Binding energy and scattering length for diatomic systems," *J. Phys. B*, vol. 37, no. 21, pp. 4273–4279, 2004.

[5] F. Mandl, *Statistical Phyiscs*. Wiley, 1988.

[6] M. Planck, "Zur Theorie des Gesetzes der Energieverteilung im Normalspektrum," *Verhandlungen der Deutschen Physikalischen Gesellschaft*, vol. 2, p. 237, 1900.

[7] Bose, S. N., "Plancks gesetz und lichtquantenhypothese," *Z. Phys*, vol. 28, p. 178, 1924.

[8] Einstein, A. , "Quantentheorie des einatomigen idealen gases," *Sitzungsber. Kgl. Preuss. Akad. Wiss, Phys. Math. Kl.*, no. 22, p. 261, 1924.

[9] C. J. Pethick and H. Smith, *Bose-Einstein Condensation in Dilute Gases*. Cambridge, 2008.

[10] F. Dalfovo, S. Giorgini, L. P. Pitaevskii, and S. Stringari, "Theory of Bose-Einstein condensation in trapped gases," *Rev. Mod. Phys.*, vol. 71, no. 3, pp. 463–512, 1999.

[11] B. H. Bransden and C. J. Joachain, *Physics of Atoms and Molecules*. Prentice Hall, 2003.

[12] J. F. Annett, *Superconductivity, Superfluids and Condensates*. Oxford: OUP, 1950.

[13] L. D. Landau, "The Theory of a Fermi Liquid," *J. Exptl. Theoret. Phys.*, vol. 30, p. 1058, 1956.

[14] L. D. Landau, "Oscillations in a Fermi Liquid," *J. Exptl. Theoret. Phys.*, vol. 32, p. 59, 1957.

[15] L. D. Landau, "On The Theory Of A Fermi Liquid," *J. Exptl. Theoret. Phys.*, vol. 35, p. 97, 1958.

[16] A. Abriskosov, L. Gorkov, and I. Dzyaloshinski, *Methods of Quantum Field Theory In Statistical Physics*. Dover, 1975.

[17] Migdal, A. B. *J. Exptl. Theoret. Phys.*, vol. 32, p. 399, 1957.

[18] Migdal, A. B. *J. Exptl. Theoret. Phys.*, vol. 5, p. 333, 1957.

[19] T. Köhler, K. Góral, and P. S. Julienne, "Production of cold molecules via magnetically tunable Feshbach resonances," *Rev. Mod. Phys.*, vol. 78, no. 4, p. 1311, 2006.

[20] J. Zhang, E. G. M. van Kempen, T. Bourdel, L. Khaykovich, J. Cubizolles, F. Chevy, M. Teichmann, L. Tarruell, S. J. J. M. F. Kokkelmans, and C. Salomon, " *P*-wave Feshbach resonances of ultracold ^{6}Li ," *Phys. Rev. A*, vol. 70, no. 3, p. 030702, 2004.

[21] J. P. Gaebler, J. T. Stewart, J. L. Bohn, and D. S. Jin, "*p*-Wave Feshbach Molecules," *Phys. Rev. Lett.*, vol. 98, no. 20, p. 200403, 2007.

[22] Y. Inada, M. Horikoshi, S. Nakajima, M. Kuwata-Gonokami, M. Ueda, and T. Mukaiyama, "Collisional Properties of *p*-Wave Feshbach Molecules," *Phys. Rev. Lett.*, vol. 101, no. 10, p. 100401, 2008.

[23] R. A. W. Maier, C. Marzok, C. Zimmermann, and P. W. Courteille, "Radio-frequency spectroscopy of ^6Li *p*-wave molecules: Towards photoemission spectroscopy of a *p*-wave superfluid," *Phys. Rev. A*, vol. 81, no. 6, p. 064701, 2010.

[24] T. M. Hanna, *Dynamics of Feshbach Molecule Production*. University of Oxford: DPhil Thesis, 2008.

[25] P. D. Lett, R. N. Watts, C. I. Westbrook, W. D. Phillips, P. L. Gould, and H. J. Metcalf, "Observation of Atoms Laser Cooled below the Doppler Limit," *Phys. Rev. Lett.*, vol. 61, no. 2, pp. 169–172, 1988.

[26] H. J. Metcalf and P. van der Straten, *Laser Cooling and Trapping*. Springer, 1999.

[27] D. J. Wineland, R. E. Drullinger, and F. L. Walls, "Radiation-Pressure Cooling of Bound Resonant Absorbers," *Phys. Rev. Lett.*, vol. 40, no. 25, pp. 1639–1642, 1978.

[28] W. Neuhauser, M. Hohenstatt, P. Toschek, and H. Dehmelt, "Optical-Sideband Cooling of Visible Atom Cloud Confined in Parabolic Well," *Phys. Rev. Lett.*, vol. 41, no. 4, pp. 233–236, 1978.

[29] W. D. Phillips and J. V. Prodan, "Chirping the light-fantastic?," in *Laser-Cooled and Trapped Atoms,* edited by W. D. Phillips (Natl. Bur. Stand., Washington, DC), Spec. Publ. 653, p. 137, 1983.

[30] W. D. Phillips, J. V. Prodan, and H. Metcalf, "Laser cooling of free neutral atoms in an atomic beam," in *Laser Spectroscopy* VI, edited by H. Weber, and W. Luthy (Springer-Verlag, Berlin), p. 162, 1983.

[31] W. D. Phillips and J. V. Prodan, "Cooling atoms with a frequency chirped laser," in *Coherence and Quantum Optics V,* edited by L. Mandel, and E. Wolf (Plenum, New York), p. 15, 1984.

[32] W. D. Phillips and J. V. Prodan, "Chirping the light-fantastic? Recent NBS atom cooling experiments," *Prog. Quantum Electron.*, vol. 8, p. 231, 1984.

[33] W. Ertmer, R. Blatt, J. L. Hall, and M. Zhu, "Laser Manipulation of Atomic Beam Velocities: Demonstration of Stopped Atoms and Velocity Reversal," *Phys. Rev. Lett.*, vol. 54, no. 10, pp. 996–999, 1985.

[34] W. D. Phillips and H. Metcalf, "Laser Deceleration of an Atomic Beam," *Phys. Rev. Lett.*, vol. 48, no. 9, pp. 596–599, 1982.

[35] J. V. Prodan, W. D. Phillips, and H. Metcalf, "Laser Production of a Very Slow Monoenergetic Atomic Beam," *Phys. Rev. Lett.*, vol. 49, no. 16, pp. 1149–1153, 1982.

[36] W. D. Phillips, J. V. Prodan, and H. Metcalf, "Neutral atomic beam cooling experiments at NBS," in *Laser-Cooled and Trapped Atoms*, edited by W. D. Phillips (Natl. Bur. Stand, Washington, DC), Spec. Publ. 653, p. 1, 1983.

[37] W. D. Phillips, J. V. Prodan, and H. Metcalf, "Laser-cooled atomic beams," in *Atomic Physics IX*, edited by R. S. Van Dyck, and E. N. Fortson (World Scientific, Singapore), p. 338, 1984.

[38] W. D. Phillips, J. V. Prodan, and H. Metcalf, "Neutral atomic beam cooling experiments at NBS," *Prog. Quantum Electron.*, vol. 8, p. 119, 1984.

[39] W. D. Phillips, J. V. Prodan, and H. Metcalf, "Laser cooling and electromagnetic trapping of neutral atoms," *J. Opt. Soc. Am. B*, vol. 2, p. 1751, 1985.

[40] A. L. Migdall, J. V. Prodan, W. D. Phillips, T. H. Bergeman, and H. J. Metcalf, "First Observation of Magnetically Trapped Neutral Atoms," *Phys. Rev. Lett.*, vol. 54, no. 24, pp. 2596–2599, 1985.

[41] V. S. Bagnato, G. P. Lafyatis, A. G. Martin, E. L. Raab, R. N. Ahmad-Bitar, and D. E. Pritchard, "Continuous Stopping and Trapping of Neutral Atoms," *Phys. Rev. Lett.*, vol. 58, no. 21, pp. 2194–2197, 1987.

[42] M. A. Helmerson, K. and P. D., "Laser cooling of magnetically trapped neutral atoms," *J. Opt. Soc. Am. B*, vol. 9, p. 1988, 1992.

[43] H. F. Hess, G. P. Kochanski, J. M. Doyle, N. Masuhara, D. Kleppner, and T. J. Greytak, "Magnetic trapping of spin-polarized atomic hydrogen," *Phys. Rev. Lett.*, vol. 59, no. 6, pp. 672–675, 1987.

[44] R. van Roijen, J. J. Berkhout, S. Jaakkola, and J. T. M. Walraven, "Experiments with Atomic Hydrogen in a Magnetic Trapping Field," *Phys. Rev. Lett.*, vol. 61, no. 8, pp. 931–934, 1988.

[45] J. Dalibard and C. Cohen-Tannoudji, "Laser cooling below the Doppler limit by polarization gradients: simple theoretical models," *J. Opt. Soc. Am. B*, vol. 6, p. 2023, 1989.

[46] M. H. Anderson, J. R. Ensher, M. R. Matthews, C. E. Wieman, and E. A. Cornell, "Observation of Bose-Einstein Condensation in a Dilute Atomic Vapor," *Science*, vol. 269, no. 5221, pp. 198–201, 1995.

[47] K. B. Davis, M. O. Mewes, M. R. Andrews, N. J. van Druten, D. S. Durfee, D. M. Kurn, and W. Ketterle, "Bose-Einstein Condensation in a Gas of Sodium Atoms," *Phys. Rev. Lett.*, vol. 75, no. 22, pp. 3969–3973, 1995.

[48] B. DeMarco and D. S. Jin, "Onset of Fermi Degeneracy in a Trapped Atomic Gas," *Science*, vol. 285, no. 5434, pp. 1703–1706, 1999.

[49] J. G. Bednorz and K. A. Müller, "Possible high T_c superconductivity in the Ba-La-Cu-O system," *Zeitschrift für Physik B Condensed Matter*, vol. 64, pp. 189–193, 1986.

[50] J. Bardeen, L. N. Cooper, and J. R. Schrieffer, "Microscopic Theory of Superconductivity," *Phys. Rev.*, vol. 106, no. 1, pp. 162–164, 1957.

[51] C. Chin, R. Grimm, P. Julienne, and E. Tiesinga, "Feshbach resonances in ultracold gases," *Rev. Mod. Phys.*, vol. 82, no. 2, pp. 1225–1286, 2010.

[52] J. P. Gaebler, J. T. Stewart, T. E. Drake, D. S. Jin, A. Perali, P. Pieri, and G. C. Strinati, "Observation of pseudogap behaviour in a strongly interacting Fermi gas," *Nat. Phys.*, vol. 6, no. 8, p. 569, 2010.

[53] A. Perali, F. Palestini, P. Pieri, G. C. Strinati, J. T. Stewart, J. P. Gaebler, T. E. Drake, and D. S. Jin, "Evolution of the Normal State of a Strongly Interacting Fermi Gas from a Pseudogap Phase to a Molecular Bose Gas," *Phys. Rev. Lett.*, vol. 106, no. 6, p. 060402, 2011.

[54] S. Nascimbène, N. Navon, K. J. Jiang, F. Chevy, and C. Salomon, "Exploring the thermodynamics of a universal Fermi gas," *Nature*, vol. 463, no. 7284, p. 1057, 2010.

[55] S. Nascimbène, N. Navon, S. Pilati, F. Chevy, S. Giorgini, A. Georges, and C. Salomon, "Fermi-Liquid Behavior of the Normal Phase of a Strongly Interacting Gas of Cold Atoms," *Phys. Rev. Lett.*, vol. 106, no. 21, p. 215303, 2011.

[56] S. Giorgini, L. P. Pitaevskii, and S. Stringari, "Theory of ultracold atomic Fermi gases," *Rev. Mod. Phys.*, vol. 80, no. 4, pp. 1215–1274, 2008.

[57] I. Bloch, J. Dalibard, and W. Zwerger, "Many-body physics with ultracold gases," *Rev. Mod. Phys.*, vol. 80, no. 3, pp. 885–964, 2008.

[58] T. Schäfer, "What atomic liquids can teach us about quark liquids," *arxiv:hep-ph/0703141v1*, 2007.

[59] P. K. Kovtun, D. T. Son, and A. O. Starinets, "Viscosity in Strongly Interacting Quantum Field Theories from Black Hole Physics," *Phys. Rev. Lett.*, vol. 94, no. 11, p. 111601, 2005.

[60] J. R. Taylor, *Scattering Theory*. New York: Dover, 2006.

[61] U. Fano, "Effects of Configuration Interaction on Intensities and Phase Shifts," *Phys. Rev.*, vol. 124, no. 6, pp. 1866–1878, 1961.

[62] H. Feshbach, "Unified theory of nuclear reactions*1," *Ann. Phys.(N.Y.)*, vol. 5, p. 357, 1958.

[63] H. Feshbach, "Unified theory of nuclear reactions*2," *Ann. Phys.(N.Y.)*, vol. 19, p. 287, 1962.

[64] E. Tiesinga, C. J. Williams, F. H. Mies, and P. S. Julienne, "Interacting atoms under strong quantum confinement," *Phys. Rev. A*, vol. 61, p. 063416, 2000.

[65] R. V. Krems, "Cold controlled chemistry," *Phys. Chem. Chem. Phys.*, vol. 10, pp. 4079–4092, 2008.

[66] M. S. Child, *Molecular Collision Theory*. Academic, 1974.

[67] J. Doyle, B. Friedrich, R. V. Krems, and F. Masnou-Seeuws, "Editorial: Quo vadis, cold molecules?," *The European Physical Journal D - Atomic, Molecular, Optical and Plasma Physics*, vol. 31, pp. 149–164.

[68] M. Olshanii, "Atomic Scattering in the Presence of an External Confinement and a Gas of Impenetrable Bosons," *Phys. Rev. Lett.*, vol. 81, pp. 938–941, 1998.

[69] P. F. Weck and N. Balakrishnan, "Importance of long-range interactions in chemical reactions at cold and ultracold temperatures," *Int. Rev. Phys. Chem.*, vol. 25, p. 283, 2006.

[70] J. M. Hutson and P. Soldan, "Molecular collisions in ultracold atomic gases," *Int. Rev. Phys. Chem.*, vol. 26, p. 1, 2007.

[71] P. Staanum, S. D. Kraft, J. Lange, R. Wester, and M. Weidemüller, "Experimental Investigation of Ultracold Atom-Molecule Collisions," *Phys. Rev. Lett.*, vol. 96, no. 2, p. 023201, 2006.

[72] N. Zahzam, T. Vogt, M. Mudrich, D. Comparat, and P. Pillet, "Atom-Molecule Collisions in an Optically Trapped Gas," *Phys. Rev. Lett.*, vol. 96, no. 2, p. 023202, 2006.

[73] E. S. Shuman, J. F. Barry, and D. DeMille, "Laser cooling of a diatomic molecule," *Nature*, vol. 467, pp. 820–823, 2010.

[74] K. M. Jones, E. Tiesinga, P. D. Lett, and P. S. Julienne, "Ultracold photoassociation spectroscopy: Long-range molecules and atomic scattering," *Rev. Mod. Phys.*, vol. 78, no. 2, pp. 483–535, 2006.

[75] J. J. Hudson, D. M. Kara, I. J. Smallman, B. E. Sauer, M. R. Tarbutt, and E. A. Hinds, "Improved measurement of the shape of the electron," *Nature*, vol. 473, no. 7348, p. 4, 2011.

[76] A. Micheli, G. K. Brennen, and P. Zoller, "A toolbox for lattice-spin models with polar molecules," *Nat. Phys*, vol. 2, p. 341, 2006.

[77] C. Regal, C. A.and Ticknor and J. D. S. Bohn, J. L., "Creation of ultracold molecules from a Fermi gas of atoms," *Nature*, vol. 424, no. 6944, pp. 47–50, 2003.

[78] A. J. Leggett, "A theoretical description of the new phases of liquid ^{3}He," *Rev. Mod. Phys.*, vol. 47, no. 2, pp. 331–414, 1975.

[79] P. Wolfle, "Low-temperature properties of liquid ^{3}He," *Rep. Prog. Phys.*, vol. 42, no. 2, p. 269, 1979.

[80] Y. Maeno, H. Hashimoto, K. Yoshida, S. Nishizaki, T. Fujita, J. G. Bednorz, and F. Lichtenberg, "Superconductivity in a layered perovskite without copper," *Nature*, vol. 372, p. 532, 1994.

[81] A. P. Mackenzie and Y. Maeno, "The superconductivity of Sr_2RuO_4 and the physics of spin-triplet pairing," *Rev. Mod. Phys.*, vol. 75, no. 2, pp. 657–712, 2003.

[82] J. L. Bohn, J. P. Burke, C. H. Greene, H. Wang, P. L. Gould, and W. C. Stwalley, "Collisional properties of ultracold potassium: Consequences for degenerate Bose and Fermi gases," *Phys. Rev. A*, vol. 59, no. 5, pp. 3660–3664, 1999.

[83] B. DeMarco, J. L. Bohn, J. P. Burke, M. Holland, and D. S. Jin, "Measurement of *p*-Wave Threshold Law Using Evaporatively Cooled Fermionic Atoms," *Phys. Rev. Lett.*, vol. 82, no. 21, pp. 4208–4211, 1999.

[84] T. Loftus, C. A. Regal, C. Ticknor, J. L. Bohn, and D. S. Jin, "Resonant Control of Elastic Collisions in an Optically Trapped Fermi Gas of Atoms," *Phys. Rev. Lett.*, vol. 88, no. 17, p. 173201, 2002.

[85] J. L. Bohn, "Cooper pairing in ultracold ^{40}K using Feshbach resonances," *Phys. Rev. A*, vol. 61, no. 5, p. 053409, 2000.

[86] C. A. Regal and D. S. Jin, "Measurement of Positive and Negative Scattering Lengths in a Fermi Gas of Atoms," *Phys. Rev. Lett.*, vol. 90, no. 23, p. 230404, 2003.

[87] M. Greiner, C. A. Regal, and D. S. Jin, "Emergence of a molecular Bose-Einstein condemsate from a Fermi gas," *Nature*, vol. 426, p. 537, 2003.

[88] C. A. Regal, M. Greiner, and D. S. Jin, "Observation of Resonance Condensation of Fermionic Atom Pairs," *Phys. Rev. Lett.*, vol. 92, no. 4, p. 040403, 2004.

[89] M. Houbiers, H. T. C. Stoof, W. I. McAlexander, and R. G. Hulet, "Elastic and inelastic collisions of ^{6}Li atoms in magnetic and optical traps," *Phys. Rev. A*, vol. 57, no. 3, pp. R1497–R1500, 1998.

[90] K. M. O'Hara, S. L. Hemmer, S. R. Granade, M. E. Gehm, J. E. Thomas, V. Venturi, E. Tiesinga, and C. J. Williams, "Measurement of the zero crossing in a Feshbach resonance of fermionic ^{6}Li ," *Phys. Rev. A*, vol. 66, no. 4, p. 041401, 2002.

[91] K. E. Strecker, G. B. Partridge, and R. G. Hulet, "Conversion of an Atomic Fermi Gas to a Long-Lived Molecular Bose Gas," *Phys. Rev. Lett.*, vol. 91, no. 8, p. 080406, 2003.

[92] J. Cubizolles, T. Bourdel, S. J. J. M. F. Kokkelmans, G. V. Shlyapnikov, and C. Salomon, "Production of Long-Lived Ultracold Li_2 Molecules from a Fermi Gas," *Phys. Rev. Lett.*, vol. 91, no. 24, p. 240401, 2003.

[93] M. W. Zwierlein, C. A. Stan, C. H. Schunck, S. M. F. Raupach, S. Gupta, Z. Hadzibabic, and W. Ketterle, "Observation of Bose-Einstein Condensation of Molecules," *Phys. Rev. Lett.*, vol. 91, no. 25, p. 250401, 2003.

[94] M. W. Zwierlein, C. A. Stan, C. H. Schunck, S. M. F. Raupach, A. J. Kerman, and W. Ketterle, "Condensation of Pairs of Fermionic Atoms near a Feshbach Resonance," *Phys. Rev. Lett.*, vol. 92, no. 12, p. 120403, 2004.

[95] M. Bartenstein, A. Altmeyer, S. Riedl, S. Jochim, C. Chin, J. H. Denschlag, and R. Grimm, "Crossover from a Molecular Bose-Einstein Condensate to a Degenerate Fermi Gas," *Phys. Rev. Lett.*, vol. 92, no. 12, p. 120401, 2004.

[96] V. Gurarie, L. Radzihovsky, and A. V. Andreev, "Quantum Phase Transitions across a *p*-wave Feshbach Resonance," *Phys. Rev. Lett.*, vol. 94, no. 23, p. 230403, 2005.

[97] V. Gurarie and L. Radzihovsky, "Resonantly paired fermionic superfluids.," *Ann. Phys.*, vol. 322, no. 1, pp. 2–119, 2007.

[98] J. Levinsen, N. R. Cooper, and V. Gurarie, "Strongly Resonant *p*-wave Superfluids," *Phys. Rev. Lett.*, vol. 99, no. 21, p. 210402, 2007.

[99] M. Iskin and C. J. Williams, "Trapped *p* -wave superfluids: A local-density approach," *Phys. Rev. A*, vol. 77, no. 4, p. 041607, 2008.

[100] M. Kagan and D. Efremov, "BCS-BEC Crossover and Chiral Anomaly in *p*-Wave Superfluids with the Symmetry of A1-Phase," *J. Low Temp. Phys.*, vol. 158, pp. 749–772, 2010.

[101] C. A. Regal, C. Ticknor, J. L. Bohn, and D. S. Jin, "Tuning *p*-Wave Interactions in an Ultracold Fermi Gas of Atoms," *Phys. Rev. Lett.*, vol. 90, no. 5, p. 053201, 2003.

[102] C. H. Schunck, M. W. Zwierlein, C. A. Stan, S. M. F. Raupach, W. Ketterle, A. Simoni, E. Tiesinga, C. J. Williams, and P. S. Julienne, "Feshbach resonances in fermionic ^{6}Li," *Phys. Rev. A*, vol. 71, no. 4, p. 045601, 2005.

[103] M. Iskin and C. A. R. S. de Melo, "Superfluidity of *p* -wave and *s* -wave atomic Fermi gases in optical lattices," *Phys. Rev. B*, vol. 72, no. 22, p. 224513, 2005.

[104] K. Günter, T. Stöferle, H. Moritz, M. Köhl, and T. Esslinger, "*p*-Wave Interactions in Low-Dimensional Fermionic Gases," *Phys. Rev. Lett.*, vol. 95, no. 23, p. 230401, 2005.

[105] C. A. Regal, M. Greiner, and D. S. Jin, "Lifetime of Molecule-Atom Mixtures near a Feshbach Resonance in *K*40," *Phys. Rev. Lett.*, vol. 92, no. 8, p. 083201, 2004.

[106] F. Chevy, E. G. M. van Kempen, T. Bourdel, J. Zhang, L. Khaykovich, M. Teichmann, L. Tarruell, S. J. J. M. F. Kokkelmans, and C. Salomon, "Resonant scattering properties close to a p-wave Feshbach resonance," *Phys. Rev. A*, vol. 71, no. 6, p. 062710, 2005.

[107] K. B. Gubbels and H. T. C. Stoof, "Theory for *p*-Wave Feshbach Molecules," *Phys. Rev. Lett.*, vol. 99, no. 19, p. 190406, 2007.

[108] W. D. Phillips and H. Metcalf, "Laser Deceleration of an Atomic Beam," *Phys. Rev. Lett.*, vol. 48, no. 9, pp. 596–599, 1982.

[109] S. Chu, L. Hollberg, J. E. Bjorkholm, A. Cable, and A. Ashkin, "Three-dimensional viscous confinement and cooling of atoms by resonance radiation pressure," *Phys. Rev. Lett.*, vol. 55, no. 1, pp. 48–51, 1985.

[110] P. Zeeman, "On the influence of Magnetism on the Nature of the Light emitted by a substance," *Phil. Mag.*, vol. 43, p. 226, 1897.

[111] H. T. C. Stoof, J. M. V. A. Koelman, and B. J. Verhaar, "Spin-exchange and dipole relaxation rates in atomic hydrogen: Rigorous and simplified calculations," *Phys. Rev. B*, vol. 38, no. 7, pp. 4688–4697, 1988.

[112] O. K. Rice, "Predissociation and the Crossing of Molecular Energy Curves," *J. Chem. Phys*, vol. 1, p. 375, 1933.

[113] A. J. Moerdijk, B. J. Verhaar, and A. Axelsson, "Resonances in ultracold collisions of ^{6}Li, ^{7}Li, and ^{23}Na," *Phys. Rev. A*, vol. 51, no. 6, pp. 4852–4861, 1995.

[114] K. Góral, T. Köhler, S. A. Gardiner, E. Tiesinga, and P. S. Julienne, "Adiabatic association of ultracold molecules via magnetic-field tunable interactions," *J. Phys. B*, vol. 37, no. 17, p. 3457, 2004.

[115] B. A. Lippmann and J. Schwinger, "Variational Principles for Scattering Processes. I," *Phys. Rev.*, vol. 79, no. 3, pp. 469–480, 1950.

[116] R. G. Newton, *Scattering Theory of Wave and Particles*. New York: Dover, 2002.

[117] A. Derevianko, W. R. Johnson, M. S. Safronova, and J. F. Babb, "High-Precision Calculations of Dispersion Coefficients, Static Dipole Polarizabilities, and Atom-Wall Interaction Constants for Alkali-Metal Atoms," *Phys. Rev. Lett.*, vol. 82, no. 18, pp. 3589–3592, 1999.

[118] T. Loftus, C. A. Regal, C. Ticknor, J. L. Bohn, and D. S. Jin, "Resonant Control of Elastic Collisions in an Optically Trapped Fermi Gas of Atoms," *Phys. Rev. Lett.*, vol. 88, no. 17, p. 173201, 2002.

[119] N. Nygaard, B. I. Schneider, and P. S. Julienne, "Two-channel R-matrix analysis of magnetic-field-induced Feshbach resonances," *Phys. Rev. A*, vol. 73, p. 042705, 2006.

[120] Z.-C. Yan, J. F. Babb, A. Dalgarno, and G. W. F. Drake, "Variational calculations of dispersion coefficients for interactions among H, He, and Li atoms," *Phys. Rev. A*, vol. 54, no. 4, pp. 2824–2833, 1996.

[121] E. R. I. Abraham, W. I. McAlexander, J. M. Gerton, R. G. Hulet, R. Côté, and A. Dalgarno, "Triplet s-wave resonance in ^{6}Li collisions and scattering lengths of ^{6}Li and ^{7}Li ," *Phys. Rev. A*, vol. 55, no. 5, pp. R3299–R3302, 1997.

[122] C. H. Schunck, M. W. Zwierlein, C. A. Stan, S. M. F. Raupach, W. Ketterle, A. Simoni, E. Tiesinga, C. J. Williams, and P. S. Julienne, "Feshbach resonances in fermionic ^{6}Li ," *Phys. Rev. A*, vol. 71, no. 4, p. 045601, 2005.

[123] K. M. Jones, E. Tiesinga, P. D. Lett, and P. S. Julienne, "Ultracold photoassociation spectroscopy: Long-range molecules and atomic scattering," *Rev. Mod. Phys.*, vol. 78, no. 2, p. 483, 2006.

[124] P. Julienne and F. Mies, "Collisions of ultracold.trapped atoms," *J. Opt. Soc. Am. B*, vol. 6, pp. 2257–2269, 1989.

[125] G. F. Gribakin and V. V. Flambaum, "Calculation of the scattering length in atomic collisions using the semiclassical approximation," *Phys. Rev. A*, vol. 48, no. 1, pp. 546–553, 1993.

[126] C. Lovelace, "Practical Theory of Three-Particle States. I. Nonrelativistic," *Phys. Rev.*, vol. 135, no. 5B, pp. B1225–B1249, 1964.

[127] A. L. Fetter and J. D. Walecka, *Quantum Theory of Many-Particle Systems*. Dover, 2003.

[128] M. H. Szymańska, K. Góral, T. Köhler, and K. Burnett, "Conventional character of the BCS-BEC crossover in ultracold gases of $K40$," *Phys. Rev. A*, vol. 72, no. 1, p. 013610, 2005.

[129] Szymańska, M. H. and Simons, B. D. and Burnett, K. , "Dynamics of the bcs-bec crossover in a degenerate fermi gas," *Phys. Rev. Lett.*, vol. 94, no. 17, p. 170402, 2005.

[130] T. Köhler, K. Góral, and T. Gasenzer, "Heating and atom loss during upward ramps of Feshbach resonance levels in Bose-Einstein condensates," *Phys. Rev. A*, vol. 70, no. 2, p. 023613, 2004.

[131] N. N. Bogoliubov, "A New Method in The Theory of Superconductivity. 1," *Sov. Phys. JETP.*, vol. 34, no. 1, p. 41, 1958.

[132] V. J. G., "Comments on the Theory of Superconductivity," *Il Nuovo Cimento*, vol. 7, no. 6, p. 41, 1958.

[133] D. M. Eagles, "Possible Pairing without Superconductivity at Low Carrier Concentrations in Bulk and Thin-Film Superconducting Semiconductors," *Phys. Rev.*, vol. 186, no. 2, pp. 456–463, 1969.

[134] A. J. Leggett, "Diatomic molecules and Cooper pairs," in *Modern Trands in the Theory of Condensed Matter. Proceedings of the XVIth Karpacz Winter School of Theoretical Physics, Karpacz, Poland*, pp. 13–27, Springer-Verlag, 1980.

[135] L. N. Cooper, "Bound Electron Pairs in a Degenerate Fermi Gas," *Phys. Rev.*, vol. 104, no. 4, p. 1189, 1956.

[136] P. W. Anderson and P. Morel, "Generalized Bardeen-Cooper-Schrieffer States and the Proposed Low-Temperature Phase of Liquid ^{3}He," *Phys. Rev.*, vol. 123, no. 6, pp. 1911–1934, 1961.

[137] R. Balian and N. R. Werthamer, "Superconductivity with Pairs in a Relative *p* Wave," *Phys. Rev.*, vol. 131, no. 4, pp. 1553–1564, 1963.

[138] P. Nozieres and S.-R. S., "Bose Condensation in an Attractive Fermion Gas: From Weak to Strong Coupling Superconductivity," *J. Low Temp. Phys.*, vol. 59, no. 3/4, p. 195, 1985.

[139] M. Holland, S. J. J. M. F. Kokkelmans, M. L. Chiofalo, and R. Walser, "Resonance Superfluidity in a Quantum Degenerate Fermi Gas," *Phys. Rev. Lett.*, vol. 87, no. 12, p. 120406, 2001.

[140] E. Timmermans, K. Furuya, P. W. Milonni, and A. K. Kerman, "Prospect of creating a composite Fermi-Bose superfluid," *Phys. Lett. A*, vol. 285, no. 3-4, pp. 228 – 233, 2001.

[141] T. Matsubara, "A New Approach to Quantum-Statistical Mechanics," *Prog. Theor. Phys.*, vol. 14, no. 4, pp. 351–378, 1955.

[142] E. Timmermans, P. Tommasini, M. Hussein, and A. Kerman, "Feshabch resonances in atomic Bose-Einstein condensates," *Phys. Rep.*, vol. 315, p. 199, 1999.

[143] E. A. Donley, N. R. Claussen, T. S. T., and C. E. Wieman, "Atom-molecule coherence in a Bose-Einstein condensate," *Nature*, vol. 417, pp. 529–533, 2002.

[144] S. T. Thompson, E. Hodby, and C. E. Wieman, "Ultracold Molecule Production via a Resonant Oscillating Magnetic Field," *Phys. Rev. Lett.*, vol. 95, no. 19, p. 190404, 2005.

[145] E. Hodby, S. T. Thompson, C. A. Regal, M. Greiner, A. C. Wilson, D. S. Jin, E. A. Cornell, and C. E. Wieman, "Production Efficiency of Ultracold Feshbach Molecules in Bosonic and Fermionic Systems," *Phys. Rev. Lett.*, vol. 94, no. 12, p. 120402, 2005.

[146] J. Herbig, T. Kraemer, M. Mark, T. Weber, C. Chin, H.-C. Nagerl, and R. Grimm, "Preparation of a Pure Molecular Quantum Gas," *Science*, vol. 301, no. 5639, pp. 1510–1513, 2003.

[147] M. Mark, T. Kraemer, J. Herbig, C. Chin, H.-C. Nägerl, and R. Grimm, "Efficient creation of molecules from a cesium Bose-Einstein condensate," *Europhys. Lett.)*, vol. 69, no. 5, p. 706, 2005.

[148] S. Dürr, T. Volz, A. Marte, and G. Rempe, "Observation of Molecules Produced from a Bose-Einstein Condensate," *Phys. Rev. Lett.*, vol. 92, no. 2, p. 020406, 2004.

[149] S. Jochim, M. Bartenstein, A. Altmeyer, G. Hendl, C. Chin, J. H. Denschlag, and R. Grimm, "Pure Gas of Optically Trapped Molecules Created from Fermionic Atoms," *Phys. Rev. Lett.*, vol. 91, no. 24, p. 240402, 2003.

[150] C. Ospelkaus, S. Ospelkaus, L. Humbert, P. Ernst, K. Sengstock, and K. Bongs, "Ultracold Heteronuclear Molecules in a 3D Optical Lattice," *Phys. Rev. Lett.*, vol. 97, no. 12, p. 120402, 2006.

[151] J. J. Zirbel, K.-K. Ni, S. Ospelkaus, T. L. Nicholson, M. L. Olsen, P. S. Julienne, C. E. Wieman, J. Ye, and D. S. Jin, "Heteronuclear molecules in an optical dipole trap," *Phys. Rev. A*, vol. 78, no. 1, p. 013416, 2008.

[152] S. B. Papp and C. E. Wieman, "Observation of Heteronuclear Feshbach Molecules from a ^{85}Rb-^{87}Rb Gas," *Phys. Rev. Lett.*, vol. 97, no. 18, p. 180404, 2006.

[153] K. Xu, T. Mukaiyama, J. R. Abo-Shaeer, J. K. Chin, D. E. Miller, and W. Ketterle, "Formation of Quantum-Degenerate Sodium Molecules," *Phys. Rev. Lett.*, vol. 91, no. 21, p. 210402, 2003.

[154] T. Mukaiyama, J. R. Abo-Shaeer, K. Xu, J. K. Chin, and W. Ketterle, "Dissociation and Decay of Ultracold Sodium Molecules," *Phys. Rev. Lett.*, vol. 92, no. 18, p. 180402, 2004.

[155] M. Dowling, *Masters thesis, University College London*. 2009.

[156] L. D. Landau *Phys. Z. Sowjetunion*, vol. 2, p. 46, 1932.

[157] C. Zener *Proc. Roy. Soc.*, vol. A 137, p. 696, 1932.

[158] F. H. Mies, E. Tiesinga, and P. S. Julienne, "Manipulation of Feshbach resonances in ultracold atomic collisions using time-dependent magnetic fields," *Phys. Rev. A*, vol. 61, no. 2, p. 022721, 2000.

[159] G. Thalhammer, K. Winkler, F. Lang, S. Schmid, R. Grimm, and J. H. Denschlag, "Long-Lived Feshbach Molecules in a Three-Dimensional Optical Lattice," *Phys. Rev. Lett.*, vol. 96, no. 5, p. 050402, 2006.

[160] B. Dobrescu and V. Pokrovsky, "Production efficiency of Feshbach molecules in fermion systems," *Phys. Lett. A*, vol. 350, no. 1-2, pp. 154 – 158, 2006.

[161] V. Gurarie, "Feshbach molecule production in fermionic atomic gases," *Phys. Rev. A*, vol. 80, no. 2, p. 023626, 2009.

[162] J. Fricke, "Transport Equations Including Many-Particle Correlations for an Arbitrary Quantum System: A General Formalism," *Ann. Phys.*, vol. 252, no. 2, pp. 479 – 498, 1996.

[163] J. Levinsen, N. R. Cooper, and V. Gurarie, "Stability of fermionic gases close to a *p*-wave Feshbach resonance," *Phys. Rev. A*, vol. 78, p. 063616, 2008.

[164] T. Weber, J. Herbig, M. Mark, H.-C. Nägerl, and R. Grimm, "Bose-Einstein Condensation of Cesium," *Science*, vol. 299, pp. 232–235, 2003.

[165] T. Lahaye, C. Menotti, L. Santos, M. Lewenstein, and T. Pfau, "The physics of dipolar bosonic quantum gases," *Rep. Prog. Phys.*, vol. 72, no. 12, p. 126401, 2009.

[166] M. Abramowitz and I. A. Stegun, *Handbook of Mathematical Functions*. New York: Dover, 1965.

[167] L. Cook, *Private Correspondence*. 2009.

[168] L. Cook, "The results of the coupled channel calculation were provided by L. Cook in private correspondence.," 2010.

[169] I. S. Gradshteyn and I. M. Ryzhik, *Tables of Integrals, Series and Products*. Academic Press, 7th ed., 2007.

[170] L. Euler, *Introduction à l'analyse infinitésimale*. Volume 2, 1748.

[171] E. W. Weisstein, "Tanc function." from *Mathworld*– A Wolfram Web Resource. `http://mathworld.wolfram.com/TancFunction.html`.